

Ministry of Education and Science of the Russian Federation
Saint Petersburg National Research University of Information
Technologies, Mechanics, and Optics

NANOSYSTEMS:
PHYSICS, CHEMISTRY, MATHEMATICS

2014, volume 5(3)

Наносистемы: физика, химия, математика

2014, том 5, № 3



NANOSYSTEMS:

PHYSICS, CHEMISTRY, MATHEMATICS

ADVISORY BOARD MEMBERS

Chairman: V.N. Vasiliev (*St. Petersburg, Russia*),
V.M. Ievlev (*Voronezh*), P.S. Kop'ev (*St. Petersburg, Russia*),
V.N. Parmon (*Novosibirsk*), A.I. Rusanov (*St. Petersburg, Russia*).

EDITORIAL BOARD

Editor-in-Chief: N.F. Morozov (*St. Petersburg, Russia*)
Deputy Editor-in-Chief: I.Yu. Popov (*St. Petersburg, Russia*)

Section Co-Editors:

Physics – V.M. Uzdin (*St. Petersburg, Russia*),
Chemistry, material science – V.V. Gusarov (*St. Petersburg, Russia*),
Mechanics – A.K. Belyaev (*St. Petersburg, Russia*),
Mathematics – I.Yu. Popov (*St. Petersburg, Russia*).

Editorial Board Members:

V.M. Adamyan (*Odessa, Ukraine*); O.V. Al'myasheva (*St. Petersburg, Russia*); S. Bechta (*Stockholm, Sweden*); V.G. Bepalov (*St. Petersburg, Russia*); A. Chatterjee (*Hyderabad, India*); S.A. Chivilikhin (*St. Petersburg, Russia*); A.V. Chizhov (*Dubna, Russia*); P.P. Fedorov (*Moscow, Russia*); E.A. Gudilin (*Moscow, Russia*); D.A. Indeitsev (*St. Petersburg, Russia*); H. Jónsson (*Reykjavik, Iceland*); A.A. Kiselev (*Madison, USA*); Yu.S. Kivshar (*Canberra, Australia*); S.A. Kozlov (*St. Petersburg, Russia*); Yu.B. Kudasov (*Sarov, Russia*); S.E. Kul'kova (*Tomsk, Russia*); P.A. Kurasov (*Stockholm, Sweden*); A.V. Lukashin (*Moscow, Russia*); V.A. Margulis (*Saransk, Russia*); I.V. Melikhov (*Moscow, Russia*); G.P. Miroshnichenko (*St. Petersburg, Russia*); H. Neidhardt (*Berlin, Germany*); K. Pankrashkin (*Orsay, France*); B.S. Pavlov (*Auckland, New Zealand*); A.V. Ragulya (*Kiev, Ukraine*); V. Rajendran (*Tamil Nadu, India*); A.A. Rempel (*Ekaterinburg, Russia*); V.P. Romanov (*St. Petersburg, Russia*); V.Ya. Rudyak (*Novosibirsk, Russia*); V.M. Talanov (*Novocherkassk, Russia*); A.Ya. Vul' (*St. Petersburg, Russia*).

Editors:

I.V. Blinova; A.I. Popov; M.A. Skryabin; A.I. Trifanov; E.S. Trifanova (*St. Petersburg, Russia*),
R. Simoneaux (*USA*).

Address: ITMO University, Kronverkskiy pr., 49, St. Petersburg 197101, Russia.

Phone: +7(812)232-67-65, **Journal site:** <http://nanojournal.ifmo.ru/>,

E-mail: popov1955@gmail.com

AIM AND SCOPE

The scope of the journal includes all areas of nano-sciences. Papers devoted to basic problems of physics, chemistry, material science and mathematics inspired by nanosystems investigations are welcomed. Both theoretical and experimental works concerning the properties and behavior of nanosystems, problems of its creation and application, mathematical methods of nanosystem studies are considered.

The journal publishes scientific reviews (up to 30 journal pages), research papers (up to 15 pages) and letters (up to 5 pages). All manuscripts are peer-reviewed. Authors are informed about the referee opinion and the Editorial decision.

Content

MATHEMATICS

T.H. Rasulov, Z.D. Rasulova

- Essential and discrete spectrum of a three-particle lattice Hamiltonian with non-local potentials** 327

PHYSICS

V.A. Ambartsumyan, E.A. Andryushchenko, K.V. Bukhensky, A.B. Dubois, E.A. Dvoretzkova, T.V. Gordova, S.I. Kucheryavy, S.N. Mashnina, A.S. Safoshkin

- Channels of electron-electron interactions in highly doped heterojunction** 343

A.V. Bespalov, E.V. Vilkova

- Time-series rate of convergence to quasi-periodic oscillations** 354

A. Drozdov, I. Pomortsev, K. Tyutyukin, Y. Baloshin

- Comparison of wavelet transform and Fourier transform applied to analysis of non-stationary processes** 363

A.M. Gerasimov, N.D. Kundikova, Yu.V. Miklyaev, D.G. Pikhulya, M.V. Terpugov

- Conversion efficiency of second harmonic generation in one-dimensional photonic crystal based from isotropic material** 374

V.V. Karpunin, V.A. Margulis

- The absorption of electromagnetic radiation in a quantum wire** 378

V.D. Lukyanov

- Relationship plurality approximation** 384

A.I. Popov, I.S. Lobanov, I.Yu. Popov, T.V. Gerya

- Benchmark solutions for nanoflows** 391

O.A. Rodygina, S.A. Chivilikhin, I.Yu. Popov, V.V. Gusarov

- Crystallite model for flow in nanotube caused by wall soliton** 400

CHEMISTRY AND MATERIAL SCIENCE

O.V. Almjashaeva, V.V. Gusarov

- Metastable clusters and aggregative nucleation mechanism** 405

I.Ya. Mittova, V.F. Kostryukov

- GaAs thermal oxidation activated by the coaction of p-block oxides** 417

K.N. Semenov, N.A. Charykov, A.S. Kritchenkov, I.A. Cherepkova, O.S. Manyakina, D.P. Tyurin, A.A. Shestopalova, V.A. Keskinov, K.V. Ivanova, N.M. Ivanova, D.G. Letenko, V.A. Nikitin, E.L. Fokina, O.V. Rakhimova

- Volume properties of water solution and refraction at 25 °C water-soluble tris-malonate of light fullerene- $C_{60}[=C(COOH)_2]_3$** 427

K.N. Semenov, N.A. Charykov, A.S. Kritchenkov, I.A. Cherepkova, O.S. Manyakina, D.P. Tyurin, A.A. Shestopalova, V.A. Keskinov, K.V. Ivanova, N.M. Ivanova, D.G. Letenko, V.A. Nikitin, E.L. Fokina, I.A. Pestov, A.O. Netrusov	
Poly-thermal solubility and complex thermal analysis of water-soluble tris-malonate of light fullerene – C₆₀[=C(COOH)₂]₃	435
P.A. Sheena, K.P. Priyanka, N. Aloysius Sabu, Bobby Sabu, Thomas Varghese	
Effect of calcination temperature on the structural and optical properties of nickel oxide nanoparticles	441
Information for authors	450

ESSENTIAL AND DISCRETE SPECTRUM OF A THREE-PARTICLE LATTICE HAMILTONIAN WITH NON-LOCAL POTENTIALS

T. H. Rasulov, Z. D. Rasulova

Bukhara State University, Bukhara, Uzbekistan

rth@mail.ru, zdrasulova@mail.ru

PACS 02.30.Tb

We consider a model operator (Hamiltonian) H associated with a system of three particles on a d -dimensional lattice that interact via non-local potentials. Here the kernel of non-local interaction operators has rank n with $n \geq 3$. We obtain an analog of the Faddeev equation for the eigenfunctions of H and describe the spectrum of H . It is shown that the essential spectrum of H consists the union of at most $n + 1$ bounded closed intervals. We estimate the lower bound of the essential spectrum of H for the case $d = 1$.

Keywords: three-particle lattice Hamiltonian, non-local interaction operators, Hubbard model, Faddeev equation, essential and discrete spectrum.

Received: 5 May 2014

1. Introduction

In the physical literature, local potentials, i.e., multiplication operators by a function, are typically used. But the potentials constructed, for example, in pseudo-potential theory [6] turn out to be non-local. Such for a periodic operator are given by the sum of local and a finite dimensional potentials. Non-local separable two-body interactions have often been used in nuclear physics and many-body problems because of the fact that the two-body Schrödinger equation is easily solvable for them, and leads to closed expressions for a large class of such interactions. They have also been used very systematically with Faddeev equations for the three-body problem. Their main feature is that the partial-wave t -matrix has a very simple form, and can be continued off the energy-shell in a straightforward manner, a feature which is most important, as is well known, in nuclear physics, and in the Faddeev equations [11].

Many works are devoted to the investigations of the essential spectrum of the discrete Schrödinger operators with local potentials, see e.g., [2,8]. In particular, in [2] it was proved that the essential spectrum of a three-particle discrete Schrödinger operator is the union of at most finitely many closed intervals even in the case where the corresponding two-particle discrete Schrödinger operator has an infinite number of eigenvalues.

In the present paper, we study the model operator H associated with a system of three particles on a d -dimensional lattice and interacting via non-local potentials, where the role of a two-particle discrete Schrödinger operator played by the Friedrichs model. Usually, such operators are arise in the Hubbard model [7,9]. It is remarkable that the Hubbard model is currently one of the most intensively studied many-electron models of metal, but very few exact results have been obtained for the spectrum and the wave functions of the crystal described by this model. Hence, it is very interesting to obtain exact results, at least in special cases, for example, in the case of non-local potentials. For this reason, we intend to discuss the case

where the kernel of non-local interaction operators (partial integral operators) has rank n with $n \geq 3$. An important problem in the spectral theory of such operators is to describe the essential spectrum and to study the number of eigenvalues located outside the essential spectrum.

The following results are obtained:

- (i) We construct an analog of the Faddeev equation for the eigenfunctions of H ;
- (ii) We describe the location of the essential spectrum of H and show that it is the union of at most $n + 1$ bounded closed intervals;
- (iii) We find upper bound of the spectrum of H ;
- (iv) We estimate the lower bound of the essential spectrum of H for the case $d = 1$.

We remark that the results (i) and (ii) has been announced in [16] without proof. This paper is devoted to the detailed proof of the results (i)–(iv).

The organization of the present paper is as follows. Section 1 is an introduction. In Section 2, the model operator H is described as a bounded self-adjoint operator in the Hilbert space. In Section 3, the main results are formulated. In Section 4, the number and location of the eigenvalues of the corresponding Friedrichs model are studied. In Section 5, an analog of the Faddeev equation and its symmetric version for the eigenfunctions of H is obtained. In Section 5, the essential spectrum of H is investigated. In Section 7, the lower bound of the essential spectrum of H is estimated for the case $d = 1$.

2. Three-particle model operator on a lattice

Let \mathbb{C} , \mathbb{R} , \mathbb{Z} and \mathbb{N} be the set of all complex, real, integer and positive integer numbers, respectively.

We consider the discrete Schrödinger operator $\hat{A} := \hat{A}_0 - \hat{K}$ acting in the space $l_2((\mathbb{Z}^d)^2)$. The kinetic energy \hat{A}_0 is given by a convolution with a function of the general form:

$$(\hat{A}_0 \hat{\psi})(s_1, s_2) = \sum_{n_1, n_2 \in \mathbb{Z}^d} u_0(s_1 - n_1, s_2 - n_2) \hat{\psi}(n_1, n_2),$$

and the potential energy \hat{K} is defined by:

$$(\hat{K} \hat{\psi})(s_1, s_2) = (u_1(s_1) + u_2(s_2)) \hat{\psi}(s_1, s_2).$$

We assume that the functions $u_0(\cdot, \cdot)$ and u_α , $\alpha = 1, 2$ satisfy the conditions

$$|u_0(s_1, s_2)| \leq C_0 \exp(-a(|s_1| + |s_2|)), \quad a > 0;$$

$$|u_\alpha(s_1)| \leq C_\alpha \exp(-b_\alpha |s_1|), \quad b_\alpha > 0, \quad \alpha = 1, 2,$$

where $|s_1| := |s_{11}| + \dots + |s_{1d}|$ for $s_1 = (s_{11}, \dots, s_{1d}) \in \mathbb{Z}^d$ and C_α , $\alpha = 1, 2, 3$ are constants.

The operator \hat{A} is a particular case of the lattice model Hamiltonian studied in [10, 18].

Let \mathbb{T}^d be the d -dimensional torus. The operations addition and multiplication by real numbers elements of $\mathbb{T}^d \subset \mathbb{R}^d$ should be regarded as operations on \mathbb{R}^d modulo $(2\pi\mathbb{Z}^1)^d$. For example, if $d = 4$ and

$$a = \left(\frac{\pi}{2}, \frac{\pi}{6}, -\frac{2\pi}{3}, \frac{2\pi}{3} \right), \quad b = \left(\frac{2\pi}{3}, -\frac{5\pi}{6}, -\frac{\pi}{2}, \frac{5\pi}{6} \right) \in \mathbb{T}^4,$$

then

$$a + b = \left(-\frac{5\pi}{6}, -\frac{2\pi}{3}, \frac{5\pi}{6}, -\frac{\pi}{2} \right), \quad 6a = (\pi, \pi, 0, 0) \in \mathbb{T}^4.$$

Let $L_2((\mathbb{T}^d)^\alpha)$ be the Hilbert space of square integrable (complex) functions defined on $(\mathbb{T}^d)^\alpha$, $\alpha = 1, 2$ and $\mathcal{F} : l_2((\mathbb{Z}^d)^2) \rightarrow L_2((\mathbb{T}^d)^2)$ be the standard Fourier transformation:

$$(\mathcal{F}\widehat{\psi})(p, q) = \frac{1}{(2\pi)^d} \sum_{n_1, n_2 \in \mathbb{Z}^d} \widehat{\psi}(n_1, n_2) \exp(i[(p, n_1) + (q, n_2)]).$$

Then, (see [18]) the operator:

$$A := \mathcal{F}\widehat{A}\mathcal{F}^{-1} : L_2((\mathbb{T}^d)^2) \rightarrow L_2((\mathbb{T}^d)^2)$$

can be represented as $A := A_0 - K_1 - K_2$, where the operators A_0 and K_α , $\alpha = 1, 2$ are defined by:

$$(A_0 f)(p, q) = k_0(p, q)f(p, q), \quad f \in L_2((\mathbb{T}^d)^2);$$

$$(K_1 f)(p, q) = \int_{\mathbb{T}^d} k_1(p-s)f(s, q)ds, \quad (K_2 f)(p, q) = \int_{\mathbb{T}^d} k_2(q-s)f(p, s)ds, \quad f \in L_2((\mathbb{T}^d)^2).$$

Here $k_0(\cdot, \cdot)$ and $k_\alpha(\cdot, \cdot)$ are the Fourier transform of the functions $u_0(\cdot, \cdot)$ and $u_\alpha(\cdot, \cdot)$, $\alpha = 1, 2$, respectively. Usually, the operator A is called the momentum representation of the discrete operator \widehat{A} .

In the Hilbert space $L_2^s((\mathbb{T}^d)^2)$ of square integrable symmetric (complex) functions defined on $(\mathbb{T}^d)^2$, we consider the model operator:

$$H := H_0 - V_1 - V_2, \tag{2.1}$$

where H_0 is the multiplication operator by the function $w(\cdot, \cdot)$:

$$(H_0 f)(p, q) = w(p, q)f(p, q)$$

and V_α , $\alpha = 1, 2$ are non-local interaction operators:

$$(V_1 f)(p, q) = \sum_{i=1}^n v_i(q) \int_{\mathbb{T}^d} v_i(s)f(p, s)ds, \quad (V_2 f)(p, q) = \sum_{i=1}^n v_i(p) \int_{\mathbb{T}^d} v_i(s)f(s, q)ds.$$

Here, $f \in L_2^s((\mathbb{T}^d)^2)$, $n \in \mathbb{N}$ with $n \geq 3$, the functions $v_i(\cdot)$, $i = 1, \dots, n$ are real-valued linearly independent continuous functions on \mathbb{T}^d and the function $w(\cdot, \cdot)$ is a real-valued symmetric continuous function on $(\mathbb{T}^d)^2$. By definition, the operators V_α , $\alpha = 1, 2$ are partial integral operators with a degenerate kernel of rank n .

Under these assumptions, the operator H is bounded and self-adjoint.

The spectrum, the essential spectrum and the discrete spectrum of a bounded self-adjoint operator will be denoted by $\sigma(\cdot)$, $\sigma_{\text{ess}}(\cdot)$ and $\sigma_{\text{disc}}(\cdot)$, respectively.

Schrödinger operators of the form (2.1), associated with a system of three particles on a lattice, were studied in [1, 3, 5, 14] for the case $n = 1$ and [15] for the case $n = 2$. In [1, 3] the sufficient conditions for the finiteness and infiniteness of the discrete spectrum are found. In [14], the Efimov effect for (2.1) was demonstrated when the parameter function $w(\cdot, \cdot)$ has a special form. In [5] the essential spectrum and the number of eigenvalues of the model (2.1) were studied for the function $w(\cdot, \cdot)$ of the form $w(p, q) = u(p)u(q)$.

3. Statements of the main results

To study the spectral properties of the operator H , we introduce a family of bounded self-adjoint operators (Friedrichs models) $h(p)$, $p \in \mathbb{T}^d$, acting on $L_2(\mathbb{T}^d)$ by the rule:

$$h(p) := h_0(p) - v,$$

where $h_0(p)$ is the multiplication operator by the function $w(p, \cdot)$ on $L_2(\mathbb{T}^d)$:

$$(h_0(p)f)(q) = w(p, q)f(q)$$

and v is the non-local interaction operator on $L_2(\mathbb{T}^d)$:

$$(vf)(q) = \sum_{i=1}^n v_i(q) \int_{\mathbb{T}^d} v_i(s)f(s)ds.$$

The perturbation v of the operator $h_0(p)$ is a self-adjoint operator of rank n . Therefore, in accordance with the Weyl theorem about the invariance of the essential spectrum under the finite rank perturbations, the essential spectrum of the operator $h(p)$ coincides with the essential spectrum of $h_0(p)$. It is evident that $\sigma_{\text{ess}}(h_0(p)) = [m(p); M(p)]$, where the numbers $m(p)$ and $M(p)$ are defined by:

$$m(p) := \min_{q \in \mathbb{T}^d} w(p, q) \quad \text{and} \quad M(p) := \max_{q \in \mathbb{T}^d} w(p, q).$$

This yields $\sigma_{\text{ess}}(h(p)) = [m(p); M(p)]$.

We remark that for some $p \in \mathbb{T}^d$ the essential spectrum of $h(p)$ may degenerate to the set consisting of the unique point $\{m(p)\}$ and hence we cannot state that the essential spectrum of $h(p)$ is absolutely continuous for any $p \in \mathbb{T}^d$. For example, if the function $w(\cdot, \cdot)$ has the form:

$$w(p, q) := \sum_{i=1}^d [3 - \cos p_i - \cos(p_i + q_i) - \cos q_i], \quad q = (q_1, \dots, q_d) \in \mathbb{T}^d,$$

and $p = \bar{\pi} := (\pi, \dots, \pi) \in \mathbb{T}^d$, then $\sigma_{\text{ess}}(h(\bar{\pi})) = \{4d\}$.

For any $p \in \mathbb{T}^d$, we define the analytic functions in $\mathbb{C} \setminus [m(p); M(p)]$ by:

$$I_{ij}(p; z) := \int_{\mathbb{T}^d} \frac{v_i(s)v_j(s)ds}{w(p, s) - z}, \quad i, j = 1, \dots, n;$$

$$\Delta(p; z) := \det (\delta_{ij} - I_{ij}(p; z))_{i,j=1}^n, \quad \delta_{ij} := \begin{cases} 1, & \text{if } i = j \\ 0, & \text{if } i \neq j \end{cases}.$$

It is clear that $I_{ij}(p; z) = I_{ji}(p; z)$ for all $i, j = 1, \dots, n$. The function $\Delta(p; \cdot)$ is called the Fredholm determinant associated with the operator $h(p)$.

Note that for the discrete spectrum of $h(p)$, the equality

$$\sigma_{\text{disc}}(h(p)) = \{z \in \mathbb{C} \setminus [m(p); M(p)] : \Delta(p; z) = 0\}$$

holds (see Lemma 4.1).

Let us introduce the following notations:

$$m := \min_{p, q \in \mathbb{T}^d} w(p, q), \quad M := \max_{p, q \in \mathbb{T}^d} w(p, q), \quad \sigma := \bigcup_{p \in \mathbb{T}^d} \sigma_{\text{disc}}(h(p)), \quad \Sigma := \sigma \cup [m; M];$$

$$L_2^{(n)}(\mathbb{T}^d) := \{g = (g_1, \dots, g_n) : g_i \in L_2(\mathbb{T}^d), i = 1, \dots, n\}.$$

For each $z \in \mathbb{C} \setminus [m; M]$, we define the $n \times n$ block operator matrices $A(z)$ and $K(z)$ acting in the Hilbert space $L_2^{(n)}(\mathbb{T}^d)$ as:

$$A(z) := (A_{ij}(z))_{i,j=1}^n, \quad K(z) := (K_{ij}(z))_{i,j=1}^n,$$

where the operator $A_{ij}(z)$ is the multiplication operator by the function $\delta_{ij} - I_{ij}(\cdot; z)$ and the operator $K_{ij}(z)$ is the integral operator with the kernel:

$$K_{ij}(p, s; z) := \frac{v_j(p)v_i(s)}{w(p, s) - z},$$

(s is the integration variable).

We note that for each $z \in \mathbb{C} \setminus [m; M]$, all entries of $K(z)$ belong to the Hilbert-Schmidt class and therefore, $K(z)$ is a compact operator.

Recall that for each $z \in \mathbb{C} \setminus \Sigma$, the operator $A(z)$ is bounded and invertible (see Lemma 5.1) and for such z we define the operator $T(z) := A^{-1}(z)K(z)$.

Now, we give the main results of the paper.

The following theorem is an analog of the well-known Faddeev’s result for the operator H and establishes a connection between eigenvalues of H and $T(z)$.

Theorem 3.1. *The number $z \in \mathbb{C} \setminus \Sigma$ is an eigenvalue of the operator H if and only if the number $\lambda = 1$ is an eigenvalue of the operator $T(z)$. Moreover, the eigenvalues z and 1 have the same multiplicities.*

We point out that the matrix equation $T(z)g = g$, $g \in L_2^{(n)}(\mathbb{T}^d)$ is an analog of the Faddeev type system of integral equations for eigenfunctions of the operator H and it plays a crucial role in the analysis of the spectrum of H .

Since for any $z \in \mathbb{C} \setminus \Sigma$ the kernels of the entries of $T(z)$ are continuous functions on $(\mathbb{T}^d)^2$, the Fredholm determinant $\Delta(z)$ of the operator $I - T(z)$, where I is the identity operator in $L_2^{(n)}(\mathbb{T}^d)$, exists and is a real-analytic function on $\mathbb{C} \setminus \Sigma$.

According to Fredholm’s theorem and Theorem 3.1, the number $z \in \mathbb{C} \setminus \Sigma$ is an eigenvalue of H if and only if $\Delta(z) = 0$, that is,

$$\sigma_{\text{disc}}(H) = \{z \in \mathbb{C} \setminus \Sigma : \Delta(z) = 0\}.$$

The following theorem describes the essential spectrum of the operator H .

Theorem 3.2. *For the essential spectrum of H , the equality $\sigma_{\text{ess}}(H) = \Sigma$ holds. Moreover the set $\sigma_{\text{ess}}(H)$ consists no more than $n + 1$ bounded closed intervals and $\max(\sigma_{\text{ess}}(H)) = M$.*

The sets σ and $[m; M]$ are called two- and three-particle branches of the essential spectrum of H , respectively.

The definition of the set σ and the equality,

$$\bigcup_{p \in \mathbb{T}^d} [m(p); M(p)] = [m; M]$$

together with Theorem 3.2, give the following equality:

$$\sigma_{\text{ess}}(H) = \bigcup_{p \in \mathbb{T}^d} \sigma(h(p)). \tag{3.1}$$

Here, the family of operators $h(p)$ have a simpler structure than the operator H . Hence, in many instances, (3.1) provides an effective tool for the description of the essential spectrum.

or $n \times n$ matrix equation

$$(\delta_{ij} - I_{ij}(p; z(p)))_{i,j=1}^n \begin{pmatrix} C_1 \\ \vdots \\ C_n \end{pmatrix} = 0$$

has a nontrivial solution $(C_1, \dots, C_n) \in \mathbb{C}^n$, i.e., if the condition $\Delta(p; z(p)) = 0$ is satisfied, where \mathbb{C}^n is the n -th Cartesian power of the set \mathbb{C} . Lemma 4.1 is proven. \square

For $\lambda \in \mathbb{R}$ and a bounded self-adjoint operator A acting in the Hilbert space \mathcal{H} denoted by $\mathcal{H}_A(\lambda)$, a subspace such that $(Af, f) < \lambda \|f\|^2$ for any $f \in \mathcal{H}_A(\lambda)$ and set

$$N(\lambda, A) := \sup_{\mathcal{H}_A(\lambda)} \dim \mathcal{H}_A(\lambda).$$

The number $N(\lambda, A)$ is equal to infinity if $\lambda > \max(\sigma_{\text{ess}}(A))$; if $N(\lambda, A)$ is finite, then it is equal to the number of the eigenvalues of A smaller than λ .

The following lemma describes the number and location of the eigenvalues of $h(p)$.

Lemma 4.2. *For any fixed $p \in \mathbb{T}^d$, the operator $h(p)$ has no more than n eigenvalues (counting multiplicities) lying on the l.h.s. of $m(p)$ and has no eigenvalues on the r.h.s. of $M(p)$.*

Proof. Let $p \in \mathbb{T}^d$ be a fixed. Since the operator v is a self-adjoint operator of rank n , applying Theorem 9.3.3 of [4] we obtain:

$$N(m(p), h_0(p)) - n \leq N(m(p), h(p)) \leq N(m(p), h_0(p)) + n;$$

$$N(-M(p), -h_0(p)) - n \leq N(-M(p), -h(p)) \leq N(-M(p), -h_0(p)) + n.$$

The equality $\sigma(h_0(p)) = [m(p); M(p)]$ implies that

$$N(m(p), h_0(p)) = N(-M(p), -h_0(p)) = 0.$$

Thus, $N(m(p), h(p)) \leq n$.

From the positivity of the operator v , it follows that the assertions:

$$((h(p) - z)f, f) = \int (w(p, s) - z)|f(s)|^2 ds - (vf, f) < 0,$$

hold for any $z > M(p)$ and $f \in L_2(\mathbb{T}^d)$. This means that the operator $h(p)$ has no eigenvalues lying on the r.h.s. of $M(p)$, that is, $N(-M(p), -h(p)) = 0$. Lemma 4.2 is proven. \square

5. An analog of the Faddeev equation for eigenfunctions of H

In this section, we derive an analog of the Faddeev type system of integral equations for the eigenfunctions, corresponding to the eigenvalues of H , that is, we prove Theorem 3.1. First, we give an additional lemma.

For any fixed $p \in \mathbb{T}^d$ we define the matrix-valued analytic functions in $\mathbb{C} \setminus [m(p); M(p)]$ by

$$A(p; \cdot) := (\delta_{ij} - I_{ij}(p; \cdot))_{i,j=1}^n, \quad \Delta_{ij}(p; \cdot) := (-1)^{i+j} M_{ij}(p; \cdot),$$

where $M_{ij}(p; z)$ is the (i, j) minor, i.e., the determinant of the submatrix formed from the original matrix $A(p; z)$ by deleting the i -th row and j -th column ($i, j = 1, \dots, n$).

Lemma 5.1. For any $z \in \mathbb{C} \setminus \Sigma$, the operator $A(z)$ is bounded and invertible. Moreover, the inverse operator $A^{-1}(z)$ is the multiplication operator by the matrix:

$$A^{-1}(p; z) := \frac{1}{\Delta(p; z)} \begin{pmatrix} \Delta_{11}(p; z) & \Delta_{21}(p; z) & \dots & \Delta_{n1}(p; z) \\ \Delta_{12}(p; z) & \Delta_{22}(p; z) & \dots & \Delta_{n2}(p; z) \\ \vdots & \vdots & \ddots & \vdots \\ \Delta_{1n}(p; z) & \Delta_{2n}(p; z) & \dots & \Delta_{nn}(p; z) \end{pmatrix}.$$

Proof. By definition, $A(z)$ is the multiplication operator by the matrix $A(p; z)$.

It is clear that for any fixed $z \in \mathbb{C} \setminus [m; M]$, the matrix-valued function $A(\cdot; z)$ is continuous on the compact set \mathbb{T}^d . This fact yields the boundedness of the operator $A(z)$. Taking into account the equality $\det(A(p; z)) = \Delta(p; z)$, we obtain that for any $p \in \mathbb{T}^d$ and $z \notin \Sigma$ the inequality $\det(A(p; z)) \neq 0$ holds. Therefore, for any $p \in \mathbb{T}^d$ and $z \notin \Sigma$ the matrix $A(p; z)$ is invertible. Now, using the definition of $A^{-1}(p; z)$, one can easily see that for any $z \notin \Sigma$, the operator $A^{-1}(z)$ is the inverse to $A(z)$ and is bounded. Lemma 5.1 is thus proved. \square

Proof of Theorem 3.1. Let $z \in \mathbb{C} \setminus \Sigma$ be an eigenvalue of the operator H and $f \in L_2^s((\mathbb{T}^d)^2)$ be the corresponding eigenfunction. Then, the function f satisfies the equation $Hf = zf$ or

$$(w(p, q) - z)f(p, q) - \sum_{i=1}^n \left[v_i(q) \int_{\mathbb{T}^d} v_i(s)f(p, s)ds + v_i(p) \int_{\mathbb{T}^d} v_i(s)f(s, q)ds \right] = 0. \tag{5.1}$$

The condition $z \notin [m; M]$ yields that the inequality $w(p, q) - z \neq 0$ holds for all $p, q \in \mathbb{T}^d$. Then, from equation (5.1), we have that the function f has form:

$$f(p, q) = \frac{1}{w(p, q) - z} \sum_{i=1}^n [v_i(q)g_i(p) + v_i(p)g_i(q)], \tag{5.2}$$

where for $i = 1, \dots, n$ the functions $g_i(\cdot)$ are defined by:

$$g_i(p) := \int_{\mathbb{T}^d} v_i(s)f(p, s)ds. \tag{5.3}$$

For any $i, j \in \{1, \dots, n\}$, $p \in \mathbb{T}^d$ and $z \notin [m; M]$, we set

$$\widehat{g}_{ij}(p; z) := \int_{\mathbb{T}^d} \frac{v_i(s)g_j(s)}{w(p, s) - z} ds.$$

Substituting the expression (5.2) for f to the equality (5.3), we obtain that the following system of n linear equations with n unknowns:

$$\begin{cases} \sum_{i=1}^n (\delta_{1i} - I_{1i}(p; z))g_i(p) = \sum_{j=1}^n v_j(p)\widehat{g}_{1j}(p; z) \\ \sum_{i=1}^n (\delta_{2i} - I_{2i}(p; z))g_i(p) = \sum_{j=1}^n v_j(p)\widehat{g}_{2j}(p; z) \\ \dots\dots\dots \\ \sum_{i=1}^n (\delta_{ni} - I_{ni}(p; z))g_i(p) = \sum_{j=1}^n v_j(p)\widehat{g}_{nj}(p; z) \end{cases}$$

or $n \times n$ matrix equation

$$A(z)g = K(z)g, \quad g = (g_1, \dots, g_n) \in L_2^{(n)}(\mathbb{T}^d) \tag{5.4}$$

has a nontrivial solution if and only if the equation (5.1) has a nontrivial solution and the linear subspaces of solutions of (5.1) and (5.4) have the same dimension.

By Lemma 5.1, for any $z \in \mathbb{C} \setminus \Sigma$, the operator $A(z)$ is invertible and hence, equation (5.4) is equivalent to the following $n \times n$ matrix equation $g = A^{-1}(z)K(z)g$, i.e. the equation $g = T(z)g$ has a nontrivial solution if and only if the equation (5.4) has a nontrivial solution. \square

It is easy to see that for any $p \in \mathbb{T}^d$ and $z < \min \Sigma$ the inequality $\Delta(p; z) > 0$ holds. This means that the operator $A(z)$ is a strictly positive and hence, there exists its positive square root, which will be denoted by $A^{-\frac{1}{2}}(z)$. So for $z < \min \Sigma$ we define the operator $\widehat{T}(z) := A^{-\frac{1}{2}}(z)K(z)A^{-\frac{1}{2}}(z)$. Then the operator equation $\widehat{T}(z)g = g$ is called the symmetric version of the Faddeev equation for the eigenfunction of the operator H . Analogously to Theorem 3.1 one can prove that the number $z < \min \Sigma$ is an eigenvalue of the operator H if and only if the number 1 is an eigenvalue of $\widehat{T}(z)$.

6. Investigations of the essential spectrum of H

In this section, applying the statements of sections 4 and 5, the Weyl criterion [17] and the theorem on the spectrum of decomposable operators [17] we prove Theorem 3.2.

Denote by $\|\cdot\|$ and (\cdot, \cdot) the norm and scalar product in the corresponding Hilbert spaces.

Proof of Theorem 3.2. We start the proof with the inclusion $\Sigma \subset \sigma_{\text{ess}}(H)$. Since the set Σ has form $\Sigma = \sigma \cup [m; M]$, first we show that $[m; M] \subset \sigma_{\text{ess}}(H)$. Let $z_0 \in [m; M]$ be an arbitrary point. We prove that $z_0 \in \sigma_{\text{ess}}(H)$. To this end, it is convenient to use Weyl criterion [17], i.e. it suffices to construct a sequence of orthonormal functions $\{f_k\} \subset L_2^s((\mathbb{T}^d)^2)$ such that $\|(H - z_0 E)f_k\| \rightarrow 0$ as $k \rightarrow \infty$. Here, E is an identity operator on $L_2^s((\mathbb{T}^d)^2)$.

From continuity of the function $w(\cdot, \cdot)$ on the compact set $(\mathbb{T}^d)^2$, it follows that there exists some point $(p_0, q_0) \in (\mathbb{T}^d)^2$ such that $z_0 = w(p_0, q_0)$.

For $k \in \mathbb{N}$ we consider the following vicinity of the point $(p_0, q_0) \in (\mathbb{T}^d)^2$:

$$W_k := V_k(p_0) \times V_k(q_0),$$

where

$$V_k(p_0) := \left\{ p \in \mathbb{T}^d : \frac{1}{k+1} < |p - p_0| < \frac{1}{k} \right\},$$

is the punctured neighborhood of the point $p_0 \in \mathbb{T}^d$.

Let $\mu(\Omega)$ be the Lebesgue measure of the set Ω and $\chi_\Omega(\cdot)$ be the characteristic function of the set Ω . We choose the sequence of functions $\{f_k\} \subset L_2^s((\mathbb{T}^d)^2)$ as follows:

$$f_k(p, q) := \frac{1}{\sqrt{\mu(W_k)}} \chi_{W_k}(p, q).$$

It is clear that $\{f_k\}$ is an orthonormal sequence.

For any $k \in \mathbb{N}$, let us consider $(H - z_0 E)f_k$ and estimate its norm:

$$\|(H - z_0 E)f_k\|^2 \leq 2 \sup_{(p,q) \in W_k} |w(p, q) - z_0|^2 + 8n \mu(V_k(p_0)) \sum_{i=1}^n \|v_i\|^2 \max_{p \in \mathbb{T}^d} |v_i(p)|^2.$$

From the construction of the set $V_k(p_0)$ and from the continuity of the function $w(\cdot, \cdot)$, it follows $\|(H - z_0 E)f_k\| \rightarrow 0$ as $k \rightarrow \infty$, i.e. $z_0 \in \sigma_{\text{ess}}(H)$. Since the point z_0 is arbitrary, we have $[m; M] \subset \sigma_{\text{ess}}(H)$.

Now, let us prove that $\sigma \subset \sigma_{\text{ess}}(H)$. Taking an arbitrary point $z_1 \in \sigma$, we show that $z_1 \in \sigma_{\text{ess}}(H)$. Two cases are possible: $z_1 \in [m; M]$ or $z_1 \notin [m; M]$. If $z_1 \in [m; M]$, then it is already proven above that $z_1 \in \sigma_{\text{ess}}(H)$. Let $z_1 \notin [m; M]$. Definition of the set σ and Lemma 4.1

imply that there exists a point $p_1 \in \mathbb{T}^d$ such that $\Delta(p_1; z_1) = 0$. Then, the system of n linear homogeneous equations with n unknowns:

$$\begin{cases} \sum_{j=1}^n (\delta_{1j} - I_{1j}(p_1; z_1))l_j = 0 \\ \sum_{j=1}^n (\delta_{2j} - I_{2j}(p_1; z_1))l_j = 0 \\ \dots\dots\dots \\ \sum_{j=1}^n (\delta_{nj} - I_{nj}(p_1; z_1))l_j = 0 \end{cases}$$

or $n \times n$ matrix equation

$$(\delta_{ij} - I_{ij}(p_1; z_1))_{i,j=1}^n \begin{pmatrix} l_1 \\ \vdots \\ l_n \end{pmatrix} = 0 \tag{6.1}$$

with respect to l_1, \dots, l_n has infinitely many solutions.

We denote by $l' := (l'_1, \dots, l'_n) \in \mathbb{C}^n$ one of the non-trivial solution of (6.1).

Let us choose a sequence of orthogonal functions $\{\tilde{f}_k\}$ as follows:

$$\tilde{f}_k(p, q) := \frac{1}{w(p, q) - z_1} \sum_{i=1}^n \left[v_i(q)g_i^{(k)}(p) + v_i(p)g_i^{(k)}(q) \right],$$

where for $i = 1, \dots, n$ and $k \in \mathbb{N}$ the function $g_i^{(k)}(\cdot)$ is defined by:

$$g_i^{(k)}(p) := l'_i c_k(p) \chi_{V_k(p_1)}(p) (\mu(V_k(p_1)))^{-1/2}.$$

Here, $\{c_k\} \subset L_2(\mathbb{T}^d)$ is chosen from the orthogonality condition for $\{\tilde{f}_k\}$, that is, from the condition:

$$(\tilde{f}_k, \tilde{f}_m) = \frac{2}{\sqrt{\mu(V_k(p_1))} \sqrt{\mu(V_m(p_1))}} \sum_{i,j=1}^n l'_i l'_j \int_{V_k(p_1)} \int_{V_m(p_1)} \frac{c_k(p)c_m(q)v_i(p)v_j(q)}{(w(p, q) - z_1)^2} dpdq = 0 \tag{6.2}$$

for $k \neq m$. The existence of $\{c_k\}$ is a consequence of the following proposition.

Proposition 6.1. *There exists an orthonormal system $\{c_k\} \subset L_2(\mathbb{T}^d)$ satisfying the conditions $\text{supp } c_k \subset V_k(p_1)$ and (6.2).*

Proof of Proposition 6.1. We construct the sequence $\{c_k\}$ by the induction method. Suppose that $c_1(p) := \chi_{V_1(p_1)}(p) \left(\sqrt{\mu(V_1(p_1))} \right)^{-1}$. Now, we choose $\tilde{c}_2 \in L_2(V_2(p_1))$ so that $\|\tilde{c}_2\| = 1$ and $(\tilde{c}_2, \varepsilon_1^{(2)}) = 0$, where:

$$\varepsilon_1^{(2)}(p) := \chi_{V_2(p_1)}(p) \sum_{i,j=1}^n l'_i l'_j v_i(p) \int_{\mathbb{T}^d} \frac{v_j(q)c_1(q)dq}{(w(p, q) - z_1)^2}.$$

Set $c_2(p) := \tilde{c}_2(p) \chi_{V_1(p_1)}(p)$. We continue this process. Suppose that $c_1(p), \dots, c_k(p)$ are constructed. Then, the function $\tilde{c}_{k+1}(\cdot) \in L_2(V_{k+1}(p_0))$ is chosen so that it is orthogonal to all functions:

$$\varepsilon_m^{(k+1)}(p) := \chi_{V_{k+1}(p_1)}(p) \sum_{i,j=1}^n l'_i l'_j v_i(p) \int_{\mathbb{T}^d} \frac{v_j(q)c_m(q)dq}{(w(p, q) - z_1)^2}, \quad m = 1, \dots, k$$

and $\|\tilde{c}_{n+1}\| = 1$. Let $c_{k+1}(p) := \tilde{c}_{k+1}(p)\chi_{V_{k+1}(p_1)}(p)$. Thus, we have constructed the orthonormal system of functions $\{c_k\}$ satisfying the assumptions of the proposition. Proposition 6.1 is proved. \square

We continue the proof of Theorem 3.2. To estimate the norm of the function \tilde{f}_k from below, we rewrite it in the form:

$$\tilde{f}_k(p, q) = \frac{(\mu(V_k(p_1)))^{-1/2}}{w(p, q) - z_1} \left[\chi_{V_k(p_1)}(p)c_k(p) \sum_{i=1}^n l'_i v_i(q) + \chi_{V_k(p_1)}(q)c_k(q) \sum_{i=1}^n l'_i v_i(p) \right].$$

Then direct calculation shows that

$$\|\tilde{f}_k\| \geq \frac{M_n}{\sqrt{\mu(V_k(p_1))}}, \quad M_n := \frac{1}{\max_{p, q \in \mathbb{T}^d} |w(p, q) - z_1|} \left\| \sum_{i=1}^n l'_i v_i \right\|. \quad (6.3)$$

By the assumption the functions $v_i(\cdot)$, $i = 1, \dots, n$ are linearly independent and hence, we have $\left\| \sum_{i=1}^n l'_i v_i \right\| > 0$.

Setting $f_k := \tilde{f}_k / \|\tilde{f}_k\|$, $k \in \mathbb{N}$, we conclude that the system of functions $\{f_k\}$ is orthonormal.

Now, for $k \in \mathbb{N}$, we consider $(H - z_1 E)f_k$ and estimate its norm as:

$$\|(H - z_1 E)f_k\| \leq \|A(z_1)G_k\| + \|K(z_1)G_k\|, \quad (6.4)$$

where the vector function G_k is defined by:

$$G_k := \left(\frac{g_1^{(k)}}{\|\tilde{f}_k\|}, \dots, \frac{g_n^{(k)}}{\|\tilde{f}_k\|} \right) \in L_2^{(n)}(\mathbb{T}^d).$$

Note that $\{G_k\} \subset L_2^{(n)}(\mathbb{T}^d)$ is a bounded orthogonal system. Indeed, the orthogonality of this system follows from the fact that for any $i = 1, \dots, n$ and $k \neq m$, the supports of the functions $g_i^{(k)}(\cdot)$ and $g_i^{(m)}(\cdot)$ do not intersect. Taking into account the equality:

$$\|G_k\|^2 = \frac{1}{\|\tilde{f}_k\|^2} \frac{1}{\mu(V_k(p_1))} \sum_{i=1}^n l_i'^2,$$

and the inequality (6.3), we conclude that the system of vector-functions $\{G_k\}$ is uniformly bounded, more exactly, the inequality:

$$\|G_k\|^2 \leq \frac{1}{M_n^2} \sum_{i=1}^n l_i'^2,$$

holds for any $k \in \mathbb{N}$.

Since the operator $K(z_1)$ is compact and $\{G_k\}$ is a bounded orthogonal system, we have $\|K(z_1)G_k\| \rightarrow 0$ as $k \rightarrow \infty$.

Let us now estimate the first summand of (6.4):

$$\|A(z_1)G_k\| \leq \frac{1}{M_n} \sup_{p \in V_k(p_1)} \|A(p; z_1)l'\|.$$

Taking into account the equality $A(p_1; z_1)l' = 0$ and the continuity of the matrix-valued function $A(\cdot; z_1)$, we get the following:

$$\sup_{p \in V_k(p_1)} \|A(p; z_1)l'\| \rightarrow 0 \quad \text{as } k \rightarrow \infty$$

and hence, by (6.4), we have $\|(H - z_1 E)f_k\| \rightarrow 0$ as $k \rightarrow \infty$. This implies that $z_1 \in \sigma_{\text{ess}}(H)$. Since the point z_1 is arbitrary, we have $\sigma \subset \sigma_{\text{ess}}(H)$. Therefore, we have proved that $\Sigma \subset \sigma_{\text{ess}}(H)$.

Now, we prove the inverse inclusion, i.e. $\sigma_{\text{ess}}(H) \subset \Sigma$. Since for each $z \in \mathbb{C} \setminus \Sigma$, the operator $K(z)$ is compact, $A^{-1}(z)$ is bounded and $\|T(z)\| \rightarrow 0$ as $z \rightarrow \infty$, the operator $T(z)$ is a compact-operator-valued function on $\mathbb{C} \setminus \Sigma$. Then from the self-adjointness of H and Theorem 3.1, it follows that the operator $(I - T(z))^{-1}$ exists if z is real and has a large absolute value. The analytic Fredholm theorem (see, e.g., Theorem VI.14 in [17]) implies that there is a discrete set $S \subset \mathbb{C} \setminus \Sigma$ such that the function $(I - T(z))^{-1}$ exists and is analytic on $\mathbb{C} \setminus (S \cup \Sigma)$ and is meromorphic on $\mathbb{C} \setminus \Sigma$ with finite-rank residues. This implies that the set $\sigma(H) \setminus \Sigma$ consists of isolated points, and the only possible accumulation points of Σ can be on the boundary. Thus $\sigma(H) \setminus \Sigma \subset \sigma_{\text{disc}}(H) = \sigma(H) \setminus \sigma_{\text{ess}}(H)$. Therefore, the inclusion $\sigma_{\text{ess}}(H) \subset \Sigma$ holds. Finally, we obtain the equality $\sigma_{\text{ess}}(H) = \Sigma$.

By Lemma 4.2 for any $p \in \mathbb{T}^d$, the operator $h(p)$ has no more than n eigenvalues (counted multiplicities) on the l.h.s. of $m(p)$ and has no eigenvalues on the r.h.s. of $M(p)$. Then, by the theorem on the spectrum of decomposable operators [17] and by the definition of the set σ , it follows that the set σ consists of the union of no more than n bounded closed intervals, which are located on the r.h.s. of the point M . Therefore, the set Σ consists of the union of no more than $n + 1$ bounded closed intervals and $\max \Sigma = M$. Theorem 3.2 is completely proved. \square

At the end of this section we give information about the upper bound of the spectrum of H . By Theorem 3.2, we have $\max(\sigma_{\text{ess}}(H)) = \max(\sigma(H_0)) = M$. Then, the positivity of the operator $V_1 + V_2$ implies:

$$((H - z)f, f) = ((H_0 - z)f, f) - ((V_1 + V_2)f, f) < 0,$$

for all $z > M$ and $f \in L_2^s((\mathbb{T}^d)^2)$, that is, the operator H has no eigenvalues greater than M . This fact, together with Theorem 3.2, gives $\max(\sigma(H)) = M$. Therefore, the eigenvalues of the operator H are located only below the bottom of the three-particle branch of its essential spectrum.

7. The lower bound of the essential spectrum of H . Case $d = 1$

In this section, we consider the special class of parameter functions $v_i(\cdot)$, $i = 1, \dots, n$ and $w(\cdot, \cdot)$ to estimate the lower bound of the essential spectrum of H when $d = 1$.

Let $d = 1$ and $P_0 \in \mathbb{T}$ be a fixed element. Throughout this section, we always assume that there exists a number $j_0 \in \{1, \dots, n\}$ such that the function $v_i(\cdot)$ is a P_0 -periodic for all $i \in \{1, \dots, n\} \setminus \{j_0\}$, and the function $v_{j_0}(\cdot)$ is an analytic function on \mathbb{T} satisfying the condition:

$$\int_{\mathbb{T}} v_{j_0}(s)g(s)ds = 0, \tag{7.1}$$

for any P_0 - periodic function $g \in L_2(\mathbb{T})$. In addition, we suppose that:

- (i) $w(\cdot, \cdot)$ is a P_0 - periodic function by the second variable;
- (ii) $w(\cdot, \cdot)$ is a twice continuously differentiable function on \mathbb{T}^2 ;
- (iii) there exists a finite subset $\Lambda \subset \mathbb{T}$ such that the function $w(\cdot, \cdot)$ has non-degenerate minima at the points of $\Lambda \times \Lambda$.

The following example shows that the class of functions $v_i(\cdot)$, $i = 1, \dots, n$ and $w(\cdot, \cdot)$, satisfying the above mentioned conditions is non empty. We set

$$v_1(x) := c_1 \cos(x), \quad v_i(x) := c_i (\cos(2x))^i, \quad c_i \in \mathbb{R} \setminus \{0\}, \quad i = 2, \dots, n.$$

Then $j_0 = 1$, the functions $v_i(\cdot)$, $i = 2, \dots, n$ are π -periodic, i.e. $P_0 = \pi$. If $g \in L_2(\mathbb{T})$ is a π -periodic function, then:

$$\int_{\mathbb{T}} v_1(s)g(s)ds = \int_{\mathbb{T}} v_1(s + \pi)g(s + \pi)ds = - \int_{\mathbb{T}} v_1(s)g(s)ds,$$

which implies the equality (7.1). One can see that the function $w(\cdot, \cdot)$ defined by:

$$w(x, y) := 2\gamma_1 + \gamma_2 - \gamma_1 \cos(2x) - \gamma_2 \cos(2x + 2y) - \gamma_1 \cos(2y), \tag{7.2}$$

with $\gamma_1, \gamma_2 > 0$ satisfy the conditions (i)–(iii) with $\Lambda := \{0, \pi\}$.

Let the operator $h_{j_0}(x)$ act in $L_2(\mathbb{T})$ as follows:

$$(h_{j_0}(x)f)(y) = w(x, y)f(y) - v_{j_0}(y) \int_{\mathbb{T}} v_{j_0}(s)f(s)ds.$$

Setting $n = 1$ and $\Delta_{j_0}(x; z) := 1 - I_{j_0j_0}(x; z)$, from Lemma 4.1, we obtain that:

$$\sigma_{\text{disc}}(h_{j_0}(x)) = \{z \in \mathbb{C} \setminus [m(x); M(x)] : \Delta_{j_0}(x; z) = 0\}. \tag{7.3}$$

Since, for any fixed $x \in \mathbb{T}$, $i \in \{1, \dots, n\} \setminus \{j_0\}$ and $z \in \mathbb{C} \setminus [m(x); M(x)]$, the function $v_i(\cdot)(w(x, \cdot) - z)^{-1}$ is a π -periodic continuous function on compact set \mathbb{T} , according to the equality (7.3) we obtain:

$$\int_{\mathbb{T}} \frac{v_{j_0}(s)v_i(s)ds}{w(x, s) - z} = 0, \quad i \in \{1, \dots, n\} \setminus \{j_0\}.$$

Then, the definition of the function $\Delta(\cdot; \cdot)$ implies that:

$$\Delta(x; z) = \Delta_{j_0}(x; z) M_{j_0j_0}(x; z),$$

where $M_{j_0j_0}(x; z)$ is defined in Section 5.

It means that $\sigma_{\text{disc}}(h_{j_0}(x)) \subset \sigma_{\text{disc}}(h(x))$. Therefore,

$$\min \sigma \leq \min \bigcup_{x \in \mathbb{T}} \sigma_{\text{disc}}(h_{j_0}(x)).$$

For $\delta > 0$ and $a \in \mathbb{T}$ we set

$$U_\delta(a) := \{x \in \mathbb{T} : |x - a| < \delta\}.$$

Now, we study the discrete spectrum of $h_{j_0}(x)$.

Lemma 7.1. *If $v_{j_0}(x_0) \neq 0$ for some $x_0 \in \Lambda$, then there exists $\delta > 0$ such that for any $x \in U_\delta(x_0)$ the operator $h_{j_0}(x)$ has a unique eigenvalue $z(x)$, lying on the left of $m(x)$.*

Proof. Since the function $w(\cdot, \cdot)$ has non-degenerate minimum at the point $(x_0, x_0) \in \mathbb{T}^2$, by the implicit function theorem there exists $\delta > 0$ and an analytic function $y_0(\cdot)$ on $U_\delta(x_0)$ such that for any $x \in U_\delta(x_0)$, the point $y_0(x)$ is the unique non-degenerate minimum of the function $w(x, \cdot)$ and $y_0(x_0) = x_0$. Therefore, we have $w(x, y_0(x)) = m(x)$ for any $x \in U_\delta(x_0)$.

Let $\tilde{w}(\cdot, \cdot)$ be the function on $U_\delta(x_0) \times \mathbb{T}$ as:

$$\tilde{w}(x, y) := w(x, y + y_0(x)) - m(x).$$

Then, for any $x \in U_\delta(x_0)$, the function $\tilde{w}(x, \cdot)$ has non-degenerate zero minimum at the point $x_0 \in \mathbb{T}$. Now, using the equality

$$\int_{\mathbb{T}} \frac{v_{j_0}^2(s)ds}{w(x, s) - m(x)} = \int_{\mathbb{T}} \frac{v_{j_0}^2(s + y_0(x))ds}{\tilde{w}(x, s)}, \quad x \in U_\delta(x_0),$$

the continuity of the function $v_{j_0}(\cdot)$, the facts that $v_{j_0}(x_0) \neq 0$ and $y_0(x_0) = x_0$, it is easy to see that:

$$\lim_{z \rightarrow m(x)-0} \Delta_{j_0}(x; z) = -\infty$$

for all $x \in U_\delta(x_0)$.

Since, for any $x \in \mathbb{T}$, the function $\Delta_{j_0}(x; \cdot)$ is continuous and monotonically decreasing on $(-\infty; m(x))$, the equality

$$\lim_{z \rightarrow -\infty} \Delta_{j_0}(x; z) = 1 \tag{7.4}$$

implies that for any $x \in U_\delta(x_0)$, the function $\Delta_{j_0}(x; \cdot)$ has a unique zero $z = z(x)$, lying in $(-\infty; m(x))$. By equality (7.3), the number $z(x)$ is the eigenvalue of $h_{j_0}(x)$. \square

Let us give an example for the function $y_0(\cdot)$ mentioned in the proof of Lemma 7.1. To this end, we consider the function $w(\cdot, \cdot)$ of the form (7.2). This function can be written as follows:

$$w(x, y) = \gamma_1 + \gamma_2 + \gamma_1(1 - \cos(2x)) - a(x) \cos(2y) - b(x) \sin(2y), \tag{7.5}$$

where the coefficients $a(x)$ and $b(x)$ are given by:

$$a(x) := \gamma_1 + \gamma_2 \cos(2x), \quad b(x) := -\gamma_2 \sin(2x). \tag{7.6}$$

Then, from the equality (7.5), we obtain following representation for $w(\cdot, \cdot)$:

$$w(x, y) = \gamma_1 + \gamma_2 + \gamma_1(1 - \cos(2x)) - r(x) \cos(2(y - y_0(x)))$$

with

$$r(x) := \sqrt{a^2(x) + b^2(x)}, \quad y_0(x) := \arcsin \frac{b(x)}{r(x)}.$$

Taking into account (7.6), we have that the function $y_0(\cdot)$ is an odd regular function and for any $x \in \mathbb{T}$ the point $y_0(x)$ is the minimum point of the function $w(x, \cdot)$.

We note that if $v_{j_0}(x_0) = 0$, then from analyticity of $v_{j_0}(\cdot)$ on \mathbb{T} , it follows that there exist positive numbers C_1, C_2 and δ such that the inequalities:

$$C_1|x - x_0|^\theta \leq |v_{j_0}(x)| \leq C_2|x - x_0|^\theta, \quad x \in U_\delta(x_0), \tag{7.7}$$

hold for some $\theta \in \mathbb{N}$. Since the function $w(\cdot, \cdot)$ has non-degenerate minima at the points of $\Lambda \times \Lambda$, there exist $C_1, C_2 > 0$ and $\delta > 0$ such that estimates:

$$C_1(|x - x'|^2 + |y - y'|^2) \leq w(x, y) - m \leq C_2(|x - x'|^2 + |y - y'|^2), \quad (x, y) \in U_\delta(x') \times U_\delta(y'); \tag{7.8}$$

$$w(x, y) - m \geq C_1 \quad (x, y) \notin \Lambda \times \Lambda. \tag{7.9}$$

Hence, if $v_{j_0}(x') = 0$ for all $x' \in \Lambda$, then using the inequalities (7.7), (7.8) and (7.9), one can easily see that for any $x \in \mathbb{T}$ the integral

$$\int_{\mathbb{T}} \frac{v_{j_0}^2(s) ds}{w(x, s) - m},$$

is positive and finite.

For $x' \in \Lambda$, the Lebesgue dominated convergence theorem yields $\Delta_{j_0}(x'; m) = \lim_{x \rightarrow x'} \Delta_{j_0}(x; m)$, and hence, if $v_{j_0}(x') = 0$ for all $x' \in \Lambda$, then the function $\Delta_{j_0}(\cdot; m)$ is continuous on \mathbb{T} .

Lemma 7.2. *Let $v_{j_0}(x') = 0$ for all $x' \in \Lambda$;*

(i) *If $\min_{x \in \mathbb{T}} \Delta_{j_0}(x; m) \geq 0$, then for any $x \in \mathbb{T}$ the operator $h_{j_0}(x)$ has no eigenvalues, lying on the left of m ;*

(ii) *If $\min_{x \in \mathbb{T}} \Delta_{j_0}(x; m) < 0$, then there exists a non empty set $G_{j_0} \subset \mathbb{T}$ such that for any $x \in G_{j_0}$ the operator $h_{j_0}(x)$ has a unique eigenvalue $z(x)$, lying on the left of m .*

Proof. First, we recall that if $v_{j_0}(x') = 0$ for all $x' \in \Lambda$, then the function $\Delta_{j_0}(\cdot; m)$ is continuous on the compact set \mathbb{T} . Two cases are possible: $\min_{x \in \mathbb{T}} \Delta_{j_0}(x; m) \geq 0$ or $\min_{x \in \mathbb{T}} \Delta_{j_0}(x; m) < 0$.

Let $\min_{x \in \mathbb{T}} \Delta_{j_0}(x; m) \geq 0$. Since for any $x \in \mathbb{T}$ the function $\Delta_{j_0}(x; \cdot)$ is monotonically decreasing on $(-\infty; m)$ we have:

$$\Delta_{j_0}(x; z) > \Delta_{j_0}(x; m) \geq \min_{x \in \mathbb{T}} \Delta_{j_0}(x; m) \geq 0,$$

that is, $\Delta_{j_0}(x; z) > 0$ for all $x \in \mathbb{T}$ and $z < m$. Therefore, by equality (7.3) for any $x \in \mathbb{T}$, the operator $h_{j_0}(x)$ has no eigenvalues in $(-\infty; m)$.

Now, we suppose that $\min_{x \in \mathbb{T}} \Delta_{j_0}(x; m) < 0$ and introduce the following subset of \mathbb{T} :

$$G_{j_0} := \{x \in \mathbb{T} : \Delta_{j_0}(x; m) < 0\}.$$

Since $\Delta_{j_0}(\cdot; m)$ is continuous on the compact set \mathbb{T} , there exists at least one point $x_0 \in \mathbb{T}$ such that:

$$\min_{x \in \mathbb{T}} \Delta_{j_0}(x; m) = \Delta_{j_0}(x_0; m),$$

that is, $x_0 \in G_{j_0}$. So, the set G_{j_0} is non empty. It is clear that, if $\max_{x \in \mathbb{T}} \Delta_{j_0}(x; m) < 0$, then $\Delta_{j_0}(x; m) < 0$ for all $x \in \mathbb{T}$ and hence $G_{j_0} = \mathbb{T}$.

Since for any $x \in \mathbb{T}$ the function $\Delta_{j_0}(x; \cdot)$ is continuous and monotonically decreasing on $(-\infty; m]$ by the equality (7.4) for any $x \in G_{j_0}$, there exists a unique point $z(x) \in (-\infty; m)$ such that $\Delta_{j_0}(x; z(x)) = 0$. By the equality (7.3) for any $x \in G_{j_0}$ the point $z(x)$ is the unique eigenvalue of $h_{j_0}(x)$.

By the construction of G_{j_0} , the inequality $\Delta_{j_0}(x; m) \geq 0$ holds for all $x \in \mathbb{T} \setminus G_{j_0}$. In this case, for any $x \in \mathbb{T} \setminus G_{j_0}$, the operator $h_{j_0}(x)$ has no eigenvalues in $(-\infty; m)$. \square

We set

$$E_{\min} := \min\{\lambda : \lambda \in \sigma_{\text{ess}}(H)\}.$$

Then, $E_{\min} \in \sigma_{\text{ess}}(H)$ and it is called the lower bound of the essential spectrum of H .

Lemma 7.3. *Let one of the following conditions hold:*

(i) $v_{j_0}(x_0) \neq 0$ for some $x_0 \in \Lambda$;

(ii) $v_{j_0}(x') = 0$ for all $x' \in \Lambda$ and $\min_{x \in \mathbb{T}} \Delta_{j_0}(x; m) < 0$.

Then $E_{\min} < m$.

Proof. Let $v_{j_0}(x_0) \neq 0$ for some $x_0 \in \Lambda$. Then, by Lemma 7.1 there exists $\delta > 0$ such that for any $x \in U_\delta(x_0)$ the operator $h_{j_0}(x)$ has a unique eigenvalue $z(x)$, lying on the left of $m(x)$. In particular, $z(x_0) < m(x_0)$. Since $m = \min_{x \in \mathbb{T}} m(x) = m(x_0)$, it follows that $\min \sigma \leq z(x_0) < m$, that is, $E_{\min} < m$.

Let $v_{j_0}(x') = 0$ for all $x' \in \Lambda$ and $\min_{x \in \mathbb{T}} \Delta_{j_0}(x; m) < 0$. Then, by part (ii) of Lemma 7.2, for any $x \in G_{j_0}$ the operator $h_{j_0}(x)$ has a unique eigenvalue $z(x)$, lying on the left of $m(x)$. Therefore, we obtain $\min \sigma \leq z(x') < m$ for all $x' \in G_{j_0}$, that is, $E_{\min} < m$. \square

Notice that if $v_{j_0}(x') = 0$ for all $x' \in \Lambda$ and $\min_{x \in \mathbb{T}} \Delta_{j_0}(x; m) \geq 0$, then the location of the bounds E_{\min} and m depends on the zeros of the function $M_{j_0 j_0}(x; \cdot)$. If for all $x \in \mathbb{T}$ this function has no zeros, lying on the l.h.s. of m , then $E_{\min} = m$. If for some $x = x_0 \in \mathbb{T}$ this function has at least one zero on $(-\infty; m)$, then $E_{\min} < m$.

We remark that the results of this section are useful when we find the conditions which guarantee the finiteness or infiniteness of the number of the eigenvalues of H , lying below the bottom of its essential spectrum, in the one dimensional case.

Acknowledgements

This work was supported by the IMU Einstein Foundation Program. T.H. Rasulov wishes to thank the Berlin Mathematical School and Weierstrass Institute for Applied Analysis and Stochastics for the invitation and hospitality.

References

- [1] Albeverio S., Lakaev S. N., Djumanova R. Kh. The essential and discrete spectrum of a model operator associated to a system of three identical quantum particles. *Rep. Math. Phys.*, **63** (3), P. 359–380 (2009).
- [2] Albeverio S., Lakaev S. N., Muminov Z. I. On the structure of the essential spectrum for the three-particle Schrödinger operators on lattices. *Math. Nachr.*, **280** (7), P. 699–716 (2007).
- [3] Albeverio S., Lakaev S. N., Muminov Z. I. On the number of eigenvalues of a model operator associated to a system of three-particles on lattices. *Russ. J. Math. Phys.*, **14** (4), P. 377–387 (2007).
- [4] Birman M. S., Solomjak M. Z. *Spectral Theory of Self-Adjoint Operators in Hilbert Space*. Dordrecht: D. Reidl P.C., 313 P. (1987).
- [5] Eshkabilov Yu. Kh., Kuchkarov R. R. Essential and discrete spectra of the three-particle Schrödinger operator on a lattice. *Theor. Math. Phys.*, **170** (3), P. 341–353 (2012).
- [6] Heine V., Cohen M., Weaire D. *The Pseudopotential Concept*. Academic Press, New York–London, 558 P. (1970).
- [7] Karpenko B. V., Dyakin V. V., Budrina G. A. Two electrons in Hubbard model. *Fiz., Met., Metalloved.*, **61** (4), P. 702–706 (1986).
- [8] Lakaev S. N., Muminov M. É. Essential and discrete spectra of the three-particle Schrödinger operator on a lattices. *Theor. Math. Phys.*, **135** (3), P. 849–871 (2003).
- [9] Mattis D. The few-body problem on a lattice. *Rev. Modern Phys.*, **58** (2), P. 361–379 (1986).
- [10] Mogilner A. I. Hamiltonians in solid state physics as multiparticle discrete Schrödinger operators: problems and results. *Advances in Sov. Math.*, **5**, P. 139–194 (1991).
- [11] Newton R. G. *Scattering Theory of Waves and Particles*. Springer-Verlag, New York, 745 P. (1982).
- [12] Rabinovich V. S., Roch S. The essential spectrum of Schrödinger operators on lattices. *J. Phys. A: Math. Gen.*, **39**, P. 8377–8394 (2006).
- [13] Rabinovich V. S. Essential spectrum of perturbed pseudodifferential operators. Applications to Schrödinger, Klein-Gordon, and Dirac operators. *Russ. J. Math. Phys.*, **12**, P. 62–80 (2005).
- [14] Rasulov T. Kh. Asymptotics of the discrete spectrum of a model operator associated with the system of three particles on a lattice. *Theor. Math. Phys.*, **163** (1), P. 429–437 (2010).
- [15] Rasulov T. Kh. Essential spectrum of a model operator associated with a three particle system on a lattice. *Theor. Math. Phys.*, **166** (1), P. 81–93 (2011).
- [16] Rasulova Z. D. Investigations of the essential spectrum of a model operator associated to a system of three particles on a lattice. *J. Pure and App. Math.: Adv. Appl.*, **11** (1), P. 37–41 (2014).
- [17] Reed M., Simon B. *Methods of modern mathematical physics. IV: Analysis of Operators*. Academic Press, New York, 396 P. (1979).
- [18] Zhukov Y. V. The Iorio-O’Carroll theorem for an N -particle lattice Hamiltonian. *Theor. Math. Phys.*, **107** (1), P. 478–486 (1996).

CHANNELS OF ELECTRON-ELECTRON INTERACTIONS IN HIGHLY DOPED HETEROJUNCTION

V. A. Ambartsumyan¹, E. A. Andryushchenko¹, K. V. Bukhenskiy¹, A. B. Dubois¹,
E. A. Dvoretzkova¹, T. V. Gordova², N. I. Ivanova³, S. I. Kucheryavyi⁴,
S. N. Mashnina², A. S. Safoshkin¹

¹ Ryazan State Radioengineering University, Ryazan, Russia

² Moscow State University of Economics, Statistics and Informatics (Ryazan filial), Russia

³ Moscow State University of Economics, Statistics and Informatics (Yaroslavl filial), Russia

⁴ Institute of Atomic Energy of National Research Nuclear University of Moscow
Engineer-Physics University, Obninsk, Russia

dubois.a.b@rsreu.ru

PACS 72.10.-d, 73.23.-b

Electron-electron interactions in a single highly doped heterojunction are considered, taking into account both intra- and intersubband transitions. Expressions are derived for the time of electron-electron interaction, matrix elements of the full screening potential and dynamic dielectric function in a 2D electron system with the fine structure of the energy spectrum, and for the electron density spatial distribution. The theoretical dependences $\tau_{ee}^{th}(T, n_s)$ provide a good description of the experimental times of Landau levels collisional broadening $\tau_q^{exp}(T, n_s)$.

Keywords: electron-electron interactions, random phase approximation, Fourier analysis, Shubnikov-de Haas oscillations.

Received: 3 May 2014

Revised: 4 June 2014

1. Introduction

Starting from the pioneering works [1] and up to the present time [2-20], electron-electron (e-e) interactions are the subject of ever growing interest because of their fundamental role in kinetic phenomena. Among others, one should note the hot electrons effects, quantum corrections to the conductivity, and damping (destruction) of Landau quantization in bulk and two-dimensional semiconductors with degenerate electrons. Also known are anomalies in the low-temperature magnetotransport arising when 2D electrons fill several size-quantized subbands. In particular, the authors of [2] predicted non-monotonous behavior of kinetic coefficients as the density of the 2D electrons is changed and several size-quantized subbands in a 2D system are filled. Experimentally, the reduction of mobility with the growth of electron surface density n_s was discovered in [3, 4]. Later [5 - 7], a complicated set of phenomena was discovered and studied in the $\text{Al}_x\text{Ga}_{1-x}\text{As}/\text{GaAs}$ heterostructure whose potential well contained two size-quantized (the main E_m , and the first excited E_p) subbands. Most interesting among them are the amplitude and the frequency modulation of the transverse Shubnikov-de Haas (SdH) magnetoresistance [8], sharp bends in the magnetic field dependence of the oscillation amplitude $\delta(1/B)$ [9, 10] as well as the non-monotonous behavior of the Dingle temperature T_D with the 2D electron density n_s and

the temperature T [11, 12]. In spite of the variety of experimental details and approaches to their interpretation, the indicated effects were all shown to be caused by filling of the second excited size-quantized subband. The mechanism triggering the non-linear effects is the intersubband interaction. In [4, 5] following point was discussed; when the doping level of the $\text{Al}_x\text{Ga}_{1-x}\text{As}$ (Si) /GaAs heterojunction is high enough for n_s to reach $8 \cdot 10^{11} \text{cm}^{-2}$, the quantum well contains two size-quantized subbands with energies E_m and E_p electron densities n_m and n_p , respectively, and the SdH oscillations of ρ_{xx} exhibit frequencies $F_{m,p} = (\pi\hbar/e) n_{m,p}$ with the periods $\Delta_{m,p} (1/B) = F_{m,p}^{-1}$. The main feature is the modulation of the main frequency F_m amplitude with the frequency F_p , the modulation depth growing with temperature and being more pronounced at the lower magnetic fields. The second feature is the development of oscillations at a different frequency $F_m - F_p$. These oscillations do not depend on temperature and transform to oscillations with a frequency F_m as the magnetic field is raised.

Assuming constant electron density and Fermi energy oscillations, Kadushkin [9, 10] explained the main features of the amplitude-frequency modulation of the SdH oscillations by the intersubband interaction. Authors of [2] derived an analytic expression for the amplitude of oscillations containing components at the frequencies $F_{m,p}$, $F_m - F_p$. They analyzed the experiments, taking into account the electron-phonon interaction. Formally, the Dingle temperature is related to the non-thermal collisional broadening time τ_q through the expression $T_D = \hbar/2\pi k\tau_q$. Description of the SdH oscillations of ρ_{xx} [8] based on the two subbands (m and p) model is in good agreement with the experimental results obtained in [12].

In the present paper, we report results from the study of e-e relaxation processes in a system of highly degenerate 2D electrons with finely structured energy spectrum and electron density spatial distribution. Expressions for the electron-electron intra- (τ_{ee}^{intra}) and intersubband (τ_{ee}^{inter}) interaction are derived and the matrix elements of the full screening potential $V_{tot}(q, \omega)$ and the dielectric function for $\chi(q, \omega)$ in the approximation far from the long wave limit are calculated. The oscillations in $\tau_q^{\text{exp}}(T, n_s) \simeq \tau_{ee}^{th}(T, n_s)$ are shown to be related to the excitation of plasmons in the components of 2D electron system and the plasmon spectrum is studied.

2. Mechanism of Landau quantization destruction

One of the important points in the derivation of expressions for τ_{ee}^{intra} and τ_{ee}^{inter} is the calculation of the full screening potential matrix elements which, within the perturbation theory approach, implies the transformation of the potential $V(r, t)$ into $V_{tot}(q, \omega)$. In our problem, this corresponds to the following physical situation.

Let us consider 2D electrons, crystal lattice, and the source of perturbation as a thermodynamic system in equilibrium at the thermal bath temperature T . The electrons interact amongst themselves and with the crystal lattice with relaxation times τ_{ee} and τ_{eph} , respectively. At lower temperatures and in a quantizing magnetic field B , the equilibrium energy and momentum distribution of 2D electrons is given by harmonic oscillators with the cyclotron frequency ω_c . The electron states are correlated and coherent because of the strong e-e interaction with the relaxation times hierarchy $\tau_{ee} \ll \tau_p \ll \tau_\varepsilon$ where τ_p and τ_ε are the relaxation times of momentum p and energy ε . The electron states on the cyclotron orbits are coherent because the lifetime on these orbits exceeds the mean free time (momentum relaxation time). Although the electron state initial phase is determined by the electron settling into the cyclotron orbit and has a random nature, the motion of electrons on cyclotron orbits is synchronized and it is precisely this point that allows one to apply the random phase approximation (RPA) to these magnetized electrons. It is worthwhile to note

that the reduced Wigner radius for the studied heterojunctions with $n_s \simeq (0.5 \div 2) \cdot 10^{12} \text{ cm}^{-2}$, $V(q, \omega)$ is $0.6 \div 1.2$, so that the use of RPA is rather justified [1].

Electron collisions with the crystal lattice defects destroy the ground quantum state (cyclotron orbits), which is seen in the broadening of Landau levels, resulting in finite values for the kinetic coefficients' oscillation amplitudes.

In the absence of an external electric field, the equilibrium state of electrons is characterized by the temperature T_D^0 which stipulated the chaotization of the 2D electrons, which are in thermodynamic equilibrium with the crystal lattice (T, T_D^0) in the quantizing magnetic field B . Note that the perturbations of the potential relief of the quantum well's 2D channel, caused by various defects, are time-independent: $V(r, t)$. The electron system state (T, T_D^0) stationary with respect to the electron-lattice interaction is controlled through the energy and momentum relaxation with the characteristic time $\tau_{eph}^{(\epsilon, p)}$.

The mechanism for the destruction of the quantum Landau state $(T, T_D^0)_B$ and development of a new equilibrium stationary state (T, T_D^*) , which is not in equilibrium with respect to the initial equilibrium state (T, T_D^0) , can be described in the following way. The electric field E causes a drift of the 2D electron system along the heterojunction quantum well (in the xy -plane) so that the electrons "scan" the spatial distribution of the heterojunction defects. In the reference frame associated with the 2D electrons, the observer sees the results of scanning the potential well defects as $V_{tot}(q, \omega)$. Here, the electric field E acts only as the means of sweeping the external (with respect to 2D electrons) perturbations, converting them into a time-dependent potential which is expressed in the transition from $V(r, t)$ to the Fourier component $V_{tot}(q, \omega)$.

In the 2D electron system perturbed by (T, T_D^0) the collisions acquire a different nature and at $T = \text{const}$ and $B = \text{const}$, the equilibrium broadening kT_D^0 is affected by the perturbation caused by the external field E so that a new equilibrium state with the broadening kT_D^0 is established. This new equilibrium state (T, T_D^*) , should be considered as a non-equilibrium one with respect to $(T, T_D^0)_B$.

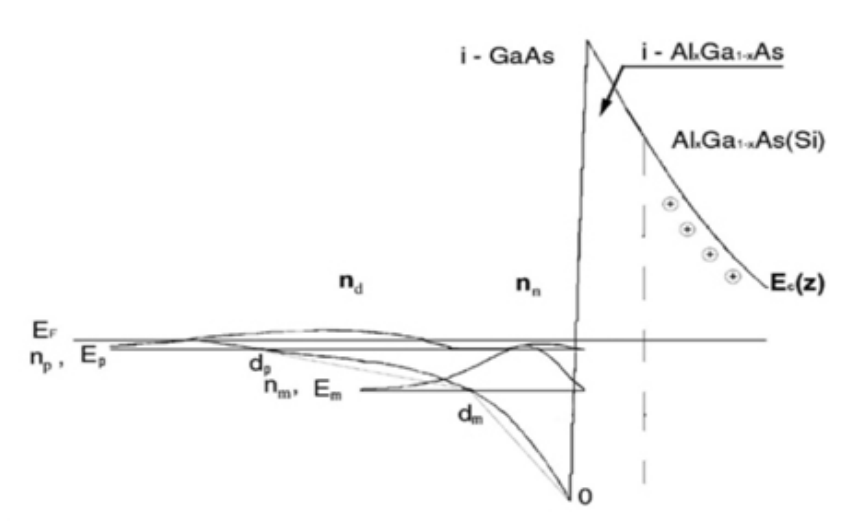


FIG. 1. The energy diagram of the conduction band $E_c(z)$ for a heterojunction with two filled size-quantized subbands E_m and E_p with electron densities n_m and $n_p = n_n + n_d$; d_p is the undoped spacer thickness, and N_D^+ , N_A^- , Δ , Λ , δx are the sources of perturbation of the 2D electron system

Our analysis of e-e interaction is based on the calculation of the conduction band energy structure $E_c(z)$. We approximate the potential well of the heterojunction by a triangular profile [11] with the sharp bends at the size-quantized levels $E_m = E_c(d_m)$ and $E_p = E_c(d_p)$.

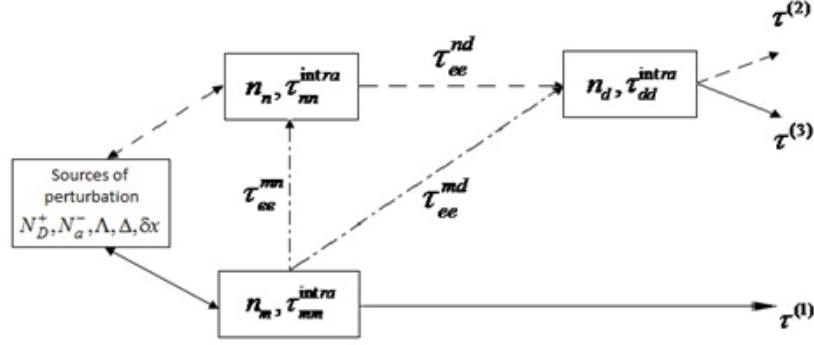


FIG. 2. Schematic model illustrating the channels through which the perturbation from the sources causing non-thermal collisional broadening of Landau levels passes. See text for details

Schematics of the e-e interactions in the 2D system is presented in Fig. 1, which also shows the typical channels through which the perturbation due to various sources, such as ionized donors N_D^+ , acceptors N_a^- , growth islands of length Λ and height Δ , as well as the mole fraction variations δx , affects the electron system. Here, n_m , is the 2D electron density in the ground (main) size-quantized subband while n_n and n_d are the satellites of the perturbed (excited) subband component $n_p = n_n + n_d$ located close to (“near”) and far from (“distant”) the heterointerface (in the following referred to as the n - and d -satellites). Of all the channels of Landau quantization damping which we consider, one should emphasize those three that reveal the major features. Since $n_m \gg n_n, n_m$, and the centers of gravity of $|\psi(z)|^2$ at the levels E_m and E_p , are spatially resolved, the perturbation is sensed (absorbed) during time $\tau^{(1)}$ by the set of 2D electrons. Then, through the intrasubband (τ_{ee}^{mn}) and intersubband ($\tau_{ee}^{mn}, \tau_{ee}^{md}, \tau_{ee}^{nd}$) e-e interactions mediated by the (τ_{ee}^{nn}) and (τ_{ee}^{dd}) intrasubband interactions, the perturbation is extended to the entire 2D system. The path of this mechanism is shown in Fig.1 by the solid line:

$$\tau^{(1)} \Rightarrow (\tau_{ee}^{mn}) \Rightarrow (\tau_{ee}^{nd}, \tau_{ee}^{mn}) \Rightarrow (\tau_{ee}^{nn}, \tau_{ee}^{dd}, \tau_{ee}^{nd}) = \tau_{ee}^{(1)}. \quad (1)$$

The major factor here is the interaction of n_m , and n_d electrons ($m-d$), while n_n , is a passive element. The second scenario corresponds to the situation where perturbation is first sensed by the n -satellite. In that case, the time needed to destroy the quantization is formed in the chain shown in Fig.1 by the dashed line:

$$\tau^{(2)} \Rightarrow (\tau_{ee}^{nn}) \Rightarrow (\tau_{ee}^{nd}) \Rightarrow (\tau_{ee}^{mn}, \tau_{ee}^{nd}) \Rightarrow (\tau_{ee}^{nn}, \tau_{ee}^{dd}, \tau_{ee}^{nd}) = \tau_{ee}^{(2)}. \quad (2)$$

Here, the system behavior is governed by the intersubband “ $n-d$ ”, “ $n-m$ ” and “ $m-d$ ” interactions. The “ $n-d$ ”- interaction is the major one in this channel and n_m , plays the role of a passive element. The third version is formed in the chain where the “ $m-n$ ” interaction dominates while n_d is a passive element:

$$\tau^{(3)} \Rightarrow (\tau_{ee}^{mm}) \Rightarrow (\tau_{ee}^{mn}, \tau_{ee}^{md}) \Rightarrow (\tau_{ee}^{nn}, \tau_{ee}^{dd}, \tau_{ee}^{nd}) = \tau_{ee}^{(3)}. \quad (3)$$

The corresponding path is shown by the dot-and-dash line. With respect to the nature of induced transitions the e-e interactions can be classified into three types: (1) interactions within a single subband limited to the transitions within the same subband; (2) intrasubband interaction exciting the intersubband transitions, and (3) intersubband interactions also resulting in intrasubband transitions.

To within the second order in the external potential $V_{tot}(q, \omega)$ in the perturbation theory expansion, the time required for the e-e interaction to change the state $\langle k|p\rangle$ into $\langle k+q|p-q\rangle$ is given by a well-known expression:

$$\frac{1}{\tau_{ij}^{ee}} = \int_{-\infty}^{\infty} d\omega \sum_{k,m} \sum_q \left| V_{tot}^{ijkl}(q, \omega) \right|^2 \times \sum_{k,p} \delta(E_j(k+q) + E_l(p-q) - E(k) - E_k(p)) f_k f_p (1 - f_{k+q}) (1 - f_{p-q}), \quad (4)$$

where indices i, j, k, l run over the set consisting of symbols m (main component) and n, d (satellites of the n_p -component) which label the electron transition type; f - Fermi-Dirac function. Using the notations given in [12 - 20], (4) can be written as:

$$\frac{1}{\tau_{ij}^{ee}} = \int_{-\infty}^{\infty} \frac{d\omega}{\pi^2 \text{ch}^2(\hbar\omega/2k_B T)} \sum_{k,m} \sum_q \left| V_{tot}^{ijkl}(q, \omega) \right|^2 \chi_{ik}(q, \omega) \chi_{jk}^*(q, \omega). \quad (5)$$

Matrix elements of the $m-n$, $m-d$ intersubband interactions were calculated with the wave functions $\psi_m(z)$ as well as the $\psi_n(z)$ and $\psi_d(z)$ components of the wave function $\psi_p(z)$ with appropriate boundary conditions.

Taking into account the parameters of the energy band diagram, the matrix elements of the full screening potential for the first and second type transitions are reduced to the form:

$$V_{tot}^{ijkl}(q, \omega) = \frac{E_j}{2d_l S (q^3 + 2\pi e^2 q^3 \chi_{ik}(q, \omega))}, \quad (6)$$

where $S = L^2$ - square of 2D system.

For $i = k$ and $j = l$, while for the third type:

$$V_{tot}^{ijkl}(q, \omega) = \frac{E_j (1 - qd_j) - E_j (1 + qd_i)}{2(d_i - d_j) S (q^3 + 2\pi e^2 q^4 \chi_{ik}(q, \omega))}, \quad (7)$$

with $i = j$ and $k = l$. In the form convenient for calculations, the relaxation times for the first and second type transitions are written as:

$$\frac{1}{\tau_{ij}^{intra}} = \frac{E_j^2 m^{*2} S}{16\pi^5 d_j^2 \hbar^4 n_i n_j} P_{-n}(T), \quad (8)$$

while for the third type:

$$\frac{1}{\tau_{li}^{inter}} = \frac{m^{*2} S}{8\pi^6 (d_i - d_m)^2 \hbar^4} \left\{ \frac{(E_i - E_m)^2}{8\pi} Q_{-n}(T) - \frac{(E_i - E_m)(E_l d_m + E_m d_i)}{\sqrt{8\pi}} W_{-n}(T) \right\} \quad (9)$$

for $i \neq l$. The polynomials in (8) and (9) are:

$$P_{-n}(T) = \frac{B_1}{T} + \frac{B_2}{T^2} + \frac{B_3}{T^3} + \dots,$$

$$Q_{-n}(T) = \frac{B_1}{T} - \frac{B_2}{T^2} + \frac{B_3}{T^3} - \dots,$$

$$W_{-n}(T) = \frac{B_2}{T^2} + \frac{B_4}{T^4} + \dots$$

with the coefficients B_k defined by the Riemann zeta-function $\zeta(z, v)$. The non-monotonous behavior of $\tau_{ee}^{-1}(T)$ is determined by the uniformly converging sums $P_{-n}(T)$, $Q_{-n}(T)$ and $W_{-n}(T)$ multiplied by the zeta- and gamma-functions [9]:

$$\zeta(z, v) = \frac{1}{\Gamma(z)} \int_0^{\infty} \frac{t^{z-1} e^{-vt}}{1 - e^{-t}} dt,$$

where $z = \frac{d_m}{d_m + d_p}$; $v = \frac{\hbar^2 \pi}{2k_B T} \left(\frac{n_m n_p}{n_m + n_p} \right)^{\frac{1}{2}}$.

The products of $P_{-n}(T)$, $Q_{-n}(T)$ and $W_{-n}(T)$ with $\zeta(z, v)$ are rather sensitive to the electron concentration in the size-quantized subbands. For example, for $n_m > 8 \cdot 10^{11} \text{cm}^{-2}$ ($n_d = 0.1n_m$, $n_n = 0.1n_d$, $d_p/d_m = 3.5$) the factor $\zeta(z, v)$ in (9) results only in some smoothening of the non-monotonous behavior while at $n_m > 8 \cdot 10^{11} \text{cm}^{-2}$ the curve $\tau_{ee}^{-1}(T)$ does not contain any non-monotonous parts at all.

Calculations of τ_{ee}^{th} were performed within the outlined schematic model of the Landau quantization destruction, taking into account the paths corresponding to channels (1-3), including both intra- and intersubband transitions according to (8) and (9) employing the Matthiessen rule $\tau_{ee}^{-1} = \sum_i (\tau_{ee}^{-1})_i$, where the summation is performed over all intra- and intersubband components of the schematic model presented in Fig. 2.

3. Electron “bottleneck”

Presented for comparison in Figs. 3a and 3b are the experimentally measured and calculated curves $\tau_q^{\text{exp}}(T, n_s)$ and $\tau_{ee}^{th}(T, n_s)$ for several heterostructure samples where 2D electrons are certainly known to fill only the lowest size-quantized subband ($n_s < 8 \cdot 10^{11} \text{cm}^{-2}$). Figures 4a and 4b show the experimental and calculated curves for the time of destruction of Landau quantization for two heterostructures with electron density sufficient for filling of the two size-quantized subbands (see [9, 10] for the details of the analysis of the experiment).

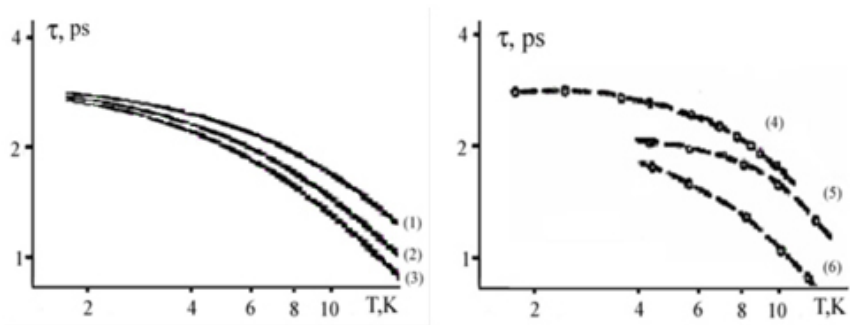


FIG. 3. Comparison of the experimental $\tau_q^{\text{exp}}(T)$ (n_m, n_d or n_n) [2] (a) and calculated $\tau_{ee}^{th}(T)$ (b) curves for different values of the m -subband electron density: $n_m, 10^{11} \text{cm}^{-2}$: 1, 4 – 8.5; 2, 5 – 6.9; 3, 6 – 6.3

The energy and geometrical parameters were taken from the energy diagrams $E(z)$ for the samples with appropriate electron densities. The first result is a quantitative “hit” of

the calculated times into the range of T in the studied temperature interval $2 \leq T \leq 12K$ for the real densities $n_m \approx 10^{12} cm^{-2}$, $n_d = 0.1n_m$, $n_n = 0.01n_m$ and, respectively, $d_p/d_m = 3$. Of all the considered versions of the model presented in Fig.2, scenario (3) is the most satisfactory one and the curve $\tau_{ee}^{th}(T, n_s)$, plotted in Fig. 4b, was calculated exactly for this scenario. Further, it should be noted that at low temperatures ($T < 5K$), the Landau quantization damping is governed by n_m -electrons. Numerical analysis of the expansion of the dielectric functions (6) reveals the appearance of non-monotonous parts in the curve $\tau_{ee}^{th}(T, n_s)$ at $n_m > 8 \cdot 10^{11} cm^{-2}$ and $T > 5K$ (see (10-13)), allowing one to argue [9,10] that the typical oscillations of $\tau_{ee}^{th}(T)$ arise only after the electrons fill the second excited size-quantized subband and for the system response to the thermal perturbation at $T > 5K$. The third obtained result is the role of n_n -satellite in the appearance of the oscillations regardless of which component of the 2D electron system senses the perturbation, as shown in Fig.2 by channel $\tau^{(3)}$.

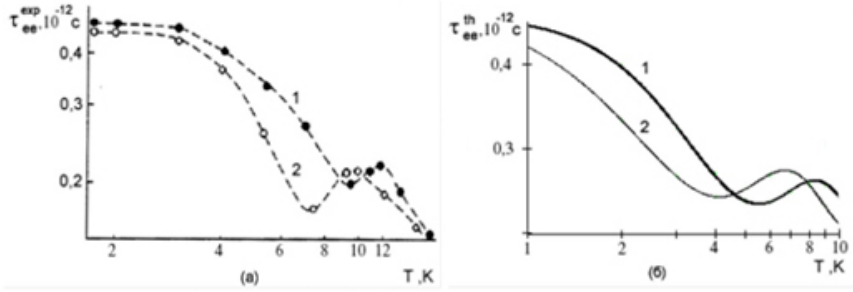


FIG. 4. Comparison of the experimental $\tau_q^{exp}(T)$ [2] (a) and calculated $\tau_{ee}^{th}(T)$ (b) curves for different values of the m -subband electron density: 1 – 9.1; 2 – 10.0

This was also directly seen in (9). Indeed, for $n_n = 0$, only $\tau_{mm}^{intra}(T)$ and $\tau_{dd}^{intra}(T)$ are different from zero and no oscillations arise in $\tau_{ee}^{th}(T)$. The bottleneck effect is explained in the following way; variation of temperature initiates the frequency scan of the external perturbation $V_{tot}(q, \omega)$ towards higher ω . The 2D electron system is transparent for $V_{tot}(q, \omega)$ until the frequency ω_τ of one of the components (n_m , n_d , or n_n) is reached. The lowest ω_τ corresponds to the n_n -satellite and it is this component or, to be more precise, its intrasubband relaxation that is the bottleneck for $V_{tot}(q, \omega)$, perturbing the 2D electron system as a whole and finally destroying the cyclotron orbit quantization (damping of Landau quantization). This bottleneck effect in the e-e interactions illustrates the coincidence of the resonant frequencies for " $m - n$ " and " $d - n$ " channels (see Fig. 5 (curves 1 and 3) below in the range of low frequencies).

Thus, the experimentally observed features in $\tau_q^{exp}(T)$ at $T < 5K$ are only related to the intrasubband e-e transitions, $\tau_q^{exp}(T) \approx \tau_{ee}^{th}(T) \approx \tau_{mm}^{intra}(T)$. At higher temperatures, a mixed mechanism of the Landau quantization destruction is realized:

$$\tau_q^{exp} \approx \tau_{ee}^3 \left[(\tau_{ee}^{mn})^{-1} = (\tau_{mn}^{intra})^{-1} + (\tau_{mn}^{inter})^{-1}; (\tau_{ee}^{nd})^{-1} = (\tau_{nn}^{intra})^{-1} + (\tau_{nd}^{inter})^{-1} \right].$$

It should be noted that by varying the well parameters, one can obtain a satisfactory agreement with experimental results. This technique offers the possibility of recovering the actual potential profile from the superposition of the curves τ_q^{exp} and τ_{ee}^{th} , measured for the

samples with different doping levels, and therefore, showing different variations of the form-factors d_p/d_m and E_p/E_m . However, this matching of the calculated curves τ_{ee}^{th} with the experimental ones τ_q^{exp} is limited by a certain arbitrariness in the adjustable parameters d_p/d_m and E_p/E_m (the potential well form-factors) since the curve $E(z)$ cannot be derived with sufficient accuracy because of the uncertainties in N_D , N_A and the band discontinuity $\Delta E_c/\Delta E_g$ for the AlGaAs/GaAs heterostructure [7, 9, 10].

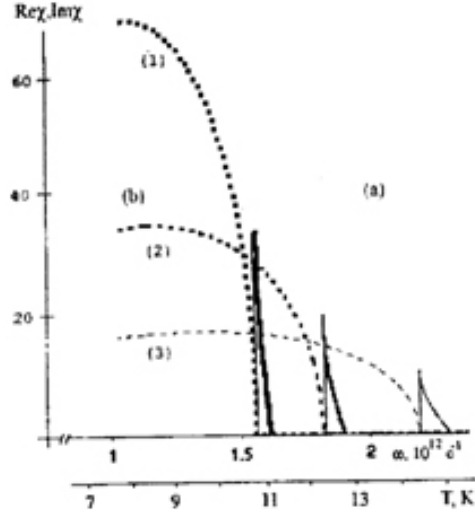


FIG. 5. Frequency dependence of the dielectric function for the interaction between the main size-quantized m -subband electrons with the n -satellite of the p -subband. $n_m, 10^{11} \text{ cm}^{-2}$: (1) – 8.5, (2) – 10, (3) – 11.5; $d_p/d_m = 3.5$

4. Spectrum of collective excitation

Bearing in mind the oscillations in τ_q^{exp} and τ_{ee}^{th} , it is natural to expect the resonant response of the components of a complex 2D electron system to the external perturbation $V_{tot}(q, \omega)$ at the plasma oscillations' frequency. The 2D system responds to the spectrum of $V_{tot}(q, \omega)$ by one of its n_m , n_n , n_d components (or their combination), and in a time τ_{ee} (τ_{ee}^{intra} , τ_{ee}^{inter}), the perturbation extends to the entire system resulting in the destruction of quantum states (cyclotron orbits), which is experimentally observed as the reduction of the $\delta(1/B)_T$ oscillations' amplitude. The latter is formally equivalent to the rise of temperature T at which the measurements are taken. Therefore, the resonant response featuring the Landau quantization destruction corresponds to a minimum in the curves τ_q^{exp} and τ_{ee}^{th} . We have performed a spectral analysis of the dispersion equations (6) for $\chi(q, \omega)$ for various channels of e-e interactions according to the scheme shown in Fig. 2 and various relative values of the densities n_m , n_n , n_d in the situation where two size-quantized subbands are occupied ($n_m > 8 \cdot 10^{11} \text{ cm}^{-2}$). The plasma oscillation frequencies ω_τ are found from the dispersion equation $\chi(q, \omega) = 0$, the minima in $\tau_{ee}^{th}(T)$ corresponding to the minima in $\text{Re} \chi(q, \omega)$ and $\text{Im} \chi(q, \omega) = 0$ while the maxima in $\tau_{ee}^{th}(T)$ correspond to $\text{Re} \chi(q, \omega) = 0$ and maxima in $\text{Im} \chi(q, \omega)$ [1, 19].

To calculate $\text{Re} \chi(q, \omega)$ and $\text{Im} \chi(q, \omega)$, the expression (6) should be take in the form of function $\chi(\omega)$:

$$\chi_{ik}(\omega) = \frac{1}{S} \sum_q \chi_{ik}(q, \omega). \quad (10)$$

Taking into account the characteristic scales $q \in \{d_m^{-1}, d_p^{-1}\}$ of the 2D electron system, the summation over q results in the expression:

$$\chi_{ik}(\omega) = f(n_i, \omega) + f(n_k, \omega), \quad (11)$$

where

$$f_i(n_i, \omega) = L\sqrt{n_i} \left\{ \frac{1}{L\sqrt{n_i}} - \left[\sqrt{2\pi} - \left(\frac{m^*\omega L}{\hbar\sqrt{n_i}\pi} - \sum_{k=1}^{\infty} \left\{ \frac{(-1)^{k-1}}{2k(2k)!} \left(\frac{m^*\omega L}{\hbar\sqrt{n_i}\pi} \right)^{2k} \right\} \right)^2 \right]^{1/2} - \left[\sqrt{2\pi} - \left(\frac{m^*\omega L}{\hbar\sqrt{n_i}\pi} - \sum_{k=1}^{\infty} \left\{ \frac{(-1)^{k-1}}{2k(2k)!} \left(\frac{m^*\omega L}{\hbar\sqrt{n_i}\pi} \right)^{2k} \right\} \right)^2 \right]^{1/2} \right\}. \quad (12)$$

The latter expression reduces to:

$$f_i(n_i, \omega) = L\sqrt{n_i} \left\{ \frac{1}{L\sqrt{n_i}} - \left[\sqrt{2\pi} - \left(\frac{m^*\omega L}{\hbar\sqrt{n_i}\pi} - \ln \left(\frac{m^*\omega L}{\hbar\sqrt{n_i}\pi} \right) + C - \text{Ci} \left(\frac{m^*\omega L}{\hbar\sqrt{n_i}\pi} \right) \right)^2 \right]^{1/2} - \left[\sqrt{2\pi} - \left(\frac{m^*\omega L}{\hbar\sqrt{n_i}\pi} + \ln \left(\frac{m^*\omega L}{\hbar\sqrt{n_i}\pi} \right) - C + \text{Ci} \left(\frac{m^*\omega L}{\hbar\sqrt{n_i}\pi} \right) \right)^2 \right]^{1/2} \right\}, \quad (13)$$

where C is the Euler constant, $f(n_k, \omega)$ is given by (12) and (13) after the substitution of n_i by n_k ; $\text{Ci}(x) = \int_{-\infty}^x \frac{\cos t}{t} dt$ - integral cosinus. The alternating sums over k in (12) prove to be rapidly converging. Fig. 5 illustrates the partial contributions of various mechanisms to the Landau quantization destruction and the density-dependent singularities. For example, plotted in Fig. 5 are the frequency dependences $\text{Re} \chi(q, \omega)$ and $\text{Im} \chi(q, \omega)$ for $n_m \approx 10^{12} \text{cm}^{-2}$ for three intersubband transition channels. It is seen that the $n_m - n_n$ and $n_n - n_d$ interactions are dominant. Moreover, the resonant frequency is determined by the n -satellite density. Shown in Fig. 5 is the influence of the second size-quantized subband filling factor. An increase in the density n_m , (and hence n_n and n_d) results in the resonant frequency shift to higher values while the discontinuity in $\text{Re} \chi(q, \omega)$ and $\text{Im} \chi(q, \omega)$ is reduced which is consistent with the third scenario of the schematic model presented in Fig. 2 (domains "a" the real and "b" the imaginary parts of $\chi(\omega)$).

Similar analysis of the other channels for paths (1) and (2) of the model presented in Figs. 2 confirmed on the whole the trends presented in Fig. 5.

It should be noted here that in [12], the curve $\tau_{ee}(T)$ was obtained for a pair of coupled rectangular wells in the long wavelength limit at $T = 0$, which is incompatible with the conditions of the experiments reported in [9]. In that case [12], the calculations of $\tau_{ee}(T)$ result in divergences which cannot be neglected when solving a particular problem. On the other hand, formulas of the type of (9) and (10) derived by us for the inter- and intrasubband e-e interactions allow one to obtain expressions for $\tau_{ee}^{intra}(T)$ and $\tau_{ee}^{inter}(T)$ given in [12] with the coefficients B_i in (8, 9) do not containing any divergencies.

5. Conclusions

In conclusion, it should be noted that a similar problem for 2D electrons seems to have been first considered in [12], and since then, numerous attempts have been undertaken [13-18] to study this problem for 2D electron system where several size-quantized subbands are filled at $T \neq 0$ in the long wavelength limit. However, the plasma oscillation spectrum has not been obtained in any of these works. Characteristic features of 2D electron systems, such as the amplitude-frequency modulation, beatings, and sharp bends in the oscillation amplitude magnetic field dependence make the description of Landau quantization damping, in terms of the Dingle temperature, rather problematic. Another point to be considered is the fact that in the magnetic field range where a strong amplitude-frequency modulation takes place, the p -subband electrons are in the state close to the quantum limit and one can only speak of the oscillation's period in a rather limited sense.

Acknowledgements

Authors thank Prof. Yu. E. Lozovik, L. A. Falkovskyy, G. S. Lukyanova and A. I. Novikov for fruitful discussions.

References

- [1] Pines D., Nozieres P. *The theory of quantum liquids*. W.A. Benjamin, Inc. New York, Amsterdam, 383 p. (1966).
- [2] Leadley D. R., Nicholas R. J., Harris J. J., Foxon C. T. Inter-subband scattering rates in GaAs-GaAlAs heterojunctions. *Sem. Sci. Tech*, **5**, P. 1081-1089 (1990).
- [3] Lee S. C., Galbraith I. Intersubband and intrasubband electronic scattering rates in semiconductor quantum wells. *Phys. Rev. B.*, **59**(24), P. 15796-15805 (1999).
- [4] Coleridge P. T. Intersubband scattering in a 2D electron gas. *Semicond. Sci. Technol.*, **5**, P. 961-968 (1990).
- [5] Coleridge P. T. Small-angle scattering in two-dimensional electron gases. *Phys. Rev. B.*, **44**(8), P. 3793-3801 (1991).
- [6] Itskovsky M. A., Maniv. T. Fourier analysis of the de Haas-van Alphen oscillations in two-dimensions electron systems with background reservoir states. *Phys. Rev. B.*, **64**(17), P. 174421/1-174421/7 (2001).
- [7] Halvorsen E., Galperin Y., Chao K. A. Optical transitions in broken gap heterostructures. *Phys. Rev. B.*, **61**(24), P. 16743-16749 (2000).
- [8] Averkiev N. S., Monakhov A. M., Sablina N. I., Koenraad P. M. On the experimental data processing of the magnetoresistance oscillations in two-dimensional electron gas. *Semiconductors*, **37**(2), P. 169-172 (2003).
- [9] Kadushkin V. I., Dubois A. B., Gorbunova Yu. N., Tsahhaev F. M. Plasma Oscillations in Q2D Electron System with the Fine Structure of Energy Spectrum. *Phys. Low-Dim. Struct.*, **5**(6), P. 107-132 (2004).
- [10] Kadushkin V. I., Dubois A. B. Bottleneck in Electron Electron Interactions and Anomalies in the Landau Quantization Damping. *Phys. Low-Dim. Struct.*, **7**(8), P. 7-24 (2003).
- [11] Dubois A. B., Zilotova M. A., Kucheryavyy S. I., Safoshkin A. S. Kinetic processes in moderately doped heterojunction. *Vestnik of RSREU*, **3**(45), P. 88-92 (2013).
- [12] Slutzky M., Entin-Wohlman O., Berk Y., Palevsky A. Electron-electron scattering in coupled quantum wells. *Phys. Rev. B.*, **53**(7), P. 4065-4072 (1996).
- [13] Hatke A. T., Zudov M. A., Pfeiffer L. N., West K. W. Role of electron-electron interactions in magnetoresistance oscillations in high-mobility 2D electron systems. *Physica E*, **42**, P. 1081-1083 (2010).
- [14] Glazov S. Yu., Kubrakov E. S., and Meshcheryakova N. E. Plasma Oscillations in Two-Dimensional Electron Systems with a Superstructure under Stark Quantization Conditions. *Physics of Wave Phenomena*, **18**(4), P. 313-317 (2010).
- [15] Hatke A. T., Zudov M. A., Pfeiffer L. N., West K. W. Role of electron-electron interactions in nonlinear transport in two-dimensional electron systems. *Phys. Rev. B.*, **79**(16), P. 161308(R) (2009).
- [16] Raichev O. E. Magnetoresistance oscillations in two-subband electron systems: Influence of electron-phonon interaction. *Phys. Rev. B.*, **81**, P. 195301 (2010).

- [17] Sica G., Polini M., Tosi M.P. Electron Electron Interactions In The 2D Ferromagnetic Electron Fluid. *Modern Physics Letters B*, **15**(24), P. 1053–1059 (2001).
- [18] Goh K.E.J., Simmons M.Y., Hamilton A.R. Electron-electron interactions in highly disordered two-dimensional systems. *Phys. Rev. B.*, **77**, P. 235410 (2008).
- [19] Dubois A. B. Electron-electron interactions in moderately-doped heterojunction. *Proceedings of Moscow Institute of Physics and Technology (State University)*, **2**, 1(5), P. 24–27 (2010).
- [20] Dubois A. B. Plasma Oscillations and Electron–Electron Interactions in 2D Electron Systems. *Journal of Physics: Conference series*, **129**, P. 012025 (2010).

TIME-SERIES RATE OF CONVERGENCE TO QUASI-PERIODIC OSCILLATIONS

A. V. Bespalov, E. V. Vilкова

ITMO University , Saint Petersburg, Russia

magisterbes@gmail.com

PACS 05.45.Tp

We propose three algorithms that can fairly accurately estimate the degree of convergence to the limit cycle using time-series generated by systems that converge to a quasi-periodic oscillation and consider their applicability ranges. As a proof-of-concept, a trivial two-dimensional case is studied. A practically important three-dimensional case is considered. Generalization of the algorithm to the space of any number of dimensions is presented. An example of these algorithms was used for estimating the Van-der-Pol system convergence.

Keywords: Time-series, Self-oscillatory modes, Lyapunov exponents, convergence rate.

Received: 1 April 2014

Revised: 3 May 2014

1. Introduction

It is quite normal that a real technical system in its operating mode converges not to a stable equilibrium, but to some self-oscillatory process (quasi-periodic limit cycle) [1, 2]. This is not always a positive feature of the system, and usually self-oscillating regimes are considered to be harmful [1, 3, 4]. In most cases, such behavior results from system nonlinearities. Moreover, a certain class of systems uses this regime as normal operating mode [1, 2, 5, 6].

The Lyapunov exponents method allows one to estimate convergence rate for processes in steadily operating systems. Exponents can be evaluated analytically from a differential equations system [7, 8, 9], or estimated from the time-series generated by system dynamics [9-12]. The largest Lyapunov exponent is a criterion for the system's trajectory convergence to the steady state [7, 9, 12]. However, in self-oscillatory modes, the largest exponent vanishes and does not provide sufficiently accurate estimates of the convergence to characterize changes in system parameters [9]. Moreover, the main approach to self-oscillatory processes analysis is frequency domain analysis, such as different modifications of harmony balance techniques and Fourier analysis [13-15]. Thus, we still face the problem of creating effective tools for time domain analysis of such processes.

In this paper, we present three time domain algorithms based on similar principles which are able to estimate the degree of convergence to the limit cycle using time-series. The first algorithm can be used for time-series generated by simple oscillations with a sine or cosine limit cycle. The second algorithm can be used for three-dimensional phase space reconstruction with unusual waveforms. The third algorithm can be used with any-dimensional phase space.

2. Algorithms inputs and assumptions

Let us consider a time-series $x(t)$ corresponding to some system trajectory in phase space, which is the solution to some differential equation:

$$x(t) = \{x(t_0), x(t_0 + \Delta t), \dots, x(t_0 + n\Delta t)\}, \quad (1)$$

where $t_0 > 0$ is the initial time moment, $\Delta t > 0$ is the time-series discretization step, $n > 0, n \in \mathbb{N}$ is the time-series length. We assume the considered trajectory to meet the conditions of continuity; system attractor (repeller) [9] not to be strange; phase space structure to be regular in the neighborhood of each trajectory point and the solution to be periodic relative to the focus $F \in \mathbb{R}$ up to space compression (or expansion) operator $H(t)$, i.e.:

$$x(t + T) = H(t + T)x(t), \quad (2)$$

where T is the solution period. It is also assumed that the trajectory is converging or diverging exponentially, i.e. $H(t) = Ae^{\mu t} + r$, $A, r, \mu \in \mathbb{R}$, $A > 0, r > 0$ within phase space area of interest. The convergence coefficient μ is to be found. In the case of $F_0 \neq 0$, the periodic solution focus is shifted to 0 by the following transformation:

$$y(t) = x(t) - x(t + \tau), \quad (3)$$

where $\tau \ll T$. This conclusion comes from the following transformations:

$$\begin{aligned} x(t) - x(t + \tau) &= (Ae^{\mu t} + r)f(t) + F_0 - ((Ae^{\mu(t+\tau)} + r)f(t + \tau) + F_0) = \\ &= (Ae^{\mu t} + r)f(t) - (Ae^{\mu(t+\tau)} + r)f(t + \tau), \end{aligned} \quad (4)$$

where $f(t)$ is the periodic function with some period. Obviously this happens when $t \rightarrow \infty$, the resulting function tends to the limit cycle "radius" r of function $f(t)$. If the condition on τ is met, the contraction operator changes very little from one period to another. Furthermore, we assume that $F_0 = 0$ for all trajectories.

3. First algorithm (trivial)

In the case of simple oscillations:

$$y(t) = H(t)\sin(\omega t) = (Ae^{\mu t} + r)\sin(\omega t), \quad (5)$$

where $\omega > 0$ is the unknown oscillation frequency, and μ can be estimated using the following procedure:

For the trajectory generated by equation (5) delay-reconstruction is performed. With delay condition $0 < \tau < T$:

$$\tilde{y}(t) = (Ae^{\mu(t+\tau)} + r)\sin(\omega(t + \tau)). \quad (6)$$

The resulting reconstructed trajectory looks like a spiral which tends to the limit cycle or is unwinding from the focus. The plane that contains the spiral can be found using two arbitrary trajectory points and focus. Since the focus point has zero coordinates, we can assume that $x_0 = z_0 = y_0 = 0$. In the case of the first order reconstruction, the coordinates of trajectory points are determined by the following vectors $p_1 = (y(t_1), \tilde{y}(t_1), 0)$, $p_2 = (y(t_2), \tilde{y}(t_2), 0)$, t_1, t_2 being arbitrary time moments, $|t_1 - t_2| \neq \frac{T}{2}n$, where $n \in \mathbb{N}$. The plane equation will be:

$$z(y(t_1)\tilde{y}(t_2) - \tilde{y}(t_1)y(t_2)) = 0. \quad (7)$$

The equation of a plane contains a vector which is perpendicular to this plane, in this case: $\tilde{N} = (0, 0, A)$. Having three points $\tilde{N} = (0, 0, A)$, $F_0 = (0, 0, 0)$, $p_1 = (y(t_1), \tilde{y}(t_1), 0)$ we can build a section plane for the spiral:

$$x(y(t_1) - A) + y(\tilde{y}(t_1) - A) = 0. \tag{8}$$

This plane intersection with reconstructed trajectory does not depend on $H(t)$, and depends only on the system period, so frequency ω can be found from the following equation:

$$\sin(\omega t_1) = y(t_1) - A. \tag{9}$$

Thereafter:

$$\omega = \frac{\arcsin(y(t_1) - A) + \pi k}{t_1}, \tag{10}$$

where $k \in \mathbb{Z}$. However, we only need one solution in case $k = 0$ and the system period $= \frac{2\pi}{\omega}$. Since we have the period, we can now make a new series consisting of the original expression (5) points:

$$Y(t) = \{y(t_1), y(t_1 + T), \dots, y(t_1 + NT)\}, N \in \mathbb{N}. \tag{11}$$

In this series, the periodic part takes the same values, and all points of the series satisfy the expression:

$$\tilde{Y}(t) = C_1 e^{\mu t} + C_2. \tag{12}$$

For the series described by expression (11), there are several well-developed tools for μ estimation [10-12]. The basic concept of this solution is shown graphically in Figure 1.

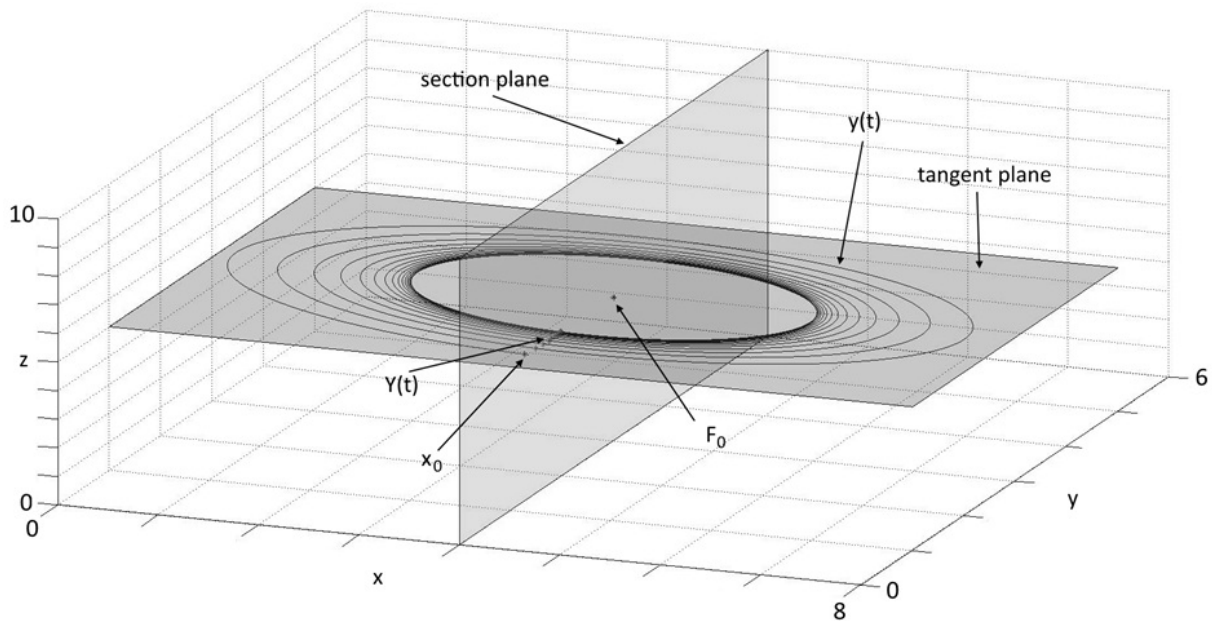


FIG. 1. Phase trajectory $y(t)$ with oscillations tending to the limit cycle. The highlighted horizontal plane contains spiral, vertical plane is the section plane. Points are the starting point x_0 , the point of focus F_0 and trajectory points lying a period apart $Y(t)$

If we initially have a discrete series, we can build the series (11) for a set of reconstructed trajectory points describing the full period of the spiral and estimate μ by averaging over all the intermediate results.

Obviously, expression (5) can be derived by less complicated considerations. However, this example is a perfect illustration of the method that can be used for more complex dynamics.

However, when the process is quasi-periodic, like this:

$$x(t) = H(t) f(t) = H(t) f(t + nT), \tag{13}$$

where $n \in \mathbb{N}$, the following difficulties arise:

- (1) Self-intersections of the reconstructed trajectory appear
- (2) Spatial trajectory does not lie in one plane
- (3) Perpendicular section plane may intersect with trajectory points which are not a period or half-period apart.

To solve these problems, we propose an algorithm that can deal with such difficulties.

4. Second algorithm (three-dimensional)

At first, we set some conditions that should apply to the reconstructed phase trajectory:

- (1) Reconstructed trajectory should have the number of dimensions sufficient to avoid self-intersections.
- (2) If at some point, $x(t_0)$, the derivative vector along the trajectory has a direction of \vec{A} , then the plane \tilde{S} that is perpendicular to S and contains the focus and $x(t_0)$ has no other codirectional to \vec{A} intersections with the trajectory near the plane S , except a number of points described by $x(t_0 + kT)$, $k \in \mathbb{N}$.

If these conditions are met for three-dimensional reconstruction of the series (1), described by expression (13), μ can be estimated by the following algorithm:

the attractor is reconstructed in phase space that has $K = 3$ dimensions with reconstruction delay τ_r . Start time is set to zero. We select three points on the trajectory. The first point $x(t_0) = x_0$, where $t_0 = \tau$, and two points $x(t_0 + \tau)$ and $x(t_0 - \tau)$. Now, we find equations of the plane S using points $[x(t_0 - \tau), x(t_0 + \tau), F_0]$; and section plane \tilde{S} using points $[x(t_0), p_1, F_0]$ where p_1 – point from the vector perpendicular to S .

Then, passing through the points of time-series (1) starting with x_0 , we seek a point $x(t_1) = x_{min}$, which is the time-series value a period after x_0 . This point is sought as follows:

first, the reconstructed vector function $x(t)$ is substituted into the equation of section plane and sign is extracted from the resulting number. This gives us function $s_0(t)$ that shows the relative to the plane side of the trajectory point. Then, passing through all the series points, we take all the points where $s_0(t_0 + k\Delta t) \neq s_0(t_0 + (k+1)\Delta t)$ and $s_0(t_0 + (k+1)\Delta t) = s_0(t_0)$, thus obtaining a series of points $h(t)$ that crosses the section plane in a certain direction.

Then, we seek for the point of series $h(t)$ with minimum distance from the section plane \tilde{S} and the plane S (in the two-dimensional case, the second condition is satisfied automatically). The distance from a point to a plane can be estimated as the absolute value which is obtained by substituting points coordinates in the equation of the plane.

Therefore, for a single period the following minimization problem can be solved:

$$J(t) = L(x(t), \tilde{S}) + L(x(t), S) + \sigma(x(t), \tilde{S}) \rightarrow min, \tag{14}$$

where $L(x(t), S) \in [0; 1]$ is the normalized per unit distance from the point $x(t)$ to the plane S , $\sigma(x(t), \tilde{S}) \in [0; 1]$ is the weight function which has a minimum value at the intersection

of the trajectory with the plane \tilde{S} in the starting point direction. The weight function, $J(t)$, is the representation of the second condition which must be applied to the trajectory. $J(t) = 0$ only when the trajectory simultaneously intersects \tilde{S} , S and $x(t)$ codirectional to the starting point. The trajectory might never intersect S near “period point” but there is only one point where the trajectory can come close to S , so that $L(x(t), S)$ is small and $\sigma(x(t), \tilde{S}) + L(x(t), \tilde{S}) = 0$ simultaneously – the period point. This ensures that $J(t)$ has only one minimum per period. In practice, $J(t) < \varepsilon$ condition is used to find $J(t)$ minimum for the entire series, ε is small and $\varepsilon > 0$.

As a result, we obtain an array of trajectory points which are period apart and then select the point with minimal time thereout.

Here is an example of such search algorithm applied to the reconstructed series generated by the expression:

$$x(t) = (\sin(3t) + 0.7\cos(5t))(e^{-0.05t} + 1), \tag{15}$$

is shown in Fig. 2, 3.

As is shown in figure 2, all $J(t)$ components tend to zero in the area outlined by the circle. The trajectory intersects the plane \tilde{S} and is tangential to the plane S , and the required side change occurs.

Also, we can follow the trajectory only up to $T/2$, using $-\sigma(x(t), \tilde{S})$ condition. Then, trajectory points evaluation ends after the first sign $s_0(t)$ change. However, this only makes sense if the trajectory is symmetric with respect to the focus.

Knowing the period, one can construct a number of series (11) for the selected set of trajectory points from the beginning to the end of the first period. Then, for each of these series, μ_i is estimated by the known formulas and the results are averaged.

This algorithm still has some problems. You have to raise the reconstruction dimension to avoid trajectory intersections. However, if the reconstruction dimension is higher than 3, the task of seeking section planes becomes more complicated, as multiple dimensions increase the number of equations in the system which defines the plane.

The third presented algorithm helps to avoid this complication.

5. Third algorithm (generalization)

This algorithm is almost the same as the second one. The main difference is that we propose to change $J(t)$. The new weight function $J(t)$ is described by the following equation:

$$J(t) = F(t) + \tilde{F}(t) + \sigma_1(t, F(t)) \rightarrow \min, \tag{16}$$

where $F(t) = -(\cos(x_0, x(t)) - 1)$ and $\cos(x_0, x(t))$ – cosine of the angle between the vectors formed by points F_0, x_0 and $F_0, x(t)$, $\tilde{F}(t) = -(\cos(\tilde{x}_0, \tilde{x}(t)) - 1)$, where $\cos(\tilde{x}_0, \tilde{x}(t))$ – cosine of the angle between vectors \tilde{x}_0 and $\tilde{x}(t)$ along the trajectory traveling through points x_0 and $x(t)$, $\sigma_1(t, F(t)) \in [0; 1]$ is the weight function that has a minimum value when the sign of the $F(t)$ derivative changes from negative to positive. For example, σ_1 can be described by the following equation:

$$\sigma_1(t, F(t)) = \begin{cases} 0, & \dot{F} = 0, \ddot{F} > 0 \\ 1, & \dot{F} = 0, \ddot{F} < 0 \\ 0.5, & \dot{F} \neq 0 \end{cases} \tag{17}$$

Analytically, this function works well with all $F(t)$ where $\ddot{F} \neq 0$ while $\dot{F} = 0$. In practice, we always can see in which direction function will change right after $\dot{F} = 0$.

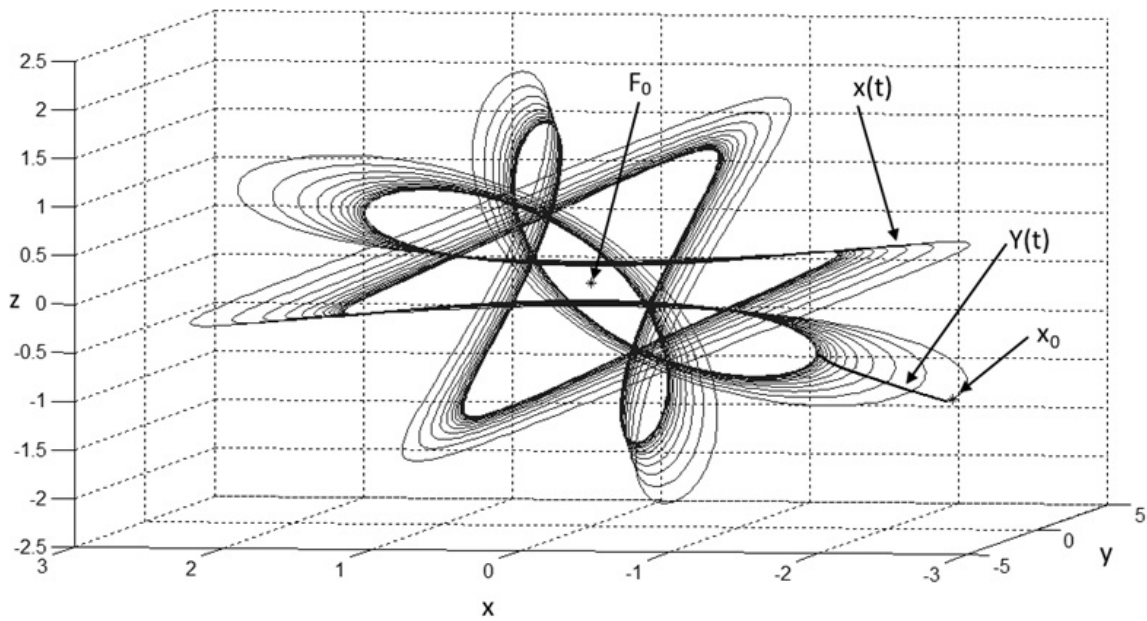


FIG. 2. Reconstructed phase trajectory $x(t)$ generated by the expression (15). Asterisks denote the starting point x_0 , the point of focus F_0 and line shows series $Y(t)$

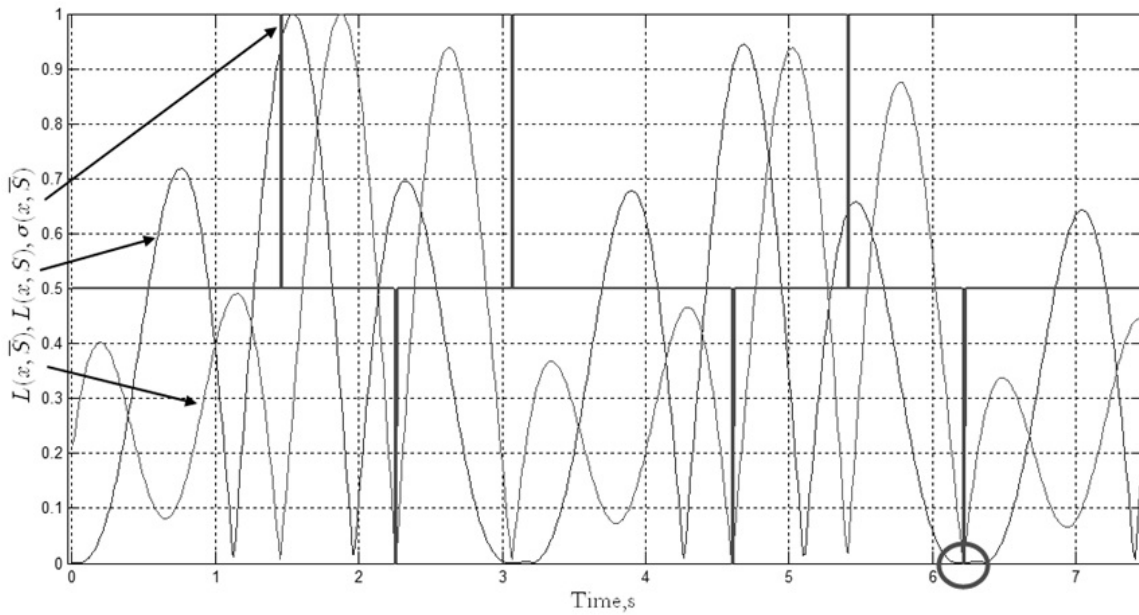


FIG. 3. $J(t)$ components for one period: $L(x(t), \tilde{S})$ – trajectory distance from \tilde{S} plane, $L(x(t), S)$ – trajectory distance from S plane, $\sigma(x(t), \tilde{S})$ – weight function which has a minimum value at the intersection of the trajectory with the plane \tilde{S} in the starting point direction

The function $F(t) = 0$ only at the points situated at the virtual plane S which contains x_0 and F_0 . Moreover, these points are situated at the virtual section plane \tilde{S} , which also contains x_0 and F_0 . It is hard to form equations of these planes, but we know that they exist and can be formed by two vectors. The function $\tilde{F}(t) = 0$ only if vectors \tilde{x}_0 and $\tilde{x}(t)$ are codirectional. Due to the second condition on the trajectory $F(t) = 0$ and $\tilde{F}(t) = 0$ only if $x(t)$ and x_0 are a period apart. This ensures that $J(t)$ has only one minimum per period. The function $\sigma_1(t, F(t))$ is not analytically necessary but it is helpful in practical implementation, where we can use $J(t) < \varepsilon$ condition to seek minimum. A constant ε limits our assumption on how near the trajectory can come to the virtual planes intersection while it is still not the period point.

An example of this search algorithm, applied to the reconstructed series generated by expression (15), is shown in Fig. 4.

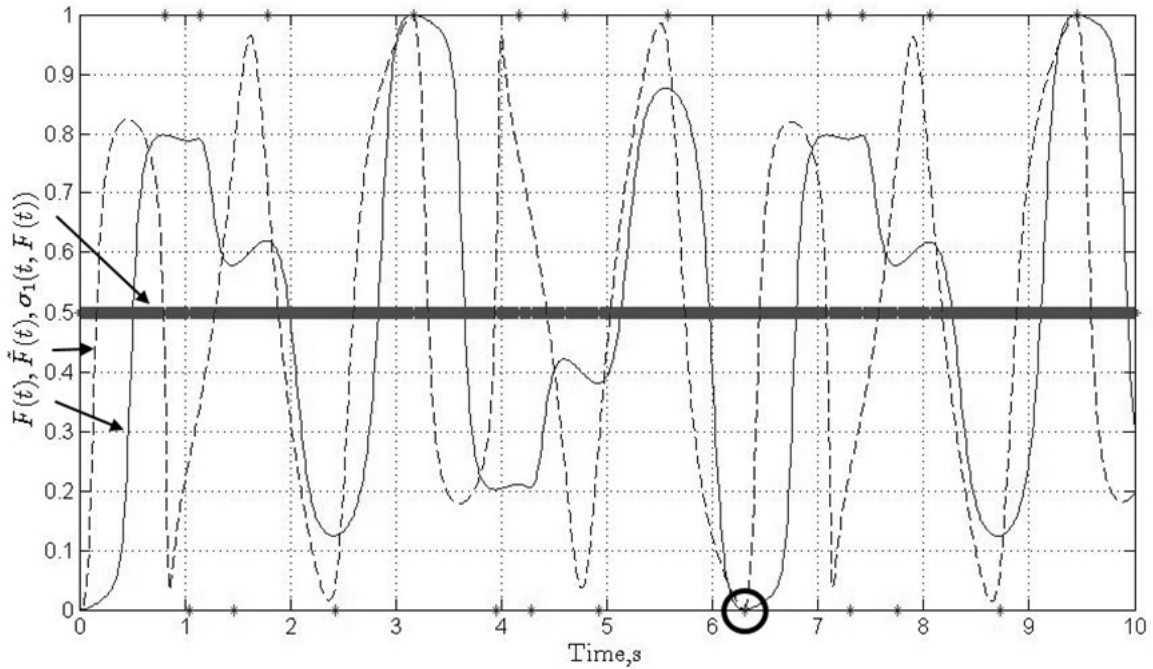


FIG. 4. $J(t)$ components for one period: $F(t)$ – solid line. Weight function based on cosine for angle between vector x_0 and vector function $x(t)$, $\tilde{F}(t)$ – dashed line. Weight function based on cosine for angle between vector \tilde{x}_0 and vector function $\tilde{x}(t)$, $\sigma_1(t, F(t))$ – the weight function that has a minimum value when the sign of the $F(t)$ derivative changes from negative to positive

The problem with this evaluation of $\sigma_1(t, F(t))$, as well as with the whole proposed algorithm, is that for a noisy process, such an approach would give a large error due to the frequent change of the derivative sign and $\sigma_1(t, F(t))$ should be evaluated differently. In three dimensions, this would not happen, because trajectory intersects section plane (usually) only once through the period, regardless of the noise.

As an example, let us evaluate μ at convergent Van-der-Pol system using second algorithm and third algorithm:

$$\begin{cases} \dot{x}_1 = x_2 \\ \dot{x}_2 = x_2(1 - x_1^2) - x_1 \\ y = x_1(e^{-0.05t} + 1) \end{cases} \quad (18)$$

The system is simulated with a step of $t = 0.01s$. for 100 s. The third algorithm gives the period value of $T_1 = 6.68$ s., the second algorithm estimated period to be $T_2 = 6.67$ s. Knowing T , we build series (11) for every 30th point of first period. For each slice, exponential convergence to the limit cycle is computed. The result is averaged over all slices. Resulting values obtained with both algorithms coincide an equal -0.054 . Simulation results are shown in Fig. 5, 6.

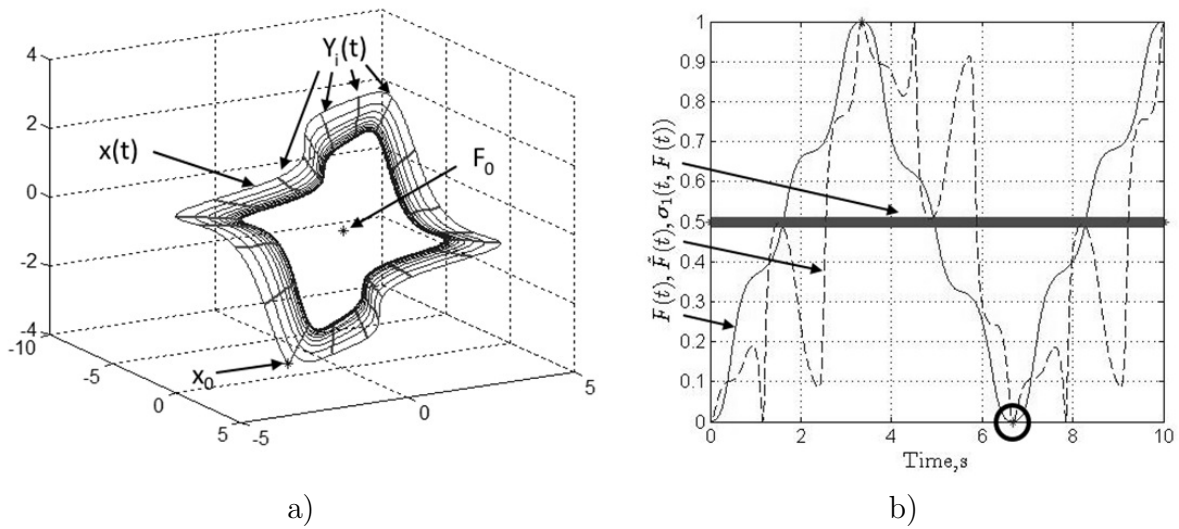


FIG. 5. a) Phase trajectory $x(t)$ of Van-Der-Pol reconstructed system (18). Straight lines indicate the sections $Y_i(t)$ for which μ is evaluated. x_0 is the starting point, F_0 is the point of focus b) $J(t)$ components for one period: $F(t)$ – solid line. Weight function based on cosine for angle between x_0 and $x(t)$, $\tilde{F}(t)$ – dashed line. Weight function based on cosine for angle between \tilde{x}_0 and $\tilde{x}(t)$, $\sigma_1(t, F(t))$ – the weight function that has a minimum value when the sign of the $F(t)$ derivative changes from negative to positive

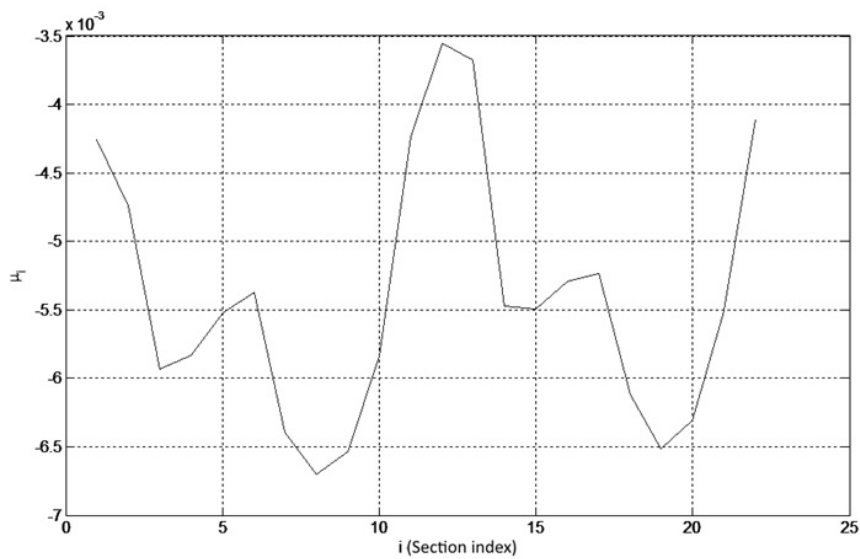


FIG. 6. Estimated μ_i for each trajectory slice

6. Conclusion

Three new algorithms to estimate the convergence rate μ to limit cycle are presented in this paper. The first proposed algorithm can be used to estimate μ for converging sine waves, but has problems with periodic processes with unusual waveforms. The second algorithm which can be used for three-dimensional reconstructions can be useful for the majority of practical cases but it can't work in case of self-intersecting trajectories. This self-intersection can happen if the three-dimensional reconstruction is not sufficient, so the third proposed algorithm solves this problem and can be used for reconstructing dimensions higher than 3. Still, the third algorithm has problems in accurate evaluation of μ for noisy time-series, due to the frequent change of the derivative sign in noisy processes. Nevertheless, all three algorithms used together allow sufficiently accurate μ estimation and can be used for quite a large number of real processes. The main advantage of the proposed methods is that they can make accurate estimations of such process characteristics as period and convergence rate without using frequency domain techniques.

References

- [1] Jenkins A., Self-oscillation, *Phys. Rep.*, **525**, P. 167–222 (2013).
- [2] Lazarus A., Barois T., Perisanu S., Poncharal P. Simple modeling of self-oscillations in nanoelectromechanical systems. *Applied Physics Letters*, **96**(19), P. 193114 (2010).
- [3] Hodges D.H., Pierce A. Introduction to structural dynamics and aeroelasticity. Cambridge (2002).
- [4] Hoque M. E. Active flutter control, LAP Lambert Academic Publishing. Germany (2010).
- [5] Lukin K. A., Maksymov P. P. Terahertz self-oscillations in reverse biased P-N junctions, in Proc Physics and Engineering of Microwaves, Millimeter and Submillimeter Waves and Workshop on Terahertz Technologies, 2007. MSMW '07. The Sixth International Kharkov Symposium, Kharkov, 25–30 June, 2007, P. 201–203.
- [6] Muljadi E., Sallan J., Sanz M. Butterfield C.P. Investigation of self-excited induction generators for wind turbine applications, in Proc. IEEE Industry Applications Conference 1999, vol. 1, P. 509–515.
- [7] Benettin G., Galgani L., Giorgilli A., Strelcyn J.M. Lyapunov characteristic exponents for smooth dynamical systems and for hamiltonian systems; a method for computing all of them, part 2: numerical application. *Meccanica*, **15**(1), P. 21–30 (1980).
- [8] Leonov G. A. Chaotic dynamics and classical theory of the dynamic stability, Research center “Regular and chaotic dynamics”, Izhevsk, 186 p.
- [9] Malinestky G., Potapov A., Podlazov A. Nonlinear dynamics: approaches, results, hopes (synergetics: “from past to future”). KomKniga, Moscow (2006), 280 p.
- [10] Bespalov A., Chistyakov Y. On the local stability estimation using first Lyapunov exponent calculation, in Proc. Eurocon 2009, Saint Petersburg, 2009, P. 1985–1990.
- [11] Rosenstein M. T., Collins J. J., De Luca C. J. A. Practical method for calculating largest Lyapunov exponents from small data sets Source, *Physica D*. **65**(1-2), P. 117–134 (1993).
- [12] Wolf A., Swift J. B., Swinney H. L. Determining Lyapunov exponents from a time series. *Physica*, P. 285–317 (1985).
- [13] Gilbert J., Kergomard J., Ngoya E. Calculation of the steady-state oscillations of a clarinet using the harmonic balance technique, *J. Acoust. Soc. Amer.*, **86**(1), P. 35–41 (1989).
- [14] Nakhla M., Vlach J. A piecewise harmonic balance technique for determination of periodic response of nonlinear systems”. IEEE Transactions on Circuits and Systems, IEEE Transactions on Circuits and Systems, 1976, CAS-23, P. 85–91.
- [15] Smirnov D. Characterization of weak coupling between self-oscillation systems from short time series: Technique and applications. *Journal of Communications Technology and Electronics*, **51**(6), P. 534–544 (2006).

COMPARISON OF WAVELET TRANSFORM AND FOURIER TRANSFORM APPLIED TO ANALYSIS OF NON-STATIONARY PROCESSES

A. Drozdov^{1,*}, I. Pomortsev², K. Tyutyukin³, Y. Baloshin^{2,**}

¹Institute for Analytical Instrumentation Russian Academy of Science, Russia

²ITMO University, St. Petersburg, Russia

³St. Petersburg State University, Physical faculty, St. Petersburg, Russia

*av@biophys.ru, **baloshin1940@mail.ru

PACS 02.60.-x, 02.70.-c

This article contains a comparison of three data analysis methods' informativity: wavelet transform, Fourier transform and short-time Fourier transform. This work contains an attempt to find the most sensitive method for the detection of quasiharmonic components in experimental data that have pronounced non-stationary behavior.

Results of high-frequency near-field sounding, IR-spectroscopy and NMR analysis of water, and also model harmonic signal were used as non-stationary processes for analysis.

Keywords: wavelet transform, Fourier transform, short-time Fourier transform, non-stationary processes analysis, quasiharmonic signal.

Received: 12 April 2014

Revised: 26 May 2014

1. Introduction

There are several cases when real experimental data is non-harmonic, contains noise, and is non-stationary in time range. This leads to difficulties in using the most popular method — the Fourier transform. The finding of quasiharmonic components is a very important problem in data analysis because this information could quite precisely show the repeatability of processes that occur in a studied system.

The wavelet transform has been recognized for the analysis of experimental data as a method that gives information about process that is not available for the Fourier transform. But there still exists no criteria for the selection of which method should be used for the analysis of experimental data.

Here, we tried to compare results of applying three methods to model signal that (as we know) contains or does not contain (quasi)harmonic components — as the first part, and applying to experimental data — as the second part. Results of such comparison give us information about the 'harmonic sensitivity' of each method and could give some criteria for selecting the appropriate method for analysis.

Let's look at the formulation of a problem. We have some signal that changes over time:

$$x = f(t).$$

This signal could contain both harmonic components and random noise. The purpose of analysis is to find quasi-harmonic components independently of noise.

The first method, coming from classical spectral analysis, is the Fourier transform. This method could be defined just using the formula of the transform (1):

$$F(w) = \frac{1}{\sqrt{2\pi}} \int_{-\infty}^{+\infty} f(t) e^{-iwt} dt. \quad (1)$$

The result of this transform shows the spectral (frequency) content of the signal. We can get the best result for this transform if the signal is harmonious on all time axes. But, if we apply this method to the signal, which apart the harmonic components also has the noise, the result will be less unambiguous.

In addition, a more significant problem is the fact that the Fourier transform of two completely different signals can be very similar — for example, for a sum of two sine waves and the signal from two successive sine waves. This problem could be partly solved using the second method — the Short-time Fourier transform (STFT). It is defined by the following formula:

$$F(t, w) = \frac{1}{\sqrt{2\pi}} \int_{-\infty}^{+\infty} f(\tau) W(\tau - t) e^{-iw\tau} d\tau. \quad (2)$$

There is function $W(t)$ that is called window function. A definite property of this function is that it has a norm that equals 1: $\int_{-\infty}^{+\infty} W(\tau) d\tau = 1$.

Insertion of the window function into the formula for the Fourier transform gives us a chance to explore signal in short-time area — the window function is defined at compact with fixed width of the support and product of the window function and the signal cuts a small part of the signal. Applying of the Fourier transform formula to this product then gives us the spectral components corresponding exactly to this part of signal. As soon as the window ‘slides’ over the signal, this gives us information about the spectral components of each such small part of the signal. But, as soon as this method is based on the first method, we still have a lot of difficulties with the detection of quasiharmonic components in a non-stationary signal.

The last method is the wavelet transform. This method is based on absolutely different premises, unlike the previous methods, and because of that, it has other properties and results of its application.

The wavelet transform is defined by the following formula:

$$T(a, b) = \frac{1}{\sqrt{|a|}} \int_{-\infty}^{+\infty} f(t) \Psi^* \left(\frac{t - b}{a} \right) d\tau. \quad (3)$$

As the ‘mother wavelet’ can be different functions, the selection of this function will give different properties to the resulting transform. These functions could be complex-valued or real-valued, could be defined as a compact set or as the whole real axis. It may or may not be based on quasi-harmonic functions. In this article, we used Morlet wavelet as the ‘mother wavelet’ for the transform. [1–5].

2. Model signals

Let’s apply these methods to model signal.

2.1. Analysis of ‘pure’ signal

‘Pure’ signal – the signal which has two harmonics with different frequencies. There is a plot of this signal on Fig. 1.

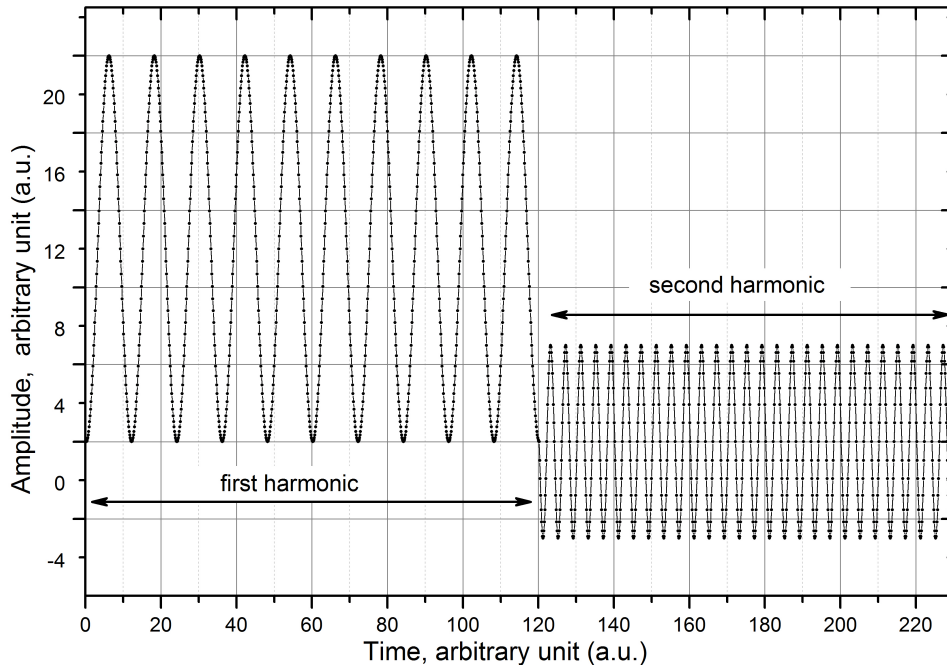


FIG. 1. Model ‘pure’ signal – the signal which has two harmonics with different frequencies

As described before, our purpose is to select method that gives us the most information about the quasiharmonic components of a signal.

The Fourier transform is shown in Fig. 2 as frequency characteristics. There are two peaks at two frequencies that correspond to two harmonic components in the signal. But even having information about the harmonic components, we have no information about true form of the signal.

Short-time Fourier transform with window height equals 200 ticks is shown in Fig. 3.

STFT of model ‘pure’ signal detects two harmonics with frequencies equal ~ 0.09 arbitrary unit (a.u.) and ~ 0.245 a.u.

The wavelet transform and its cross-sections are shown in Fig. 4(a–c). Dashed lines in Fig. 4a show positions of the cross sections.

Analysis of the obtained results shows us that the wavelet transform allows us to precisely detect harmonic components of the signal and gives us good representation of analyzed signal.

2.2. Analysis of ‘pure’ signal with a noise

In this section we add ‘white noise’ with an amplitude that almost equals the amplitude of the ‘pure’ signal. Our purpose is also to find two harmonic components using three methods. The plot of this signal is available in Fig. 5, its Fourier transform is in Fig. 6, short-time Fourier transform is given in Fig. 7 and its wavelet transform is in Fig. 7(a–c).

The Fourier transform of the ‘noised’ signal gives us precise information about the harmonic components in the signal, as for the ‘pure’ signal.

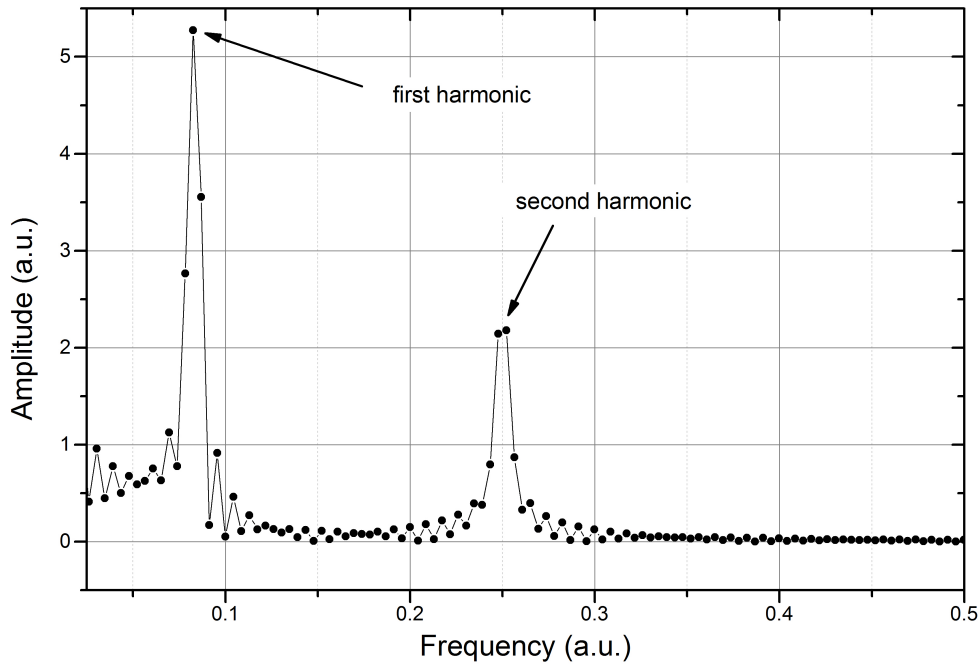


FIG. 2. Fourier transform of model 'pure' signal

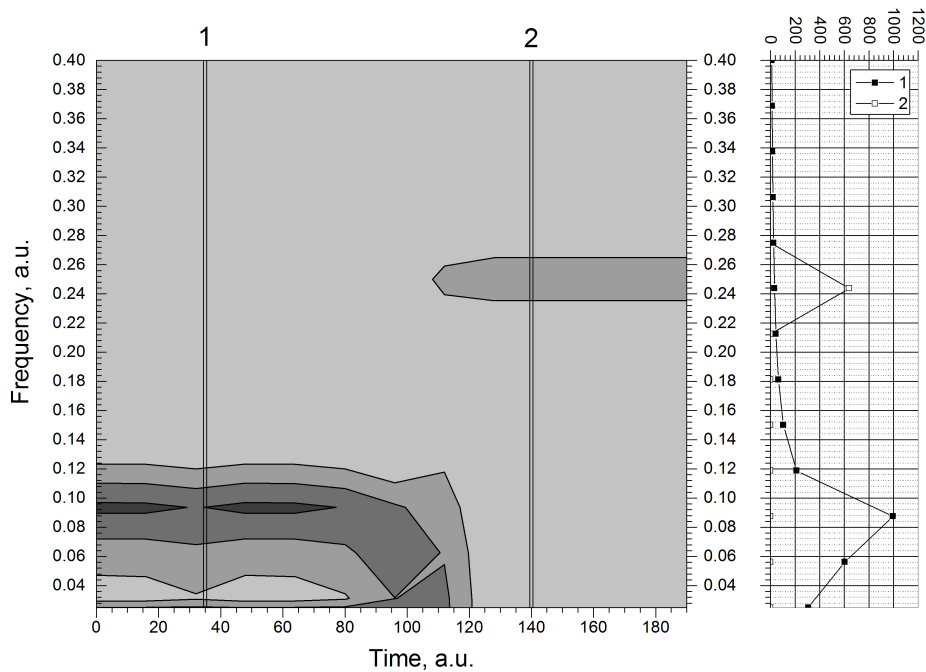


FIG. 3. Short time Fourier transform of model 'pure' signal and its cross-sections at $t = 30$ ticks and $t = 140$ ticks

STFT of model 'noised' signal (Fig. 7) allows us to detect two harmonic components with frequencies ~ 0.09 a.u. and ~ 0.245 a.u. that are very close to true values of these components.

Figures 8(a-c) shows the wavelet transform of the model 'noised' signal and its harmonic components (along dashed lines) that the signal contains.

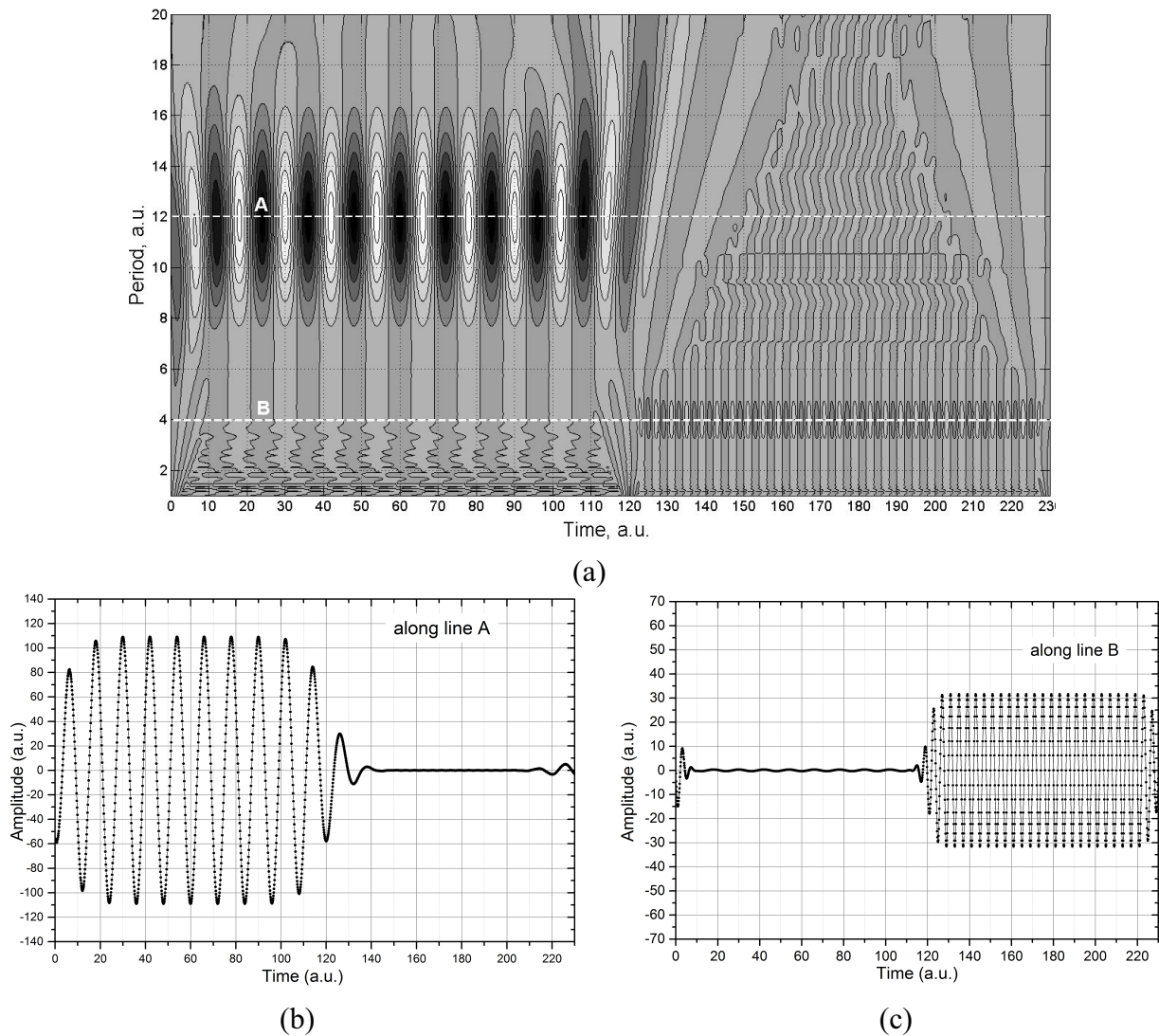


FIG. 4. (a) – Wavelet transform of model ‘pure’ signal. Dashed line shows harmonic components that form the signal; (b, c) – Cross-section of harmonic component along a dashed line A (b) and B (c) (fig. 4(a))

So, the wavelet transform of the ‘noised’ signal gives precise information about values of components’ frequencies and common image of signal.

3. Experimental signal

This section refers to the application of these methods to the experimental result by analogy with signals from the first paragraph.

The experimental result is dynamics of the integrated intensity of Nuclear Magnetic Resonance (NMR) from water protons in magnetic field of Earth. There is a plot of this signal on Fig. 9.

Results of data from the Fourier transform analysis show us that the detection of the harmonic components in this signal is ambiguous (Fig. 10).

Using STFT (Fig. 11), we could suppose that the signal contains only one harmonic component with frequency equals ~ 0.02 a.u.

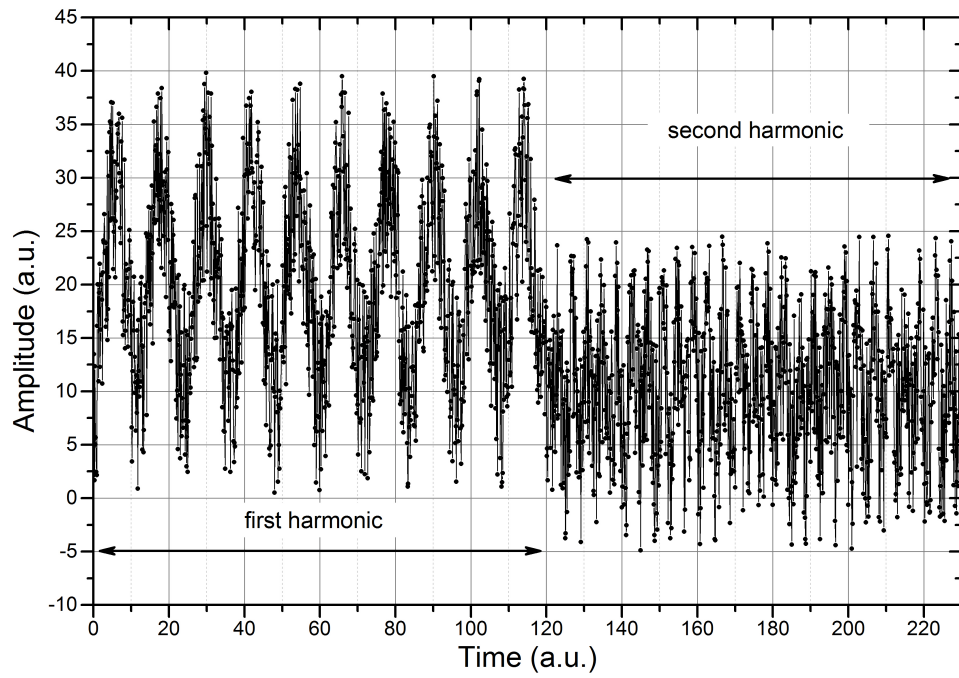


FIG. 5. Model 'noised' signal

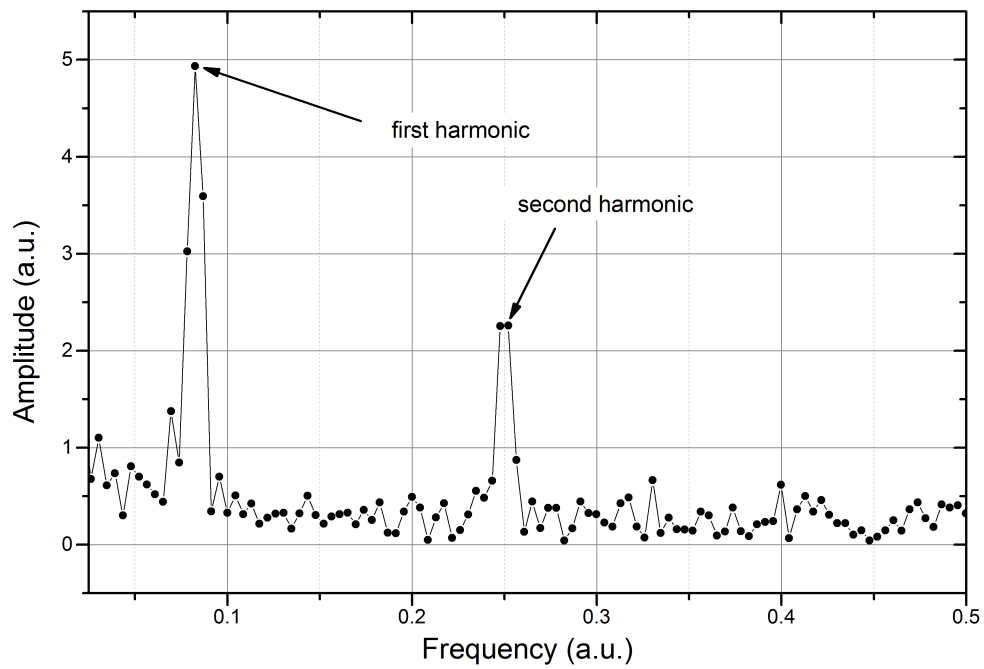


FIG. 6. Fourier transform of model 'noised' signal

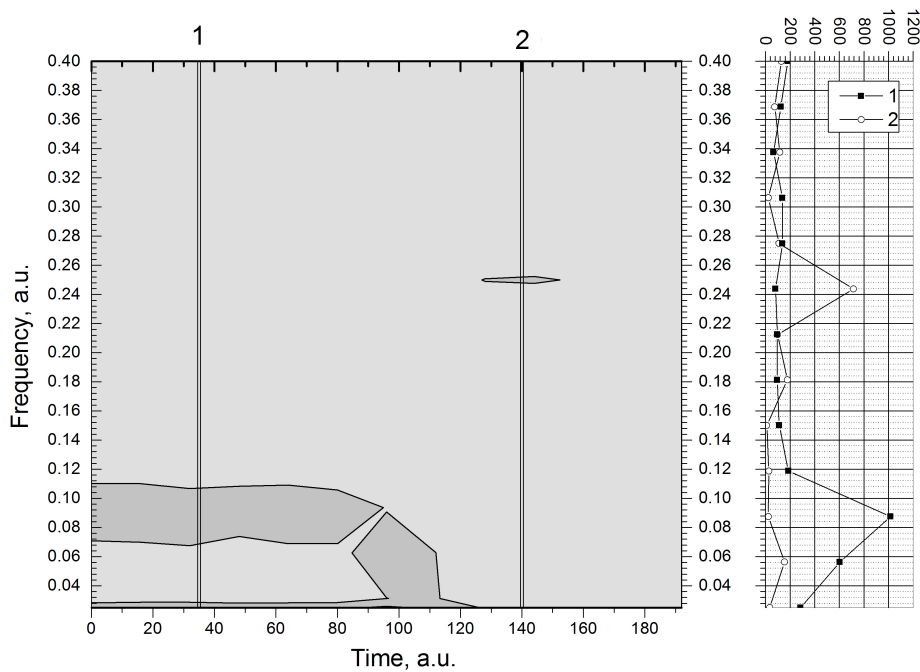


FIG. 7. Short-time Fourier transform with cross-sections of 'noised' signal

In contrast with the Fourier methods, the Wavelet transform allows us to detect the existence of quasi-harmonic components in the signal (Fig. 12(b,c)) with the periods equal ~ 20 a.u. and ~ 50 a.u. (frequencies ~ 0.05 and ~ 0.025 a.u. respectively). Wavelet analysis in this case gives us adequate description of the dynamics of quasi-harmonic processes that take place in the system.

The two-dimensional scan of one-dimensional process, where frequency and time are considered as two independent variables, allows us to analyze the properties of the studied process simultaneously in frequency- and in time-fields, which is very important for the analysis of many experiments.

4. Conclusion

As a result of the comparison of these three methods, we can say that the wavelet transform at least gives us some information that could be compared with the results of conventional Fourier methods. The application of this method to the experimental data shows us that the Wavelet transform:

- allows us to claim the hypothesis about existence of quasi-harmonic components in non-stationary (in time-field) signals with some frequencies (periods);
- gives us a full and precise image of the quasi-harmonic components' dynamics in signal.

So, almost all fields of science where the Fourier transform is a conventional method for analyzing experimental data, the Wavelet transform can be used as a higher quality method for finding quasi-harmonic components in any signals [6–9].

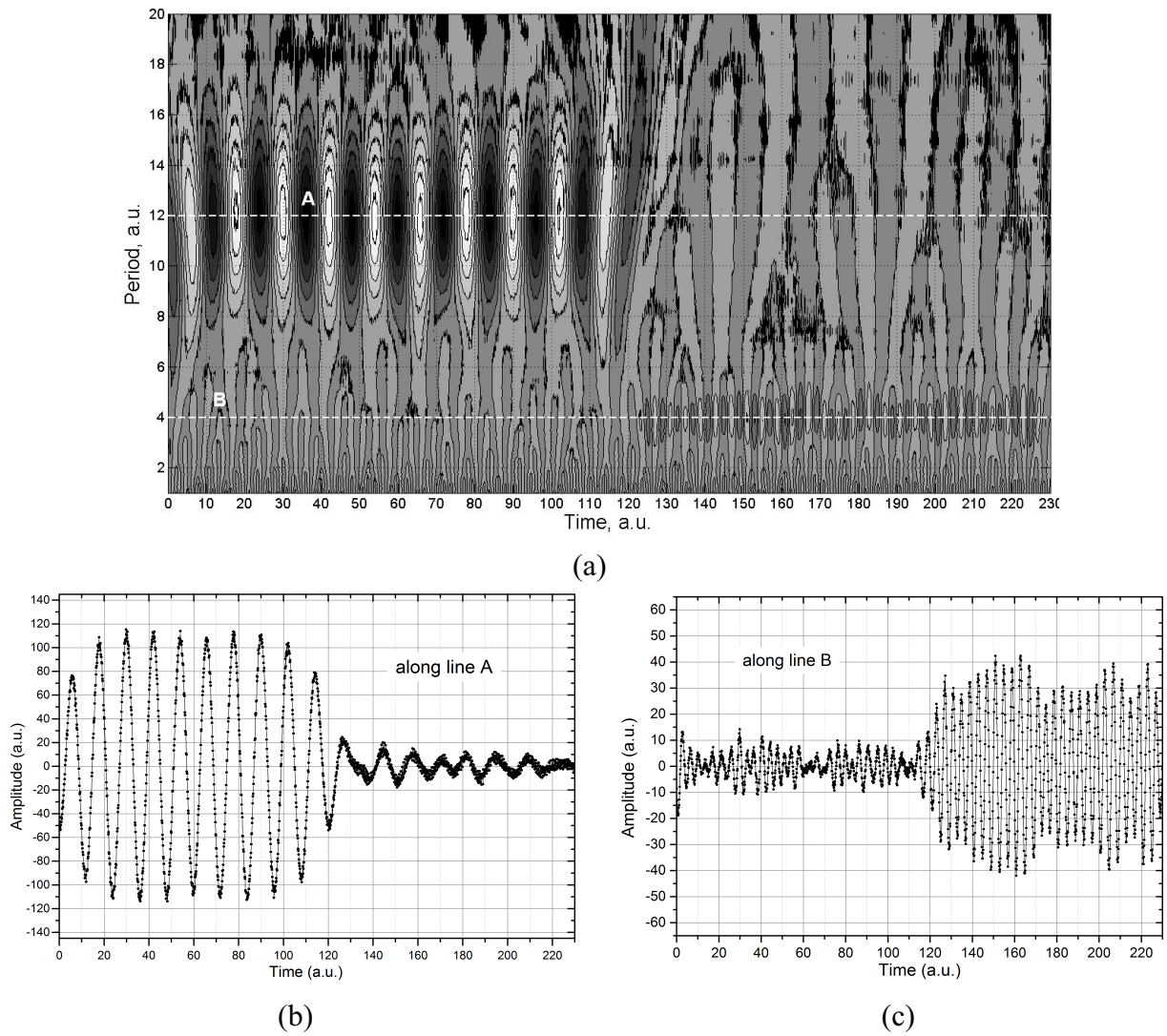


FIG. 8. (a) – Wavelet transform of ‘noised’ signal with dashed lines at harmonic components; (b, c) – Cross-section of harmonic component at line A (b) and B (c)

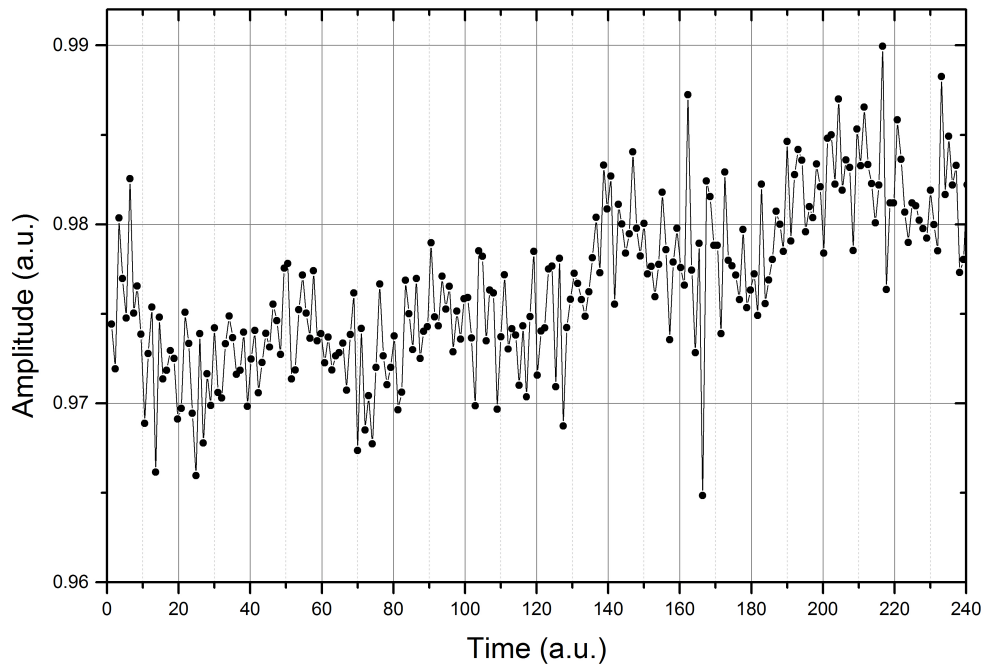


FIG. 9. Plot of experimental signal (the integrated intensity of Nuclear Magnetic Resonance signal from water protons in magnetic field of the Earth)

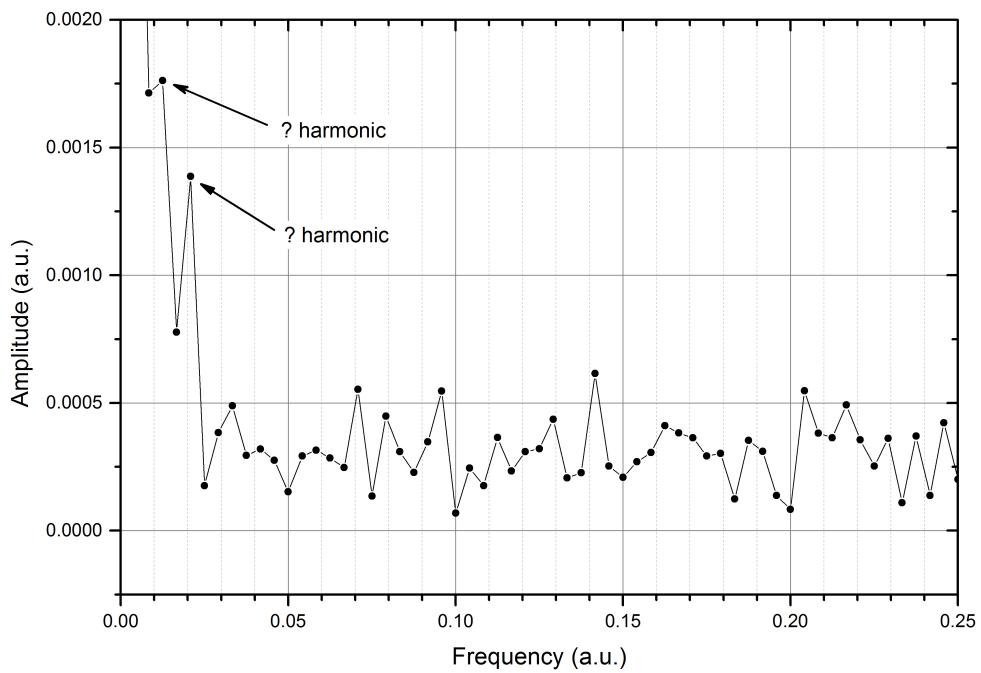


FIG. 10. Fourier transform of the experimental signal

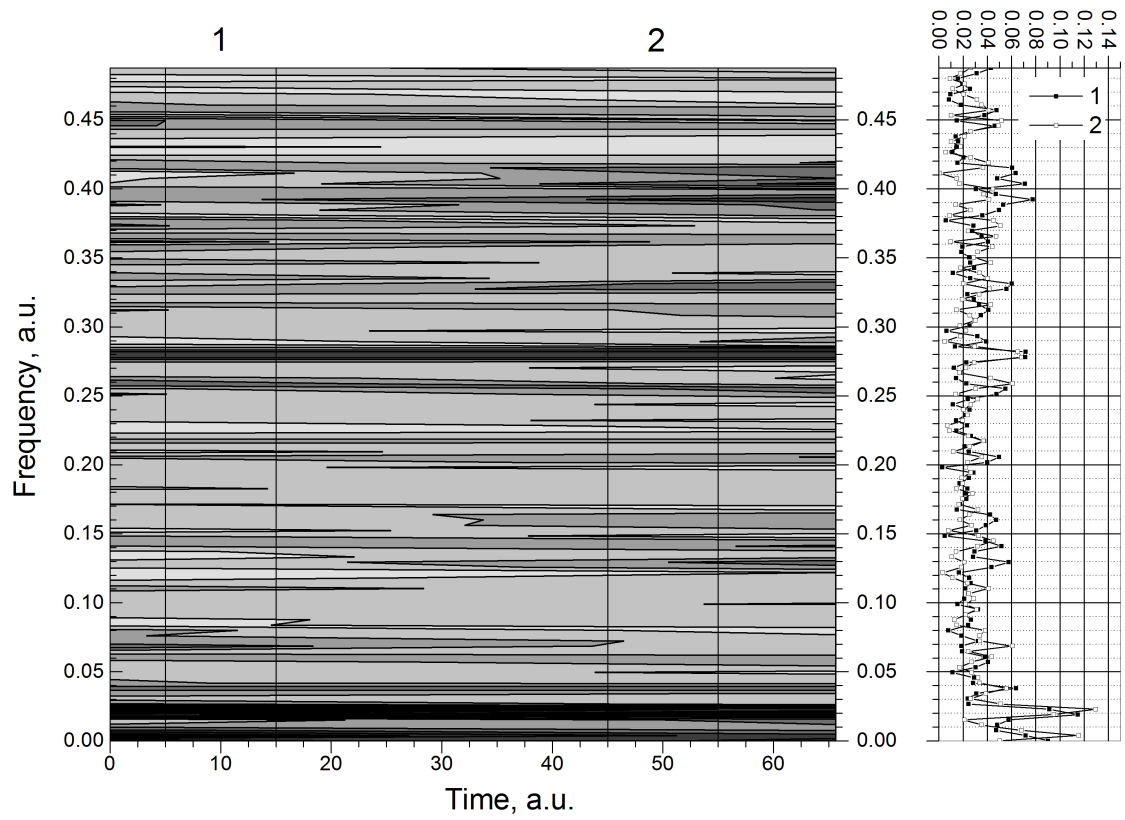


FIG. 11. Short-time Fourier transform of the experimental signal with its cross-sections

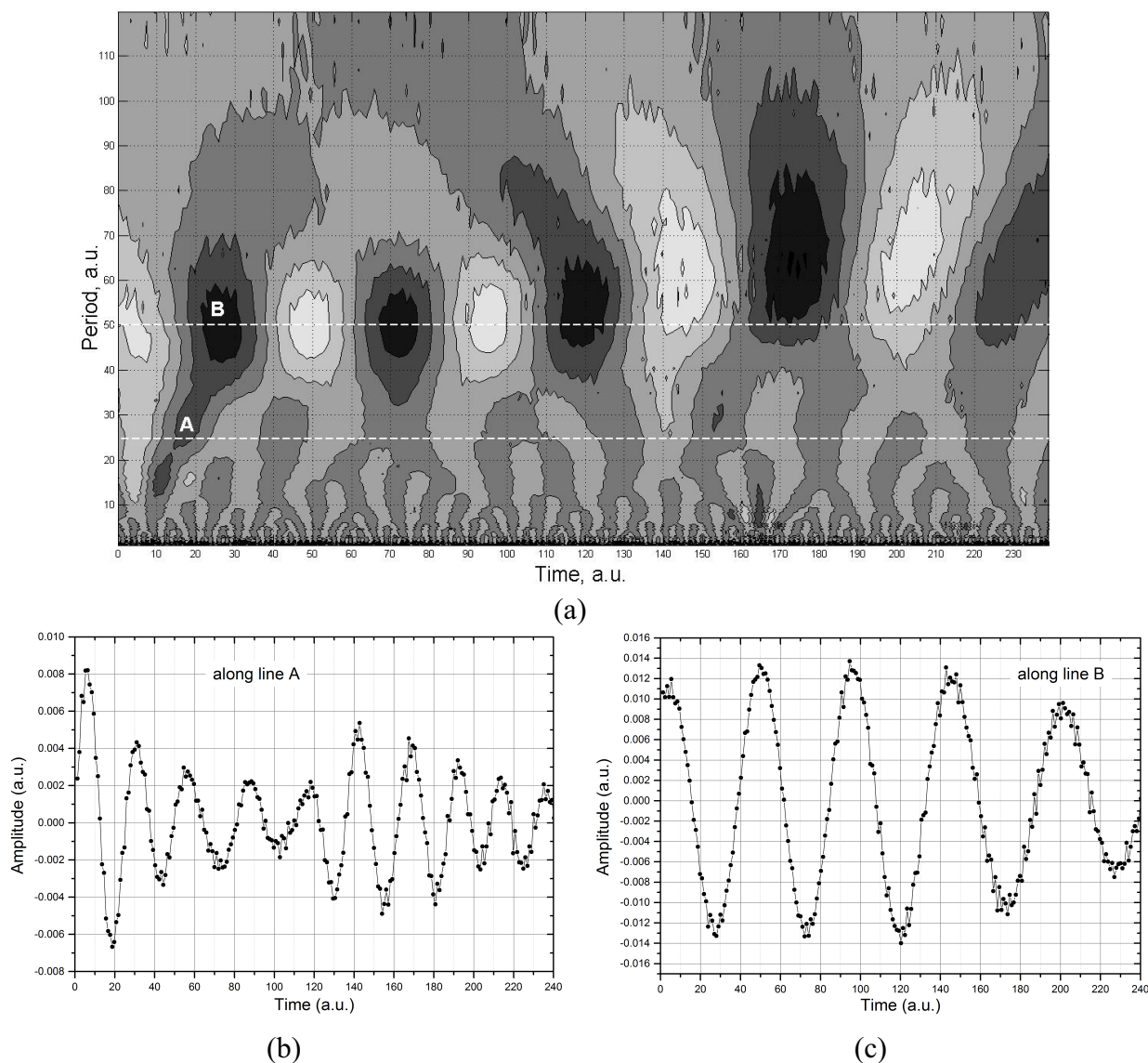


FIG. 12. (a) – Wavelet transform of the experimental signal. Dashed lines show harmonic components that have been found in the experimental signal; (b, c) – Cross-section of harmonic component along dashed line A (b) and B (c)

References

- [1] I. Daubechies. *Ten lectures on wavelets*. Philadelphia: S.I.A.M. (1992).
- [2] N.M. Astaf'eva. Wavelet analysis: basic theory and some applications. *Phys. Usp.*, **39**, P. 1085–1108 (1996).
- [3] A.N. Pavlov. Wavelet-analysis and samples of usages. *Proceedings of Higher Education. Applied Nonlinear Dynamics*, **17** (5), P. 99 (2009).
- [4] I.M. Dremin, O.V.Ivanov, V.A.Nechitailo. Wavelets and their uses. *Phys. Usp.*, **44**, P. 447–478 (2001).
- [5] S. Mallat. *A Wavelet Tour of Signal Processing*. Academic Press, Third Edition, San Diego, California (2008).
- [6] G. Bachman, L. Narici and E. Beckenstein. *Fourier and Wavelet Analysis*. Springer-Verlag, Berlin (2000).
- [7] J.F. Muzy, E. Bacry, A. Arneodo. Wavelets and multifractal formalism for singular signals: Application to turbulence data. *Phys. Rev. Lett.*, **67**, P. 3515–3518 (1991).
- [8] G. Kaiser. *A friendly guide to wavelet*. Boston, Basel, Berlin: Birkhauser (1994).
- [9] S.G. Krantz. *A panorama of harmonic analysis*. The mathematical association of America, Washington, D.C. (1999).

CONVERSION EFFICIENCY OF SECOND HARMONIC GENERATION IN ONE-DIMENSIONAL PHOTONIC CRYSTAL BASED ON ISOTROPIC MATERIAL

A. M. Gerasimov¹, N. D. Kundikova^{1,2}, Yu. V. Miklyaev^{1,2},
D. G. Pikhulya¹, M. V. Terpugov¹

¹South Ural State University, Chelyabinsk city – 454139, Russia

²The Institute of Electrophysics of the Ural Division of the Russian Academy of Sciences,
Ekaterinburg city - 620016, Russia

alexandro.gerasimov@gmail.com, kundikovand@susu.ac.ru, miklyaev@mail.ru,
denisp@land.ru, mterpugov@gmail.com

PACS 42.65.Ky

The investigation of second-harmonic generation in a one-dimensional photonic crystal was carried out. The calculation of the $\chi^{(2)}$ – grating recording in a periodic system consisted of air and glass layers and second-harmonic generation in it was performed. The frequency conversion efficiency at different wavelengths of the first harmonic was estimated.

Keywords: one-dimensional photonic crystal, second harmonic generation, optical nonlinearity, conversion efficiency.

Received: 9 February 2014

Revised: 28 May 2014

1. Introduction

There is intense interest in the work on the second harmonic generation in isotropic media. Nonlinear materials traditionally used for frequency doubling optical radiation nonlinear materials are quite expensive and difficult to handle, although capable of converting radiation into the second harmonic with an efficiency of about 50–60%. At the same time, isotropic media allow you to create structures and objects of almost any complexity of forms and structures, but do not provide the efficient conversion of radiation into the second harmonic.

Second harmonic generation in one-dimensional photonic crystal has been well studied, but this study was done only for non-linear media. For example, in Ref. [1], second-harmonic generation was attained in a one-dimensional photonic crystal with a conversion efficiency of about 1%. In another study, the conversion efficiency was calculated for the second harmonic nonlinear in a photonic crystal [2]. The conversion efficiency was 10^{-2} – 10^{-3} .

Second harmonic generation in isotropic media is difficult to realize because of the lack of such media in second-order nonlinearity, and because of implementation of phase-matching condition. At the same time, for the case of a one-dimensional photonic crystal, phase matching is realized automatically. In spite of the inversion symmetry in isotropic media, it is also possible to make an effective second harmonic generation. Second harmonic generation in an isotropic medium was first observed in 1981, when second harmonic generation was accidentally found via neodymium laser radiation in germanium-silicate fibers

[3,4]. In this case, the conversion efficiency was low and amounted to about 10^{-8} . Further, in 1987, a mechanism was proposed for explaining the emergence of second-order nonlinearity in isotropic media [5]. According to the theory, radiation propagation in a fiber at the first and the second harmonics occurs if ordered reorientation defects with $\chi^{(2)} \neq 0$, which subsequently causes second harmonic generation under irradiation only the first harmonic [6]. To test this hypothesis, an experiment was made with an optical fiber, which has achieved an efficiency of converting the radiation into the second harmonic of 0.03 %.

In this work, we offer a theoretical study of $\chi^{(2)}$ -grating formation in one-dimensional photonic crystal with the subsequent frequency conversion of this grating.

2. Second harmonic generation in one-dimensional photonic crystal

2.1. Making $\chi^{(2)}$ lattice in one-dimensional photonic crystal

According to ref.[5], second-order nonlinearity may appear in an isotropic medium if we have an electromagnetic wave with nonzero average cube field, $\langle E^3 \rangle \neq 0$. If we illuminate an isotropic medium simultaneously by the first and second harmonic radiation, we get the total field with a nonzero average cube field, and in such an environment, we can create a $\chi^{(2)}$ grating with following amplitude:

$$\chi^{(2)}(R) = \alpha E_{2\omega}(R) E_{\omega}^*(R) E_{\omega}^*(R), \quad (1)$$

where the coefficient α must be determined experimentally and is much smaller than unity.

We have done a simulation of $\chi^{(2)}$ -grating formation process in 1D photonic crystal using a software package MEEP [7]. The structure of one-dimensional photonic crystal “glass-and-air” was given. The refractive index of air was equal to 1.0, and refractive index of glass was equal to 1.5. The thickness of glass and air gaps layers was taken equal to $0.266 \mu\text{m}$ and $\lambda/6=0.177 \mu\text{m}$, which was taken equal to $\lambda/4$ and $\lambda/6$ for radiation with a wavelength of $1.064 \mu\text{m}$ – is the first harmonic of neodymium laser. A thickness ratio corresponding to the refractive index of glass is required to align the optical paths in the glass and in the air.

To generate a second order nonlinear coefficient ($\chi^{(2)}$) in the structure, we illuminate it simultaneously by the fundamental harmonic and doubled frequency radiation for different wavelengths. Calculated intensity distributions of both harmonics inside photonic crystal are shown on the Fig. 1. Two fundamental wavelengths were taken for an example: $1.060 \mu\text{m}$ and $1.266 \mu\text{m}$.

One can see that the character of the distribution is quite different for first and second harmonics. If we know field distribution for both harmonics, we can calculate a $\chi^{(2)}$ -grating inside a glass, according to formula (1). The resulting $\chi^{(2)}$ -grating is depicted on the Fig. 2. Factor α in (1) was equal to 0.01.

This figure shows that the $\chi^{(2)}$ grating is formed non-uniformly along the entire length of the photonic crystal and is absent in air gaps, because of absence of $\chi^{(3)}$ -nonlinearity.

2.2. Conversion efficiency of second harmonic generation in one-dimensional photonic crystal

After the $\chi^{(2)}$ - grating is formed in the photonic crystal structure, we simulate a second harmonic generation if we have at the input only fundamental harmonic radiation. Fig. 3(a-b) and Fig. 4(a-b) show the ration of second-harmonic intensity at the output of the photonic crystal to the input intensity of first harmonic on different wavelengths, for example $1.266, 1.246, 1.226, 1.206 \mu\text{m}$. The frequency of 0.08 in MEEP units corresponds to the first harmonic.

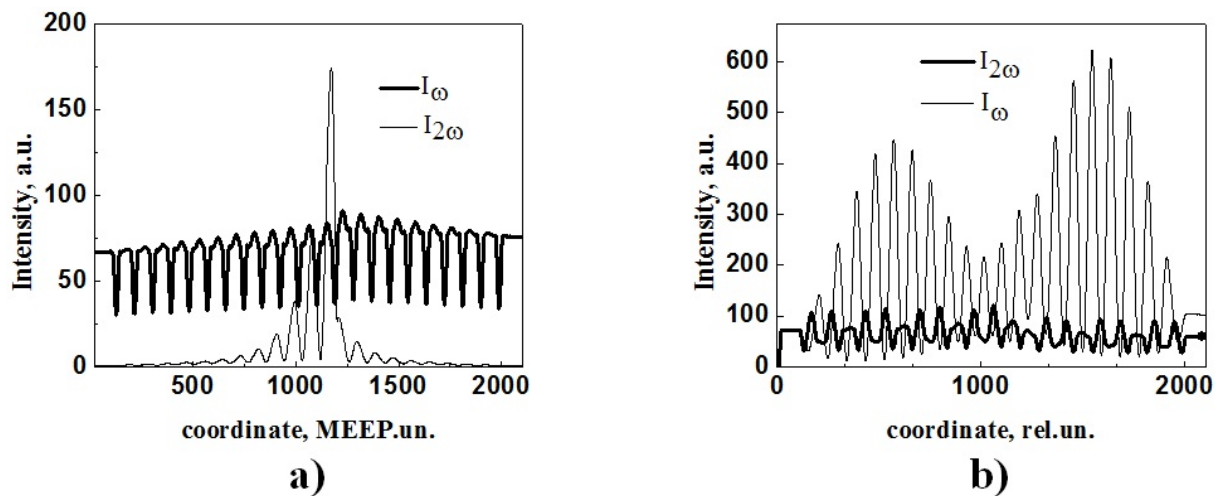


FIG. 1. The intensity distribution of the first and second harmonics of the one-dimensional photonic crystal at the wavelengths of the first harmonic: a) $1.060 \mu\text{m}$ and $0.530 \mu\text{m}$ b) $1.266 \mu\text{m}$ and $0.633 \mu\text{m}$

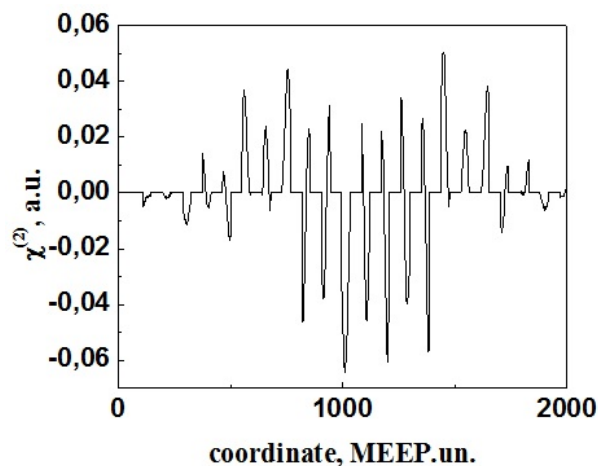


FIG. 2. Sample distribution of the quadratic nonlinearity in one-dimensional photonic crystal

3. Conclusions

As can be seen from Fig. 3-4, the SHG efficient generation is observed for different wavelengths of the incident radiation of the first harmonic. At the first harmonic wavelength, equal to $1.226 \mu\text{m}$, we see not only the second generation, but the third harmonic, which arose from the summation of frequencies of the first and second harmonic. In this case, the SHG efficiency was 0.2 %.

Thus, the $\chi^{(2)}$ -grating recording process is simulated in the one-dimensional photonic crystal made from glass and air. Second harmonic generation is predicted for different wavelengths. A conversion efficiency of about 0.2% was obtained for the $1.226 \mu\text{m}$ wavelength.

Acknowledgement

This work has been performed in the framework of Basic Research Program of Ministry of Education and Science of the Russian Federation (888/2014 102-GZ).

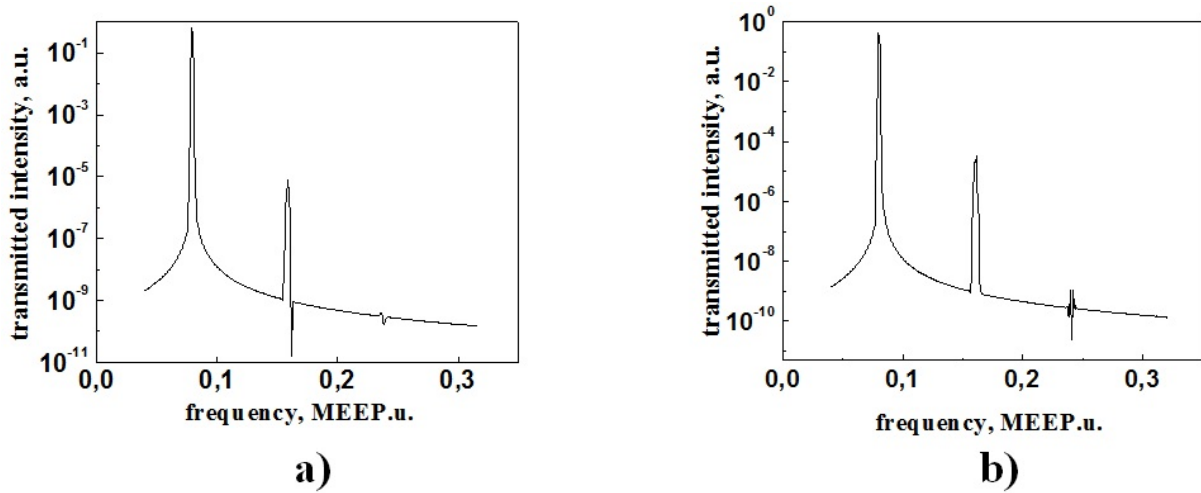


FIG. 3. SHG in one dimensional photonic crystal. Wavelength of fundamental harmonic by recording process is equal to: a) $1.266 \mu\text{m}$ b) $1.246 \mu\text{m}$.

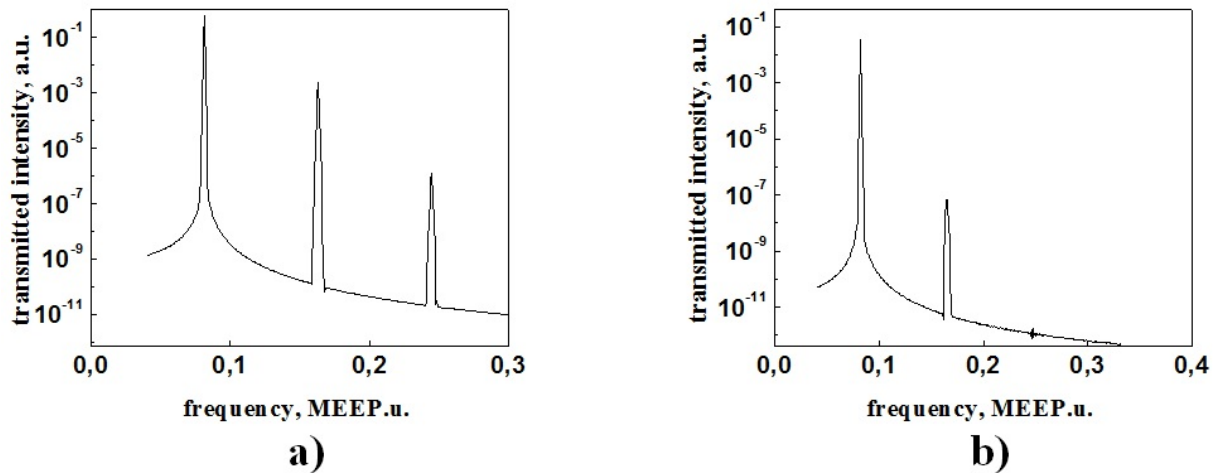


FIG. 4. SHG in one dimensional photonic crystal. Wavelength of fundamental harmonic by recording process is equal to: a) $1.226 \mu\text{m}$ b) $1.206 \mu\text{m}$.

References

- [1] Zaporozhchenko R.G. Relation between Efficiency of Second Harmonic Generation and Spectral Properties of a One-Dimensional Photonic Crystal. *Optics and Spectroscopy*, **95**(6), P. 976–982 (2003).
- [2] Zhao L.M., Li C., Zhou Y.S., Wang F.H. Multiple wavelength second-harmonic generation in one-dimensional nonlinear photonic crystals. *J. Opt. Soc. Am. B*, **25**(12), P. 2010–2014 (2008).
- [3] Sasaki Y., Ohmori Y. Phase-matched sum-frequency light generation in optical fibers. *Appl. Phys. Lett.*, **39**(6), P. 466–468 (1981).
- [4] Sasaki Y., Ohmori Y. Two-Wave Sum-Frequency Light Generation in Optical. *IEEE Journal of Quantum Electronics*, **18**(4), P. 758–762 (1982).
- [5] Baranova N.B., Zel'dovich B.Y. Expanding the field of holography to multifrequency. *JETP Letters*, **45**(12), P. 562–565 (1987).
- [6] Stolen R.H., Tom H.W.K. Self-organized phase-matched harmonic generation in optical fibers. *Optics Letters*, **12**(8), P. 585–587 (1987).
- [7] <http://ab-initio.mit.edu/wiki/index.php/Meep>.

THE ABSORPTION OF ELECTROMAGNETIC RADIATION IN A QUANTUM WIRE

V. V. Karpunin^{1,2}, V. A. Margulis²

¹ Mordovian State Pedagogical Institute, Saransk, Russia

² Mordovian State University, Saransk, Russia
karpuninvv@mail.ru, theorphysics@mrsu.ru

PACS 63.20.Kr, 78.67.-n

The analytical expression for the absorption coefficient of the electromagnetic radiation by electrons a quantum wire is obtained. We used the first-order perturbation theory. The cases of linear and circular polarization of the electromagnetic wave are investigated. The resonance character of the absorption is shown and resonant frequencies are found.

Keywords: quantum wire, electron-photon interaction, absorption coefficient.

Received: 15 April 2014

1. Introduction

Optical and electronic properties of low-dimensional semiconductor structures are important part of the modern physics of semiconductors. In the last decade, scientists have investigated a number of similar systems. The splitting lines for the cyclotron resonance (CR) in the heterostructure of InAs/GaSb placed in a tilted magnetic field were theoretically and experimentally studied Ref. [1]. This splitting was shown to be stipulated by the mixing of electron and hole states, and the suppression of the splitting in a tilted magnetic field was also shown.

The splitting lines of the cyclotron resonance in weak magnetic fields in heterostructures of InSb/AlInSb with quantum wells is considered Ref. [2]. To explain this effect, the Rashba model the spin-orbital interaction was used. It was shown that this effect was not associated with nonparabolicity of conduction zone InSb.

In Ref. [3], the cyclotron resonance holes in InGaAs/GaAs heterostructures quantum wells in a quantizing magnetic fields were experimentally investigated.

The intraband absorption of light in parabolic quantum wells, located in the electric and the magnetic fields was theoretically studied [4]. The expression of the absorption coefficient (AC) for direct optical transitions, as well as for indirect transitions, when electron scattering occurs at an impurity center was obtained. The limiting cases were considered: the absence of a magnetic and an electric field. It was shown that in strong magnetic fields, the electron-impurity interaction increases.

Theoretical investigation of the absorption coefficient of light by an impurity with the use of the multiphonon model of optical processes was considered [5]. The expression of the AC was obtained with the used wave functions in the zero radius potential model. The dependence of the AC on frequency have the peaks of the Gaussian type.

The coefficient of the interband magneto-absorption in a constant electric field and a resonant laser radiation was calculated Ref. [6]. The paper considered the influence of the longitudinal electric field on the interband absorption coefficient (size-infrared resonance).

The oscillatory dependence of the AC on the frequency in the high-frequency region was marked.

Cyclotron resonance of electrons in narrow gap heterostructures HgTe/CdTe(013) in quantizing magnetic fields was theoretically and experimentally studied [7]. The experimental values of the cyclotron transitions energies were found to exceed the calculated values.

The absorption coefficient of electromagnetic radiation by a two dimensional electron gas is calculated [8]. The calculation was conducted taking into account the scattering of electrons by optical phonons. Consider the case of a tilted magnetic field. It was shown that the resonance curve had a doublet structure. The dependence of the absorption coefficient on the angle of tilted magnetic field to the plane of confinement was investigated.

Optical properties of three-dimensional quantum wires and the quantum cylinder were studied theoretically in Ref. [9]. Analytical expressions of the absorption coefficients were obtained and the form of the resonance curve was found. Cases of nondegenerate and degenerate electron gases were considered. It was shown that in the case of a degenerate electron gas, the curve of absorption had fractures.

The hybrid – phonon resonance in the three-dimensional anisotropic parabolic quantum well was investigated in [10]. Investigation of the resonance peak forms revealed their doublet structure.

The hybrid-photon resonances in a three-dimensional quantum wire was investigated [11]. Parabolic potential confinement and the model of a hard wall potential were used. The resulting formula for the absorption coefficient was obtain.

The absorption of electromagnetic radiation by electron gas, taking into account processes related to the combination scattering by ionized impurities was also studied in various nanostructures. This phenomenon in the three-dimensional anisotropic quantum wire was considered [12]. The expression of the absorption coefficient was obtained, the dependence of AC upon the radiation frequency and magnetic fields was studied.

Hybrid-impurity resonances in anisotropic quantum dots were studied [13]. The expression of the absorption coefficient was obtained, the dependence of the AC upon the magnetic field was also investigated. A decrease of absorption intensity at the increase of the electron quantum number was considered.

The theory of the one-phonon intraband resonance scattering of electromagnetic radiation in anisotropic quantum dots placed in a perpendicular magnetic field was developed [14]. The expression of the differential scattering cross sections was obtained. In the case of DO phonons, a doublet structure was found in the dependence of the differential cross section of scattering upon the magnetic field.

The purpose of this work is to obtain and study analytical expressions for the absorption coefficient of electromagnetic radiation of a quantum wire. We consider both cases the linear polarization of electromagnetic waves and the circular polarization. We analyze the dependence of AC upon the frequency of the electromagnetic radiation.

2. Absorption coefficient (case of linear polarization)

The Hamiltonian of an electron in the anisotropic parabolic wire has the form:

$$\hat{H} = \frac{p_z^2}{2m^*} + \frac{m^*}{2}(\omega_1^2 x^2 + \omega_2^2 y^2), \quad (1)$$

where m^* is the electron effective mass, ω_1 and ω_2 is frequencies of the parabolic confinement potential, p_z is momentum along the z-axis.

The corresponding wave function has the form:

$$\psi = \frac{1}{\sqrt{L_z}} \exp(ip_z z / \hbar) \varphi_{n_1} \left(\frac{x}{l_1} \right) \varphi_{n_2} \left(\frac{y}{l_2} \right), \quad (2)$$

where l_1, l_2 is characteristic length, φ_n is oscillator function.

It is the Hamiltonian of two disconnected oscillators. This spectrum has the form:

$$E_{n_1, n_2, p_z} = \hbar\omega_1 \left(n_1 + \frac{1}{2} \right) + \hbar\omega_2 \left(n_2 + \frac{1}{2} \right) + \frac{p_z^2}{2m^*}. \quad (3)$$

If we choose the polarization vector along the Oy axis, then the operator of the electron-photon interaction has the form:

$$H_R = -\frac{ie\hbar}{m^*} \sqrt{\frac{2\pi\hbar N_f}{\epsilon\omega}} \frac{\partial}{\partial y}, \quad (4)$$

where N_f is the number of photons.

Matrix elements H_R has the form:

$$\begin{aligned} \langle n_1, n_2, p_z | H_R | n'_1, n'_2, p'_z \rangle = & -\frac{ie\hbar}{ml_2} \sqrt{\frac{2\pi\hbar N_f}{\epsilon\omega}} \delta_{p_z, p'_z} \delta_{n_1, n'_1} \times \\ & \left(\sqrt{\frac{n_2 + 1}{2}} \delta_{n_2, n'_2 - 1} - \sqrt{\frac{n_2}{2}} \delta_{n_2, n'_2 + 1} \right). \end{aligned} \quad (5)$$

where $\delta_{m, m'}$ is Kronecker delta symbol.

The absorption coefficient Γ , was calculated in first order of the perturbation theory by analogy with [9]. We consider only the case of the nondegenerate electron gas. Thus, the absorption coefficient can be expressed as:

$$\Gamma = \frac{2\pi\sqrt{\epsilon}}{c\hbar N_f} \sum_{n_1 n_2 p_z} \sum_{n'_1 n'_2 p'_z} f_0(E_{n_1, n_2, p_z}) \times \quad (6)$$

$$|\langle n_1, n_2, p_z | H_R | n'_1, n'_2, p'_z \rangle|^2 \delta(E_{n_1, n_2, p_z} - E_{n'_1, n'_2, p'_z} + \hbar\omega),$$

where $f_0(E_{n_1, n_2, p_z})$ is the electron distribution function, $\delta(E_{n_1, n_2, p_z} - E_{n'_1, n'_2, p'_z} + \hbar\omega)$ is Dirac delta function.

After calculating the sums entering (6), we obtain the expression:

$$\begin{aligned} \frac{\Gamma}{\Gamma_0} = \frac{\omega_2}{\omega} \left[\frac{1}{1 + (\omega - \omega_2)^2} \left(\frac{\exp(\hbar\omega_2/2T)}{(\exp(\hbar\omega_2/T) - 1)^2} + \frac{\exp(\hbar\omega_2/2T)}{\exp(\hbar\omega_2/T) - 1} \right) - \right. \\ \left. \frac{1}{1 + (\omega + \omega_2)^2} \frac{\exp(\hbar\omega_2/2T)}{(\exp(\hbar\omega_2/T) - 1)^2} \right], \end{aligned} \quad (7)$$

where

$$\Gamma_0 = \frac{4e^2 n_e \tau \pi}{c\sqrt{\epsilon} m^*} \sinh(\hbar\omega_2/2T),$$

here n_e is the concentration of electrons, τ is relaxation time, T is temperature.

The expression (7) was obtained with taking into consideration Lorentz broadening delta peaks [9]:

$$\delta(x) = \frac{(\pi\tau)^{-1}}{\tau^{-2} + x^2}. \quad (8)$$

3. Absorption coefficient (case of circular polarization)

Next, we consider the case of circular polarization of an electromagnetic wave. Expression for electron–photon interaction of this case is taken to be:

$$H_R = -\frac{e\hbar}{m^*} \sqrt{\frac{2\pi\hbar N_f}{\epsilon\omega}} \left(i\frac{\partial}{\partial x} + \frac{\partial}{\partial y} \right). \quad (9)$$

The matrix element of the electron-photon interaction is found to be:

$$\begin{aligned} \langle n_1, n_2, p_z | H_R | n'_1, n'_2, p'_z \rangle &= -\frac{ie\hbar}{m^*l_1} \sqrt{\frac{2\pi\hbar N_f}{\epsilon\omega}} \delta_{p_z, p'_z} \delta_{n_2, n'_2} \times \\ &\left(\sqrt{\frac{n_1+1}{2}} \delta_{n_1, n'_1-1} - \sqrt{\frac{n_1}{2}} \delta_{n_1, n'_1+1} \right) - \\ &\frac{e\hbar}{m^*l_2} \sqrt{\frac{2\pi\hbar N_f}{\epsilon\omega}} \delta_{p_z, p'_z} \delta_{n_1, n'_1} \left(\sqrt{\frac{n_2+1}{2}} \delta_{n_2, n'_2-1} - \sqrt{\frac{n_2}{2}} \delta_{n_2, n'_2+1} \right). \end{aligned} \quad (10)$$

Expression of AC with matrix element (10) has the form:

$$\begin{aligned} \Gamma &= \frac{2\pi\sqrt{\epsilon}}{c\hbar N_f} \frac{2\pi\hbar N_f}{\epsilon\omega} \sum_{n_1 n_2 p_z} \sum_{n'_1 n'_2 p'_z} f_0(E_{n_1, n_2, p_z}) \times \\ &\left[\left(\frac{e\hbar}{m^*l_1} \right)^2 \delta_{p_z, p'_z} \delta_{n_2, n'_2} \left(\frac{n_1+1}{2} \delta_{n_1, n'_1-1} - \frac{n_1}{2} \delta_{n_1, n'_1+1} \right) + \right. \\ &\left. \left(\frac{e\hbar}{m^*l_2} \right)^2 \delta_{p_z, p'_z} \delta_{n_1, n'_1} \left(\frac{n_2+1}{2} \delta_{n_2, n'_2-1} - \frac{n_2}{2} \delta_{n_2, n'_2+1} \right) \right] \times \\ &\delta(E_{n_1, n_2, p_z} - E_{n'_1, n'_2, p'_z} + \hbar\omega). \end{aligned} \quad (11)$$

As in the previous case, in calculating the AC (6), we use (8). We consider only the case of a nondegenerate electron gas. After calculating all sums in (11), we get the final expression:

$$\begin{aligned} \frac{\Gamma}{\Gamma_0} &= \sinh(\hbar\omega_1/2T) \frac{\omega_1}{\omega} \left[\frac{1}{1 + (\omega - \omega_1)^2} \left(\frac{\exp(\hbar\omega_1/2T)}{(\exp(\hbar\omega_1/T) - 1)^2} + \frac{\exp(\hbar\omega_1/2T)}{\exp(\hbar\omega_1/T) - 1} \right) - \right. \\ &\left. \frac{1}{1 + (\omega + \omega_1)^2} \frac{\exp(\hbar\omega_1/2T)}{(\exp(\hbar\omega_1/T) - 1)^2} \right] + \\ &\sinh(\hbar\omega_2/2T) \frac{\omega_2}{\omega} \left[\frac{1}{1 + (\omega - \omega_2)^2} \left(\frac{\exp(\hbar\omega_2/2T)}{(\exp(\hbar\omega_2/T) - 1)^2} + \frac{\exp(\hbar\omega_2/2T)}{\exp(\hbar\omega_2/T) - 1} \right) - \right. \\ &\left. \frac{1}{1 + (\omega + \omega_2)^2} \frac{\exp(\hbar\omega_2/2T)}{(\exp(\hbar\omega_2/T) - 1)^2} \right], \end{aligned} \quad (12)$$

where

$$\Gamma_0 = \frac{4e^2 n_e \tau \pi}{c\sqrt{\epsilon} m^*}.$$

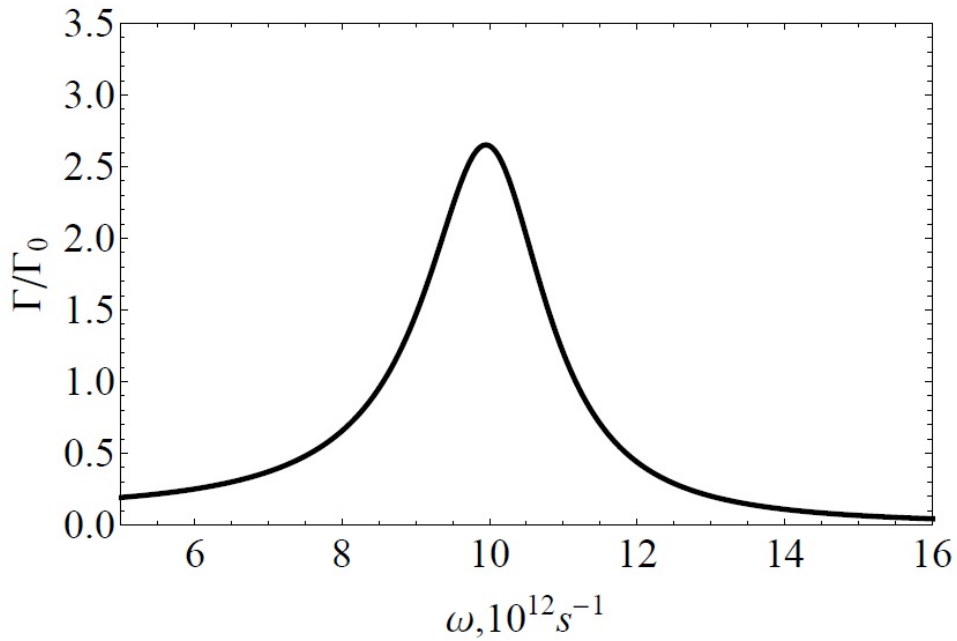


FIG. 1. The dependence of the absorption coefficient of electromagnetic radiation upon the radiation frequency. $\omega_1 = 10 \cdot 10^{12} \text{ c}^{-1}$, $\tau = 10^{-12} \text{ c}$, $T = 100 \text{ K}$ (linear polarization)

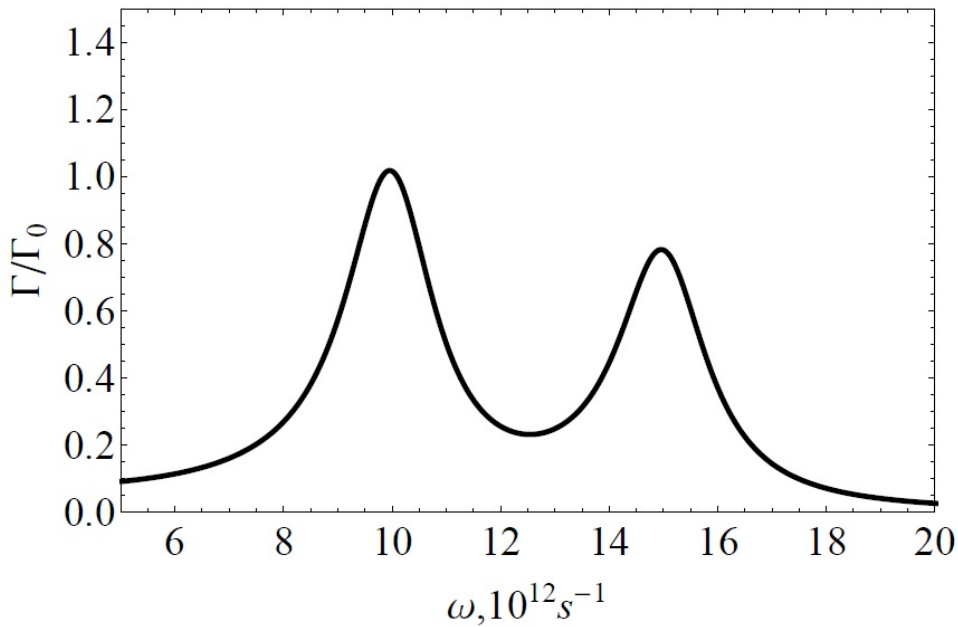


FIG. 2. The dependence of the absorption coefficient of electromagnetic radiation upon the radiation frequency. $\omega_1 = 10 \cdot 10^{12} \text{ c}^{-1}$, $\omega_2 = 15 \cdot 10^{12} \text{ c}^{-1}$, $\tau = 10^{-12} \text{ c}$, $T = 100 \text{ K}$ (circular polarization)

4. Conclusion

An analytic expression for the AC of electromagnetic radiation in a quantum wire was obtained. The cases of linear and circular polarization of an electromagnetic wave are investigated.

In the case of linear polarization, there can be only one resonance peak at the frequency $\omega = \omega_1$ (Fig.1). Another resonance frequency, $\omega = \omega_2$, appears in case when the polarization vector is directed along the ox axis.

Under conditions of circular polarization of the electromagnetic wave, a doublet structure is obtained for the resonance peaks (Fig.2). In the case of equal of frequencies, i.e. $\omega_1 = \omega_2$, there is only one resonance peak.

Acknowledgements

The work was financially supported by Russian Ministry of Education and Science by the project 2.2.1.2. Research and development of educational laboratory “Basics of nanotechnology and scanning probe microscopy”.

References

- [1] Greshnov A. A., Zegrya G. G., Vasil'ev Yu. B., Suchalkin S. D., Mel'tser B. Ya., Ivanov S. V., Kop'ev P.S. Cyclotron resonance in the InAs/GaSb heterostructure in an inclined magnetic field. *JETP Letters*, **76**, P. 222–226 (2002).
- [2] Vasilyev Yu. B., Gouider F., Nachtwei G., Buckle P. D. The cyclotron resonance in heterostructures with the InSb/AlInSb quantum wells. *Semiconductors*, **44**, P. 1511–1514 (2010).
- [3] Ikonnikov A. V., Spirin K. E., Gavrilenko V. I., Kozlov D. V., Drachenko O., Schneider H., Helm M. The cyclotron resonance of holes in InGaAs/GaAs heterostructures with quantum wells in quantizing magnetic fields. *Semiconductors*, **44**, P. 1492–1494 (2010).
- [4] Sinyavskii E. P., Sokovnich S. M. Intraband light absorption in quasi-two-dimensional systems in external electric and magnetic fields. *Semiconductors*, **33**, P. 761–764 (1999).
- [5] Sinyavskii E. P., Sokovnich S. M. Impurity absorption of light in confined systems subjected to a longitudinal magnetic field. *Semiconductors*, **34**, P. 815–816 (2000).
- [6] Sinyavskii E. P., Karapetyan S. A. Influence of an electric field on the magnetoabsorption in a field of resonant laser radiation. *Physics of the Solid State*, **48**, P. 962–965 (2006).
- [7] Ikonnikov A. V., Zholudev M. S., Marem'yanin K. V., Spirin K. E., Lastovkin A. A., Gavrilenko V. I., Dvoret'skii S. A., Mikhailov N. N. Cyclotron resonance in HgTe/CdTe(013) narrowband heterostructures in quantized magnetic fields. *JETP Letters*, **95**, P. 406–410 (2012).
- [8] Margulis V. A. A hybrid-phonon resonance in a quasi-two-dimensional nanostructure. *JETP*, **84**, P. 603–611 (1997).
- [9] Galkin N. G., Margulis V. A., Shorokhov A. V. Intraband absorption of electromagnetic radiation by quantum nanostructures with parabolic confinement potential. *Physics of the Solid State*, **43**, P. 530–538 (2001).
- [10] Margulis V. A., Shorokhov A. V. Hybrid-phonon resonances in a three dimensional anisotropic quantum well. *Phys.Rev. B*, **66**, P. 165324(1)-165324(6) (2002).
- [11] Margulis V. A., Shorokhov A. V. Hybrid-phonon resonances in a three dimensional quantum wire. *Phys.stat.sol (c)*, **1**, P. 2642–2645 (2004).
- [12] Margulis V. A., Pavlova N. F., Shorokhov A. V. Hybrid impurity resonance in a three-dimensional anisotropic quantum wire. *Physics of the Solid State*, **48**, P. 935–939 (2006).
- [13] Margulis V. A., Shorokhov A. V. Hybrid-impurity resonances in anisotropic quantum dots. *Physica E*, **41**, P. 483–486 (2009).
- [14] Shorokhov A. V., Margulis V. A. Intraband resonance scattering of electromagnetic radiation in anisotropic quantum dots. *Nanosystems: physics, chemistry, mathematics*, **1**, P. 178–187 (2010).

RELATIONSHIP PLURALITY APPROXIMATION

V. D. Lukyanov

JSC Avangard, Saint Petersburg, Russia

lukyanovvd@rambler.ru

PACS 02.30.Mv

An algorithm for the approximation of relationship pluralities is set by linear combinations of functions with unknown coefficients, which in part coincides in all relationship pluralities having been built using ordinary least squares. Examples of the algorithm's realization, when finding particular solutions plurality of linear nonhomogeneous differential equations, have been given.

Keywords: approximation, ordinary least squares, dependences plurality.

Received: 4 June 2014

1. Introduction

During experimental data processing, there arises a problem of analytical dependence recovery being a linear combination of basic functions with unknown coefficients. It is possible to face this situation when the data obtained in the experiment is not for one relationship, but for several of such equations of curves, that for instance describe the same physical process at different values of external parameters. We assume that these differences in the context of the experiment provide data that lead to analytical dependences, differing from each other by values of some linear combination of coefficients; all other coefficients for relationship pluralities are the same. In this case we shall talk about dependences plurality approximation.

In order to evaluate relationship pluralities, we may face approximation of the solution of linear nonhomogeneous differential equation (LNDE) of N -th order with constant coefficients with special right-hand side:

$$\frac{d^N y}{dx^N} + b_{N-1} \frac{d^{N-1} y}{dx^{N-1}} + \dots + b_0 y = \sum_{m=1}^M a_m f_m(x). \quad (1)$$

Let R plurality of particular solutions be built when working out R various Cauchy problems for LNDE (1):

$$y_r = y_r(x) = \sum_{n=1}^N C_n^{(r)} \varphi_n(x) + \sum_{m=1}^M A_m f_m(x), \quad (2)$$

where r is a serial number of a particular solution, $r = 1, 2, \dots, R$; functions $\varphi_1(x), \varphi_2(x), \dots, \varphi_N(x)$ are linearly independent solutions of homogeneous equation, the second summand is LNDE particular solution. Coefficients A_1, A_2, \dots, A_M are calculated by finding a particular solution for the nonhomogeneous differential equation and they are the same for all solutions. Coefficients $C_1^{(r)}, C_2^{(r)}, \dots, C_N^{(r)}$ are calculated from the initial conditions of the Cauchy problem or from boundary conditions and determine LNDE particular solution.

Function (2) is the expansion of $y_r(x)$ functions on a given basis, consisting of a plurality of linearly independent functions $\{\varphi_n(x)\}_1^N$ and $\{f_m(x)\}_1^M$.

The set of equations given by representation of function (3) shall be called the relationship plurality, if some of the coefficients of linear functions combination — here they are A_1, A_2, \dots, A_m coefficients — are equal for all relationships of the plurality, and the other coefficients $C_1^{(r)}, C_2^{(r)}, \dots, C_N^{(r)}$ for varied relationships differ in at least one value. The number of coefficients in function (2) equals $N_R = M + RN$.

We have R equations of dependences plurality for type (2). For each equation of this plurality, we know several pairs of x argument and $y(x)$ function values, however, the function values are known approximately. For the r -th relationship, we have $S_r > 0$ of x_{rs} argument values with $s = 1, 2, \dots, S_r$ and approximate y_{rs} function values. For each relationship argument, values may not match, as well as the number of these values.

In total, we have S values for the entire relationship plurality, $S = \sum_{r=1}^R S_r$, while $S > N_R$.

We pose the task to determine all N_R of analytical dependence coefficients (2) with the help of these data. Briefly, we shall name the task as (M, N, R) task, where M is the number of coefficients whose relationship plurality values are the same, N — number of coefficients whose values are different and R is the number of relationships in the plurality.

To solve the problem, we shall use ordinary least squares (OLS) [1–4]. For the s -th curve of the plurality, with every x_{rs} argument value, we shall calculate a deviation square $\delta(x_{rs})$ function preset value y_{rs} of the set function (2) value, while argument value equals: $\delta(x_{rs}) = y_{rs} - y_r(x_{rs})$. Then, we shall calculate F value — mean square deviation $\delta(x_{rs})$ for all argument values:

$$F = \frac{1}{S} \sum_{r=1}^R \sum_{s=1}^{S_r} \delta^2(x_{rs}) = \frac{1}{S} \sum_{r=1}^R \sum_{s=1}^{S_r} \left(y_{rs} - \sum_{n=1}^N C_n^{(r)} \varphi_n(x_{rs}) - \sum_{m=1}^M A_m f_m(x_{rs}) \right)^2. \quad (3)$$

The F function depends on N_R arguments: A_1, A_2, \dots, A_M coefficients, as well as on all $C_1^{(r)}, C_2^{(r)}, \dots, C_N^{(r)}$ coefficients with $r = 1, 2, \dots, R$.

For brevity, we shall use the designation for two types of function $G(x)$ averaging: data averaging for r -th dependence $\overline{G_r} = \frac{1}{S_r} \sum_{s=1}^{S_r} G(x_{rs})$ and averaging over all data $\langle G \rangle =$

$$\frac{1}{S} \sum_{r=1}^R \sum_{s=1}^{S_r} G(x_{rs}) = \frac{1}{S} \sum_{r=1}^R S_r \overline{G_r}. \text{ In this designation, it will be } F = \langle \delta^2 \rangle \text{ function.}$$

According to ordinary least squares, values of unknown coefficients can be obtained from minimum F function condition. Setting all the partial derivatives of all function arguments to zero is a necessary condition for the function's minimum.

Calculating partial derivatives gives:

$$\frac{1}{2S_r} \frac{\partial F}{\partial A_i} = \left\langle \sum_{n=1}^N C_n^{(r)} \overline{\varphi_n(x_r) f_i(x_r)} \right\rangle + \sum_{m=1}^M A_m \left\langle \overline{f_m(x_r) f_i(x_r)} \right\rangle - \left\langle \overline{y_r f_i(x_r)} \right\rangle,$$

when $i = 1, 2, \dots, M$,

$$\frac{S}{2S_r} \frac{\partial F}{\partial C_j^{(r)}} = \sum_{n=1}^N C_n^{(r)} \overline{\varphi_j(x_r) \varphi_n(x_r)} + \sum_{m=1}^M A_m \overline{\varphi_j(x_r) f_m(x_r)} - \overline{y_r \varphi_j(x_r)},$$

when $j = 1, 2, \dots, N$.

Equating partial derivatives $\partial F/\partial A_i$ and $\partial F/\partial C_j^{(r)}$ to zero, and performing elementary transformations for every r value, we obtain a nonhomogeneous system of linear equations (SLE), which we write in matrix form:

$$\begin{cases} \langle \overline{\mathbf{Q}}^{(r)} \mathbf{C}^{(r)} \rangle + \langle \overline{\mathbf{P}}^{(r)} \rangle \mathbf{A} = \langle \overline{\mathbf{B}}_1^{(r)} \rangle, \\ \overline{\mathbf{R}}^{(r)} \mathbf{C}^{(r)} + \overline{\mathbf{T}}^{(r)} \mathbf{A} = \overline{\mathbf{B}}_2^{(r)}, \quad r = 1, 2, \dots, R, \end{cases} \quad (4)$$

where matrix columns are introduced $\mathbf{C}^{(r)} = (C_1^{(r)}, C_2^{(r)}, \dots, C_N^{(r)})^T$, $\mathbf{A} = (A_1, A_2, \dots, A_M)^T$, $\overline{\mathbf{B}}_1^{(r)} = (\overline{y_r f_1(x_r)}, \overline{y_r f_2(x_r)}, \dots, \overline{y_r f_M(x_r)})^T$, $\overline{\mathbf{B}}_2^{(r)} = (\overline{y_r \varphi_1(x_r)}, \overline{y_r \varphi_2(x_r)}, \dots, \overline{y_r \varphi_N(x_r)})^T$, T is the operation of matrix transposition, $\overline{\mathbf{Q}}^{(r)} = (q_{mn})_{M,N} = (\overline{f_m(x_r) \varphi_n(x_r)})_{M,N}$ – matrix of $M \times N$ size with $q_{mn} = \overline{f_m(x_r) \varphi_n(x_r)}$, $\overline{\mathbf{P}}^{(r)} = (\overline{f_m(x_r) f_j(x_r)})_{M,M}$, $\overline{\mathbf{R}}^{(r)} = (\overline{\varphi_n(x_r) \varphi_j(x_r)})_{N,N}$, $\overline{\mathbf{T}}^{(r)} = (\overline{\varphi_n(x_r) \varphi_j(x_r)})_{N,N}$ elements, in this designations it is believed that during matrix averaging, the averaging of its elements also takes place.

In order to solve SLE (4), $\mathbf{C}^{(r)}$ column matrices shall be excluded from its first matrix equation with the help of other R matrix equations. Taking into account the nonsingularity of $\overline{\mathbf{Q}}^{(r)}$ matrix, at all $r = 1, 2, \dots, R$, we obtain:

$$\mathbf{C}^{(r)} = (\overline{\mathbf{R}}^{(r)})^{-1} \overline{\mathbf{B}}_2^{(r)} - (\overline{\mathbf{R}}^{(r)})^{-1} \overline{\mathbf{T}}^{(r)} \mathbf{A}. \quad (5)$$

Substitution of proportion (5) into the first matrix equation in SLE (4) gives a linear matrix equation for the unknown \mathbf{A} matrix, which can be rewritten as

$$\left(\langle \overline{\mathbf{P}}^{(r)} \rangle - \langle \overline{\mathbf{Q}}^{(r)} (\overline{\mathbf{R}}^{(r)})^{-1} \overline{\mathbf{T}}^{(r)} \rangle \right) \mathbf{A} = \langle \overline{\mathbf{B}}_1^{(r)} \rangle - \langle \overline{\mathbf{Q}}^{(r)} (\overline{\mathbf{R}}^{(r)})^{-1} \overline{\mathbf{T}}^{(r)} \rangle.$$

Assuming nondegeneracy of this equation, we find the required \mathbf{A} matrix whose elements are A_m coefficients in function (2)

$$\mathbf{A} = \left(\langle \overline{\mathbf{P}}^{(r)} \rangle - \langle \overline{\mathbf{Q}}_1^{(r)} (\overline{\mathbf{R}}^{(r)})^{-1} \overline{\mathbf{T}}^{(r)} \rangle \right)^{-1} \left(\langle \overline{\mathbf{B}}_1^{(r)} \rangle - \langle \overline{\mathbf{Q}}^{(r)} (\overline{\mathbf{R}}^{(r)})^{-1} \overline{\mathbf{T}}^{(r)} \rangle \right).$$

After finding \mathbf{A} column matrix by means of formulas (7) we shall calculate $\mathbf{C}^{(r)}$ column matrices.

Let us consider the implementation of this technique for solving of some particular (M, N, R) tasks. It is necessary to note that the solution of $(1, 1, R)$ task at approximation of R linear function pluralities $y_r = C^{(r)}x + A$ is given in [2].

2. Function plurality approximation in $(1, 1, R)$ task

Let's define the relationship plurality $y_r = y_r(x) = C^{(r)}\varphi(x) + A f(x)$.

SLE (4) takes the form of:

$$\begin{cases} \langle \overline{f^2(x_r)} \rangle A + \langle \overline{\varphi(x_r) f(x_r)} \rangle C^{(r)} = \langle \overline{y_r f(x_r)} \rangle, \\ \overline{f(x_r) \varphi(x_r)} A + \overline{\varphi^2(x_r)} C^{(r)} = \langle \overline{y_r \varphi(x_r)} \rangle, \quad r = 1, 2, \dots, R. \end{cases} \quad (6)$$

$C^{(r)}$ values shall be excluded from the first equation by means of solving of the following R equations:

$$C^{(r)} = \frac{1}{\overline{\varphi^2(x_r)}} \left(\overline{y_r \varphi(x_r)} - A \overline{f(x_r) \varphi(x_r)} \right), \quad (7)$$

with $r = 1, 2, \dots, R$. Exclusion of $C^{(r)}$ values leads to a linear equation for the A value. The solution of this equation has the following form: $A = \Delta_1 / \Delta$, where

$$\Delta_1 = \left\langle \overline{y_r f(x_r)} \right\rangle - \left\langle \frac{\overline{y_r \varphi(x_r)}}{\overline{\varphi^2(x_r)}} \overline{f(x_r) \varphi(x_r)} \right\rangle, \Delta = \left\langle \overline{\psi^2(x_r)} \right\rangle - \left\langle \frac{\overline{f(x_r) \varphi(x_r)^2}}{\overline{\varphi^2(x_r)}} \right\rangle.$$

After finding A value, we shall calculate $C^{(r)}$ coefficients using function (7).

3. Functions plurality approximation in (2, 1, R) task

Having the relationship plurality, $y_r = y_r(x) = C^{(r)} \varphi(x) + A_1 f_1(x) + A_2 f_2(x)$, SLE (4) takes the form:

$$\begin{cases} \left\langle \frac{\overline{\varphi(x_r) f_1(x_r)} C^{(r)}}{\overline{\varphi^2(x_r)}} + \left\langle \frac{\overline{f_1^2(x_r)}}{\overline{\varphi^2(x_r)}} \right\rangle A_1 + \left\langle \frac{\overline{f_1(x_r) f_2(x_r)}}{\overline{\varphi^2(x_r)}} \right\rangle A_2 = \left\langle \frac{\overline{y_r f_1(x_r)}}{\overline{\varphi^2(x_r)}} \right\rangle, \\ \left\langle \frac{\overline{\varphi(x_r) f_2(x_r)} C^{(r)}}{\overline{\varphi^2(x_r)}} + \left\langle \frac{\overline{f_1(x_r) f_2(x_r)}}{\overline{\varphi^2(x_r)}} \right\rangle A_1 + \left\langle \frac{\overline{f_2^2(x_r)}}{\overline{\varphi^2(x_r)}} \right\rangle A_2 = \left\langle \frac{\overline{y_r f_2(x_r)}}{\overline{\varphi^2(x_r)}} \right\rangle, \\ \overline{\varphi^2(x_r)} C^{(r)} + \overline{\varphi(x_r) f_1(x_r)} A_1 + \overline{\varphi(x_r) f_2(x_r)} A_2 = \overline{y_r \varphi(x_r)}, \quad r = 1, 2, \dots, R. \end{cases} \quad (8)$$

From the last R equations, we obtain the following:

$$C^{(r)} = \frac{1}{\overline{\varphi^2(x_r)}} \left(\overline{y_r \varphi(x_r)} - A_1 \overline{\varphi(x_r) f_1(x_r)} - A_2 \overline{\varphi(x_r) f_2(x_r)} \right), \quad (9)$$

with $r = 1, 2, \dots, R$. After exclusion of $C^{(r)}$ value from the first two equations in SLE (10) we move to SLE of the second order for matrix $\mathbf{A} = (A_1, A_2)^T$: $\mathbf{V}\mathbf{A} = \mathbf{D}$, where \mathbf{V} matrix and \mathbf{D} column matrix have the following elements:

$$V_{ij} = \left\langle \overline{f_i(x_r) f_j(x_r)} \right\rangle - \left\langle \frac{\overline{\varphi(x_r) f_i(x_r)} \overline{\varphi(x_r) f_j(x_r)}}{\overline{\varphi^2(x_r)}} \right\rangle, D_i = \left\langle \overline{y_r f_i(x_r)} \right\rangle - \left\langle \frac{\overline{\varphi(x_r) f_i(x_r)} \overline{y_r \varphi(x_r)}}{\overline{\varphi^2(x_r)}} \right\rangle,$$

where $i, j = 1, 2$.

Let's find the required $\mathbf{A} = \mathbf{V}^{-1}\mathbf{D}$ matrix. With the help of A_1 and A_2 coefficients obtained from the function (9), we shall find $C^{(r)}$ coefficients with $r = 1, 2, \dots, R$.

4. Second order LNDE partial solutions plurality approximation according to experimental data for partial solutions (task (1, 2, R))

For a second order LNDE, we have a general solution in the form of:

$$y_r(x) = C_1^{(r)} \varphi_1(x) + C_2^{(r)} \varphi_2(x) + A f(x). \quad (10)$$

Coefficients $C_1^{(r)}$, $C_2^{(r)}$ and A in function (10) shall be obtained from SLE (4):

$$\begin{cases} \langle C_1^{(r)} \overline{\varphi_1(x_r) f(x_r)} \rangle + \langle C_2^{(r)} \overline{\varphi_2(x_r) f(x_r)} \rangle + A \langle \overline{f^2(x_r)} \rangle = \langle \overline{y_r(x_r) f(x_r)} \rangle, \\ C_1^{(r)} \overline{(\varphi_1(x_r))^2} + C_2^{(r)} \overline{\varphi_1(x_r) \varphi_2(x_r)} + A \overline{\varphi_1(x_r) f(x_r)} = \overline{y_r(x_r) \varphi_1(x_r)}, \quad r = 1, 2, \dots, R, \\ C_1^{(r)} \overline{\varphi_1(x_r) \varphi_2(x_r)} + C_2^{(r)} \overline{(\varphi_2(x_r))^2} + A \overline{\varphi_2(x_r) f(x_r)} = \overline{y_r(x_r) \varphi_2(x_r)}, \quad r = 1, 2, \dots, R. \end{cases} \tag{11}$$

From every r -th pair, consisting of the second and third equation of function (11), we shall express the unknown $C_1^{(r)}$ and $C_2^{(r)}$ values, through the sought quantity A :

$$C_1^{(r)} = \frac{T_{12}(x_r) - A P_{12}(x_r)}{\Delta(x_r)}, \quad C_2^{(r)} = \frac{T_{21}(x_r) - A P_{21}(x_r)}{\Delta(x_r)}, \tag{12}$$

where

$$\begin{aligned} T_{ij}(x_r) &= \overline{y_r(x_r) \varphi_i(x_r)} \cdot \overline{\varphi_j^2(x_r)} - \overline{\varphi_1(x_r) \varphi_2(x_r)} \cdot \overline{y_r(x_r) \varphi_j(x_r)}, \\ P_{ij}(x_r) &= \overline{f_r(x_r) \varphi_i(x_r)} \cdot \overline{\varphi_j^2(x_r)} - \overline{\varphi_1(x_r) \varphi_2(x_r)} \cdot \overline{f_r(x_r) \varphi_j(x_r)}. \end{aligned}$$

Using formulas (12), we shall exclude $C_1^{(r)}$ and $C_2^{(r)}$ values from the first equation of function (11). Thus we shall obtain a linear equation for A value, whose solution has the form:

$$A = \frac{\Delta_1}{\Delta}, \tag{13}$$

where

$$\begin{aligned} \Delta &= \langle \overline{f^2(x)} \rangle - \left\langle \overline{\varphi_1(x_r) f(x_r)} \frac{P_{12}(x_r)}{\Delta(x_r)} \right\rangle - \left\langle \overline{\varphi_2(x_r) f(x_r)} \frac{P_{21}(x_r)}{\Delta(x_r)} \right\rangle, \\ \Delta_1 &= \langle \overline{y(x) f(x)} \rangle - \left\langle \overline{\varphi_1(x_r) f(x_r)} \frac{T_{12}(x_r)}{\Delta(x_r)} \right\rangle - \left\langle \overline{\varphi_2(x_r) f(x_r)} \frac{T_{21}(x_r)}{\Delta(x_r)} \right\rangle. \end{aligned}$$

5. Example

Figure 1 shows the result of LNDE partial solutions approximation

$$y'' + y + 9.250y = -0.275 \sin(4x).$$

Its general solution has the form:

$$y = C_1 e^{-0.5x} \cos(4x) + C_2 e^{-0.5x} \sin(4x) + 0,3 \sin(4x). \tag{14}$$

In order to set the initial data, values of x arguments in function (14) have been obtained using a generator of uniformly distributed random numbers in the interval [0,3] for curves 1 and 3, and in the interval [1,2] for curve 2. Initial data for approximation, simulating experimental values were obtained after addition of calculated values, according to function (14) with the values of normally distributed random variable with zero mean of distribution and mean-square deviation $\sigma = 0.1$.

Initial data are marked at Fig. 1: crosses – for the first solution, points – for the second, squares – for the third one. Solid lines – graphics of functions approximating initial data, where the coefficients are calculated according to functions (12) and (13). Dashed lines shows a dependence diagram of type (14) with coefficients $C_1 = 1, C_2 = 1$ (curve 1), $C_1 = -1, C_2 = 1$ (curve 2), $C_1 = 0, C_2 = 1$ (curve 3).

Figure 2 compares the proposed OLS method of relationship plurality recovery and a traditional OLS for one relationship. We approximate the data for curve No. 2 at Fig. 1. Dashed and solid lines are taken from Fig. 1 and are constructed by method of relationship plurality approximation. Dash-dot line is the reconstructed relationship of a private solution

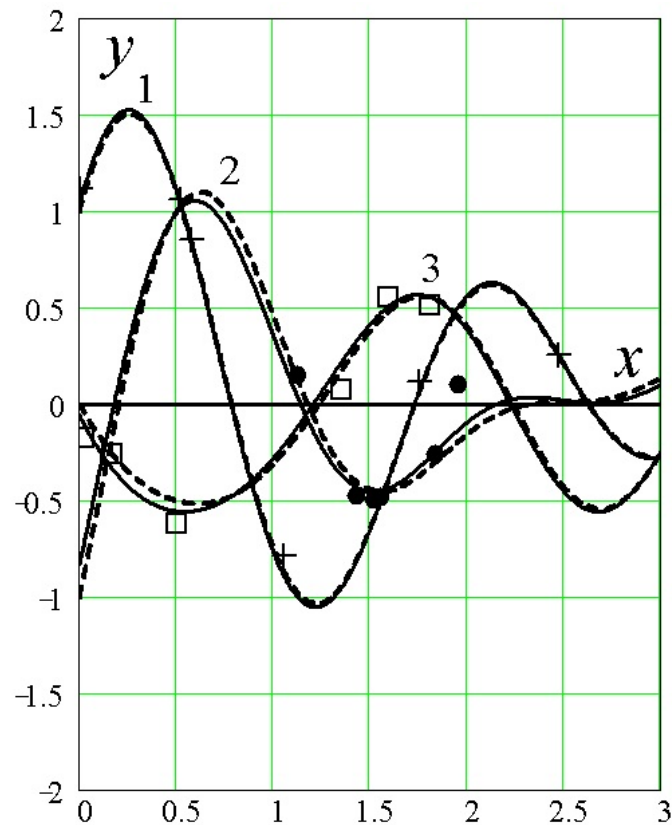


FIG. 1. Results of approximation of family of private solutions of LNDE

only according to data for curve No. 2. The calculated formulae are obtained by solving a SLE, if we assume that there is only one relationship ($R = 1$). An unsatisfactory result on the last relationship recovery at $[0, 3]$ is explained by small data quantity for this curve, grouped near the middle of the gap. However, curve approximation as a representative of curves plurality gives quite a satisfactory result.

The proposed OLS usage for analytical relationship plurality approximation allows consideration of a certain function feature, combining them into a plurality. Relationships are set by a linear combination of known functions with the desired coefficients. Analytic plurality properties are given by the fact that a part of linear combination coefficients are the same for all the relationship pluralities. Coefficients are calculated using OLS, which provides a minimum of the average of data deviation square for all functional relationship pluralities. Combining data for all functional relationships leads to good results for their approximation, even when only having a small amount of data for some of the relationships.

Practical application of the proposed approximation algorithm of function plurality showed the recovery efficiency for the analytic dependence, included into the relationship plurality, with insufficient quantity of measured values or with unsuccessful location of interpolation point of some curves in this plurality. Availability of data for other plurality relationships allows quite satisfactorily the approximation of the equation and these curves.

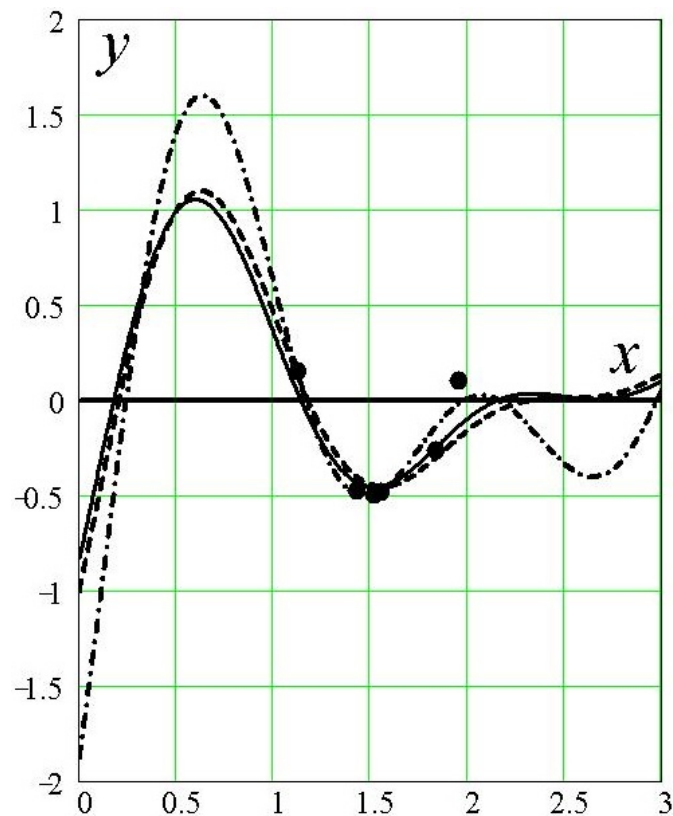


FIG. 2. Comparison of two approximations of one of solutions of LNDE. The first approximation (the continuous line) is received with use of all data for family of curves. The second approximation (the dash-dotted line) — according to the data noted by points, only for this decision. The shaped line — the exact solution of LNDE

References

- [1] Kobzar' A.I. *Applied Mathematical Statistics. For Engineers and Scientists*. Moscow, Fizmatlit, 2006.
- [2] Seber G.A.F. *Linear Regression Analysis*. John Wiley and Sons. New York, London, Sydney, Toronto, 1977.
- [3] Williams E.J. *Regression Analysis*. New York, Wiley, 1959.
- [4] Sprent P. *Models in Regression and Related Topics*. London, Methuen, 1969.
- [5] Lukyanov V.D. On the Issue of Interpolation Approximation Polynomial Construction. *Nanosystems: Physics, Chemistry, Mathematics*, 3 (6), P. 5–15 (2012).

BENCHMARK SOLUTIONS FOR NANOFLOWS

A. I. Popov¹, I. S. Lobanov¹, I. Yu. Popov¹, T. V. Gerya²

¹ ITMO University, Kronverkskiy 49, 197101, St. Petersburg, Russia

² Institute of Geophysics, Department of Earth Sciences, Swiss Federal Institute of Technology Zurich (ETH), 5 Sonnegstrasse, CH-8092 Zurich, Switzerland

popov239@gmail.com, taras.gerya@erdw.ethz.ch

PACS 47.10.ad, 47.11.Fg

Essential viscosity variation creates additional difficulties for numerical investigation of flows through nanotubes and nanochannels. Benchmark solutions of the Stokes and continuity equations with variable viscosity are suggested. This is useful for testing of numerical algorithms applied to this problem.

Keywords: nanotube, Stokes flow, benchmark solution.

Received: 03 May 2014

Revised: 11 May 2014

1. Introduction

Flows through nanotubes and other nanostructures have many interesting peculiarities. One of them is the viscosity variation (see, e.g., [1], [2], [3]). Flows in nano-channels are influenced by local heterogeneity of molecular structure of the liquid if its size is compared with the channel width. A hypothesis about the existence of locally-ordered structures in liquid was put forward in [4]. Investigations of fluid flows in nano-sized domains show that it is strongly influenced by local ordering of nano-sized scale. Experiments [5], [6] show that the effective viscosity of water in nanochannel with hydrophilic walls is essentially greater than the corresponding macroscopic value. Experimental and theoretical investigations of water state in carbon nanotube [7], [8] show that there is an ice-like envelope with liquid water inside in the nanotube. Increasing of effective fluid viscosity via channel diameter was marked in [9] for channels of a few micrometers diameters. Thus, experiments confirm high viscosity variations for the flow in a nanotube, which creates computational problems. Namely, the convergence of the numerical algorithms in the case of strongly varying viscosity is not good, and, moreover, is not guaranteed ([10], [11]). Correspondingly, one need an instrument to choose an appropriate numerical scheme. One can make a choice by using of benchmark solutions (see, e.g., [12], [13], [14])

In present work, we suggest methods for algorithm checking. The scheme of the algorithm testing is as follows. Consider a rectangular domain. Calculate the values of the benchmark solutions at the rectangle's boundary. Take these values as the boundary conditions. Due to the uniqueness theorem the solution of the boundary problem should coincide with our benchmark solution. So, we obtain a solution of the specific boundary problem. Note that we derived the solution analytically. Next, we solve the same boundary problem by a numerical algorithm, then we compare results and estimate the quality of the numerical algorithm.

We have found exact analytical solutions of the Stokes and continuity equations in the two-dimensional case for linearly varying viscosity. These solutions are convenient to use as benchmarks for numerical algorithm testing. The efficiency of the approach was

demonstrated on a numerical algorithm for calculations of the Stokes flow with varying viscosity.

2. Formulation of Stokes and continuity equations with variable viscosity

Consider the plane flow. 2D Stokes equations for the case of varying viscosity has the form:

$$2\eta \frac{\partial^2 v_x}{\partial x^2} + 2 \frac{\partial \eta}{\partial x} \frac{\partial v_x}{\partial x} + \eta \frac{\partial^2 v_x}{\partial y^2} + \eta \frac{\partial^2 v_y}{\partial y \partial x} + \frac{\partial \eta}{\partial y} \frac{\partial v_x}{\partial y} + \frac{\partial \eta}{\partial y} \frac{\partial v_y}{\partial x} - \frac{\partial P}{\partial x} = -\rho G_x, \quad (1)$$

$$\eta \frac{\partial^2 v_y}{\partial x^2} + \eta \frac{\partial^2 v_x}{\partial y \partial x} + \frac{\partial \eta}{\partial x} \frac{\partial v_x}{\partial y} + \frac{\partial \eta}{\partial x} \frac{\partial v_y}{\partial x} + 2 \frac{\partial \eta}{\partial y} \frac{\partial v_y}{\partial y} + 2\eta \frac{\partial^2 v_y}{\partial y^2} - \frac{\partial P}{\partial y} = -\rho G_y, \quad (2)$$

$$\frac{\partial v_x}{\partial x} + \frac{\partial v_y}{\partial y} = 0. \quad (3)$$

Here (v_x, v_y) is the flow velocity, $\eta = \eta(x, y)$ is the viscosity, P is the pressure, ρ is the density, (G_x, G_y) is the gravitational force. Note that (3) is the continuity equation.

Let us change the variables v_x, v_y, P in such a way that:

$$\frac{\partial v_x}{\partial x} = \frac{1}{\eta} \frac{\partial u_x}{\partial x}, \quad \frac{\partial v_x}{\partial y} = \frac{1}{\eta} \frac{\partial u_x}{\partial y}, \quad (4)$$

$$\frac{\partial v_y}{\partial x} = \frac{1}{\eta} \frac{\partial u_y}{\partial x}, \quad \frac{\partial v_y}{\partial y} = \frac{1}{\eta} \frac{\partial u_y}{\partial y}. \quad (5)$$

$$\frac{1}{\eta} \frac{\partial P}{\partial x} = \frac{\partial \tilde{P}}{\partial x}, \quad \frac{1}{\eta} \frac{\partial P}{\partial y} = \frac{\partial \tilde{P}}{\partial y}. \quad (6)$$

The correctness conditions for such replacement are as follows:

$$\frac{\partial}{\partial y} \left(\frac{1}{\eta} \frac{\partial u_x}{\partial x} \right) = \frac{\partial}{\partial x} \left(\frac{1}{\eta} \frac{\partial u_x}{\partial y} \right), \quad \frac{\partial}{\partial y} \left(\frac{1}{\eta} \frac{\partial u_y}{\partial x} \right) = \frac{\partial}{\partial x} \left(\frac{1}{\eta} \frac{\partial u_y}{\partial y} \right),$$

$$\frac{\partial}{\partial y} \left(\eta \frac{\partial \tilde{P}}{\partial x} \right) = \frac{\partial}{\partial x} \left(\eta \frac{\partial \tilde{P}}{\partial y} \right).$$

These conditions lead to the following correlations:

$$\frac{\partial \eta}{\partial y} \frac{\partial u_x}{\partial x} = \frac{\partial \eta}{\partial x} \frac{\partial u_x}{\partial y}, \quad \frac{\partial \eta}{\partial y} \frac{\partial u_y}{\partial x} = \frac{\partial \eta}{\partial x} \frac{\partial u_y}{\partial y},$$

$$\frac{\partial \eta}{\partial y} \frac{\partial \tilde{P}}{\partial x} = \frac{\partial \eta}{\partial x} \frac{\partial \tilde{P}}{\partial y}.$$

All conditions give one the same characteristic equation:

$$\frac{\partial \eta}{\partial x} dx + \frac{\partial \eta}{\partial y} dy = 0.$$

Evidently, $\eta(x, y) = C$ is an integral of the equation. Hence, the solutions of our equations, which predetermine the correctness of replacement suggested above, are

$$u_x = \Phi(\eta), \quad u_y = \Psi(\eta), \quad \tilde{P} = \tilde{P}(\eta).$$

After replacement, the Stokes equations (1), (2) and the continuity condition (3) transform to the following form:

$$2\frac{\partial^2 u_x}{\partial x^2} + \frac{\partial^2 u_x}{\partial y^2} + \frac{\partial^2 u_y}{\partial y \partial x} - \eta \frac{\partial \tilde{P}}{\partial x} = -\rho G_x, \tag{7}$$

$$\frac{\partial^2 u_y}{\partial x^2} + \frac{\partial^2 u_x}{\partial y \partial x} + 2\frac{\partial^2 u_y}{\partial y^2} - \eta \frac{\partial \tilde{P}}{\partial y} = -\rho G_y, \tag{8}$$

$$\frac{\partial u_x}{\partial x} + \frac{\partial u_y}{\partial y} = 0. \tag{9}$$

Inserting the expressions for u_x, u_y into (7), (8), (9), one obtains the following equations:

$$2\Phi' \frac{\partial^2 \eta}{\partial^2 x} + 2\Phi'' \left(\frac{\partial \eta}{\partial x} \right)^2 + \Phi' \frac{\partial^2 \eta}{\partial^2 y} + \Phi'' \left(\frac{\partial \eta}{\partial y} \right)^2 + \Psi' \frac{\partial^2 \eta}{\partial y \partial x} + \Psi'' \frac{\partial \eta}{\partial y} \frac{\partial \eta}{\partial x} - \eta \tilde{P}' \frac{\partial \eta}{\partial x} = -\rho G_x, \tag{10}$$

$$2\Psi' \frac{\partial^2 \eta}{\partial^2 y} + 2\Psi'' \left(\frac{\partial \eta}{\partial y} \right)^2 + \Psi' \frac{\partial^2 \eta}{\partial^2 x} + \Psi'' \left(\frac{\partial \eta}{\partial x} \right)^2 + \Phi' \frac{\partial^2 \eta}{\partial y \partial x} + \Phi'' \frac{\partial \eta}{\partial y} \frac{\partial \eta}{\partial x} - \eta \tilde{P}' \frac{\partial \eta}{\partial y} = -\rho G_y, \tag{11}$$

$$\Phi' \frac{\partial \eta}{\partial x} + \Psi' \frac{\partial \eta}{\partial y} = 0. \tag{12}$$

3. Exponentially varying viscosity

Let us construct the second benchmark solution. Next, we assume that the viscosity is the exponential function of the Cartesian coordinates:

$$\eta = c \exp(ax + by). \tag{13}$$

General consideration up to (10), (11), (12) is the same as earlier. By inserting (13) into (10), (11), (12) and taking into account that:

$$\frac{\partial \eta}{\partial x} = a\eta, \quad \frac{\partial \eta}{\partial y} = b\eta,$$

one obtains the following system of equations:

$$\begin{aligned} (2a^2 + b^2)(\Phi'' \eta^2 + \Phi' \eta) + ab(\Psi'' \eta^2 + \Psi' \eta) - a\tilde{P}' \eta^2 &= -\rho G_x, \\ ab(\Phi'' \eta^2 + \Phi' \eta) + (a^2 + 2b^2)(\Psi'' \eta^2 + \Psi' \eta) - b\tilde{P}' \eta^2 &= -\rho G_y, \\ a\Phi' + b\Psi' &= 0. \end{aligned}$$

Using the last relation, we exclude Ψ from the first two equations:

$$\begin{aligned} (a^2 + b^2)(\Phi'' \eta^2 + \Phi' \eta) - a\tilde{P}' \eta^2 &= -\rho G_x, \\ -\frac{a^3 + ab^2}{b}(\Phi'' \eta^2 + \Phi' \eta) - b\tilde{P}' \eta^2 &= -\rho G_y, \\ \Psi' &= -\frac{a}{b}\Phi'. \end{aligned} \tag{14}$$

One can see that we obtain a linear algebraic system with respect to $(\Phi''\eta^2 + \Phi'\eta)$ and \tilde{P}' . The solution is as follows:

$$\tilde{P}' = \frac{f_1(\eta)}{\eta^2}, \quad (15)$$

$$\Phi''\eta^2 + \Phi'\eta = bf(\eta). \quad (16)$$

Remark. It is interesting that these formulas contain the same functions $f(\eta)$, $f_1(\eta)$.

Equation (16) is a well-known Euler ordinary differential equation. One can get its solution for arbitrary function f :

$$u_x = \Phi(\eta) = b \int_1^\eta \log\left(\frac{\eta}{\eta_1}\right) \frac{f(\eta_1)}{\eta_1} d\eta_1 + bc_1 \log \eta + c_2. \quad (17)$$

Taking into account relation (14), one obtains u_y :

$$u_y = \Psi(\eta) = -a \int_1^\eta \log\left(\frac{\eta}{\eta_1}\right) \frac{f(\eta_1)}{\eta_1} d\eta_1 - ac_1 \log \eta + c_3. \quad (18)$$

Taking into account (4), (5), one obtains v_x , v_y :

$$\begin{aligned} v_x &= b \int_1^\eta \frac{d\eta_1}{\eta_1^2} \int_1^{\eta_1} d\eta_2 \frac{f(\eta_2)}{\eta_2} - bc_1 \frac{1}{\eta} + bc_1 + c_2 = \\ &= b \int_1^\eta d\eta_2 \frac{f(\eta_2)}{\eta_2} \int_{\eta_2}^\eta \frac{d\eta_1}{\eta_1^2} - bc_1 \frac{1}{\eta} + bc_1 + c_2. \end{aligned}$$

Hence, we get the expression for v_x and analogously, for v_y :

$$v_x = b \int_1^\eta d\eta_2 \frac{f(\eta_2)}{\eta_2} \frac{\eta - \eta_2}{\eta\eta_2} - bc_1 \frac{1}{\eta} + bc_1 + c_2, \quad (19)$$

$$v_y = -a \int_1^\eta d\eta_2 \frac{f(\eta_2)}{\eta_2} \frac{\eta - \eta_2}{\eta\eta_2} + ac_1 \frac{1}{\eta} + c_3. \quad (20)$$

As for the pressure, we obtain it from (15) by taking into account (6):

$$\tilde{P} = \int_1^\eta d\eta_1 \frac{f_1(\eta_1)}{\eta_1^2} + c_4.$$

Hence,

$$P = \int_1^\eta d\eta_1 \frac{f_1(\eta_1)}{\eta_1} + c_4. \quad (21)$$

For a simple particular case (constant gravitational term), when $f(\eta) = A = const$, $f_1(\eta) = A_1 = const$ one has:

$$\begin{aligned} v_x &= -\frac{b(A + c_1)}{\eta} - \frac{bA \log \eta}{\eta} + \tilde{c}_2, \\ v_y &= \frac{a(A + c_1)}{\eta} + \frac{aA \log \eta}{\eta} + \tilde{c}_3, \\ P &= A_1 \log \eta + c_4 - b_1, \end{aligned}$$

A more complicated case is when the density is a linear function of the viscosity, $\rho = \beta_1\eta + \beta_2$, i.e.

$$f(\eta) = a_1\eta + a_2, \quad f_1(\eta) = b_1\eta + b_2,$$

where constants a_1, a_2, b_1, b_2 are the same as in the previous section. It is simple to evaluate integrals in (19), (20), (21). In such a way, one obtains:

$$v_x = ba_1 \log \eta + \frac{b(a_1 - a_2 - c_1)}{\eta} - ba_2 \frac{\log \eta}{\eta} + \tilde{c}_2,$$

$$v_y = -aa_1 \log \eta - \frac{a(a_1 - a_2 - c_1)}{\eta} + aa_2 \frac{\log \eta}{\eta} + \tilde{c}_3,$$

$$P = b_1\eta + b_2 \log \eta + \tilde{c}_4,$$

where $\tilde{c}_2 = c_2 + bc_1 + ba_2 - ba_1$, $\tilde{c}_3 = c_3 + aa_1 - aa_2 - ac_1$, $\tilde{c}_4 = c_4 - b_1$.

4. Example problems and numerical convergence tests

The scheme of algorithm testing is as follows: initially, we have obtained particular solutions of the Stokes and continuity equations for the exponential type of viscosity variation. Let us choose a domain, e.g., a rectangle in 2D case. We calculate values for velocity and pressure given by our analytical solution and take these values as the boundary conditions. Then, due to the uniqueness theorem, the solution of the boundary problem in the domain should coincide with our analytical solution. Let us compute the solution of the boundary problem by a numerical method. Comparison of the result with the exact analytical solution shows the quality of the numerical algorithm.

4.1. Exponentially varying viscosity

Consider a simple example of such flow in a rectangle $0 \leq x \leq x_{size}, 0 \leq y \leq y_{size}$. We assume that $\eta = ax + by + c$. We will mark the exact solution obtained in Section 2 as $v_{x,a}, v_{y,a}, P_a$. It is the solution of the boundary problem in the rectangle Ω with the following conditions at the boundary $\partial\Omega = \{x = 0, x = x_{size}, y = 0, y = y_{size}\}$:

$$v_y|_{\partial\Omega} = v_{y,a}, \quad v_x|_{\partial\Omega} = v_{x,a}.$$

Let us compute the velocity and pressure using the finite-difference scheme. The corresponding solution is marked as $v_{x,n}, v_{y,n}, P_n$. The deviation of these values from the exact solution ($v_{x,n} - v_{x,a}, v_{y,n} - v_{y,a}, P_n - P_a$) is related with the error of the numerical scheme. We calculate the relative errors of three types: L_∞, L_1, L_2 for different viscosity contrasts, i.e. different values of the coefficients a, b . We test the program Stokes2D-variable-viscosity1 from [10]. The results are presented in Fig. 1-6. Namely, figures 1-3 correspond to low viscosity contrast, Figures 4-6 — to high viscosity contrast. Particularly, Fig. 1 and Fig. 4 show pressure and velocity components distributions. Fig. 2 and Fig. 5 characterize the viscosity and the density distributions. Fig. 3 and Fig. 6 contain plots of relative errors via the grid resolutions in logarithmic scale. The viscosity contrast, i.e. the values of the coefficients in the expression for the viscosity, is determined by the given values of the viscosity at three rectangle corners. The value of the viscosity at the initial rectangle corner is 1, η_2, η_3 are the values of the viscosity at two adjacent corners. For all figures, “n” means “numerical solution”, “a” means “analytical solution” (benchmark).

For the case of exponentially varying viscosity, we made calculations for the following system parameters:

$$\begin{aligned} C &= \eta_1, a = (\log(\eta_3) - \log(\eta_1))/x_{size}, \\ b &= (\log(\eta_2) - \log(\eta_1))/y_{size}, \\ \eta &= C \exp(ax + by), \\ \rho &= \beta_1\eta + \beta_2 \\ x_{size} &= y_{size} = 1, \\ G_x &= 10, G_y = 10, \\ \eta_1 &= 1, \beta_1 = 1, \beta_2 = 3 \times 10^3, \end{aligned}$$

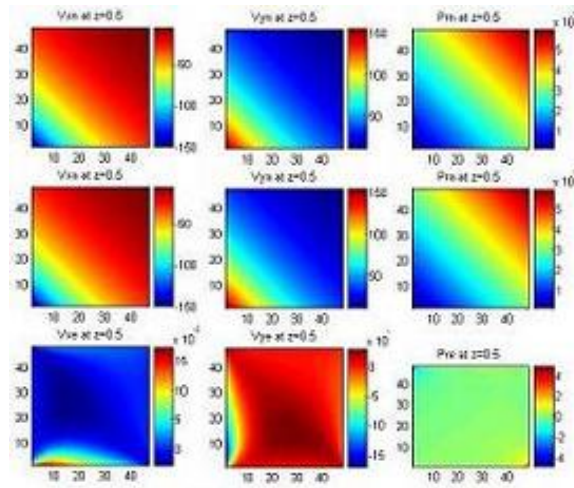


FIG. 1. Distribution of v_x , v_y and P ; 2D case, exponentially varying viscosity, low viscosity contrast ($\eta_2 = \eta_3 = 5$).

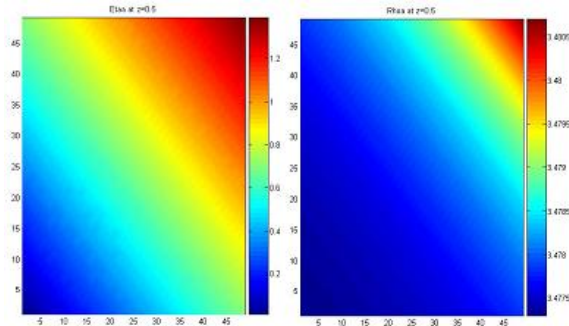


FIG. 2. Distribution of viscosity η and density ρ ; 2D case, exponentially varying viscosity, low viscosity contrast ($\eta_2 = \eta_3 = 5$).

One can see that there is rather high accuracy for the numerical approach. Figures 1-3 corresponds to the case of low viscosity contrast, figures 4-6 — to the case of high viscosity contrast. We observe the conventional situation — L_∞ -error is the largest among the considered errors norms, and L_1 -error and L_2 -error are similar. The calculations show that one has good convergence of the numerical scheme for small viscosity contrast, but it is not so for high viscosity contrast (compare Fig. 3 and Fig. 6).

5. Conclusion

Numerical analysis of geophysical flows presents many difficulties. It is related with complex dependence of material parameters on spatial coordinates. Different schemes of numerical calculations are suggested. To establish the quality of suggested approach it is possible to compare the results of different numerical methods. More reliable examination of the approach is given by the comparison with the exact solution of the problem, similar to the considered one. For this purpose, one needs such a benchmark solution. In the present paper, we suggest a benchmark solution for the Stokes equation coupled with the continuity equation where the viscosity is exponentially dependent upon the spatial Cartesian coordinates. Comparison of the numerical result with this exact solution allows us to determine the order of convergence, the quality of discretization, etc.

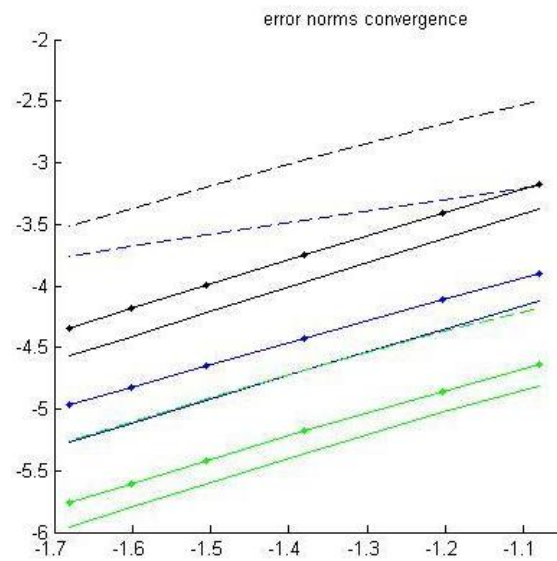


FIG. 3. Logarithm of the relative error via logarithm of the grid step; 2D case, exponentially varying viscosity, low viscosity contrast ($\eta_2 = \eta_3 = 5$); blue line - pressure, green - v_x , black - v_y ; line - L_1 -error, dashed line - L_∞ -error, line with dots - L_2 -error.

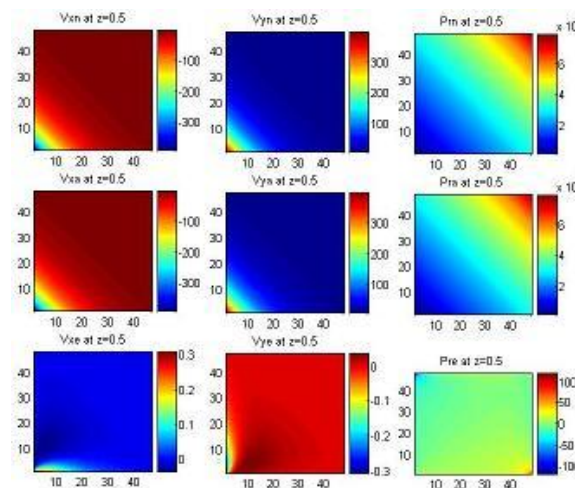


FIG. 4. Distribution of v_x , v_y and P ; 2D case, exponentially varying viscosity, high viscosity contrast ($\eta_2 = \eta_3 = 100$).

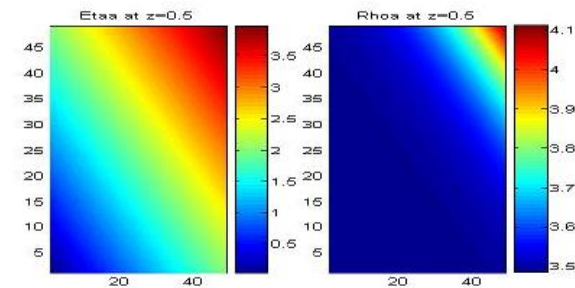


FIG. 5. Distribution of viscosity η and density ρ ; 2D case, exponentially varying viscosity, high viscosity contrast ($\eta_2 = \eta_3 = 100$).

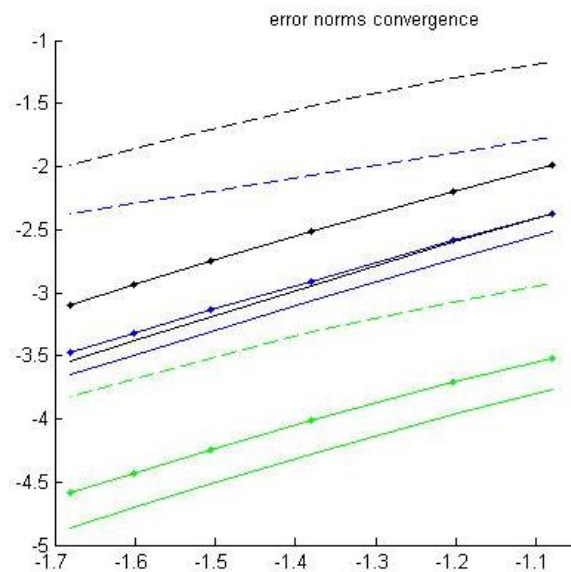


FIG. 6. Logarithm of the relative error via logarithm of the grid step; 2D case, exponentially varying viscosity, high viscosity contrast ($\eta_2 = \eta_3 = 100$); blue line - pressure, green - v_x , black - v_y ; line - L_1 -error, dashed line - L_∞ -error, line with dots - L_2 -error.

Acknowledgement

This work was partially financially supported by the Government of the Russian Federation (grant 074-U01), by the Ministry of Science and Education of the Russian Federation (GOSZADANIE 2014/190, Project 14.Z50.31.0031), by grants of the President of Russia (state contracts 14.124.13.2045-MK and 14.124.13.1493-MK).

References

- [1] Li, D. (Ed.) *Encyclopedia of Microfluidics and Nanofluidics*. Springer, New York (2008).
- [2] Popov I.Yu. Statistical derivation of modified hydrodynamic equations for nanotube flows, *Phys. Scripta.*, **83**, P. 045601/1-3 (2011).
- [3] I.Yu. Popov, S.A. Chivilikhin, V.V. Gusarov. Flows in nanostructures: hybrid classical-quantum models. *Nanosystems: Phys., Chem., Math.*, **3**(1), P. 7–26 (2012).
- [4] Frenkel Ya. I. New development of the theory of liquid state. *Appl. Uspekhi Fiz. Nauk.*, **25**. P. 1-18 (1941).
- [5] Antognozzi M., Humphris A. D. L., Miles M. J. Observation of molecular layering in a confined water film and study of the layers viscoelastic properties. *Appl. Phys. Lett.*, **78**, P. 300-302 (2001).
- [6] Li T.-D., Gao J., Szoszkiewicz R., Landmann U., Riedo E. Structured and viscous water in subnanometer gaps. *Phys. Rev. B.*, **75**, P. 115415-1115415-6 (2007).
- [7] Kolesnikov A.I., Zanotti J.-M., Loong Ch.-K., and Thiyagarajan P. Anomalous Soft Dynamics of Water in a Nanotube: A Revelation of Nanoscale Confinement. *Phys. Lett.*, **93**, P. 035503-1035503-4 (2004).
- [8] Kolesnikova A.I., C.-K. Loonga C.K., de Souzaa N.R., Burnhamb C.J. Moravskyc A.P. Anomalous soft dynamics of water in carbon nanotubes. *Physica B*, **385386**, P. 272–274 (2006).
- [9] Deryagin B. V., Ovcharenko F. D., Churaev V. N. (Eds.) *Water in Disperse Systems*. Moscow, Nauka (1989).
- [10] Gerya T. *Introduction to Numerical Geodynamic Modelling*, Cambridge University Press, Cambridge (2010).
- [11] Gerya T.V., May D.A., Duretz T. An adaptive staggered grid finite difference method for modeling geodynamic Stokes flows with strongly variable viscosity. *Geochem., Geophys., Geosyst.* **14**, DOI: 10.1002/ggge.20078 (2013).

- [12] Blankenbach B., Busse F., Christensen U. et al, A benchmark comparison for mantle convection codes. *Geophysical Journal International* **98**, P. 23–38 (1989).
- [13] Gerya T.V., Yuen D.A., Characteristic-based marker-in-cell method with conservative finite-difference schemes for modeling geological flows with strongly variable transport properties. *Phys. Earth Planetary Interiors*, **140**, P. 293–318 (2003).
- [14] Gerya T.V., Yuen D.A. Robust characteristics method for modeling multiphase visco-elasto-plastic thermo-mechanical problems. *Phys. Earth Planetary Interiors*, **163**, P. 83–105 (2007).

CRYSTALLITE MODEL FOR FLOW IN NANOTUBE CAUSED BY WALL SOLITON

O. A. Rodygina¹, S. A. Chivilikhin¹, I. Yu. Popov¹, V. V. Gusarov²

¹ITMO University, Kronverkskiy, 49, St. Petersburg, 197101, Russia

²Ioffe Physical-Technical Institute RAS, Polytechnicheskaya, 26, St. Petersburg, Russia

olgarodygina@gmail.com

PACS 68.90.+g, 05.60.-k

Fluid flow in a nanotube, caused by a moving soliton-like perturbation of its wall, is considered. We use a crystallite model for nanotube flow. A picture of the flow is described. The formula for crystallite velocity is derived, allowing one to find fluid flux through a nanotube.

Keywords: nanotube, soliton, flow.

Received: 2 April 2014

Revised: 10 April 2014

1. Introduction

Fluid flow in nanotubes were intensively investigated in our previous studies. This was inspired by the intriguing prospects for the possible applications to nanomembrane, nanoreactor, nanoaccumulator, etc. It should be mentioned that nanotube flow obeys a set of remarkable peculiarities, distinguishing it from classical tube flow [1-6]. It poses a problem of theoretical description of such flows. Creation of new nanodevices based on nanoflows is impossible without theoretical models giving prediction of flow character. Currently, there is no general theory for nanoflow. One has only particular models, describing some specific nanoflow features. (see, e.g., [7,8]). In the present paper, we consider fluid flow in nanotube caused by mechanical waves propagating in its walls. Such flows were actively studied in recent years [9-11]. Such deformation may be caused by mechanical action on the nanotube [12]. We consider the problem in the framework of crystallite model of nanoflow, suggested in [13,14]. The model was developed theoretically [15]. The existence of ice-like clusters, resembling a solid, was observed in earlier experiments [3]. Additional confirmation for this hypothesis was given by experiments with multi-component flow through nanotubes. The authors observed structure separation predicted by the crystallite model.

2. Model description

We consider cylindrical nanotube filled by liquid. The smallness of the Reynolds number for the nanotube flow allows us to use Stokes' approximation [15]. We treat the problem in the framework of the crystallite model. Correspondingly, we assume that the nanotube contain solid-like part of the liquid concentrated near the nanotube axis. It is separated from the nanotube boundary by liquid layer (usually, one refers to this layer as the non-autonomous phase) [18]. One can note that due to thermodynamics arguments, we can conclude that both the crystallite and the non-autonomous phase layer have some equilibrium size (radius, which depends on the temperature, type of the liquid, etc. These

two factors are competitive in the nanotube, leading to some correlation between their widths in particular cases.

Thus, we have the following equations for the flow of the liquid layer (non-autonomous phase) in the nanotube under the assumption of an axisymmetric character for the flow ((r, z) are the cylindrical coordinates):

$$\begin{aligned} \frac{\partial^2 v_z}{\partial z^2} + \frac{1}{r} \frac{\partial}{\partial r} \left(r \frac{\partial v_z}{\partial r} \right) &= \frac{1}{\mu} \frac{\partial p}{\partial z}, \\ \frac{\partial^2 v_r}{\partial z^2} + \frac{1}{r} \frac{\partial}{\partial r} \left(r \frac{\partial v_r}{\partial r} \right) - \frac{1}{r^2} v_r &= \frac{1}{\mu} \frac{\partial p}{\partial r}, \\ \frac{\partial v_z}{\partial z} + \frac{1}{r} \frac{\partial}{\partial r} (r v_r) &= 0, \end{aligned} \quad (1)$$

where t is time, v_r and v_z are radial and longitudinal components of the velocity, p is the pressure, μ is the fluid viscosity. Note that the last equation is the continuity equation. We assume that the central part of the nanotube is occupied by a crystallite of radius R_c , R is the cylindrical nanotube radius. We assume that there is moving wall soliton, i.e. moving boundary perturbation. In our model, the nanotube is assumed to be cylindrical. To take into account the soliton, we pose the following non-homogeneous boundary condition at the cylinder boundary $r = R$:

$$v_z|_{r=R} = 0, \quad v_r|_{r=R} = \frac{\partial h}{\partial t} \equiv -V \frac{\partial h}{\partial z}. \quad (2)$$

Here, $h = h(z, t)$ is the radial perturbation of nanotube wall due to the soliton, V is the soliton velocity (given). As for the internal cylinder (crystallite-fluid boundary), the following boundary conditions are assumed:

$$v_z|_{r=R_c} = V_c, \quad v_r|_{r=R_c} = 0. \quad (3)$$

Here, V_c is the crystallite velocity, which is not predetermined. We consider the equilibrium state and determine the crystallite velocity using conditions of vanishing friction force (crystallite-fluid). One can present the velocity in the layer between the wall of the nanotube and the crystallite in the following form:

$$v_r = -\frac{1}{r} \frac{\partial \Psi}{\partial z}, \quad v_z = \frac{1}{r} \frac{\partial \Psi}{\partial r} + V_c \frac{\ln(R/r)}{\ln(R/R_c)}. \quad (4)$$

Substituting (4) into (1), one obtains the equation for Ψ . We present Ψ in the following form: $\Psi = \psi + \psi_0$, where ψ_0 has the form:

$$\psi_0 = \frac{V_c}{4 \ln\left(\frac{R}{R_c}\right)} \left[r^2 \left(1 - 2 \ln\left(\frac{r}{R}\right) \right) - R_c^2 \left(1 - 2 \ln\left(\frac{R_c}{R}\right) \right) \right].$$

Then, the solution : ψ satisfying boundary conditions (2), (3) has the following form:

$$\psi(z, r) = \int_{-\infty}^{\infty} G(z - z', r) h(z') dz', \quad G(z, r) = \frac{V}{\pi} \int_0^{\infty} g_k(r) \cos(kz) dk, \quad (5)$$

where

$$\begin{aligned} g_k(r) &= \frac{r(q_1 p_1 - q_2 p_2)}{\gamma(kR)(U_{11}(R)U_{22}(R) - U_{12}(R)U_{21}(R))}, \\ q_1 &= (U_{21}(R)I_0(kR) + U_{22}(R)K_0(kR)), \\ p_1 &= (U_{11}(r)I_1(kr) + U_{12}(r)K_1(kr)), \end{aligned}$$

$$q_2 = (U_{11}(R) I_0(kR) + U_{12}(R) K_0(kR)),$$

$$p_2 = (U_{21}(r) I_1(kr) + U_{22}(r) K_1(kr)).$$

Here,

$$U_{11}(r) = -\frac{1}{k} \int_{R_c}^r \frac{I_1(kr') K_1(kr') dr'}{\gamma(kr')}, \quad U_{12}(r) = \frac{1}{k} \int_{R_c}^r \frac{I_1^2(kr') dr'}{\gamma(kr')},$$

$$U_{21}(r) = -\frac{1}{k} \int_{R_c}^r \frac{K_1^2(kr') dr'}{\gamma(kr')}, \quad U_{22}(r) = \frac{1}{k} \int_{R_c}^r \frac{I_1(kr') K_1(kr') dr'}{\gamma(kr')},$$

$$\gamma(kr) = I_1(kr) K_0(kr) - I_0(kr) K_1(kr),$$

where $I_0(x)$, $K_0(x)$, $I_1(x)$, $K_1(x)$ are, correspondingly, the modified Bessel function and the modified Neumann function of the 0th and the 2nd orders.

Fig. 1 shows the pattern of the flow in the nanotube between the crystallite (on the left) and the nanotube wall (on the right).

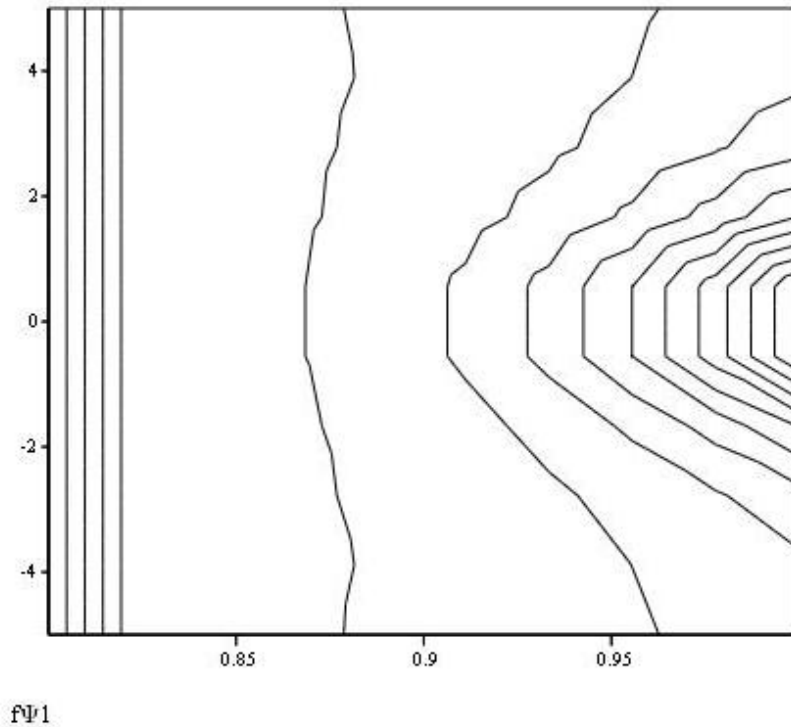


FIG. 1. Picture of the streamlines in the nanotubes

Fig. 2 shows the pattern of the flow in the nanotube. The streamlines form reflects the impact of the soliton in the right part of the figure.

Note that at present, our solution has a free parameter V_c (velocity of the crystallite). To calculate the speed of the crystallite, we use the condition of vanishing viscous friction force applied to the crystallite (more precisely, linear force density, i.e. the force, corresponding to the unit length). Then, we have:

$$V_c = \frac{2VR_c}{\pi L} \ln\left(\frac{R}{R_c}\right) \int_0^\infty \frac{\sin(kL/2) h_k (q_1 I_1(kR_c) - q_2 K_1(kR_c))}{k\gamma(kR) (U_{11}(R) U_{22}(R) - U_{12}(R) U_{21}(R))} dk, \quad (6)$$

where L — crystallite length, h_k is the Fourier transform of h . Incorporating this formula with the expression for the stream function, one obtains the fluid flux through the nanotube.

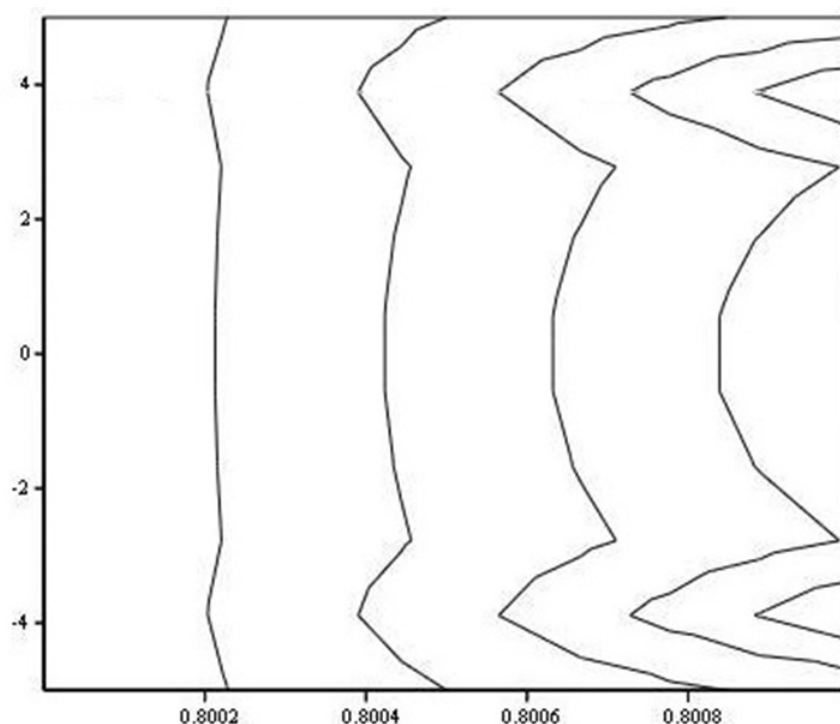


FIG. 2. Picture of the streamlines in the nanotubes

Acknowledgements

This work was partially financially supported by the Government of the Russian Federation (grant 074-U01), by the Ministry of Science and Education of the Russian Federation (GOSZADANIE 2014/190, Project 14.Z50.31.0031), by grants of the President of Russia (state contracts 14.124.13.2045-MK and 14.124.13.1493-MK).

References

- [1] Encyclopedia of microfluidics and nanofluidics / edited by Dongqing Li. New York : Springer (2008).
- [2] Li T.-D., Gao J., Szoszkiewicz R., Landman U., Riedo E. Structured and viscous water in subnanometer gaps. *Phys. Rev. B.*, **75**, P. 115415-1 – 115415-6 (2007).
- [3] Mashl R. J., Joseph S., Aluru N. R., Jakobsson E. Anomalous Immobilized Water: A New Water Phase Induced by Confinement in Nanotubes. *Nano Letters*, **3**(5), P. 589–592 (2003).
- [4] Kolesnikova A.I., C.-K. Loong C.K., de Souza N.R., Burnham C.J. Moravskyc A.P. Anomalous soft dynamics of water in carbon nanotubes. *Physica B*, **385–386**, P. 272–274 (2006).
- [5] A.I. Kolesnikov, J.-M. Zanotti, Ch.-K. Loong, and P. Thiyagarajan Anomalous Soft Dynamics of Water in a Nanotube: A Revelation of Nanoscale Confinement. *Phys. Rev. Lett.*, **93**(3), P. 035503 (2004).
- [6] J.K. Holt, H. Gyu Park, Y.Wang, M.Stadermann, A.B. Artyukhin, C.P.Grigoropoulos, A.Noy, O.Bakajin. Fast Mass Transport Through Sub-2-Nanometer Carbon Nanotubes *Science* 312, **1034**, P. 1034–1037 (2006).
- [7] V.P. Maslov. Superfluidity of classical liquid in a nanotube for even and odd numbers of neutrons in a molecule. *Theoretical and Mathematical Physics*, **153**(3), P. 1677–1796 (2007).
- [8] Hanasaki I., Nakatani A. Fluidized piston model for molecular dynamics simulations of hydrodynamic flow. *Modelling Simul. Mater. Sci. Eng.*, **14**, P. 9–20 (2006).
- [9] Belonenko M.B., Chivilikhin S.A., Gusarov V.V., Popov I.Yu. and Rodygina O.A. Soliton-induced flow in carbon nanotubes. *Europhysics Letters*, **101**(6), P. 66001-p1-66001-p3 (2013).
- [10] M. Chen, J. Zang, D. Xiao, et al. Nanopumping Molecules via a Carbon Nanotube. *Nano Research*, **2**(12), P. 938–944 (2009).

- [11] Z.Insepov, D.Wolf, A.Hassanein. Nanopumping using carbon nanotubes. *Nano Lett.*, **6**(9), P. 1893–1895 (2006).
- [12] M.Chen, J.Zang, D.Xiao, et al. Mechanical wave propagation in carbon nanotubes driven by an oscillating tip actuator. *J. Appl. Phys.*, **105**(2), P. 026102 (2009).
- [13] Chivilikhin S.A., Gusarov V.V., Popov I.Yu. Flows in nanostructures: hybrid classical-quantum models. *Nanosystems: Physics, Chemistry, Mathematics*, **3**(1), P. 7–26 (2012).
- [14] Chivilikhin S.A., Gusarov V.V., Popov I.Yu., Svitenkov A. I. Model of fluid flow in a nano-channel. *Russian J. Math. Phys.*, **15**(3), P. 410–412 (2008).
- [15] Popov I.Yu. Statistical derivation of modified hydrodynamic equations for nanotube flows. *Physica Scripta*, **83**, P. 045601/1-3 (2011).
- [16] V.V. Gusarov, I.Yu. Popov. Flows in two-dimensional non-autonomous phases in polycrystalline systems. *Nuovo Cim.*, **18D**(7), P. 799–805 (1996).

METASTABLE CLUSTERS AND AGGREGATIVE NUCLEATION MECHANISM

O. V. Almjashaeva^{1,2}, V. V. Gusarov²

¹St. Petersburg State Electrothechnical University “LETI”, St. Petersburg, Russia

²Ioffe Institute, St. Petersburg, Russia

almjashaeva@mail.ru

PACS 64.60.Q, 82.60.Nh

Feasible nucleation in condensed media by the aggregation mechanism of small metastable crystalline clusters is demonstrated. The presence of the stable small clusters in the initial phases makes the homogeneous and heterogeneous nucleation processes more similar.

Keywords: nucleation, homogeneous and heterogeneous nucleation, clusters.

Received: 10 June 2014

Revised: 16 June 2014

1. Introduction

The formation of particles of a new phase, due to the first-order phase transition or chemical reaction, has been long-studied [1-56]. Traditionally, nucleation mechanisms have been classified as homogeneous and heterogeneous [6-10, 23, 27, 31, 42, 48].

The first studies regarding homogeneous nucleation were presented in [1-10]. Subsequently, homogeneous nucleation for processes in various media and under various conditions was considered in [6-10]. These studies made the basis for development of the classical homogeneous nucleation theory that is known as the Volmer-Weber-Becker-Dering-Frenkel-Zel'dovich theory [6-10]. In subsequent theoretical studies, attempts were made to refine the homogeneous nucleation models, primarily by removing or weakening the constraints that underlie classical homogeneous nucleation models [6-10]. By way of example, reference may be made to [11, 14, 20, 23, 24, 27, 34, 36].

A different trend in the development of the nucleation theory is associated with the description of the processes within the heterogeneous nucleation mechanism [4-48]. The heterogeneous nucleation theory was considered in many studies devoted to the analysis of new phase formation in inhomogeneous media [1, 3, 4, 36]. The effect of the heterogeneous centers of various shapes, sizes, chemical compositions, and structures on the nucleation is perceived as providing a significantly wider scope for possible nucleation models as compared to processes in homogeneous media. At the same time, the existing general regularities of the heterogeneous nucleation, irrespective of the nature of the heterogeneous center, make the range of the numerous heterogeneous nucleation models not so wide as one might suppose [42, 48].

One of the attributes whereby the nucleation models are classified is how far the initial state of a system is from equilibrium. First-order phase transitions are usually treated as bimodal or spinodal phase decomposition [42]. In the former case, nucleation is considered within the classical nucleation theory based on the heterophase fluctuation processes [6-10]. Many original and review publications are also devoted to the nucleations due to the

spinodal decomposition mechanism, based on the homogeneous fluctuation models [12, 13, 27, 34, 42, 44]. The nonequilibrium phase transformations and transformations in systems far from equilibrium are analyzed in a number of studies, for example in [57-60].

Differences in approaches to the description of formation processes for a new phase and the corresponding nucleation models are associated with the aggregate state form of the initial media and produced phase [27, 32, 48]. At present, the vapor condensation and liquid evaporation processes are studied in most detail [1, 3, 4, 6-10, 36, 37, 48]. The issues of crystallization of substances from liquid and gaseous media are elucidated to a much lesser extent in the literature [11, 12, 24]. An even smaller number of studies are devoted to the analysis of the nucleation processes during crystal transition to the liquid or any other crystalline state. In particular, this is caused by a significant complication of the aforementioned processes due to the necessary allowance for the diversity of the structural (phase) states of crystalline substances and their anisotropy. It should be noted that, though it is stated that the first-order phase transitions in condensed systems involve crystalline phases, however, the anisotropy of these phases, which is exhibited in the tensor character of the surface energy of the particles, is commonly ignored in the study of such phase transitions [61, 62]. Moreover, the tensor nature of the chemical potential of crystals is also not taken into consideration [63-65]. We are not aware of any studies in which simultaneous nucleation of several phases with different crystal structure would have been analyzed, particularly, cases when the nonequilibrium phases are crystallized simultaneously with the equilibrium phase. A theory of simultaneous nucleation of crystalline phases in the indifferent equilibrium state or close to that is unavailable. At the same time, numerous cases of such phase formation are known [66-70]. Analysis of phase formation processes for such cases may substantially extend the scope of the nucleation theory. Another problem with the description of crystalline phase nucleation arises from their anisotropy, which is ignored in classical nucleation theories [6-10, 27, 48]. Furthermore, the nucleation of the crystalline phases in some cases may result in the formation of unusual nanostructures, e.g., phasoids [6-10, 27, 48], apparently, due to the crystal's anisotropy.

The purpose of this study is to analyze the role of the metastable clusters in the nucleation process during the formation of solids. The effect of the structural diversity, shape, size, and interaction behavior of these clusters on the nucleation mechanisms and formation of crystalline solids is considered.

2. Small clusters in liquid media

A large number of publications are devoted to the theoretical analysis of the feasibility of the stable existence of small clusters in disperse systems [75-79]. The discussion on this subject, which occurred in the second half of the 20th century in research groups headed by B.V. Deryagin and, alternatively, by A.I. Rusanov and P.A. Rebinder [80], resulted in the recognition of the theoretical substantiation for conclusions on the feasibility of the existence of small clusters of a size smaller than that of a critical nucleus [75-77, 81-85].

Many experimental studies also demonstrated the presence of solid-like clusters in liquids [87-90]. These nanosized clusters were revealed in water and aqueous solutions, metal melts, and inorganic compounds. The structural studies of the melts showed the crystal structure of the clusters [89, 90]. The number of small clusters in a liquid increases as the temperature approaches to the crystallization temperature (the melting temperature of the bulk phase). It should be noted that the formation of the small clusters with the ordered structure was also demonstrated by computer-aided experiments simulating the liquid-phase state of a substance [91].

Therefore, to date, the hypothesis for the presence of stable small (nanosized) clusters with the ordered structure can be deemed theoretically substantiated and experimentally corroborated. Using a thermodynamic analysis, the distribution of cluster sizes in a disperse system was determined in [84, 85]. Specifically, in [84], the following equation was derived for the distribution of cluster sizes in a single-component system:

$$\rho_{\{\nu\}} \approx K \nu^{1/2} \exp \left(a\nu - b\nu^{2/3} + c\nu^{1/3} \right), \quad (1)$$

where

$$K = \left(\frac{6}{\pi} \right)^{1/3} \cdot \rho_{\infty} \cdot \left(\frac{3}{5} kT \chi_{\infty} \right)^{-3/2};$$

$$a = \frac{(\mu - \mu_{\infty})}{kT};$$

$$b = 4\pi\sigma_{\infty} \frac{(4\pi\rho_{\infty}/3)^{-2/3}}{kT};$$

$$c = 8\pi\sigma_{\infty} \frac{(4\pi\rho_{\infty}/3)^{-1/3} ((\chi_{\infty}\sigma_{\infty}/3) + \delta)}{kT}.$$

Here, ν is the number of molecules; symbol $\{\nu\}$ denotes the corresponding set of molecules in the particle (cluster); ρ is the bulk concentration (quantities ρ , ν , and diameter D are interrelated through the relationship $\nu = \rho (\pi/6) D^3$); $\rho_{\{\nu\}}$ is the bulk concentration of particles (clusters) with the number of molecules in the particle (cluster) equal to $\{\nu\}$; μ is the chemical potential; χ is the isothermal compressibility; σ is the surface tension; ρ_{∞} , μ_{∞} , χ_{∞} , and σ_{∞} are, respectively, the bulk concentration, chemical potential, isothermal compressibility, and surface tension at the particle—vacuum interface at particle diameter $D \rightarrow \infty$; δ is some constant comparable in value with the thickness of the interphase layer; k is the Boltzmann constant, and (K) is the temperature.

Analysis of Eq. (1) shows that, according to the relationship between the values of the surface tension and bulk components of the free energy, different shapes of the curves plotting $\rho_{\{\nu\}}$ as a function of ν (Fig. 1) are possible. Curve 1 in Fig. 1 corresponds to the equilibrium state of the small clusters and curve 2 to their metastable state. The minimum in curve 2 corresponds to the size of the critical nucleus of a new phase. The absence of the metastable clusters in a system is potentially possible as well (curve 3). The presence or absence of the small metastable or equilibrium clusters depends on the relationship between quantities a , b , and c in Eq. (1).

In Eq. (1), an asymptotic equation describing the dependence of surface tension on the particle size for large particles is used [92-95]. Apparently, in this case, it would have been more correct to use the asymptotic equation for small particles proposed by A.I. Rusanov [62]. This equation can be represented as:

$$\sigma = \sigma_{\infty} \cdot \frac{D}{D_0}, \quad (2)$$

where D_0 is some constant. It should be noted that, in the region $D \approx D_0$, the surface tension is reduced to constant $\sigma = \sigma_{\infty}$ (Fig. 2). In this case, the dependence of the Gibbs energy on the particle size for a case similar to that depicted as curve 2 ($\rho_{\{\nu\}}$ vs. ν) looks as that plotted in Fig. 3.

In contrast to Eq. (1), which describes a version of the cluster formation neglecting the differences in the cluster structure, metastable clusters consisting of atoms (ions,

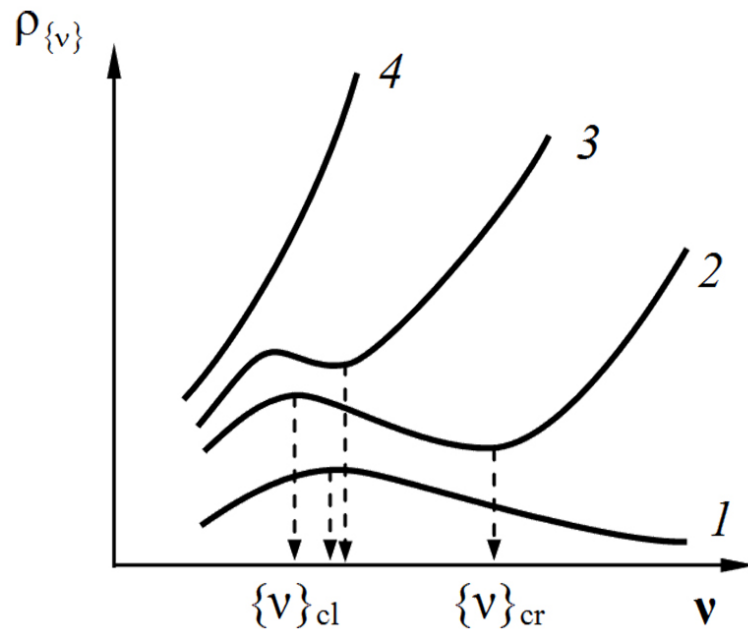


FIG. 1. Typical forms of the distribution of cluster sizes according to Eq.(1). $\{\nu\}_{cr}$ is the size of the critical nucleus of a new phase; $\{\nu\}_{cl}$ is the size of the equilibrium (curve 1) and metastable (curves 2, 3) cluster

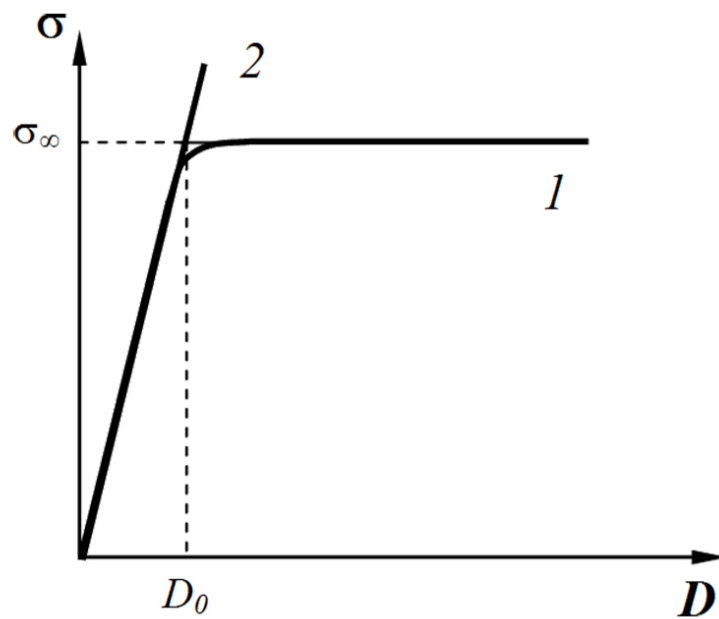


FIG. 2. Particle size (diameter) dependence of the particle surface tension

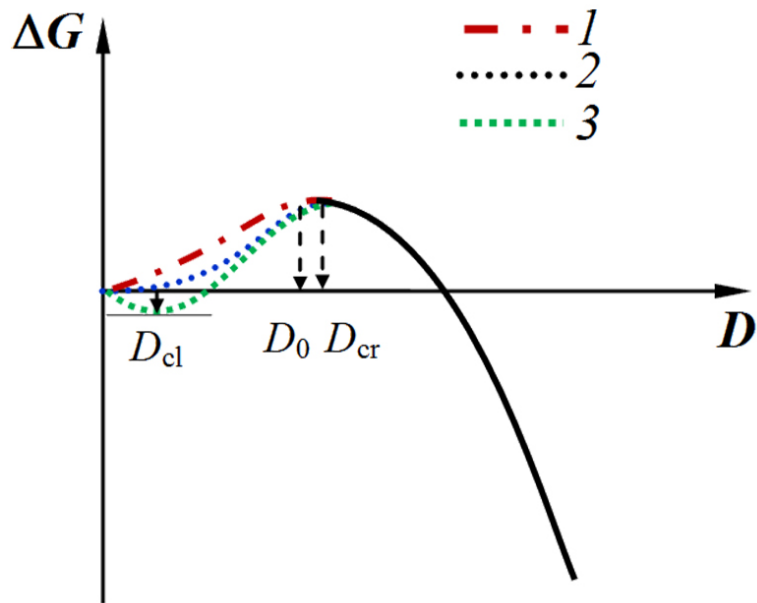


FIG. 3. Variation in the Gibbs energy during formation of the particles of a new phase of size D . Curve 1 corresponds to the case of $\sigma = \sigma_\infty$. Curve 2 corresponds to the dependence of the surface tension depicted in Fig. 2. Curve 3 illustrates the case when both the particle size dependence of the surface tension and the contribution of the Brownian motion to the stability of the small particles (clusters) in disperse systems are taken into account

molecules) of one type, but having different structure, may be formed in real systems. In some cases, the differences in the thermodynamic states of clusters with different structures may be so insignificant that their existence in the state close to the indifferent equilibrium may be anticipated. Such a version of the formation of small clusters can be graphically represented as a set of curves depicted in Fig. 4.

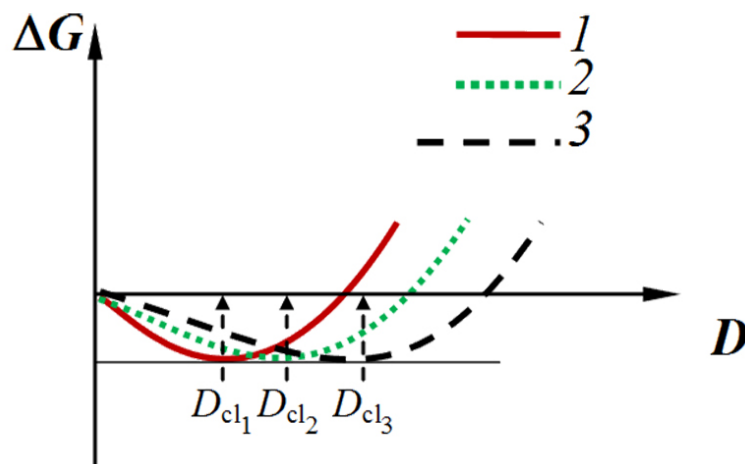


FIG. 4. Variation in the Gibbs energy during formation of small clusters of different structures (curves 1, 2, and 3) and sizes (D_{cl1} , D_{cl2} , and D_{cl3}) that occur in the state of indifferent equilibrium relative to one another

One of the types of such variance of the cluster structure arises from the anisotropy of the crystal structure; hence, from the anisotropy of the surface tension of clusters. To describe such structures in Eq. (1) in terms of thermodynamics, the surface tension and, probably, the chemical potential should be considered as tensor quantities rather than scalar ones. For example, if the surface tension of a crystal in a plane normal to some direction is significantly smaller than that in other planes, the predominant formation of crystalline clusters having a platelet shape could be anticipated. At the same time, the formation of clusters with some other crystal structure and/or other shape is also possible. It should be noted that a set of the metastable clusters in a medium consisting of particles of different types would be even more diverse. In this case, the diversity of the metastable cluster states, their Gibbs energies being insignificantly different, may be anticipated not only due to the difference in the cluster structure and shape, but also due to the difference in their composition.

Thus, the analysis of Eq. (1) proposed in [84] and made in this study for the case of formation of crystalline clusters with due account of their anisotropy, diversity of their structure and composition demonstrates that, under certain conditions, the stable state of a disperse system containing small crystalline clusters of various compositions, structures, shapes, and sizes is feasible. The clusters under consideration are sized smaller than critical nuclei and may take part as building blocks in the processes of homogeneous nucleation. Furthermore, these clusters, existing in a medium initially treated as a homogeneous medium, may become the nucleation centers if the phase formation process is considered within the heterogeneous nucleation process. This inference implies a certain conditionality in classification of the nucleation processes as homogeneous and heterogeneous nucleations. This conditionality arises from the fact that the media initially treated as homogeneous are actually nanoheterogeneous media due to formation of clusters. Accordingly, the classification of the nucleation mechanisms as homogeneous and heterogeneous nucleations is primarily governed by the interaction of the building blocks that form stable nuclei of a new phase rather than by the presence of impurity phases in the initial system.

3. Aggregation of metastable clusters and formation of critical nuclei

As pointed out in the previous section, theoretical study and analysis of experimental data indicate that melts, irrespective of their chemical composition, may contain small (nanosized) crystalline clusters. The composition and thermodynamic parameters of the melt specify the chemical composition, structure, size, and shape of small clusters [84-91]. The combined existence of clusters of various compositions, structures, shapes, and sizes is potentially possible in the initial phase.

The composition, structure, shape, and size of the clusters may essentially govern the nature of the nucleation process. The formation of a new phase will be also strongly affected by the diversity of small clusters in respect of their composition, structure, shape, size, and mutual orientation. The relationship of the above-listed parameters for stable small clusters in the initial phase and corresponding parameters of the critical nuclei of the formed new phase is also important for the occurrence of an appropriate nucleation mechanism. By way of example, schematic diagrams for the formation of new-phase nuclei from stable clusters existing in the initial phase is shown Fig. 5. The majority of these schematic diagrams illustrate the aggregative mechanism for the formation of critical new-phase nuclei. In the aggregative nucleation mechanism, the clusters, when aggregating, form the critical new-phase nucleus, take part as the main building blocks. Because of the large size of the building blocks, this mechanism provides a potentially higher nucleation rate than

in the case of critical nucleus growth due the transfer of atoms, ions, and molecules to the nucleation center. Under certain conditions, the critical nucleus may be formed as shown in Fig. 5b even when only two crystalline clusters come in contact with one another.

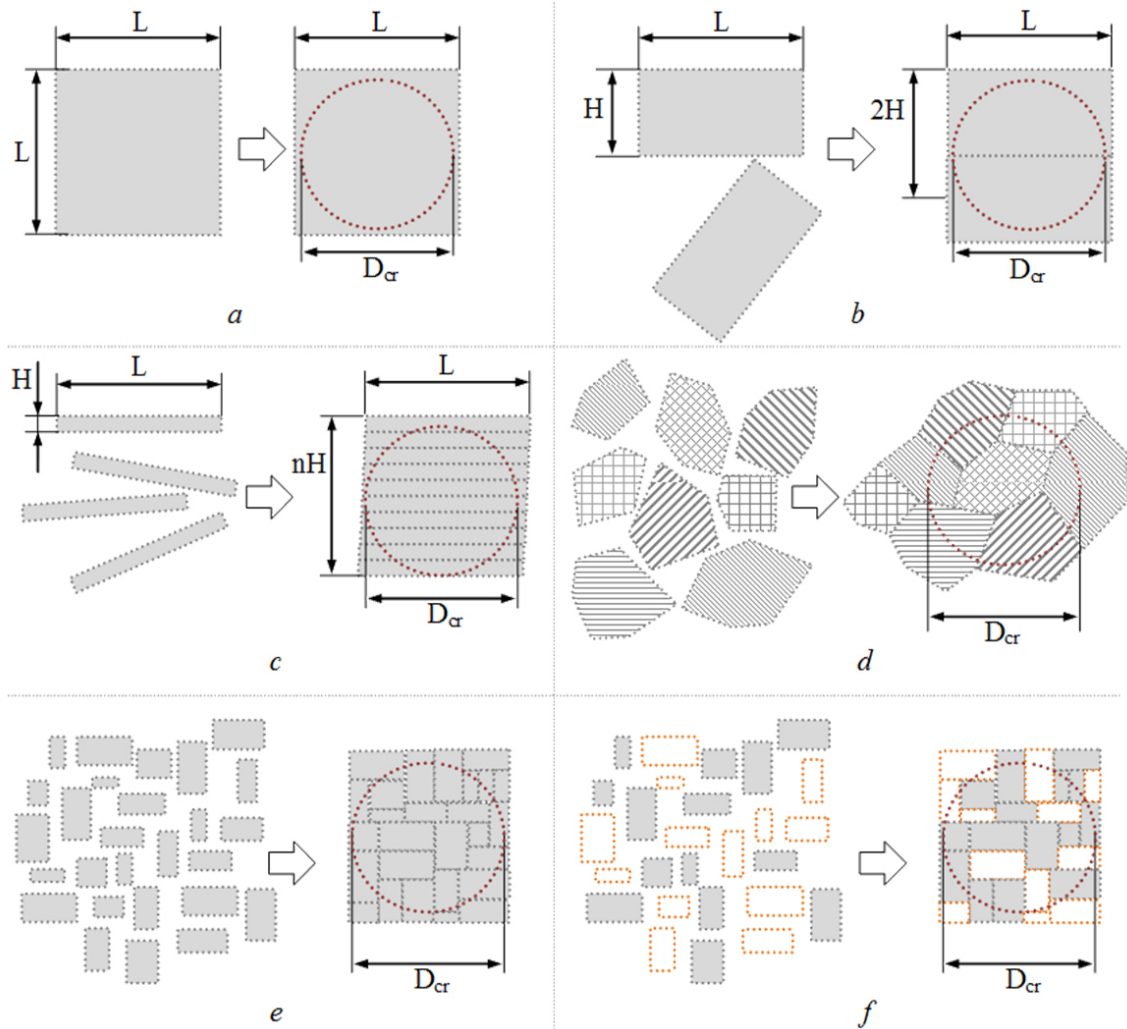


FIG. 5. Schematic diagrams of the aggregative nucleation. In the left insert, a–f, the clusters in the initial phase are schematically depicted. In the right insert, the particles of a new phase formed by the aggregation of the clusters are schematically depicted; the sizes of the critical nuclei of a new phase are denoted by the dashed lines

The formation of the critical nucleus from a single nanocluster is a special case. The scheme of such nucleation depicted in Fig. 5a is applicable to comparable sizes of the crystalline cluster in the initial phase and the new-phase critical nucleus. This size ratio is possible, for example, at certain temperatures of the initial and formed phases (Fig. 1, curves 1, 3). In addition, this nucleation scheme is applicable and subject to the high rate of the temperature variation that provides the size retention of the metastable cluster up to the instant of its steady growth in the nucleation process.

In the case when, due to anisotropy, the crystalline clusters are shaped as thin plates of thickness H and width L , which are comparable in size with the critical nucleus of a new phase, $D \approx L$, the nucleation process can be represented according to the schematic diagram

depicted in Fig. 5c. Such a nucleation mechanism apparently takes place during formation of zirconium dioxide nanocrystals under hydrothermal conditions, as was shown in [69, 70, 96].

Another nucleation case allowing for a specific feature of the crystalline cluster structure in the initial phase is the nucleation of a solid involving the clusters with the different structures in the stable state in the initial phase (Fig. 4). The aggregation of the clusters with different structures, resulting in the formation of particles of the size larger than that of the heterogeneous critical nucleus [53, 54], makes the particles steadily grow. The further steady growth of these particles may proceed either by the Ostwald ripening mechanism [97] with the deposition of molecules (atoms, ions) on the particles or by the aggregative mechanism described in [98-101]. It should be noted that the existence of the solid particles consisting of fragments with different structures was revealed long ago [102, 103]. The aggregative nucleation mechanism allows one to understand the causes and process for the formation of such particles and phasoid-like structures [71]. The mechanism of aggregation of the differently structured clusters is presented in Figs. 5d,e.

Allowing for the fact that clusters not only have different morphology and structure, but also different composition, may exist in the initial multicomponent phases, it can be stated that much more diverse formed structures may be observed in such media during phase formation (see Figs. 5e,f). For example, not only the eutectic crystallization, but also the aforementioned formation of phasoid-like structures, are possible in such media [71].

4. Conclusions

The analysis made here has demonstrated feasible nucleation in condensed media by the mechanism of aggregation of the metastable small crystalline clusters. The feasibility and conditions for the implementation of this mechanism depend on the relationship of the structure, shape and size of the small clusters in the initial phase and the corresponding parameters of the critical nucleus of the phase being formed. The presence of small stable clusters in the initial phases makes the homogeneous and heterogeneous nucleation processes more similar.

The feasibility for the formation of solids with the nano-inhomogeneous composition and structure due to the structural and compositional inhomogeneity of the small clusters that stably exist in the initial phase has been demonstrated.

Acknowledgments

This work was supported by Russian Foundation for Basic Research (grant No 13-03-00888).

References

- [1] Wilson C.T.R. Condensation of water vapour in the presence of dust-free air and other gases. *Phil. Trans. R. Soc. Lond. A*, **189**, P. 256–307 (1897).
- [2] Tammann G. Über die abhängigkeit der zahl der kerne, welche sich in verschiedenen unterkühlten flüssigkeiten bilden, von der temperature. *Zeit. f. Physik. Chemie*, **25**, P. 441 (1898).
- [3] Wilson C.T.R. On the condensation nuclei produced in gases by the action of Rontgen rays, uranium rays, ultra-violet light, and other agents. *Phil. Trans. R. Soc. Lond. A*, **192**, P. 403–453 (1899).
- [4] Wilson C.T.R. On the comparative efficiency as condensation nuclei of positively and negatively charged ions. *Phil. Trans. R. Soc. Lond. A*, **93**, P. 289–308 (1900).
- [5] Tammann G. *Aggregatzustände*. Verlag von Leopold Voss, Leipzig, 237 p. (1922).
- [6] Volmer M., Weber A. Keimbildung in übersättigten gebilden. *Z. Phys. Chem.*, **119**, P. 277 (1926).
- [7] Becker R., Döring W. Kinetische behandlung der keimbildung in übersättigten dämpfen. *Ann. Phys.*, **416**(8), P. 719–752 (1935).

- [8] Volmer M. *Kinetik der Phasenbildung*. Steinkopff, Dresden-Leipzig (1939).
- [9] Frenkel J. A general theory of heterophase fluctuations and pretransition phenomena. *J. Chem. Phys.*, **7**(7), P. 538–546 (1939).
- [10] Zel'dovch Ya. On the theory of new phase formation. *Cavitation. ZhETF*, **12**(11/12), P. 525–538 (1942), (in Russian).
- [11] Pound G.M., La Mer V.K. Kinetics of crystalline nucleus formation in supercooled liquid tin. *J. Amer. Chem. Soc.*, **74**, P. 2323 (1952).
- [12] Hillert M. A. *Theory of nucleation for solid metallic solutions*. Sc. D. Thesis, MIT (1955).
- [13] Cahn J.W., Hilliard J.E. Free energy of a nonuniform system. III. Nucleation in a two-component incompressible fluid. *J. Chem. Phys.*, **31**(3), P. 688–700 (1959).
- [14] Courtney W.G. Remarks on homogeneous nucleation. *J. Chem. Phys.*, **35**(6), P. 2249 (1961).
- [15] Lothe J., Pound G.M. Reconsideration of nucleation theory. *J. Chem. Phys.*, **36**(8), P. 2080–2085 (1962).
- [16] Reiss H., Katz J.L. Resolution of the translation-rotation paradox in the theory of irreversible condensation. *J. Chem. Phys.*, **46**(7), P. 2496–2499 (1962).
- [17] Flettcher N.H. *The physics of rainclouds*. University Press, Cambridge (1962).
- [18] Reiss H., Katz J.L., Cohen E.R. Translation-rotation paradox in the theory of nucleation. *J. Chem. Phys.*, **48**(12), P. 5553–5560 (1968).
- [19] Lothe J. Concentration of clusters in nucleation and the classical phase integral. *J. Chem. Phys.*, **48**(4), P. 1849–1852 (1968).
- [20] Abraham F.F. Re-examination of homogeneous nucleation theory: statistical thermodynamics aspects. *J. Chem. Phys.*, **48**(2), P. 732–740 (1968).
- [21] Lin J. Equilibrium distribution of droplets in the theory of nucleation. *J. Chem. Phys.*, **48**(9), P. 4128–4130 (1968).
- [22] Stillinger F.H. Comment on the translation-rotation paradox in the theory of irreversible condensation. *J. Chem. Phys.*, **48**(3), P. 1430–1431 (1968).
- [23] Kuni F.M., Rusanov A.I. The homogeneous nucleation theory and the fluctuation of the center of mass of a drop. *Phys. Letters.*, **29A**(6), P. 337–338 (1969).
- [24] Wood G.R., Walton A.G. Homogeneous nucleation kinetics of ice from water. *J. Appl. Phys.*, **41**(7), P. 3027–3036 (1970).
- [25] Reiss H. Treatment of droplike clusters by means of the classical phase integral in nucleation theory. *J. Stat. Phys.*, **2**(1), P. 83–104 (1970).
- [26] Blander M., Katz J.L. The thermodynamics of cluster formation in nucleation theory. *J. Stat. Phys.*, **4**(1), P. 55–59 (1972).
- [27] Abraham F.F. *Homogeneous nucleation theory*. Academic Press, NY, (1974).
- [28] Bendig L.L., Larson M.A. Nuclei generation from repetitive contacting. *AIChE Symposium Series*, **25**, P. 57 (1976).
- [29] Katz J.L. Nucleation theory without Maxwell Demons. *J. Coll. Interface Sci.*, **61**(2), P. 351–355 (1977).
- [30] Khambaty S., Larson M.A. Crystal regeneration and growth of small crystals in contact nucleation. *I&EC Fundamentals*, **17**, P. 160 (1978).
- [31] Katz J.L., Donohue M.D. A kinetic approach to homogeneous nucleation theory. *Adv. Chem. Phys.*, **40**, P. 137 (1979).
- [32] Slezov V.V., Sagalovich V.V. Diffusive decomposition of solid solutions. *Sov. Phys. Usp.*, **30**(1), P. 23–45 (1987).
- [33] Garnier J.P., Mirabel P., Rabeony H. Experimental results of homogeneous nucleation of supersaturated vapors, *J. Chem. Phys.*, **79**(4), P. 2097–2098 (1983).
- [34] Ruth V., Hirth J.P., Pound G.M. On the theory of homogeneous nucleation and spinodal decomposition in condensation from the vapor phase. *J. Chem. Phys.*, **88**(11), P. 7079 (1988).
- [35] Larson M.A. Solute clustering and secondary nucleation. Conference on Advances in Industrial Crystallization. 1990, College of Engineering Iowa State University, Preprint 91130.
- [36] Girshick S.L., Chiu C.P. Kinetic nucleation theory: A new expression for the rate of homogeneous nucleation from an ideal supersaturated vapor. *J. Chem. Phys.*, **93**(2), P. 1273–1278 (1990).
- [37] Zeng X.C., Oxtoby D.W. Gas-liquid nucleation in Lennard-Jones fluids. *J. Chem. Phys.*, **94**(8), P. 4472–4478 (1991).
- [38] Cahn R.W., Haasen P. Kramer E.J. *Materials Science and technology*, 5 (Phase transformation in materials), VCH (1991).

- [39] Brener E.A., Marchenko V.I., Formation of nucleation centers in a crystal. *JETP Lett.*, **56**(7), P. 368–372 (1992).
- [40] Adachi M., Okuyama K., Seinfeld J.H. Experimental studies of ion-induced nucleation. *J. Aerosol. Sci.*, **23**(4), P. 327–337 (1992).
- [41] Girshick S.L. Comment on: “Self-consistency correction to homogeneous nucleation theory”. *J. Chem. Phys.*, **94**(1), P. 826–828 (1991).
- [42] Olemskoi A.I., Koplyk I.V. The theory of spatiotemporal evolution of nonequilibrium thermodynamic systems. *Phys. Usp.*, **38**(10), P. 1061–1097 (1995).
- [43] Oxtoby D.W. Nucleation of first-order phase transitions. *Acc. Chem. Res.*, **31**(2), P. 91–97 (1998).
- [44] Antonov N.M., Popov I.Yu., Gusarov V.V. Model of spinodal decomposition of phases under hyperbolic diffusion. *Phys. Solid State.*, **41**(5), P. 824–826 (1999).
- [45] Gorbachev Yu.E., Nikitin I.S. Evolution of cluster size distribution during nucleation with rapidly changing dynamic gas processes. *Tech. Phys.*, **45**(12), P. 1538–1548 (2000).
- [46] Yau S.-T., Vekilov P.G. Quasi-planar nucleus structure in apoferritin crystallization. *Nature*, **406**, P. 494–497 (2000).
- [47] Oxtoby D.W. Phase transitions: Catching crystals at birth. *Nature*, **406**, P. 464–465 (2000).
- [48] Kuni F.M., Shchekin A.K., Grinin A.P. Theory of heterogeneous nucleation for vapor undergoing a gradual metastable state formation. *Phys. Usp.*, **44**(4), P. 331–370 (2001).
- [49] Radhakrishnan R., Trout B.L. A new approach for studying nucleation phenomena using molecular simulations: application to CO₂ hydrate clathrates. *J. Chem. Phys.*, **117**(4), P. 1786–1796 (2002).
- [50] Auer S., Frenzel D. Numerical predication of absolute crystallization rates in hard-sphere colloids. *J. Chem. Phys.*, **120**(6), P. 3015–3029 (2004).
- [51] Xu D., Johnson W.L. Geometric model for the critical-value problem of nucleation phenomena containing the size effect of nucleating agent. *Phys. Rev. B.*, **72**, P. 052101 (2005).
- [52] Bushuev Yu.G., Davletbaeva S.V. Molecular dynamics simulation of the kinetics of nucleation of supercooled NaCl melt clusters. *Russ. J. Phys. Chem. A*, **83**(4), P. 630–636 (2009).
- [53] Al'myashev O.V., Gusarov V.V. Features of the phase formation in the nanocomposites. *Russ. J. Gen. Chem.*, **80**(3), P. 385–390 (2010).
- [54] Al'myasheva O.V., Gusarov V.V. Nucleation in media in which nanoparticles of another phase are distributed. *Dokl. Phys. Chem.*, **424**(2), P. 43–45 (2009).
- [55] Fedoseev V.B., Fedoseeva E.N. Size effects during phase transformations in stratifying systems. *Russ. J. Phys. Chem. A*, **88**(3), P. 436–441 (2014).
- [56] Fedoseev V.B., Fedoseeva E.N. State supersaturated solution in systems of limited size. *JETP Lett.*, **97**(7), P. 408 (2013).
- [57] Ebeling W., Engel A., Feistel R. *Physik der Evolutionsprozesse*. Akademie-Verlag, Berlin, 371 p (1990).
- [58] Prigogine I. *From Being to Becoming*. Nauka, Moscow (1985). (in Russian)
- [59] Klimontovich Yu.L. *Statistical theory of open systems* V.1. Yanus, Moscow (1995). (in Russian)
- [60] Klimontovich Yu.L. Relative ordering criteria in open systems. *Phys. Usp.*, **39**(11), P. 1169–1179 (1996).
- [61] Rusanov A.I. *Thermodynamics of surface phenomena*. Leningrad University, Leningrad (1960). (in Russian)
- [62] Rusanov A.I. Phase equilibria and surface phenomena. Khimiya, Leningrad (1967). (in Russian); German edition; Rusanov A.I. Phasengleichgewichte und Grenzflächenerscheinungen. Akademie-Verlag, Berlin (1978).
- [63] Rusanov A.I. *Thermodynamic fundamentals of mechanochemistry*. Nauka, Saint-Petersburg, 221 p. (2006). (in Russian)
- [64] Grinfeld M.A. *Methods of continuum mechanics in theory of phase transformations*. Nauka, Moscow (1990). (in Russian)
- [65] Gusarov V.V. Statics and dynamics of systems based on polycrystalline refractory oxides. Sc. D. Thesis, St. Petersburg State Technological Institute (Technical University), St. Petersburg (1996). (in Russian)
- [66] Lomanova N.A., Gusarov V.V. Influence of synthesis temperature on BiFeO₃ nanoparticles formation. *Nanosystems: physics, chemistry, mathematics*, **4**(5), P. 696–705 (2013).
- [67] Lomanova N.A., Gusarov V.V. Effect of surface melting on the formation and growth of nanocrystals in the Bi₂O₃-Fe₂O₃ system. *Russ. J. Gen. Chem.*, **83**(12), P. 2251–2253 (2013).
- [68] Lomanova N.A., Gusarov V.V. Effect of the phase composition of the starting mixture on the formation of the layered perovskite-like compound Bi₇Fe₃Ti₃O₂₁. *Russ. J. Inorg. Chem.*, **55**(10), P. 1541–1545 (2010).

- [69] Pozhidaeva O.V., Korytkova E.N., Romanov D.P., Gusarov V.V. Formation of ZrO_2 nanocrystals in hydrothermal media of various chemical compositions. *Russ. J. Gen. Chem.*, **72**(6), P. 849–853 (2002).
- [70] Pozhidaeva O.V., Korytkova E.N., Drozdova I.A., Gusarov V.V. Phase state and particle size of ultradispersed zirconium dioxide as influenced by conditions of hydrothermal synthesis. *Russ. J. Gen. Chem.*, **69**(8), P. 1219–1222 (1999).
- [71] Rao C. N. R., Raveau B. *Transition metal oxides: structure, properties, and synthesis of ceramic oxides*. Wiley, NY, 392 p. (1998).
- [72] Svensson G. HREM Studies of intergrowth between NbO and perovskite in the Ba-, Sr and K-Nb-O systems. *Microsc. Microanal. Microstruct.*, **1**(5-6), P. 343–356 (1990).
- [73] Magnéli A. On heterogeneous crystalline compounds and the phasoid concept. *Microsc. Microanal. Microstruct.*, **1**(5-6), P. 299–302 (1990).
- [74] Bernuy-Lopez C., Pelloquin D., Raveau B., Allix M., Claridgea J.B., Rosseinskya M. J., Wangc P., Blelochc A. Phasoid intergrowth between the double perovskite Sr_2MgMoO_6 and the n=2 R-P phase $Sr_3Mo_2O_7$. *Solid State Ionics*, **181**(19-20), P. 889–893 (2010).
- [75] Rusanov A.I., Shchukin E.D. Rebinder P.A. On the theory of dispersion. I. Thermodynamics of monodisperse systems. *Colloid J. USSR*, **30**(5), P. 428 (1968). (in Russian)
- [76] Rusanov A.I., Kuni F.M., Shchukin E.D. Rebinder P.A. On the theory of dispersion. 3. Dispersion in liquid medium. *Colloid J. USSR*, **30**(5), P. 561 (1968). (in Russian)
- [77] Rebinder P.A., Shchukin E.D. Surface phenomena in solids during the course of their deformation and failure. *Sov. Phys. Usp.*, **15**(5), P. 533 (1973).
- [78] Shchukin E.D., Pertsov A.V. Thermodynamic criterion of spontaneous dispersion. Colloid and interface science series. V. 1. Colloid stability: The role of surface forces. Part 1. Wiley, NY (2007). P. 23.
- [79] Samsonov V.M., Murav'ev S.D., Bazulev A.N. Surface characteristics, structure and stability of nano-sized particles. *Russ. J. Phys. Chem. A*, **74**(11), P. 1791–1795 (2000).
- [80] <http://www.chem.msu.su/rus/history/Rebinder/17.html>
- [81] Rebinder P.A. Formation and aggregative stability of disperse systems. *Colloid J. USSR*, **20**(5), P. 493–502 (1958).
- [82] Shchukin E.D., Rebinder P.A. The formation of new surfaces at deformation and destruction of a rigid body in a surface-active medium. *Koll. Zh.*, **20**(5), P. 645–654 (1958).
- [83] Kligman F.I., Rusanov A.I. On the thermodynamic equilibrium states of disperse systems with solid particles. *Koll. Zh.*, **39**(1), P. 44–47 (1977). (in Russian)
- [84] Kuni F.M., Rusanov A.I. Statistical theory of aggregative equilibrium. *Theor. Math. Phys*, **2**(2), P. 192–206 (1970).
- [85] Rusanov A.I. On thermodynamic conditions of spontaneous dispergation of solids. *Vestn. Leningr. Univ.*, **10**, P. 38–49 (1983). (in Russian)
- [86] Rusanov A.I. Thermodynamics of solid surface. *Surf. Sci. Rep.*, **23**, P. 173–247 (1996).
- [87] Ubbelode A. R. *The Molten State of Matter*. London University, London, 384 p. (1978).
- [88] Denisov V.M., Belousova N.V., Istomin S.A., Bahvalov S.G., Pastukhov E.A. *Structure and properties of molten oxides*. Ural Division of RAS, Ekateriburg (1999). (in Russian)
- [89] Vatolin N.A., Pastukhov E.A. *Diffraction studies of high-temperature melts*. Nauka, Moscow, 188 p. (1980). (in Russian)
- [90] Vatolin N.A., Kern E.M., Lisin V.L. *X-ray diffraction study of the structure of silicate melts. Structure and physical-chemical properties of metal and oxide melts*. Sverdlovsk, P. 38–56 (1986). (in Russian)
- [91] Polukhin V.A. *Nanostructure and precursor modeling*. Ural Division of RAS, Ekateriburg, 208 p. (1999). (in Russian)
- [92] Tolman R.C. The effect of droplet size on surface tension. *J. Chem. Phys.*, **17**(3), P. 333 (1949).
- [93] Bykov T.V., Shchekin A.K. Surface tension, Tolman length, and effective rigidity constant in the surface layer of a drop with a large radius of curvature. *Inorg. Mater.*, **35**(6), P. 641–644 (1999).
- [94] Magomedov M. N. Dependence of the surface energy on the size and shape of a nanocrystal. *Phys. Solid State*, **46**(5), P. 954–968 (2004).
- [95] Rekhviashvili S.Sh., Kishtikova E.V. On the size dependence of the surface tension. *Techn. Phys.*, **56**(1), P. 143–146 (2011).
- [96] Sharikov F.Yu., Almjasheva O.V., Gusarov V.V. Thermal analysis of formation of ZrO_2 nanoparticles under hydrothermal conditions. *Russ. J. Inorg. Chem.*, **51**(10), P. 1538–1542 (2006).
- [97] Ostwald W. Ober die vermeintliche Isomerie des roten und gelben Quecksilberoxyds und die Oberflächenspannung fester. *Z. Phys. Chem. Stoechiom. Verwandtschaftsl.*, **34**, P. 495–503 (1900).

- [98] Penn R.L., Banfield J.F. Morphology development and crystal growth in nanocrystalline aggregates under hydrothermal conditions: insights from titania. *Geochimica et Cosmochimica Acta*, **63**(10), P. 1549–1557 (1999).
- [99] Banfield J.F., Veblen D.R. Conversion of perovskite to anatase and TiO₂ (B): A TEM study and the use of fundamental building blocks for understanding relationships among the TiO₂ minerals. *Am. Mineralogist*, **77**, P. 545–557 (1992).
- [100] Penn R.L., Banfield J.F. Oriented attachment and growth, twinning, polytypism, and formation of metastable phases: Insights from nanocrystalline TiO₂. *Am. Mineralogist*, **83**, P. 1077–1082 (1998).
- [101] Penn R.L., Banfield J.F. Imperfect Oriented Attachment: Dislocation Generation in Defect-Free Nanocrystals. *Science*, **281**(5379), P. 969–971 (1998).
- [102] Mitsuhashi T., Ichihara M., Tatsuke U. Characterization and Stabilization of Metastable Tetragonal ZrO₂. *J. Am. Ceram. Soc.*, **57**(2), P. 97–101 (1974).
- [103] Chaim R., Heuer A.H., Brandon D.G. Phase equilibration in ZrO₂-Y₂O₃ alloys by liquid film migration. *J. Am. Ceram. Soc.*, **69**(3), P. 243–248 (1986).

GaAs THERMAL OXIDATION ACTIVATED BY THE COACTION OF P-BLOCK OXIDES

I. Ya. Mittova, V. F. Kostryukov

Voronezh State University, Universitetskaya pl. 1, Voronezh, 394893 Russia
vc@chem.vsu.ru

PACS 81.05.Ea

This study summarizes the results for the investigation of the process of gallium arsenide thermal oxidation processes activated by the coaction of the oxides in $\text{Sb}_2\text{O}_3+\text{Bi}_2\text{O}_3$, $\text{Sb}_2\text{O}_3+\text{PbO}$ and $\text{PbO}+\text{Bi}_2\text{O}_3$ binary compositions was studied. The analysis of the character and nature of nonlinear effect of various compositions of chemostimulators on the GaAs-supported oxide layer thickness grown on the GaAs surface was performed. It is shown that the actual oxide layer thickness is different from the additive value. The main patterns of the impact for binary compositions of p-element oxides of p-elements on thermal oxidation of gallium arsenide determined by physico-chemical nature of chemostimulators, the nature of their interaction and the method of administration in the system were described.

Keywords: semiconductors, gallium arsenide, thin films, thermal oxidation, nonlinear effects.

Received: 16 March 2014

Revised: 16 April 2014

1. Introduction

Good quality of function layers and improvement of properties of the semiconductor/film and film/ambient boundaries are one of the main objectives in forming heterostructures with the set properties in A^{III}B^V . This is particularly relevant to the binary semiconductors with the volatile GaAs, which have a tendency towards both material and oxide degradation at high temperatures. The nature of the process itself does not allow for good heterostructures formed by the GaAs oxidation, as the parallel oxidation stages are interrelated by the reaction $\text{As}_2\text{O}_3 + \text{Ga} \Rightarrow \text{Ga}_2\text{O}_3 + \text{As}$ [1]. This results in arsenic segregation on the inner boundary, which leads to its degradation. The growing film consists mainly of Ga_2O_3 acting as a semiconductor, and the semiconductor/insulator heterostructure can barely be formed. Therefore, we can define the said reaction as a ‘negative feedback channel’ between the GaAs oxidation process steps that is determined by thermodynamics.

Applying the present technological solutions of the problem, it is not possible to predict and control these properties. Usually, only one property of the structure is improved (e.g. surface-charge density) and the others remain at a level typical of the oxide layer [2–4]. Furthermore, they are all complicated in practice and can be extremely toxic (e.g., oxidation with the arsenic oxide vapor back pressure, [5]).

Chemostimulated thermal oxidation of semiconductors is one of the solutions to this problem [1]. The suggested approach is based on the idea of the kinetic locking of the ‘negative feedback’, enhanced by engaging the oxidized semiconductor components in new fast processes with the chemostimulator compositions, i.e. creating ‘positive feedback’ that enable faster building-up of the target product and modification of its properties. When the chemostimulators are introduced into the reaction zone through the vapor phase (by evaporation), their impact — providing that oxygen can be thermodynamically transferred to the substrate components — is

determined by the pressure and composition of the vapor that determines the surface active particles concentration. After the oxygen transfer act, the chemostimulator element is oxidized once again and then continues transferring the oxygen to the substrate components. This chemostimulated semiconductor oxidation process was called redox transit interaction [1]. When the chemostimulator regeneration is complete (the process turns cyclic), it becoming similar to the catalysis [6].

Therefore, the introduction of chemostimulators in GaAs oxidation provides for the new multichannel process with the kinetically conjugated, and adjoint catalytic stages, determined by the chemostimulators and their transformation products, and forming positive feedback between the semiconductor oxidation stages. One chemostimulator may contain two or more active components. Then, the process branches and, as a result, the chemostimulating activity in general increases. The process, however, becomes difficult to control.

When two chemostimulator compositions are used simultaneously, it allows us to manipulate the components of the oxide films growing on the GaAs surface and their properties by regulating the composition components and their quantity.

The purpose of this work was to review and analyze of the main results of the GaAs thermal oxidation process pattern stimulated by the p-block oxide compositions and interpretation of the nonlinear effects of combined effects of chemostimulators.

2. Experimental

We used a polished single-crystal (111)-oriented Sn-doped GaAs wafers (SAGOCh-1 brand). The carrier density was $1.5 \cdot 10^{18} - 2.5 \cdot 10^{18} \text{ cm}^{-3}$; resistivity — $0.010 - 0.018 \text{ } \Omega \cdot \text{cm}$. The working side of the semiconductor wafer was the ‘gallic’ side. Side A (the gallic one) had numerous etch pits, while there were no such pits on side B (the arsenic one). Immediately before the oxidation process, the samples were put into 49% HF for 10 min., and rinsed with doubly distilled water. Variable binary compositions of antimony (III), bismuth (III) and lead (II) (puriss. p.a.) in increments of 10 mol% were used as chemostimulators. The composition-stimulated GaAs oxidation stimulated by the compositions was carried out in a horizontal quartz reactor (d 30mm) of the MTP-2M-50-500 furnace at $530 \text{ } ^\circ\text{C}$ for 10 – 40 min. The distance from the oxides surface to the working side of the sample was the same all the time (10 mm). The flowing oxygen speed was 30 l/h. The temperature stability ($\pm 1 \text{ } ^\circ\text{C}$) in the reactor was ensured by the TRM-10 sensor unit. A new composition of chemostimulator oxides was prepared for each experiment. The thickness of oxide films was measured each 10 min. using an LEF-754 ($\lambda = 632.8 \text{ nm}$) laser ellipsometer with an accuracy of $\pm 2 \text{ nm}$.

Chemical transformations occurring during GaAs thermal oxidation in the oxides used and their compositions were analyzed by X-ray powder diffractometer DRON-4 (Co K_α -radiation, $\lambda = 1.79021 \text{ } \text{Å}$). The composition of the oxide films grown on GaAs surface was determined by IR spectroscopy (IKS, Infralyum FT-02, UR-10), X-ray fluorescence analysis (XRF, VRA-30, Carl Zeiss Yena), electron probe X-ray microanalysis (EPXMA, CamScan), and ultrasoft X-ray emission spectroscopy (USXES, C-500). The composition of vapor from the chemostimulators’ mixture evaporation was studied using mass spectrometry (MS-1301) and Knudsen effusion method.

3. Results and discussion

To determine the difference between the separate and mixture chemostimulator effects, the thickness of the oxide film was plotted as functions of the composition components in Fig. 1. From the plots, we may infer that the nonlinear effect changed qualitatively with the chemostimulator composition and its nature. For the chemostimulator system $\text{Sb}_2\text{O}_3 + \text{Bi}_2\text{O}_3$,

a negative anomaly was observed over the entire range of compositions, i.e. the oxides in the composition act like inhibitors. In the presence of the lead oxide, anomalies are of variable sign. The anomaly type, however, varies, depending on the second element introduced. The composition $\text{Bi}_2\text{O}_3 + \text{PbO}$ acts like inhibitor (similar to $\text{Sb}_2\text{O}_3 + \text{Bi}_2\text{O}_3$ system). The composition of $\text{PbO} + \text{Bi}_2\text{O}_3$, on the contrary, stimulates the latter and enhances its effectiveness. In $\text{PbO} + \text{Sb}_2\text{O}_3$, the chemostimulators act completely differently: Sb_2O_3 results in the non additive increase in the oxide layer thickness on the GaAs surface, while $\text{PbO} + \text{Sb}_2\text{O}_3$ inhibits the chemostimulating effect, which was expected, considering their individual chemostimulating effect [7–9].

The observed nonlinear effects develop appropriately as the process continues. For the composition $\text{Sb}_2\text{O}_3 + \text{Bi}_2\text{O}_3$ composition, the negative anomaly increases in absolute magnitude, with the minimum value almost fixed on the composition axis at ~ 40 mol.%. Bi_2O_3 , within any oxidation process length. In the other two chemostimulator compositions, the negative anomaly increases both in magnitude and in composition, depending on the oxidation process length. Hence, for a larger range of compositions, the mutual inhibition becomes greater with time. The positive anomaly in such compositions, however, is qualitatively different. For the composition $\text{PbO} + \text{Sb}_2\text{O}_3$ mixture, it decreases both in magnitude and in the composition range. When GaAs oxidation is activated by $\text{PbO} + \text{Bi}_2\text{O}_3$, it decreases only in the composition range, while the maximum positive anomaly increases in magnitude.

Hence, introduction of a more active chemostimulator results in nonlinear acceleration of the process, while introduction of a less active oxide — in inhibition as compared to the additive value. The more the chemostimulators differ, the greater the mutual effect. Bismuth oxide, being the least effective, inhibits both PbO and Sb_2O_3 , especially the latter. Lead oxide, having medium effectiveness, inhibits Sb_2O_3 , but stimulates Bi_2O_3 effect. However, the most active Sb_2O_3 in composition with Bi_2O_3 does not enhance the process and the film thickness on the GaAs surface stays practically unchanged (see Fig. 1a), which can be seen as inhibiting effect in relation to the additive effect.

Nonadditivity of the antimony, lead and bismuth oxide compositions impact on the gallium arsenide thermal oxidation demonstrates, therefore, the mutual influence of the chemostimulators.

To define the process of chemostimulator coactions, we have studied the composition of the obtained films (**USXES, IR spectra**) and the phase composition alterations of the chemostimulators annealed in an oxygen atmosphere at 530°C for 40 min. (**X-ray powder diffraction**). The composition was determined according to the concentration function extreme points of the films thickness dependencies.

The composition analysis data of the layers obtained by **USXES** is presented in Table 1. We did not study the films for oxygen presence. X-rays penetration was 40 nm. The method showed that the main film component is gallium (as the oxide). After gallium comes arsenic (also as the oxide) with 10 at %. The films obtained using compositions with lead oxide, contain small amounts of lead. The lower the lead oxide content there is in compositions with antimony oxides and bismuth oxides, the less lead there is in the obtained film obtained. However, there were no traces found of either of antimony or bismuth (for the respective compositions) in the films as studied by this method.

The **USXES** method does not allow us to detect either the presence or absence of antimony in the films. The IR spectra analysis showed that the main component of the films is gallium oxide. In the films obtained using the chemostimulator compositions with antimony and bismuth oxides, there are absorption bands corresponding to Pb-O and Sb-O , while there

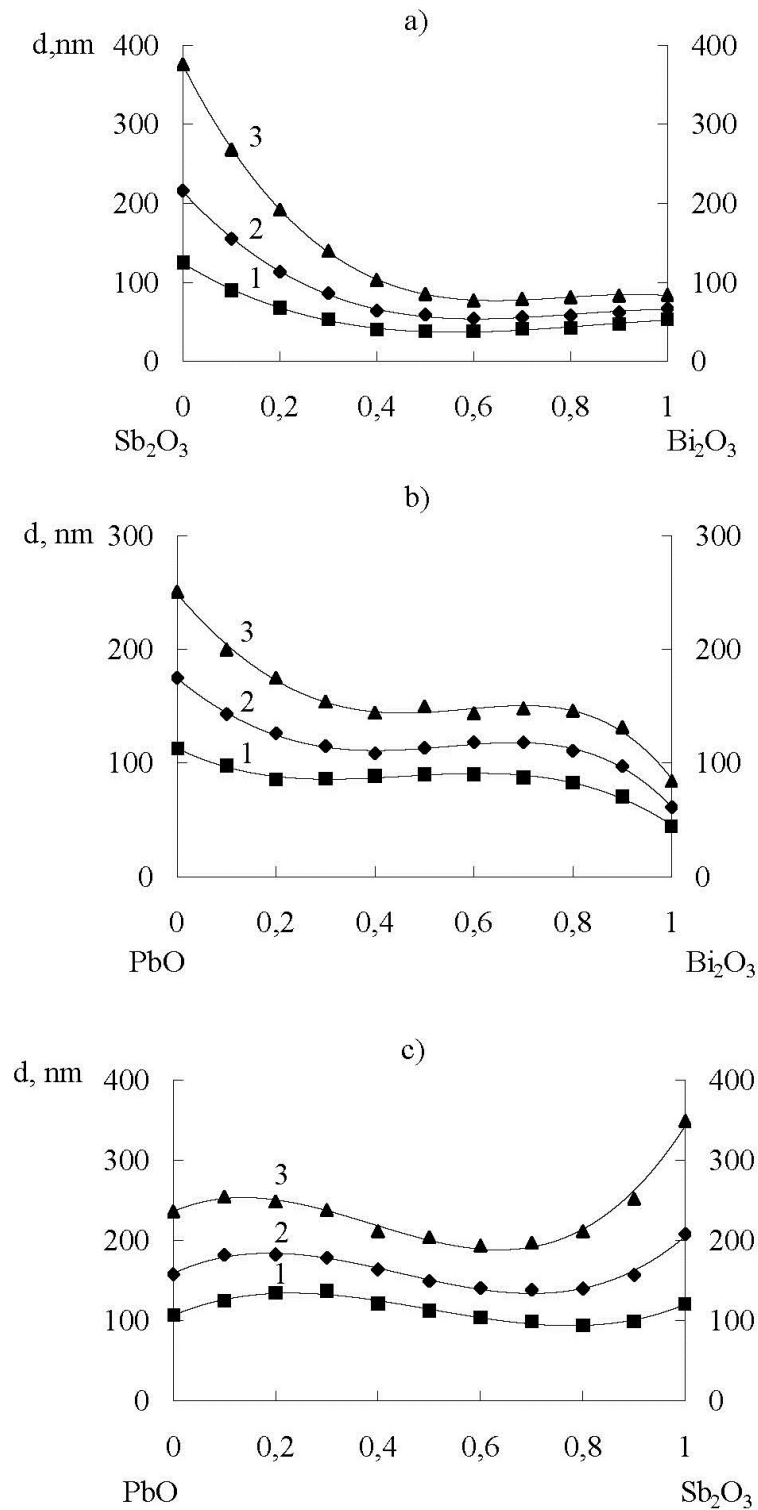


FIG. 1. Oxide film thickness on GaAs surface versus the composition a) $Sb_2O_3 + Bi_2O_3$; b) $PbO + Bi_2O_3$; c) $PbO + Sb_2O_3$: 1 – 10 minutes, 2 – 20 minutes, 3 – 40 minutes

TABLE 1. USXES data for the films obtained by GaAs thermal oxidation stimulated by the coaction of two chemostimulator oxides

Chemostimulator composition, % Bi ₂ O ₃	Film thickness, nm	Composition at %			
Sb ₂ O ₃ + Bi ₂ O ₃					
		Ga	As	Sb	Bi
40	103	58	9	–	–
50	85	51	9	–	–
70b	79	47	8	–	–
PbO + Bi ₂ O ₃					
Chemostimulator composition, % Bi ₂ O ₃					
		Ga	As	Pb	Bi
30	146	54	10	4	–
50	150	49	12	2	–
80	175	44	12	Traces	–
PbO + Sb ₂ O ₃					
Chemostimulator composition, % Sb ₂ O ₃					
		Ga	As	Pb	Sb
20	248	56	9	6	–
50	204	50	8	3	–
70	197	45	8	1	–

are no bismuth traces in the films even when the bismuth oxide concentration in the activator composition is maximum.

The X-ray powder diffraction data given in Table 2 showed that the starting oxides become main elements in chemostimulator compositions and that after annealing Sb₂O₃ transforms into Sb₂O₄. Apart from the bands, however, characteristic of the individual chemostimulators, there are distinct peaks that we could not define. This, nonetheless, allows us to presume that there are intermediate stages, according to the state diagram [10].

Nonlinear dependence of the oxide film thickness on the GaAs surface on the chemostimulator composition, and the X-ray powder diffraction data demonstrate their interactions, which result in the nonlinear effects observed.

The total additive anomaly in general may be caused by the oxides' interaction in the solid (activator sample) and vapor phases and especially on the surface of the sample being oxidized. To solve the problem, the reactor used in the experiment was modified as follows: the weighed batches of individual oxides were placed into a container separated by a partition in order to rule out any contact. This ensured that there would be no interactions in the solid phase. After the process, the oxides from the two parts of the container were studied using X-ray fluorescence analysis that showed that there were no traces of the second oxide found. Thus, the oxides from different parts of the container do not interact in the vapor phase either. The modified container scheme is shown in Fig. 2.

TABLE 2. Interplanar distance (d_{hkl} , Å) defined by the X-ray powder diffraction method for various binary compositions of activator oxides

Sb ₂ O ₃ + Bi ₂ O ₃			
Phase	Composition, mol. % Bi ₂ O ₃		
	40	50	70
Sb₂O₄	3.062; 2.936; 2.649; 1.777	3.062; 2.928; 2.642; 1.777	3.062; 2.936; 2.649; 1.777
Bi₂O₃	3.433; 3.298; 3.238; 1.948	3.436; 3.298; 3.238; 1.952	3.436; 3.298; 3.238; 1.948
PbO + Bi ₂ O ₃			
Phase	Composition, mol. % Bi ₂ O ₃		
	30	50	80
PbO	2.936; 2.389; 2.024; 1.848	2.928; 2.379; 2.003; 1.858	2.936; 2.389; 1.996; 1.858
Bi₂O₃	3.433; 3.298; 3.238; 1.948	3.436; 3.298; 3.238; 1.952	3.436; 3.298; 3.238; 1.948
Intermediate phase	3.371; 2.227; 1.748; 1.578	3.298; 2.227; 1.740; 1.637	3.371; 2.227; 1.746; 1.624
PbO + Sb ₂ O ₃			
Phase	Composition, mol. % Sb ₂ O ₃		
	20	50	70
PbO	2.936; 2.389; 2.024; 1.848	2.928; 2.379; 2.003; 1.858	2.936; 2.389; 1.996; 1.858
Sb₂O₄	3.062; 2.936; 2.649; 1.777	3.062; 2.928; 2.642; 1.777	3.062; 2.936; 2.649; 1.777
Intermediate phase	5.480; 4.548; 1.650; 1.622	5.918; 3.612; 1.753; 1.687	5.818; 4.490; 1.650; 1.574

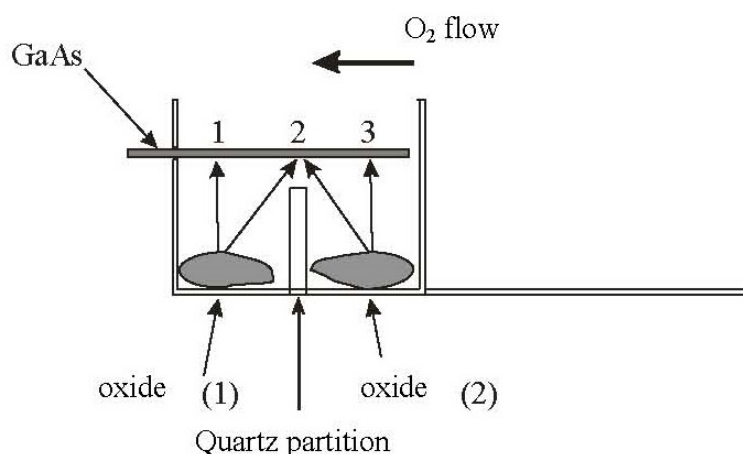


FIG. 2. Spatially separated activators coaction scheme

Due to this spatial separation, three distinct areas (1, 2, 3) appear on the GaAs surface. They are different both in appearance and in the film properties (thickness and composition). Area (1) – the film obtained using practically only the first oxide; (3) – the second; (2) – both oxides acting simultaneously. Oxide films from areas (1) and (3) contain the chemostimulator above which they are placed. The concentration of the second oxide, in these cases, is very low (EPXMA, see below). Consequently, the oxide film thickness in these areas is similar to those obtained using only first or second oxide. In area (2), both chemostimulators are present, and the film thickness is rather different from areas (1) and (3). Thus, the film in area (2) results from simultaneous interaction of chemostimulators separated spatially in the container, but can interact in the vapor phase (through which the interaction of the oxide composition and the oxidized sample is carried out) and on the GaAs surface itself. The following comparison of the spatially separated oxides and the mixture effects will be based on the area (2) data. The nonlinear effect, in this case, results from the mutual influence of the oxides only on the GaAs surface and in the vapor phase. When the oxide film thickness in area (2) is identical to the one grown after the oxide mixture evaporation, it means that the oxides do not interact in the solid phase and the nonlinear effect results completely from the interaction of the activators on GaAs surface and in the vapor phase. When the film thicknesses differ, there is certain interaction in the weighed batch between the activators during the mixture sublimation evaporation. The difference is then equal to the contribution of the interactions in the solid phase to the total nonlinear effect. The contribution may be either positive or negative.

To rule out the interaction on GaAs surface, we carried out a number of experiments, when GaAs had its own pre-grown oxide layer of 50 nm. Thus, the oxide surface took the place of GaAs surface. Here, again, if the pre-oxidized and not pre-oxidized film thickness is the same, then the surface has no influence and the nonlinear effect is caused by the activators' interaction in the vapor phase and in the weighed batches of activators. If they differ, then the activators interact on GaAs surface.

The experiments described, make it possible to determine the contribution from the solid phase interactions and interactions on GaAs surface, and to calculate the contribution of the activator interaction in the vapor phase. To make the discussion more convenient, let the samples with the pre-grown oxide layers be denoted as B-series, the as-received samples – A-series, activator mixture evaporation sublimation in the oxidizing atmosphere – Mode I, spatial separation of the activators – Mode II. We used $\text{Sb}_2\text{O}_3 + \text{Bi}_2\text{O}_3$ composition as a model, as in this system the oxides are the least similar (X-ray powder diffraction), which makes it easier to interpret the results.

The functions obtained are presented in Fig. 3. The given isotherms show the maximum time, since, as stated above, the additive anomaly increases proportionally to the process length.

Clearly, when the activator oxides are introduced separately, there is certain anomaly (curve 2), which proves that the activators interact, despite the spatial separation. Hence, they may interact on the semiconductor surface, or in the vapor phase or in both cases.

In both with the separate and mixture sublimation of the chemostimulators (Modes I and II, Fig. 3. curve 1 and 2) there is a negative anomaly; only with the mixture evaporation is it much larger. The film thickness grown on GaAs surface with (B-series) and without (A-series) the pre-grown oxide layer depends on the activator composition in the same way both in Mode I (curve 1, 3) and II (curve 2, 4). So, replacing the pure GaAs sample surface by the oxide layer has hardly any effect on the GaAs oxidation process. Hence, there is either no interaction between the activators on the pure surface of the semiconductor in the temperature-time range used, or it is insignificant. These results were quite predictable, considering the fact that even after the preprocessing, GaAs surface is not atomically clean and is always covered

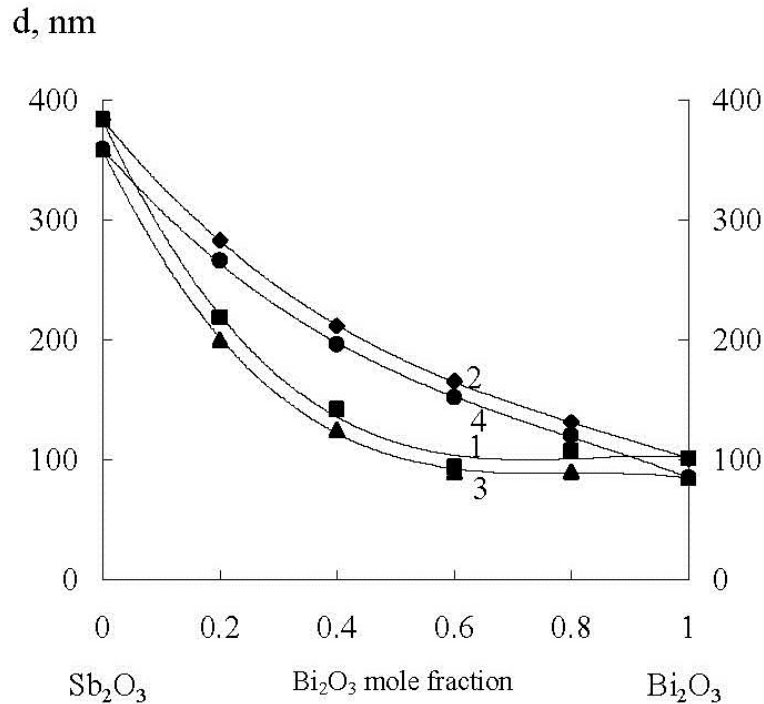


FIG. 3. Oxide film thickness on GaAs surface versus the composition of $\text{Sb}_2\text{O}_3+\text{Bi}_2\text{O}_3$ at 530 °C and an oxidation time of 40 min. 1 – A series, Mode I; 2 – A series, Mode II; 3 – B series, Mode I; 4 – B series, Mode II

by a thin oxide layer. Hence, when the activators are used separately and there is no chance of their interaction in the solid phase (curve 2, 4), the anomalies are caused by the mutual influence of the activators in the vapor phase.

The GaAs samples obtained both with mixture and separate sublimation of antimony and bismuth oxides and oxidized by chemostimulator composition of 60% Sb_2O_3 + 40% Bi_2O_3 for 40 min. were studied using EPXMA. When the chemostimulators are introduced separately, three different areas appear on the sample. That is why we have analyzed three different parts of the wafer corresponding to the said areas (1, 2, 3 in Fig. 2). When the chemostimulators are vaporized from the mixture, there is no such effect. Still, three different areas of the wafer were analyzed. The obtained data (Table 3) shows, that in both cases the main components of the films are As and Ga (the latter prevailing), which, judging by the substantial amount of oxygen, are oxidized (Ga_2O_3 , As_2O_3). Such concentration of the chemostimulator in the film (less than 3%) and its oxide nature allow us to suggest using such films as a solid-state component of a gas sensor.

The films contain chemostimulators as well as the substrate components. After the mixture sublimation, they are distributed in the sample in equally low concentrations (see Table 3). After separate sublimation, there is much more antimony in the films than bismuth and it is concentrated largely in area (1) (2.23 at %). In area (2) its concentration becomes approximately three times lower. In area (3), which is above Bi_2O_3 , the antimony concentration is even lower (~ 0.05 at %), but this value, however, is five times higher than the bismuth concentration (0.01 at %). Bismuth is distributed very regularly in the film. Bismuth concentration in the film after separate sublimation is nearly 10 times lower than after mixture sublimation. Thus, after mixture sublimation of antimony and bismuth oxides, the antimony oxide enhances incorporation of the bismuth oxide in the oxide film growing on the surface, while Bi_2O_3 prevents

TABLE 3. EPXMA data for the samples obtained by GaAs thermal oxidation in the presence of a 60% Sb_2O_3 + 40% Bi_2O_3 composition using the mixture activation and spatial separation

Area on the GaAs surface (Fig. 2)	Film composition				
	Ga	As	Sb	Bi	O
	at %	at %	at %	at %	at %
Mixture evaporation					
1	21.1	12.5	0.02	0.03	66.35
2	21.3	15.6	0.05	0.04	63.01
3	22.0	17.3	0.09	0.04	60.57
Activating composition – 1.5 : 1					
Film – 1.25 : 1					
Spatial separation					
1	16.2	10.8	2.23	0.01	70.76
2	21.6	19.1	0.67	0.01	58.62
3	23.9	22.4	0.05	0.01	53.64
Activating composition – 1.5 : 1					
Film – 67 : 1					

incorporation of Sb_2O_3 in it. Both the vapor composition and the vapor pressure over antimony and bismuth oxide during their coaction are, therefore, not determined by the additive sum of these values for individual oxides [11].

As we cannot rule out the mutual influence of the chemostimulators in the vapor phase (in this phase the oxides are transferred from the weighed batches of oxides to the surface), the next vital stage was to study the vapor components over the composition. The analysis was carried out using mass spectrometry method (MS-1301). The vapor over the composition of 60% Sb_2O_3 and 40% Bi_2O_3 was analyzed. The mass spectra of the vapor at 690 K has shown Sb_4O_6^+ peaks and a small number of SbO^+ , Sb_3O_4^+ peaks. Antimony oxide activity was about 0.55. Bi^+ ion peaks were registered starting with 730 K. At such temperatures, bismuth concentration in the vapor does not exceed 0.3 %. The pressure and vapor composition data obtained correlates well both with reference data [11] and with EPXMA data concerning the activator incorporation in the film growing on GaAs surface. Antimony oxide activity (0.55) is similar to activator mole fraction in the composition, which, together with X-ray powder diffraction data indicates that the interaction between the activators in the starting weighed sample of oxides is weak.

4. Conclusions

GaAs thermal oxidation activated by chemostimulators demonstrates a nonlinear effect in the dependence of the oxide film thickness on the surface of GaAs from the compositions.

These effects result from the interactions between chemostimulators, which create additional feedback and are localized with comparable impact during the solid and vapor phases. They do not show on the GaAs surface. The study determined the composition of thin films

grown on GaAs surfaces from chemostimulator binary compositions, and allows us to suggest their use as solid-state gas sensors.

Acknowledgements

This work was supported by the Ministry of Education and Science of the country-regionplaceRussian Federation in line with government order for Higher Education Institutions in the field of science for 2014-2016 years (project No. 673) and by RFBR grant No. 13-03-00705-a.

References

- [1] Mittova I.Ya., Pshestanchik V.R. The chemistry of processes which create dielectric layers with functional group substituents on semiconductors by impurity thermo-oxidation. *Russian Chemical Reviews*, **60** (9), P. 967–980 (1991).
- [2] Ke Y., Malino S., et al. Structural studies of sulfur-passivated GaAs (100) surfaces with LEED and AFM. *Surface Science*, **415**, P. 29–36 (1998).
- [3] Bang K.-H., Hwang D.-K., et al. Comparative studies on structural and optical properties of ZnO films grown on c-plane sapphire and GaAs (001) by MOCVD. *Solid State Communication*, **126** (11), P. 623–627 (2003).
- [4] Panin A.V., Shugurov A.R., Kalygina V.M. Effect of Sulfur and Selenium on the Surface Relief of Insulating Films and Electrical Characteristics of Metal-Insulator-p-GaAs Structures. *Semiconductors*, **35** (1), P. 78–83 (2001).
- [5] Takagi H., Kano G., Teramoto I. Thermal oxidation of GaAs in arsenic trioxide vapor. *J. Electrochem. Soc.*, **125** (4), P. 579–581 (1978).
- [6] Mittova I.Ya., Tomina E.V., Lapenko A.A., Sladkopevtcev B.V. The catalytic action of vanadium and its oxide (V) in the oxidation processes of $A^{III}B^V$ semiconductors. *Nanosystems: physics, chemistry, mathematics*, **3** (2), P. 116–138 (2012).
- [7] Mittova I.Ya., Pshestanchik V.R., Kostryukov V.F. Thermal oxidation of Gallium Arsenide in oxygen: combined effect of Antimony and Bismuth oxides. *Russian Journal of Inorganic Chemistry*, **42** (2), P. 182–186 (1997).
- [8] Mittova I.Ya., Pshestanchik V.R., Kostryukov V.F. Alternating nonlinearity of the joint activating effect of binary mixtures of p-element oxides on the chemically activated thermal GaAs oxidation. *Doklady Chemistry*, **378** (4–6), P. 165–167 (2001).
- [9] Mittova I.Ya., Pshestanchik V.R., Kostryukov V.F., Donkareva I.A. Spatial localization of interactions between activating additives during chemostimulated thermal oxidation of GaAs. *Doklady Chemistry*, **386** (4–6), P. 258–260 (2002).
- [10] Galachov F.Ya. *Refractory oxide system state diagram*. Science, Moscow, 1986, 353 p. (in Russian)
- [11] Kazenas E.K., Tsvetkov Yu.V. *Evaporation of oxides*. Science, Moscow, 1997, 543 p. (in Russian)

VOLUME PROPERTIES OF WATER SOLUTIONS AND REFRACTION AT 25 °C WATER-SOLUBLE TRIS-MALONATE OF LIGHT FULLERENE – $C_{60} [= C(COOH)_2]_3$

K. N. Semenov¹, N. A. Charykov^{2,3}, A. S. Kritchenkov¹, I. A. Cherepkova², O. S. Manyakina², D. P. Tyurin², A. A. Shestopalova², V. A. Keskinov², K. V. Ivanova², N. M. Ivanova¹, D. G. Letenko⁴, V. A. Nikitin⁵, E. L. Fokina¹, O. V. Rakhimova³

¹St. Petersburg State University, Saint-Petersburg, Russia

²St. Petersburg State Technological Institute (Technical University), Saint-Petersburg, Russia

³St. Petersburg State Electro-Technical University (LETI), Saint-Petersburg, Russia

⁴St. Petersburg State University Architecture Academy, Saint-Petersburg, Russia

⁵St. Petersburg State Technical University, Saint-Petersburg, Russia

keskinov@mail.ru

PACS 61.48.+c

The volume Properties of water soluble tris-malonate of light fullerene – $C_{60} [= C(COOH)_2]_3$ were investigated with the help of quartz pycnometers at 25 °C, including the concentration dependence of density, average molar volume of the solutions and partial molar volumes of $C_{60} [= C(COOH)_2]_3$ and H_2O . Concentration dependence of the refraction index in water solutions of $C_{60} [= C(COOH)_2]_3$ was also determined with the help of refractometer, specific and molar refraction of the components were calculated with the help of the rules of the additive refraction of solution components.

Keywords: tris-malonate of light fullerene, volume properties, refraction.

Received: 19 February 2014

Revised: 14 March 2014

1. Introduction

This article further develops the investigations, which were initiated by the article [1], devoted to the description of the synthesis and identification of tris-malonate $C_{60} [= C(COOH)_2]_3$ (the original synthesis of this water soluble derivative was described earlier in [2]).

2. Concentration dependence of density of water solutions of tris-malonate of light fullerene – $C_{60} [= C(COOH)_2]_3$

The concentration dependence for the density of aqueous solutions of the tris-malonate $C_{60} [= C(COOH)_2]_3$ at 25 °C was investigated by the method of pycnometry with the help of quartz pycnometers (Volume nearly $V \approx 2.5 \text{ cm}^3$), accuracy of thermostat was $\Delta T = \pm 0.05$ grad. Data, concerning the densities of the solutions are represented lower in the Table 1 and in Fig. 1.

Aqueous solutions of the tris-malonate $C_{60} [= C(COOH)_2]_3$ were prepared by the following method; first, a basic solution (Ctris-malonate = 336 g/dm^3) was prepared by the direct dissolution of previously-synthesized $C_{60} [= C(COOH)_2]_3$ in the distilled water, double filtration of the solution through a ‘blue’ paper filter; the concentration of the solution was determined

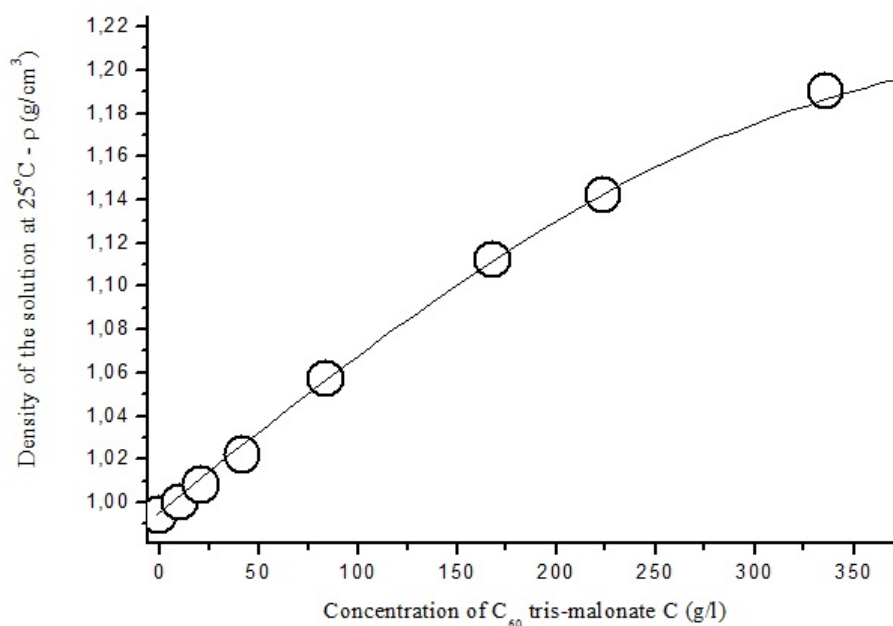


FIG. 1. Concentration dependence of density of water solutions of tris-malonate $C_{60}[= C(COOH)_2]_3$ at 25 °C

TABLE 1. Concentration dependence of Volume Properties of water solutions of tris-malonate $C_{60}[= C(COOH)_2]_3$

N of solution	Concentration C (g/dm ³)	Density ρ (g/cm ³)	Average molar volume of solution \bar{V} (cm ³ /mole)	Partial molar volume of H ₂ O V_{H_2O} (cm ³ /mole)	Partial molar volume of tris-malonate $V_{tris-malonate}$ (cm ³ /mole)
1	0	0.994	18.000	18.00	1021.00
2	10.5	1.000	18.187	18.00	1021.00
3	21.0	1.008	18.382	18.00	1021.00
4	42.0	1.022	18.792	18.00	1021.00
5	84.0	1.057	19.720	18.00	1021.00
6	168	1.112	22.045	18.00	1021.00
7	224	1.142	24.041	17.99	1020.99
8	336	1.190	29.643	17.99	1020.99

gravimetrically by soft drying in a vacuum dry box at 65 °C and residual pressure ≈ 0.1 mm Hg for 2 hours. More dilute solutions were prepared from the basic one by the direct dilution of the determined mass of the basic solution by water to the calculated volume at $T = 25 \pm 0.05$ °C.

3. Average and partial molar volumes

Average molar volume of solution can be calculated as [3,4]:

$$\bar{V} = V / (n_{H_2O} + n_{tris-malonate}), \quad (1)$$

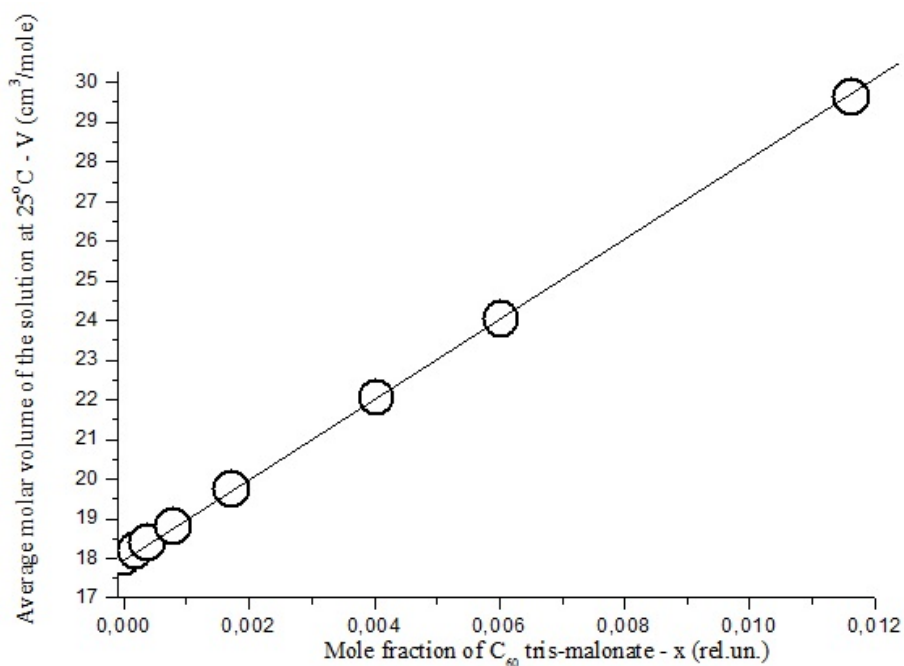


FIG. 2.1. Concentration dependence of the function \bar{V}

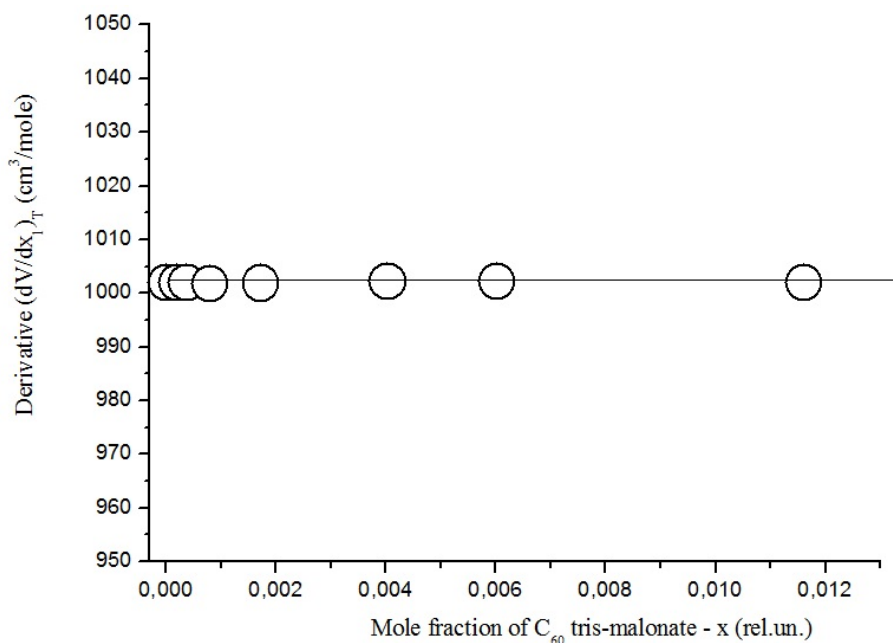


FIG. 2.2. Concentration dependence of the function $(\partial\bar{V}/\partial x_j)_{T,P}$

where: V — volume of 1 dm³ of the solution, n_i — moles of i -th component in 1 dm³ of the solution are also represented in the Table 1 and in Fig. 2.1.

Partial molar volume of the components of the solution: V_{H_2O} and $V_{tris-malonate}$ according to the connection between average molar and partial molar functions [3,4]:

$$V_i = (\partial V / \partial n_i)_{T,P,n_j} = \bar{V} - x_j (\partial \bar{V} / \partial x_j)_{T,P}, \quad (2)$$

where: x_i — mole fraction of i -th component in the solution are also represented in the Table 1 (concentration dependence of the function $(\partial\bar{V}/\partial x_j)_{T,P}$ is represented in Fig. 2.2).

From the obtained volume data, one can see the following:

1. the dependence $\bar{V}(x_{\text{tris-malonnate}})$ is practically linear,
2. so, the derivative is insignificant $(\partial\bar{V}/\partial x_{\text{tris-malonnate}})_{T,P} \approx 0$,
3. so, partial molar volumes of both components are practically constant: $V_{\text{HOH}} \approx 18.0$, $V_{\text{tris-malonnate}} \approx 1021 \text{ cm}^3/\text{mole}$, i.e. both components are built in the structure of the solution without any visible complicating interactions. We will try to explain the reasons for such anomalous behavior below.

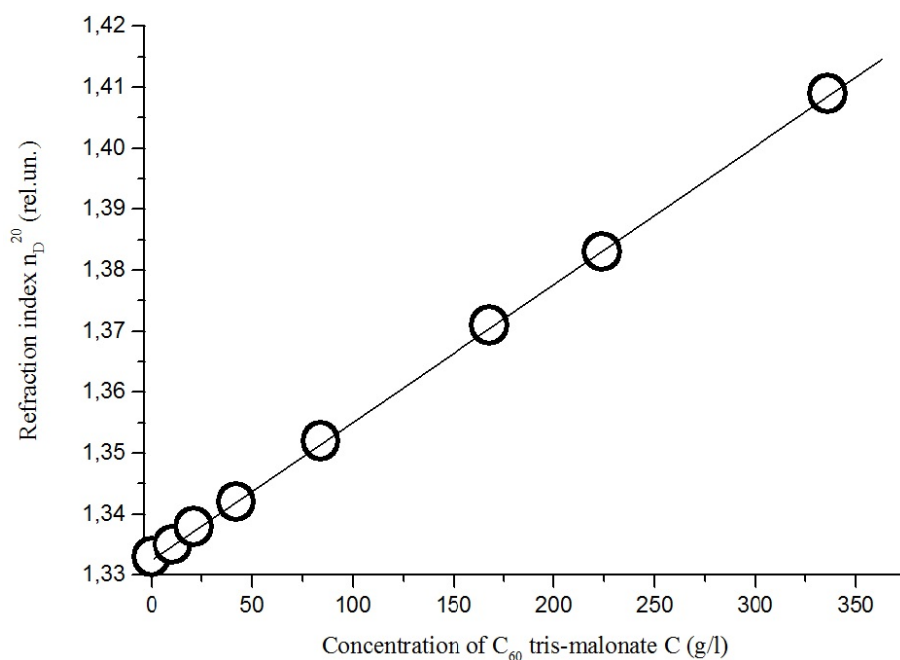


FIG. 3.1. Refraction indexes of queous tris-malonnate $C_{60}[=C(\text{COOH})_2]_3$ solutions at 25 °C

4. Refraction of the solution

Concentration dependence of the refraction index (n_D) in aqueous solutions of $C_{60}[=C(\text{COOH})_2]_3$ was also determined with the help of a Mettler Toledo refractometer. Data is presented in Table 2 and Fig. 3.1. The specific refraction of aqueous solutions of $C_{60}[=C(\text{COOH})_2]_3$ was calculated according to the well-known formula:

$$r = \left(n_D^2 - 1/n_D^2 + 2 \right) (1/\rho), \quad (3)$$

and is represented in Fig. 3.2.

According to the specific refraction additivity rule:

$$r = r_{\text{tris-malonnate}} \cdot w_{\text{tris-malonnate}} + r_{\text{HOH}}(1 - w_{\text{tris-malonnate}}), \quad (4)$$

where r_i , w_i — specific refraction of i -th component of the solution, we also calculated specific refraction of components — tris-malonnate and H_2O (see Table 2 and Fig.3.3).

We also calculated molar refraction of $C_{60}[=C(\text{COOH})_2]_3$ aqueous solutions according to the formula:

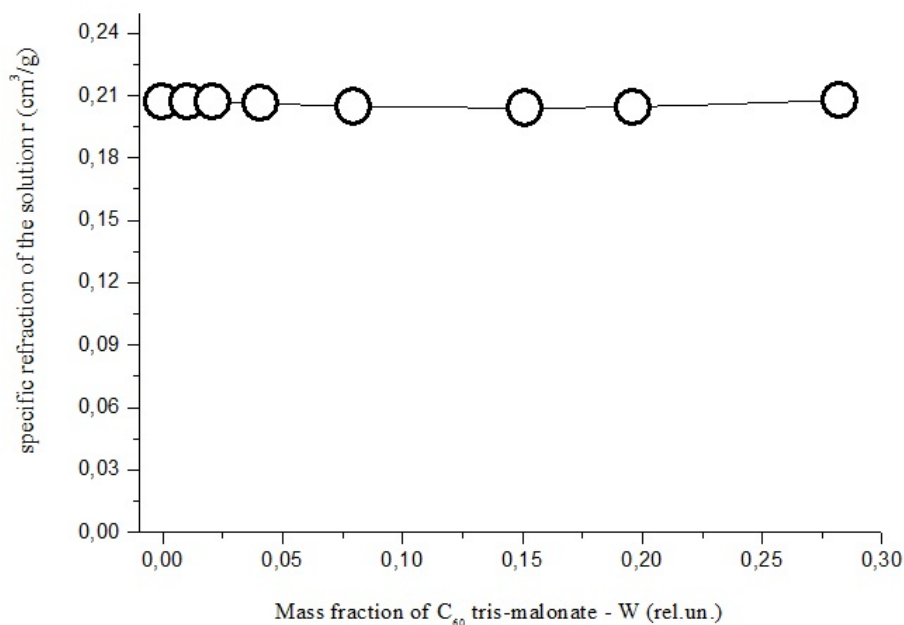


FIG. 3.2. Specific refraction of queous tris-malonate $C_{60}[= C(COOH)_2]_3$ solutions at 25 °C

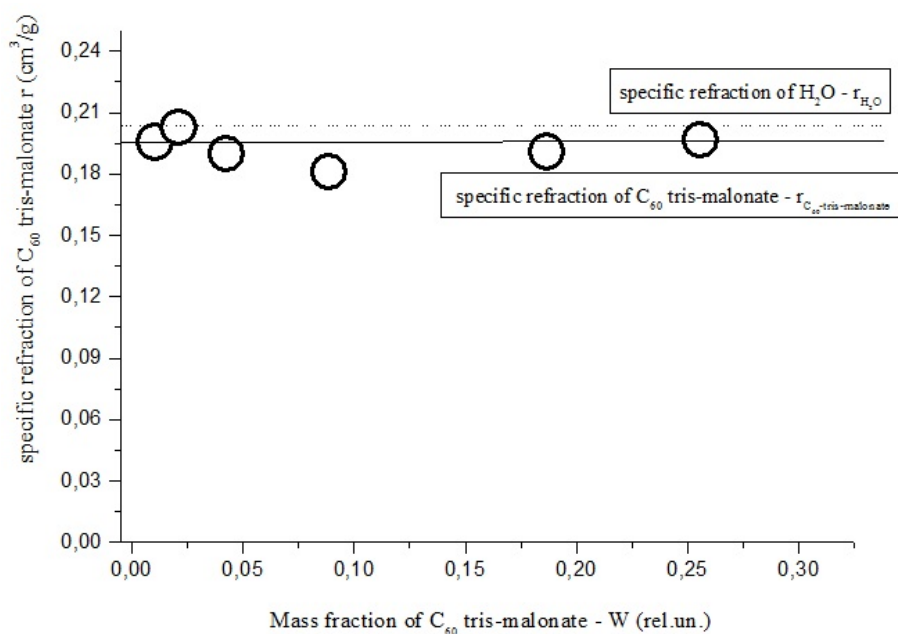


FIG. 3.3. Specific refraction of tris-malonate $C_{60}[= C(COOH)_2]_3$ and water (for the comparison) in aqueous solutions at 25 °C

$$R = (n_D^2 - 1/n_D^2 + 2)(\bar{M}/\rho), \quad (5)$$

where \bar{M} — average molar mass of the components of the solution ($\bar{M} = M_{\text{tris-malonate}} \cdot x_{\text{tris-malonate}} + M_{\text{H}_2\text{O}}(1 - x_{\text{tris-malonate}})$), M_i — mass of tris-malonate C_{60} (1026 a.un.) and H_2O (18 a.u.), x_i — molar fraction of i -th component. Data are represented in the Fig. 4.1 and Table 2.

TABLE 2. Concentration dependence of refraction indexes of aqueous tris-malonate $C_{60}[=C(COOH)_2]_3$ solutions and specific and molar refraction of the components at 25 °C

<i>N</i> of solution	Refraction index n_D^{20} (rel. un.)	Specific refraction of the solution r (cm ³ /g)	Specific refraction of tris-malonate $r_{\text{tris-malonate}}$ (cm ³ /g)	Molar refraction of the solution R (cm ³ /mole)	Molar refraction of tris-malonate $R_{\text{tris-malonate}}$ (cm ³ /mole)
1	1.333	0.2069	–	3.7260	–
2	1.335	0.2068	0.1954	3.7625	200.50
3	1.338	0.2068	0.2022	3.8004	207.59
4	1.342	0.2062	0.1887	3.8803	194.47
5	1.352	0.2046	0.1777	4.0611	185.52
6	1.371	0.2039	0.1868	4.5141	195.61
7	1.383	0.2043	0.1932	4.9027	201.57
8	1.409	0.2077	0.2098	5.9939	214.42

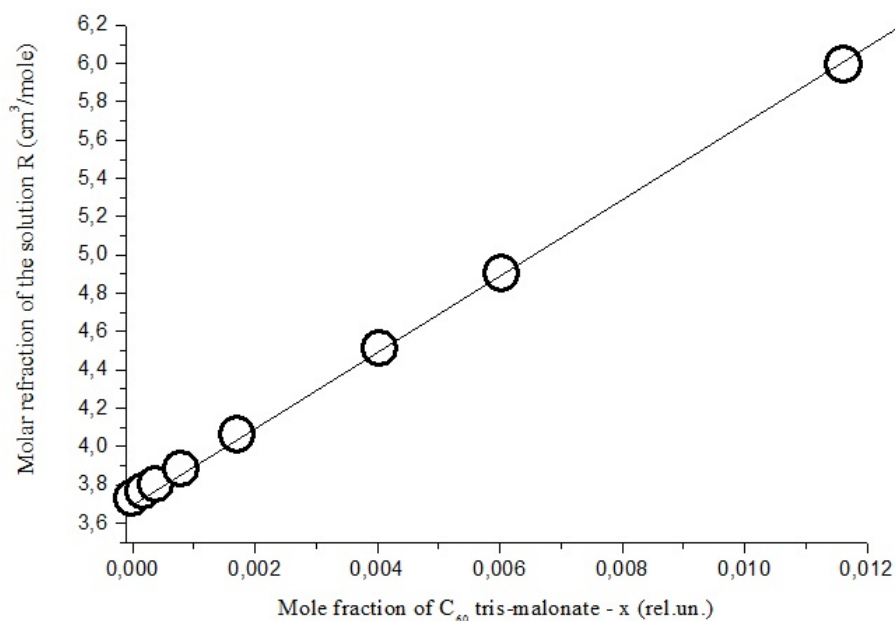


FIG. 4.1. Molar refraction of aqueous tris-malonate $C_{60}[=C(COOH)_2]_3$ solutions at 25 °C

According to the obvious parity, connecting specific and molar (R_i) refractions of the components:

$$R_i = r_i \cdot M_i, \quad (6)$$

we also calculated last ones (see Table 2 and Fig. 4.2).

From obtained refraction data one can see the following:

1. The dependence $n_D(C)$ is nearly linear;

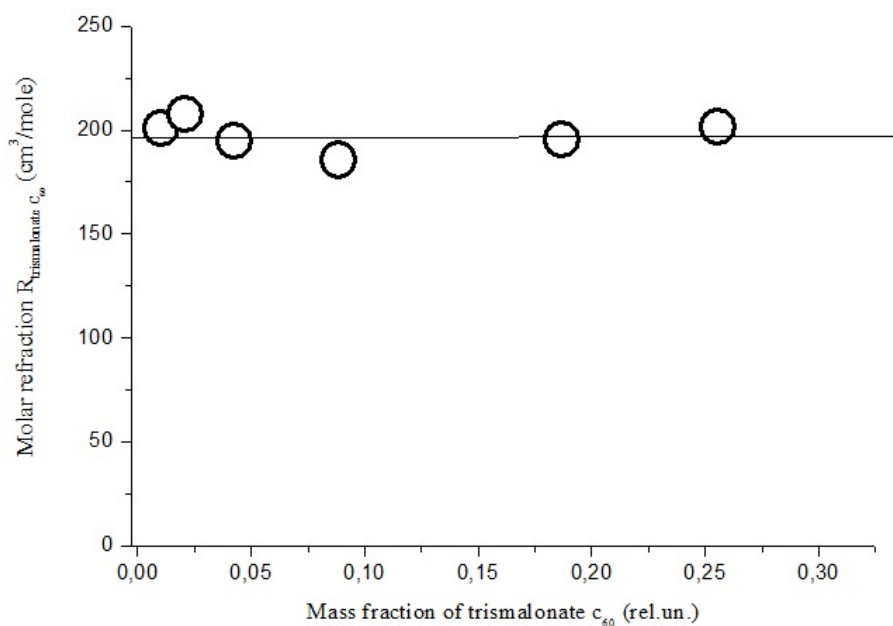


FIG. 4.2. Molar refraction of tris-malonate in aqueous solutions at 25 °C

- Specific refraction of the solution practically is independent of the concentration ($r \approx 0.205 \pm 0.002 \text{ cm}^3/\text{g}$);
- Specific refractions for both components of the solution are also practically independent of the concentration and absolutely unexpectedly are very similar:

$$r_{\text{tris-malonate}} \approx 0.195 \pm 0.1 \approx r_{\text{H}_2\text{O}} \approx 0.206 \pm 0.1 \text{ cm}^3/\text{g}; \quad (7)$$

- The concentration dependence of molar refraction of water solutions of tris-malonate at 25 °C $R(x_{\text{tris-malonate}})$ is also nearly linear;
- Molar refraction of tris-malonate $R_{\text{tris-malonate}}$ is practically independent of the concentration:

$$R_{\text{tris-malonate}} \approx 201 \pm 7 \text{ cm}^3/\text{mole}; \quad (8)$$

- That in essence the casual fact for the specific refractions' similarity of both components (at a huge difference of the molecular dimensions) determines such simple concentration behavior for the refraction characteristics. Specific refraction is accepted to be associated with the volume of electronic orbits falling on the mass unit of the phase, and in the case of our solutions, the casual equality of these components' characteristics allows to them form the mixed solution in such a way that the intermolecular forces are compensatory.
- We also check ourselves, by calculating molar refraction of tris-malonate C_{60} by the additivity rule (R^{add}):

$$R^{\text{add}} \approx 69R_c + 6R_{\text{O}(-\text{OH})} + 6R_{\text{O}(=\text{C}=\text{O})} + 6R_H \approx 195.3 - 200.3 \text{ cm}^3/\text{mole}, \quad (9)$$

where: $R_{i(j)}$ – atomic refraction of i -th atom in j -th functional group. Some discrepancy in the calculation connected with the choice of the different spectral lines: for the line $H_\alpha[\lambda = 658.3(\text{nm})]$ - $R^{\text{add}} \approx 195.3 \text{ cm}^3/\text{mole}$; and for the line $H_\gamma[\lambda = 436.1(\text{nm})]$ - $R^{\text{add}} \approx 200.3 \text{ cm}^3/\text{mole}$ (data, according to Eizenlor).

Alternative calculation (according to Fogel [5]) gives the following result:

$$R^{\text{add}} \approx 63R_c + 6R_{-\text{COOH}} \approx 205.2 \text{ cm}^3/\text{mole}, \quad (10)$$

where $R_{-\text{COOH}}$ is the refraction of carboxylic group. In the both cases, the result of the calculation is considered more or less successful and confirms the experimental data.

5. Conclusion

Thus, the partial and average molar volume and refractive properties of aqueous solutions of the water soluble light fullerene derivative- $\text{C}_{60}[\text{C}(\text{COOH})_2]_3$, at 25 °C were investigated.

Acknowledgement

Research was performed with using the equipment of the Resource Center ‘GeoModel’ of Saint-Petersburg State University.

This work has been accomplished as the part of the Ministry of Education and Science of the placecountry-region Russian Federation research assignment ‘Realization of scientific research (fundamental studies, applied research and advanced developments)’. Project code: 2548.

References

- [1] K.N.Semenov, N.A.Charykov, A.S.Kritchenkov, et al. Synthesis and identification water-soluble tris-malonate of light fullerene – $\text{C}_{60}[\text{C}(\text{COOH})_2]_3$. *Nanosystems: Physics, Chemistry, Mathematics*, **5** (2), P. 315–319 (2014).
- [2] I.Lamparth, A.Hirsch. Water-soluble malonic acid derivatives of C_{60} with a defined three-dimensional structure. *J. Chem. Soc Chem. Commun.*, P. 1727–1728 (1994).
- [3] A.V.Storonkin. *Thermodynamics of Heterogeneous Systems*. Rus. Leningrad: LGU, Book 1, Part 1, 2. 467 pp. (1967).
- [4] A.Muenster. *Chemical thermodynamics*. Rus. Transl. from Engl. Moscow: Mir (1971).
- [5] *Atomic refractions according to Fogel*. Directory of Chemist/ red. B.P. Nikol’skiy. Rus. Leningrad: Chemistry, 1, 395 pp. (1982).

POLY-THERMAL SOLUBILITY AND COMPLEX THERMAL ANALYSIS OF WATER-SOLUBLE TRIS-MALONATE OF LIGHT FULLERENE — $C_{60} [= C(COOH)_2]_3$

K. N. Semenov¹, N. A. Charykov^{2,3}, A. S. Kritchenkov¹, I. A. Cherepkova², O. S. Manyakina²,
D. P. Tyurin², A. A. Shestopalova², V. A. Keskinov², K. V. Ivanova², N. M. Ivanova¹,
D. G. Letenko⁴, V. A. Nikitin⁵, E. L. Fokina¹, I. A. Pestov², A. O. Netrusov²

¹St. Petersburg State University, Saint-Petersburg, Russia

²St. Petersburg State Technological Institute (Technical University), Saint-Petersburg, Russia

³St. Petersburg State Electro-Technical University (LETI), Saint-Petersburg, Russia

⁴St. Petersburg State University Architecture Academy, Saint-Petersburg, Russia

⁵St. Petersburg State Technical University, Saint-Petersburg, Russia

keskinov@mail.ru

PACS 61.48.+c

The poly-thermal solubility of the tris-malonate $C_{60} [= C(COOH)_2]_3 - H_2O$ binary system was investigated from 20 – 80 °C with the help of the method of isotherm saturation in ampoules. Concentration of tris-malonate $C_{60} [= C(COOH)_2]_3$ in solutions was determined by light absorption at 330 nm. A diagram of the solubility is non-monotonic, consisting of 2 branches, which correspond to 2 different crystal-hydrates of $C_{60} [= C(COOH)_2]_3$ and one non-variant point, corresponding to the saturation both crystal-hydrates. Complex thermal analysis of $C_{60} [= C(COOH)_2]_3$ crystal hydrates, in equilibrium with a saturated aqueous solution at room temperature, was performed from 20 – 600 °C. Consecutive effects of the losses of C=O and C=O + H₂O were determined.

Keywords: tris-malonate of light fullerene, solubility, density, complex thermal analysis.

Received: 17 March 2014

1. Introduction

This article continues investigations which were initiated in previous studies [1, 2], which were devoted to the description of the synthesis and identification of tris-malonate $C_{60} [= C(COOH)_2]_3$ [1] (the original synthesis of this water soluble derivative was described earlier in [3]) and the investigation of volume and refraction properties of its aqueous solutions at 25 °C [2]. This article is devoted to the investigation of poly-thermal solubility in binary system: tris-malonate $C_{60} [= C(COOH)_2]_3 - H_2O$. It is well-known that fullerenes themselves are practically insoluble in water and aqueous solutions. For example, the real solubility of C_{60} in water at 25 °C is $1.3 \cdot 10^{-11}$ g/dm³ and C_{70} is $1.1 \cdot 10^{-13}$ g/dm³ [4–10]. This fact sufficiently limits the application of fullerenes in medicine, pharmacology, food industry etc., because fullerenes are incompatible with water and water based ‘physiological liquids’ such as blood, lymph, gastric juice etc. So, the synthesis and studying of the main properties, first of all solubility in water-based systems is very important. Such water soluble derivatives of light fullerenes as fullerenols, different malonates, complex esters of amino-acids etc have been investigated widely (see, for example [4, 11–13]).

TABLE 1. Solubility in binary system: tris-malonate $C_{60}[=C(COOH)_2]_3 - H_2O$ from 20 – 80 °C

No.	Temperature (°C)	Solubility C (g/dm ³)	Density of saturated solutions ρ (g/sm ³)	Solid phase
1	20	254	1.112	$C_{60}[=C(COOH)_2]_3 \cdot 3H_2O$
2	30	315	1.128	– " –
3	40	342	1.131	– " –
4	50	399	1.133	– " –
5	60	437	1.136	$C_{60}[=C(COOH)_2]_3 \cdot 3H_2O^+$ $C_{60}[=C(COOH)_2]_3$
6	70	389	1.111	$C_{60}[=C(COOH)_2]_3$
7	80	357	0.948	– " –

2. Poly-thermal solubility of tris-malonate $C_{60}[=C(COOH)_2]_3$ in water

Poly-thermal solubility in binary system: tris-malonate $C_{60}[=C(COOH)_2]_3 - H_2O$ from 20 – 80 °C is investigated with the help of the isotherm saturation method in ampoules (frequency $\nu \approx 2 \text{ sec}^{-1}$, temperature accuracy $\Delta T \approx 0.05 \text{ deg.}$, time of saturation $t \approx 6 \text{ h}$). Concentration of tris-malonate $C_{60}[=C(COOH)_2]_3$ in saturated solutions was determined by light absorption at 330 nm (after the dilution and cooling of saturated solutions) see [1]:

$$C_{\text{tris-malonate}}(\text{mg/dm}^3) \approx 146D_{330} \quad (l = 1 \text{ cm}), \quad (1)$$

where D_{330} – is optical density of the solution at $\lambda = 330 \text{ nm}$ and ditch width $l = 1 \text{ cm}$.

Experimental solubility data are represented in the Table 1 and Fig. 1. One can see the following:

1. The solubility tris-malonate $C_{60}[=C(COOH)_2]_3$ is very high thousands g/dm³, these values correspond to the solubility of such well-soluble phases as fullerenol-d [11–13] or, for example halite – NaCl.
2. Solubility against temperature changes non-monotonically, crossing through the maximum at 60 °C.
3. Diagram consists of 2 branches, which correspond to 2 different compounds: a trihydrate – $C_{60}[=C(COOH)_2]_3 \cdot 3H_2O$ and an anhydrous form – $C_{60}[=C(COOH)_2]_3$ and one non-variant point (O in Fig. 1), corresponding to the saturation both compounds. Such parity at room temperature (one molecule of crystal-hydrate water per two carboxyl groups of malonate is typical for malonates – for example for sodium malonate – $Na-COO-CH_2-COO-Na \cdot H_2O$ [14].

3. Poly-thermal densities of saturated tris-malonate $C_{60}[=C(COOH)_2]_3$ aqueous solutions

To calculate the volume concentration of saturated tris-malonate $C_{60}[=C(COOH)_2]_3$ aqueous solutions and also in order to have the possibility of recalculating the solubility diagram into the other concentration scales (for example mass % or mole fraction), one needs to investigate the concentration poly-thermal density. These data were obtained by the method of

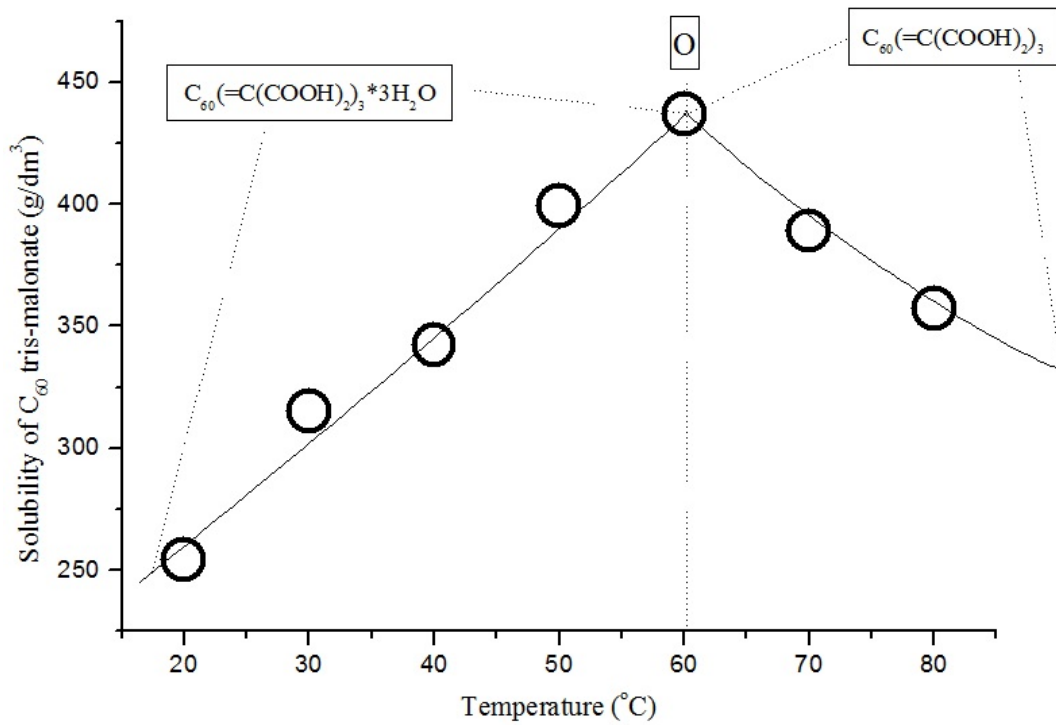


FIG. 1. Solubility in binary system: tris-malonate $C_{60}[=C(COOH)_2]_3 - H_2O$

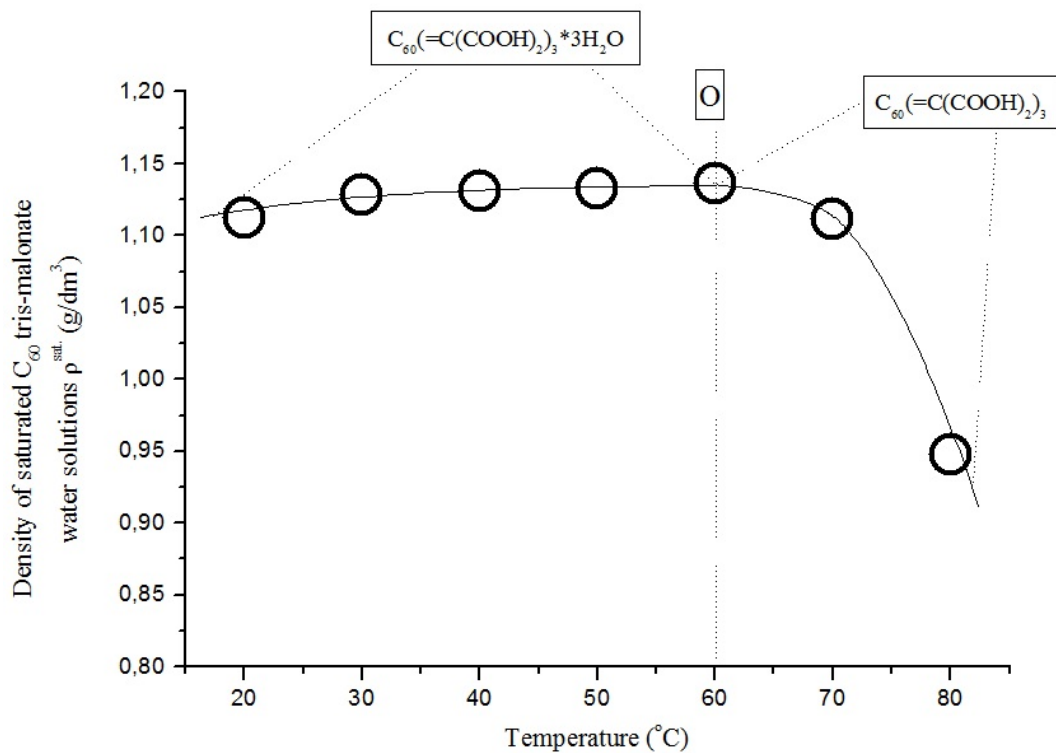


FIG. 2. Poly-thermal densities of saturated tris-malonate $C_{60}[=C(COOH)_2]_3$ aqueous solutions

pycnometry with the help of quartz pycnometers [2]. Data are also represented in the Table 1 and Fig. 2.

TABLE 2. The results of complex thermal analysis of crystal-hydrates of $C_{60}[=C(COOH)_2]_3$

No. of thermal effect (i)	T^m ($T_b \div T_e$) (°C)	$\Delta m_i/\Delta m_0$ calcu- lation (%)	$\Delta m_i/\Delta m_0$ experi- ment (%)	Process	Product of decomposition
0	—	0.0	0.0	—	$C_{60}(=C(COOH)_2)_3 \cdot 3H_2O$
1	97 (60 ÷ 130)	5.2	5.0	–3HOH	$C_{60}(=C(COOH)_2)_3$
2	150 (140 ÷ 180)	2.6	2.5	–C=O	$C_{60}(=C(COOH)_2)_2COH(COOH)$
3	208 (195 ÷ 240)	2.6	2.8	–C=O	$C_{60} = C(COOH)_2(COH(COOH))_2$
4	271 (255 ÷ 295)	2.6	2.7	–C=O	$C_{60}(COH(COOH))_3$
5	337 (320 ÷ 385)	4.3	4.1	–C=O–HOH	$C_{60} = CO(COH(COOH)_2)$
6	420 (400 ÷ 440)	4.3	4.3	–C=O–HOH	$C_{60}(=CO)_2COHCOOH$
7	488 (480 ÷ 520)	4.3	4.2	–C=O–HOH	$C_{60}(=CO)_3$
Sum effect	25 – 560	25.9	25.6	–3HOH– –6C=O– –3HOH	$C_{60}(=CO)_3$

where: T^m – temperature maximum of thermal effect, T_b and T_e – temperatures of the beginning and end of the effect, $\Delta m_i/\Delta m_0$ – the mass loss, m_0 – initial mass.

One can see the following:

1. Diagram has one singular point (O in Fig. 2), where the type of crystal-hydrates and course of the curve are changing $\rho^{sat}(T)$.
2. Before point O ($T = 20 \rightarrow 60^\circ C$), the density is practically constant, and after point O ($T = 60 \rightarrow 80^\circ C$), the density starts to decrease comparatively quickly. The last fact is connected with two reasons: the solubility of ‘more heavy component’ – tris-malonate decreases (see Fig. 1), and the density of the solvent decreases while temperature is also increasing.

4. Complex thermal analysis of crystal-hydrates of $C_{60}[=C(COOH)_2]_3$

Complex thermal analysis of $C_{60}[=C(COOH)_2]_3$ hydrates, in equilibrium with saturated aqueous solution at room temperature, was performed from 20 – 600 °C. A NETZSCH STA 449F3 thermo-gravimeter was used (velocity of the analysis $v \approx 5$ K/min, atmosphere – air, sample mass $m \approx 27.3$ mg). Results are represented in the Table 2 and Fig. 3.

One can see the following:

1. The first effect of losing 3 molecules of H_2O from the trihydrate proves the solubility data (the start of the effect $T_b \approx 60$ °C corresponds to the singular points in the Fig. 1, 2).
2. The subsequent three effects correspond to ‘decarbonylation’ (C=O removal) from the three different malonate groups, thus each removal stabilizes residual groups. ‘Rigid

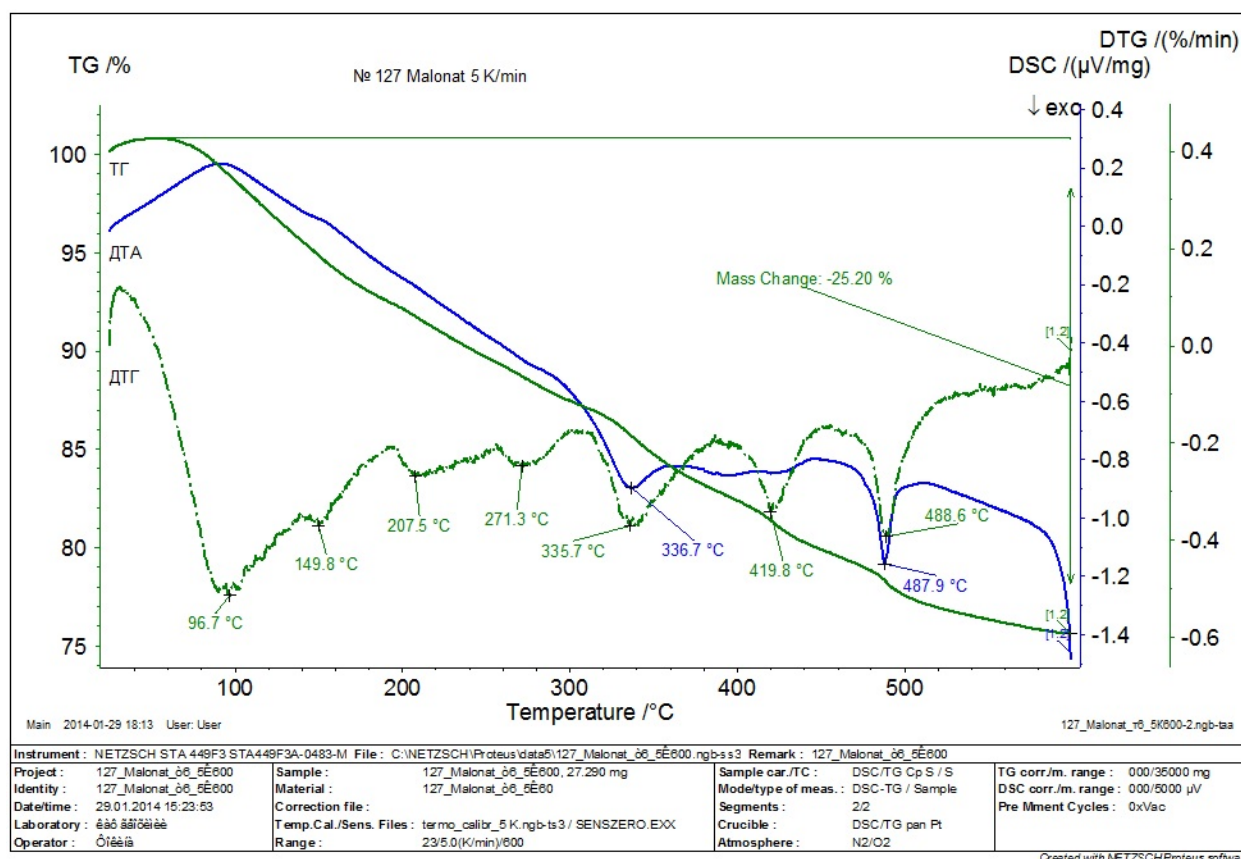


FIG. 3. The results of complex thermal analysis of crystal-hydrates of $C_{60}[=C(COOH)_2]_3$ (curves in the left axis Thermo-Gravimetry (TG) – top; Differential Thermo-Gravimetry (DTG) – bottom; Differential Thermal Analysis (DTA) – middle)

decarboxylation' (CO_2 removal) did not occur because of the tertiary nature of the carbon atom with geminally-substituted carboxyl groups.

- The subsequent three effects also correspond to 'decarbonylation with dehydration' ($C=O$ and H_2OH loss) from the three different malonate groups, thus against each allocation stabilizes residual groups. In these cases such process cannot occur without dehydrogenation because ketone hydrates (one carbon atom with two hydroxyl groups, $OH - (R_2)C(R_1) - OH$) are usually unstable.
- One can see that (according to TG curve) mass effect of the first three allocations is nearly 60 relative % from the mass effect of second three allocations, which also proves the complex mechanism of malonate decomposition.

Thus, poly-thermal solubility of water soluble tris-malonate of light fullerene – $C_{60}[=C(COOH)_2]_3$ from 20 – 80 °C and complex thermal analysis of the last one in the temperature range 25 – 600 °C were investigated. One can see that diagram of solubility in the binary system consists of two branches, which correspond to the crystallization of the C_{60} – tris-malonate trihydrate and tris-malonate without water, correspondingly. Complex thermal analysis demonstrates six-stage soft and crude decarbonylation processes, with the formation of gaseous CO and $CO + H_2O$, correspondingly.

Acknowledgment

Research was performed using equipment of the Resource Center 'GeoModel' of Saint-Petersburg State University.

References

- [1] K.N. Semenov, N.A. Charykov, A.S. Kritchenkov, et al. Synthesis and identification water-soluble tris-malonate of light fullerene – $C_{60}[=C(COOH)_2]_3$. *Nanosystems: Physics, Chemistry, Mathematics*, **5** (2), P. 315–319 (2014).
- [2] K.N.Semenov, N.A.Charykov, A.S.Kritchenkov et al. Volume properties of water solutions and refraction at 25 °C water soluble tris-malonate of light fullerene – $C_{60}[=C(COOH)_2]_3$. *Nanosystems: Physics, Chemistry, Mathematics*, **5** (3), P. 427–434 (2014).
- [3] I.Lamparth, A.Hirsch. Water-soluble malonic acid derivatives of C_{60} with a defined three-dimensional structure. *J. Chem. Soc Chem. Commun.*, P. 1727–1728 (1994).
- [4] L.B.Piotrovskiy, O.I.Kiselev. *Fullerenes in biology*. Rus. S-Petersburg, (2006) 334 pp.
- [5] D.Heymann. Solubility of C_{60} in alcohols and alkanes. *Carbon*, **34** (5), P. 627–631 (1996).
- [6] M.T.Beck, G.Mandi. Solubility of C_{60} . *Fullerene science and technology*, **5**, P. 291–310 (1997).
- [7] M.V.Korobov, A.L.Smith. Solubility of Fullerenes. *Fullerenes: Chemistry, Physics and Technology*, John Wiley & Sons, New York, P. 53–59 (2000).
- [8] K.N.Semenov, N.A.Charykov, V.A.Keskinov, et al. Solubility of light Fullerenes in Organic Solvents. *J. Chem. Eng. Data*, **55**, P. 13–36 (2010).
- [9] D. Heymann. Solubility of fullerenes C_{60} and C_{70} in seven normal alcohols and their deduced solubility in water. *Fullerene Science and Technology*, **4** (3), P. 509–515 (1996).
- [10] D. Heymann. Solubility of fullerenes C_{60} and C_{70} in water. *Lunar and Planetary Science*, **27**, P. 543–544 (1996).
- [11] K.N. Semenov, N.A. Charykov, V.A. Keskinov. *Synthesis and Identification. Properties of Fullerenol Water Solutions*. *J. Chem. Eng. Data*, **56**, P. 230–239 (2011).
- [12] K.N. Semenov, N.A Charykov. Solubility of light fullerenes and fullerenol in biocompatible with human beings solvents. Chapter in Handbook: *Grapes: Cultivation, Varieties and Nutritional Uses*. Nova Sciences Publishers, Inc., Editor R.P.Murphy et al., P. 1–48 (2011).
- [13] K.N. Semenov, N.A. Charykov. Phase Equilibria in the Fullerene-Containing Systems. Handbook on Fullerene: Synthesis, Properties and Applications, Editor R.F.Verner, C.Benvegny, P. 1–91 (2012).
- [14] Rus. Technical Conditions (TU) 6-09-4921-80. CAS Number 141-95-7.

EFFECT OF CALCINATION TEMPERATURE ON THE STRUCTURAL AND OPTICAL PROPERTIES OF NICKEL OXIDE NANOPARTICLES

P. A. Sheena¹, K. P. Priyanka², N. Aloysius Sabu², Boby Sabu², Thomas Varghese^{2,*}

¹M. E. S. Asmabi College, P. Vemballur - 680671, Kerala, India

²Nanoscience Research Centre (NSRC), Department of Physics, Nirmala College, Muvattupuzha - 686 661, Kerala, India

*nanoncm@gmail.com

PACS 78.67.Bf, 81.16.Be, 81.07.Bc

Herein, we report the effect of calcination on the structural and optical properties of nanocrystalline NiO. NiO nanoparticles were synthesized by chemical precipitation method using nickel nitrate hexahydrate and ammonium carbonate. Thermogravimetric analysis was done to determine the thermal behavior of the precursor. The samples were characterized by X-ray diffraction (XRD), energy dispersive X-ray analysis (EDAX), high resolution transmission electron microscopy (HRTEM), Fourier transform infrared spectroscopy (FTIR), UV-visible and photoluminescence (PL) spectroscopy. Crystallite size and lattice strain on peak broadening of NiO nanoparticles have been studied using Williamson–Hall (WH) analysis. Significant modifications were observed in the crystallite size, absorption spectra and photoluminescence intensity due to calcination. The desired structural and optical properties of NiO nanoparticle make it as a promising material for optoelectronic applications.

Keywords: nickel oxide nanoparticles, chemical precipitation, calcination, crystallite size, optical band gap.

Received: 8 May 2014

Revised: 24 May 2014

1. Introduction

In recent years nanocrystalline transition metal oxides have attracted extensive interest due to their different potential applications. Out of these, Nickel oxide (NiO) is an attractive material due to its chemical stability. NiO has a wide intrinsic band gap of ~ 3.6 eV. It shows interesting optical, electrical and magnetic properties [1, 2]. It is a promising candidate for wide range of applications such as smart windows, gas sensors [3], catalysts [4-6], anode material in Li ion batteries and nanoscale optoelectronic devices such as electro chromic display [7, 8]. As an ion storage material, NiO semiconductor becomes a motivating topic in the new era of research. These applications can be enhanced by decreasing the particle size and hence a precise control of the size and distribution in the nanometer region is required.

Various techniques have been adopted for the synthesis of NiO nanostructures such as sol-gel [9-12], co-precipitation [12], hydrothermal [13], solvo-thermal [14] and chemical precipitation [6, 15]. In the present study, we have prepared NiO nanoparticles using the chemical precipitation route which can yield high purity products at low cost starting from easily available materials. Synthesized NiO nanoparticles have been characterized by XRD, EDAX, TEM, FTIR spectroscopy, UV-visible and PL spectroscopy.

2. Experimental details

Nickel nitrate hexahydrate ($\text{Ni}(\text{NO}_3)_2 \cdot 6\text{H}_2\text{O}$) (99.8%, Merck) and ammonium carbonate ($(\text{NH}_4)_2\text{CO}_3$) (99.9%, Merck) were used without further purification for the synthesis of NiO. Distilled water was used in all synthesis procedures.

2.1. Preparation of the sample

Nanocrystalline NiO samples were prepared by reacting aqueous solutions of nickel nitrate hexahydrate and ammonium carbonate (0.1M each) under stirring. The green precipitate formed was washed with distilled water several times to remove the unreacted salts, and dried in a hot air oven at 70°C for 20 h. The precursor obtained was calcined in a muffle furnace at different temperatures, ranging from 400–600°C for 2 hours, which resulted in a black solid mass. NiO samples calcined at 400°C, 500°C and 600°C are denoted as S1, S2 and S3 respectively.

2.2. Characterization techniques

Thermogravimetric (TG) analysis of the precursor was carried out using a Perkin Elmer, Diamond instrument with a heating rate of 10.00°C/min. The structural characterization of the samples were done by X-ray powder diffraction using Bruker D8 Advance X-ray diffractometer ($\lambda = 1.5406 \text{ \AA}$, step size = 0.020° and dwell time = 31.2 s) with $\text{CuK}\alpha$ radiation in 2θ range from 20 to 80°. EDAX spectrum was obtained on a JEOL Model JED-2300 equipment with an accelerating voltage of 30 kV. TEM and HRTEM images were recorded on a JEOL-2010 at an accelerating voltage of 200 kV. Fourier transform infrared spectra of the samples were recorded using Thermo Nicolet, Avatar 370 instrument. Shimadzu 2600/2700 UV-Visible spectrophotometer was used to record the optical absorption spectra of the samples in a wavelength range of 200 to 600 nm. Photoluminescence spectra were measured over wavelengths ranging from 250–650 nm at room temperature by a Fluoromax3 spectrophotometer.

3. Results and discussion

3.1. Thermogravimetric analysis

Fig. 1 shows the thermal decomposition result of the precursor from the ambient temperature to 700°C using both the thermogravimetric and the differential thermogravimetric (DTG) curves. The TG curve indicates that the weight loss of the precursor occurred from 50°C to 350°C. This suggests that the precursor decomposed completely at 350°C to become nickel oxide [10, 16]. Therefore the choice of suitable calcination temperature is highly dependent on the results of TG analysis. Two distinct intervals of weight loss were observed in the TG curve, accompanied by two peaks of weight loss rate in the DTG curve. The first peak located around 100°C might be attributed to the thermal dehydration of the precursor and the evaporation of physically adsorbed impurities. The second peak near 300°C may be related to the decomposition of nickel carbonate. Based on the results of TGA, a temperature of 400°C was chosen to ensure the complete decomposition of the precursor to form nickel oxide.

3.2. XRD analysis

The phase composition, purity and structure of the samples were examined using XRD. Fig. 2 depicts the XRD patterns of the samples calcined at different temperatures. Well defined diffraction peaks are observed in the figure corresponding to (111), (200), (220),

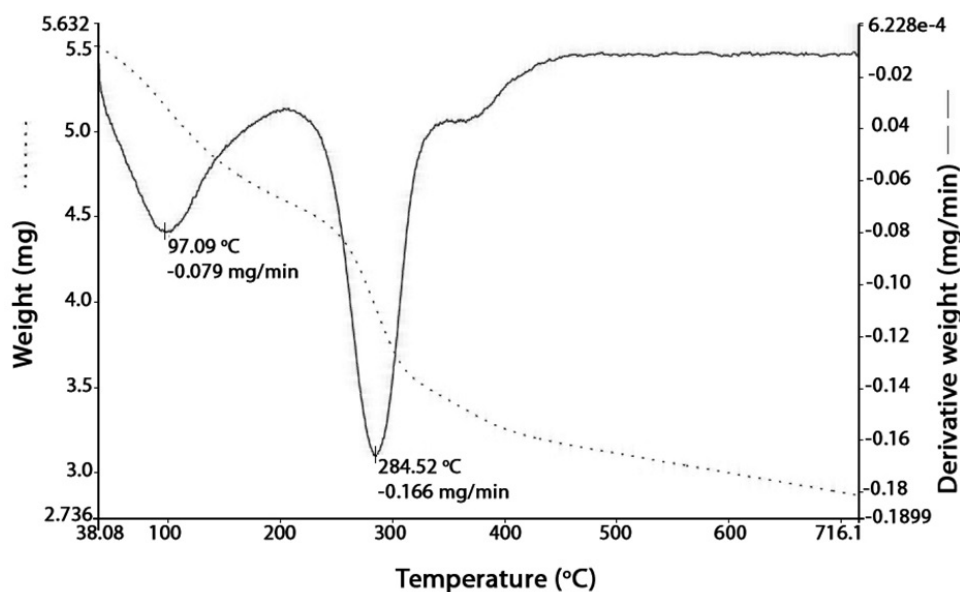


FIG. 1. TG/DTG curve for NiO nanoparticles

(311) and (222) planes of cubic NiO crystals, which are in accordance with the standard spectrum (JCPDS, No.73-1519) [11]. From the analysis of positions and relative intensities of the diffracted peaks, the presence of single phase cubic structure of NiO with a space group $Fm\bar{3}m$ is confirmed. Lattice constants calculated from XRD data are 0.4180 nm, 0.4176 nm and 0.4171 nm respectively, for samples S1, S2 and S3 which are in good agreement with the reported data [17].

Fig. 2 shows that the diffraction peaks become intense and their full width at half maximum (FWHM) gradually decreases with increasing calcination temperatures. The reason is that at higher calcination temperatures, the formed crystallites are larger in size, which can be attributed to the thermally promoted crystallite growth.

The crystallite sizes of all samples were calculated from the line broadening of the diffraction peaks using Scherrer's formula [18]. The crystallite size was found to increase with an increase in the calcination temperature. Williamson- Hall analysis was carried out to calculate the contributions of size and micro-diffraction to XRD line broadening. The W-H equation [19-21] is given by,

$$\beta \cos \theta = k\lambda/D + 4\varepsilon \sin \theta. \quad (1)$$

The results are presented in table 1. The very small micro-diffraction values for all the samples lead to the close agreement between the crystallite sizes estimated from Scherrer's equation and W-H analysis. The presence of O vacancies, structural imperfections and surface defects in NiO nanoparticles can introduce micro-diffraction that results in the broadening of XRD peaks [22, 23]. It is found that the micro-diffraction for NiO calcined at 400°C has large value, which decreases with increase in calcination temperature. This occurs because defects like dislocations, edges or cuts are probably removed during the calcination process [22].

3.3. Energy dispersive X- ray analysis

Nickel (II) oxide is generally known as a non-stoichiometric compound ($Ni_{1-x}O$) with color varying from gray to black. EDAX analysis was carried out to know the presence of

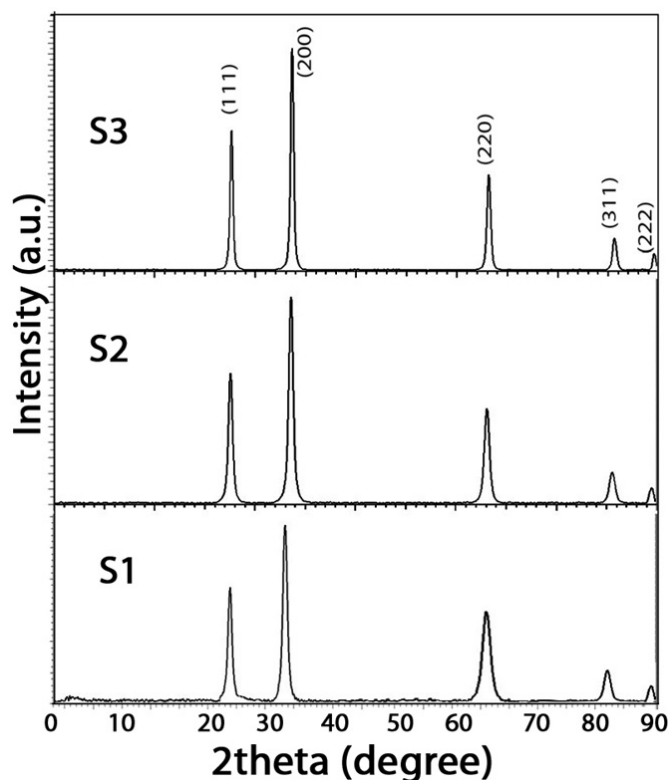


FIG. 2. XRD patterns of the NiO nanoparticle samples

TABLE 1. Geometric parameters of NiO nanoparticle from XRD spectra

Sample	Particle size (nm)	W-H method	
	Sherrer's equation	Particle size (nm)	Microstrain ($\times 10^{-3}$)
S1	9.82 ± 0.196	10.83 ± 0.217	6.67 ± 0.13
S2	16.84 ± 0.337	16.91 ± 0.338	0.65 ± 0.013
S3	23.54 ± 0.47	26.16 ± 0.523	0.1 ± 0.002

nickel oxide in the sample. The EDAX pattern (Fig. 3) of the sample shows the presence of nickel and oxygen. The mass percentage and the atom percentage of the prepared sample are given in table 2. EDAX confirmed that the NiO sample contains nickel and oxygen with a molecular ratio of 1 : 1, with no trace of any other materials.

TABLE 2. EDAX data for NiO nanoparticles

Elements	keV	Mass %	Atom %
O K	0.525	9.3 ± 0.186	27.34 ± 0.547
Ni K	7.471	90.7 ± 1.814	72.66 ± 1.453
Total		100	100

3.4. TEM analysis

In order to reveal the morphology and size of the synthesized products, typical TEM and HRTEM images have been recorded, as shown in Fig. 4. Fig. 4(a) shows the TEM

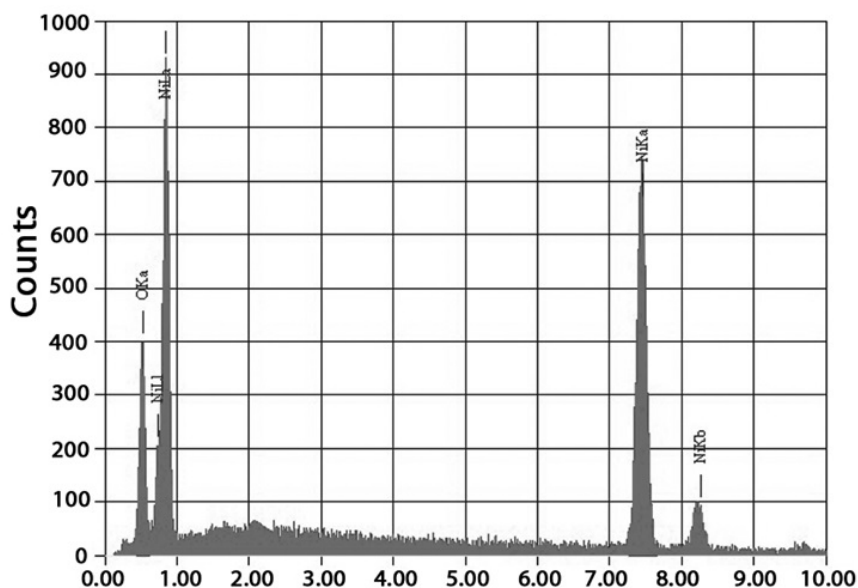


FIG. 3. EDAX pattern of NiO nanoparticles

bright field images of NiO nanoparticles calcined at 400°C. It can be clearly observed that the synthesized product consisted of nearly cube shaped particles with size around 13 nm. However, average crystallite sizes obtained from Scherrer's formula and W-H analysis show a slight decrease from that of TEM images, because of the difference in averaging particle size distribution. The lattice fringes can be clearly seen from the HRTEM image (Fig. 4(b)), in which inter planar distance is determined to be about 0.21 nm, which is consistent with the d spacing of (200) of cubic NiO. From HRTEM image the unidirectional fringe patterns are clearly observed, which indicates single crystalline nature of NiO nanoparticle.

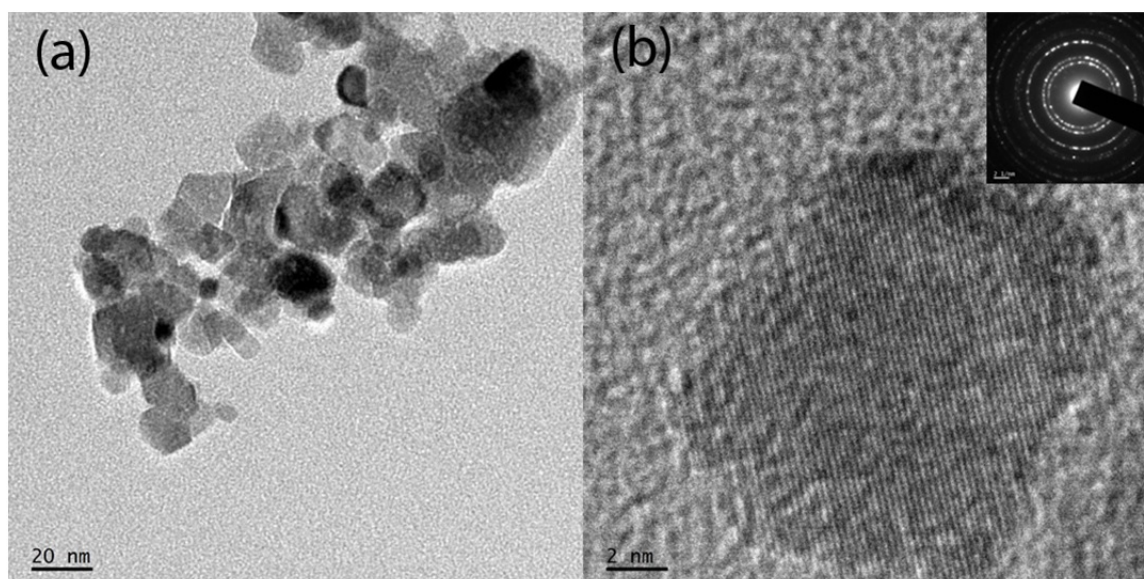


FIG. 4. TEM images of NiO nanoparticles calcined at 400°C

Selected area electron diffraction pattern (SAED) originated from the NiO nanoparticles is shown in the inset of Fig. 4 (b). The appearance of strong diffraction spots rather

than diffraction rings confirmed the formation of single crystalline cubic nickel oxide. Size distribution and abundance of NiO nanoparticles is plotted in histogram shown in Fig. 5.

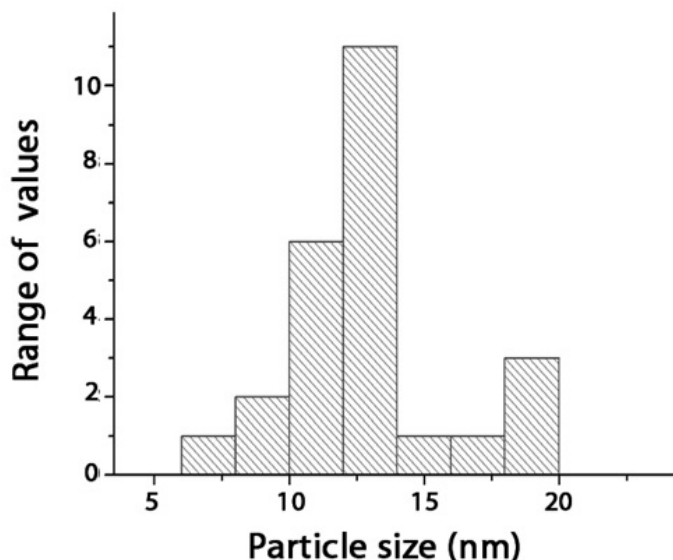


FIG. 5. Size distribution of NiO nanoparticles

3.5. FTIR analysis

The FTIR spectra of the samples calcined at 400°C and 500°C are shown in Fig. 6. The spectrum has several significant absorption peaks recorded in the range of 4000 cm^{-1} to 400 cm^{-1} . The broad absorption band centered at 3450 cm^{-1} is assigned to O–H stretching vibrations and the band at 1630 cm^{-1} is attributable to H–O–H bending vibration mode. These indicate the presence of traces of water in the sample. The broad absorption band in the region 430–490 cm^{-1} is assigned to Ni–O stretching vibration mode [14]. The broadness of the band indicates the nanocrystalline nature of the samples.

3.6. UV - Vis studies

Fig. 7 shows UV-visible absorption spectra and $(\alpha h\nu)^2$ versus energy plot for NiO nanoparticles samples. It can be seen (Fig. 7 (a)) that there is an exponential decrease in the intensity of absorption with increase in wavelength. This behavior is typical for many semiconductors and can occur due to various reasons like internal electric fields within the crystal, deformation of lattice due to strain caused by imperfection and inelastic scattering of charge carriers by phonons [9]. It can be seen from Fig. 7 (a) that the absorption edge corresponding to samples S1, S2 and S3 are at 365, 375 and 415 nm respectively. Small blue shift was exhibited by samples S1 and S2 because of their small particle sizes.

Optical band gap energy values obtained from Fig. 7 (b) are 3.385, 3.30, and 3.18 eV respectively for the samples S1, S2 and S3. The optical band gap of NiO in the present study is lower than the bulk value (3.65 eV). This may be due to the chemical defects or vacancies present in the crystal generating new energy level to reduce the band gap energy. However, the band gap is found to decrease with an increase in the calcination temperature due to the crystallite growth.

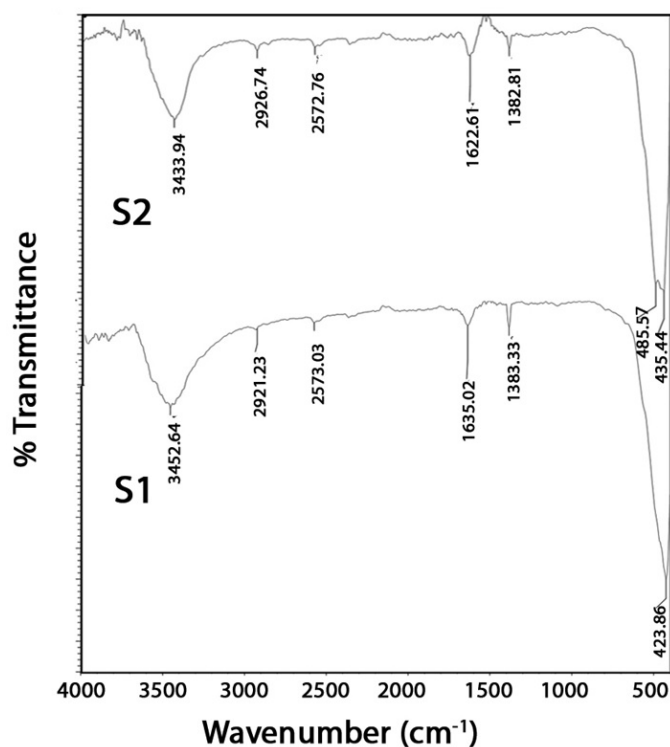
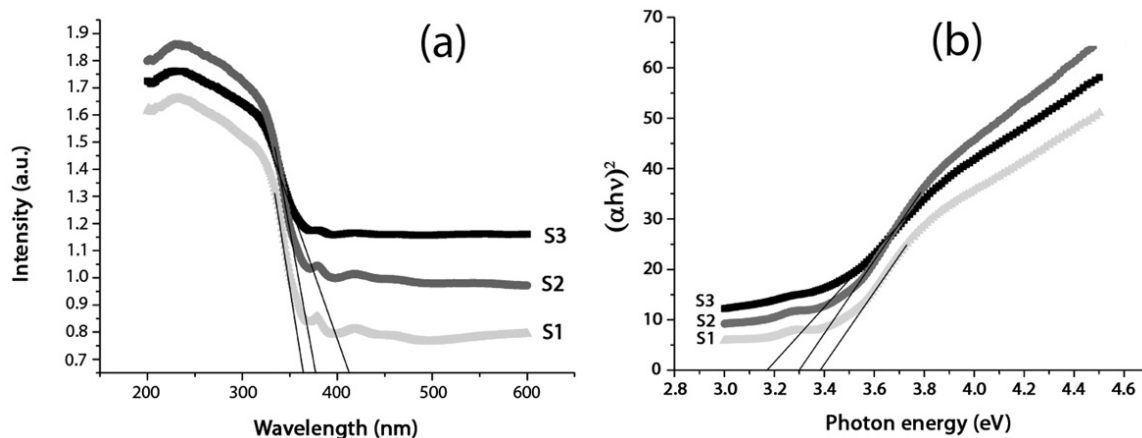


FIG. 6. FTIR spectra of NiO nanoparticle samples

FIG. 7. (a) UV-Visible absorbance spectra and (b) $(\alpha h\nu)^2$ vs energy plot for NiO samples

3.7. PL studies

Room temperature photoluminescence emission spectra of NiO nanoparticle samples calcined at different temperatures are shown in Fig. 8. NiO nanoparticles exhibit a strong and wide peak in the 350 to 425 nm range with an excited wavelength of 280 nm. The figure shows two obvious PL peaks at about 448 and 466 nm along with some shoulder emission peaks at 370, 380, 396, 410, 481 and 490 nm. The origin of photoluminescence peaks is attributed to electronic transitions involving $3d^8$ electrons of the Ni^{2+} ions [14].

The broad peak in PL spectra corresponds to the direct recombination between electrons in the conduction band and holes in the valence band. It is found that the PL intensity

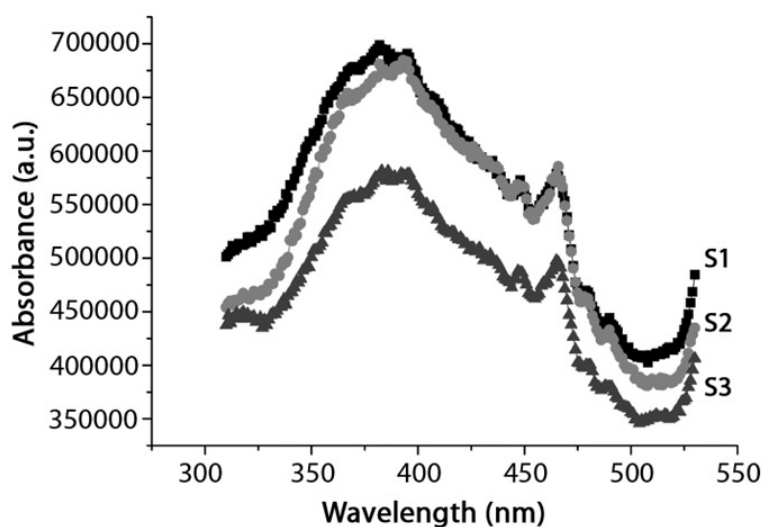


FIG. 8. Room temperature PL spectra for NiO samples

remains the same for samples S1 and S2. However, there was a decrease in intensity for the sample S3. If the size of particle is smaller, oxygen vacancy content is larger, and absorption over UV and visible range increases. Hence, samples S1 and S2 have higher chance of exciton occurrence, which in turn cause stronger PL signal. Moreover, calcination can result in decreased PL intensity due to crystal growth.

4. Conclusions

Nanostructured NiO particles have been successfully synthesized through the chemical precipitation technique using nickel nitrate hexahydrate and ammonium carbonate. TGA results show a sharp weight loss at 350°C, caused by the conversion of nickel carbonate into nickel oxide. The results obtained from XRD and TEM confirms the nanocrystalline nature of the synthesized particles and the crystallite size was found to increase with increase in calcination temperatures. W-H analysis found that the micro-diffraction for NiO calcined at 400°C has large value, which decreases with increase in calcination temperature. UV-visible absorption studies revealed that an increase in the calcination temperature produces a blue shift in the absorption spectrum, and a decrease of band gap being a consequence of the increase in particle size. Also, photoluminescence studies showed that an increase in calcination temperature causes a decrease in PL intensity due to crystal growth. Furthermore, calcination temperature plays a vital role in controlling the particle size, which in turn helps to modify structural and optical properties of the formed NiO nanoparticles. Based on these systematic observations, it is concluded that NiO nanoparticles can be a promising material for optoelectronic applications because of its desired structural and optical properties.

Acknowledgements

Authors thank Nirmala College, Muvattupuzha for providing all the facilities to undertake this study. Authors are grateful to KSCSTE, Thiruvananthapuram, India for providing financial support. First author is thankful to U G C, New Delhi, India for providing financial grant under minor research project.

References

- [1] Dharmaraj N., Prabu P., Nagarajan S., Kim C.H., Park J.H., Kim H.Y. Synthesis of nickel oxide nanoparticles using nickel acetate and poly(vinyl acetate) precursor. *Materials Science and Engineering B*, **128**, P. 111–114 (2006).
- [2] Feldman C., Jungk H.O. Polyol-Mediated preparation of nanoscale oxide particles. *Angew Chem. Int. Ed.*, **40**, P. 359 (2001).
- [3] Matsumiya M., Qiu F., et al. Thin-film Li-doped NiO for thermoelectric hydrogen gas sensor. *Thin Solid Films*, **419**(1-2), P. 213–217 (2002).
- [4] Wang, Y., Zhu, J., et al. Preparation of NiO nanoparticles and their catalytic activity in the thermal decomposition of ammonium perchlorate. *Thermochim. Acta*, **437** (1–2), P. 106–109 (2005).
- [5] Ichiyonagi Y., Wakabayashi N., et al. Magnetic properties of NiO nanoparticles. *Physica B*, **329–333** (Part 2), P. 862–863 (2003).
- [6] Biju V., Abdul Khadar M. Analysis of AC electrical properties of nanocrystalline nickel oxide. *Mater. Sci. Eng. A*, **304–306**, P. 814–817 (2001).
- [7] Li F., Chen H., Wang C., Hu K. A novel modified NiO cathode for molten carbonate fuel cells. *J. Electroanal. Chem.*, **531**(1), P. 53–60 (2002).
- [8] Nuli Y., Zhao S., Qin Q. Nanocrystalline tin oxides and nickel oxide film anodes for Li-ion batteries. *J. Power Sources*, **114**(1), P. 113–120 (2003).
- [9] Mallick P., Sahoo C. S., Mishra N. C. Structural and Optical Characterization of NiO nanoparticles synthesized by sol-gel route. *AIP Conf. Proc.*, **1461**, P. 229–232 (2012).
- [10] Alagiri M., Ponnusamy S., Muthamizhchelvam C. Synthesis and Characterization of NiO nanoparticles by sol-gel method. *J. Mater Sci: mater Electron*, **23** P. 728–732 (2012).
- [11] Jeevanandam P., Ranga Rao Pulimi V. Synthesis of nanocrystalline NiO by sol-gel and homogeneous precipitation methods. *Indian J Chem.*, **51A**, P. 586–590 (2012).
- [12] Mallick P., Chandana rath, Biswal R., Mishra N. C. Structure and magnetic properties of Fe doped NiO. *Indian J. Phys.*, **83**, P. 517 (2009).
- [13] Takami S., Hayakawa R., Wakayama Y., Chikyow T. Continuous hydrothermal synthesis of nickel oxide nanoplates and their use as nanoinks for p-type channel material in a bottom-gate field-effect transistor. *Nanotechnol*, **21**, P. 134009 (2010).
- [14] Anandan K., Rajendran V. Morphological and size effects of NiO nanoparticles via solvothermal process and their optical properties. *Mater. Sci. Semicond. Process*, **14**, P. 43 (2011).
- [15] Chakrabarty S., Chatterjee K. Synthesis and characterization of nanodimensional NiO semiconductor. *J. Phy. Sci.*, **13**, P. 245–250 (2008).
- [16] Jianfen Li, Rong Yan, et al. Preparation of nano-nio particles and evaluation of their catalytic activity in pyrolyzing biomass components. *American Chem. Soc.*, P. 1021 (2008).
- [17] Jahromi S. P., Huang N. M., Muhamad M. R., Lim H. N. Solvothermal synthesis of SnO₂/graphene nanocomposites for supercapacitor application. *Ceram. Int.*, **39**, P. 3909 (2008).
- [18] Varghese T., Balakrishna K. M. *Nanotechnology: An introduction to synthesis, properties and applications*. Atlantic Publishers, New Delhi, 2011, P. 111.
- [19] Mote V.D., Purushotham Y., Dole B.N. Williamson-Hall analysis in estimation of lattice strain in nanometer-sized ZnO particles. *J. Theor Appl Phys*. **6**:1–8 (2012).
- [20] Prabhu Y. T., Venkateswara K. R., Sesha V.S.K. and Siva Kumari B. X-ray analysis of Fe doped ZnO nanoparticles by Williamson-Hall and size-strain methods. *Int. J. Engg. Adv. Tech.*, **2**(4), P. 268 (2013).
- [21] Williamson G.K. Hall W. H. X-ray line broadening from fcc Al and W. *Acta Metall.*, **1**, P. 22 (1953).
- [22] Fernández G. M., Martínez-Arias A., Hanson J. C., Rodríguez J. A. Nanostructured oxides in chemistry: Characterization and properties. *Chem. Rev.*, **104**, P. 4063 (2004).
- [23] Di Monte R., Kašpar J. Nanostructured CeO₂-ZrO₂ mixed oxides. *Catal. Today*, **100**, P. 27 (2005).



NANOSYSTEMS:

PHYSICS, CHEMISTRY, MATHEMATICS

INFORMATION FOR AUTHORS

The journal publishes research articles and reviews, and also short scientific papers (letters) which are unpublished and have not been accepted for publication in other magazines. Articles should be submitted in English. All articles are reviewed, then if necessary come back to the author to completion.

The journal is indexed in Chemical Abstract Service of the American Chemical Society and in Russian Scientific Citation Index.

Author should submit the following materials:

1. Article file in English, containing article title, the initials and the surname of the authors, Institute (University), postal address, the electronic address, the summary, keywords, MSC or PACS index, article text, the list of references.
2. Files with illustrations, files with tables.
3. The covering letter in English containing the article information (article name, MSC or PACS index, keywords, the summary, the literature) and about all authors (the surname, names, the full name of places of work, the mailing address with the postal code, contact phone number with a city code, the electronic address).
4. The expert judgement on possibility of publication of the article in open press (for authors from Russia).

Authors can submit a paper and the corresponding files to the following addresses: nanojournal.ifmo@gmail.com, popov1955@gmail.com.

Text requirements

Articles should be prepared with using of text editors MS Word or LaTeX (preferable). It is necessary to submit a pdf copy. In the name of files the English alphabet is used. The recommended size of short communications (letters) is 4-6 pages, research articles – 6-15 pages, reviews – 30 pages.

Recommendations for text in MS Word:

Formulas should be written using Math Type. Figures and tables with captions should be inserted in the text. Additionally, authors present separate files for all figures and Word files of tables.

Recommendations for text in LaTeX:

Please, use standard LaTeX without macros and additional style files. The list of references should be included in the main LaTeX file. Single LaTeX file of the paper with the corresponding pdf file should be submitted.

References in the article text are given in square brackets. The list of references should be prepared in accordance with the following samples:

- [1] N. Surname. *Book Title*. Nauka Publishing House, Saint Petersburg, 281 pp. (2000).
- [2] N. Surname, N. Surname. Paper title. *Journal Name*, **1**(5), P. 17-23 (2000).
- [3] N. Surname, N. Surname. Lecture title. In: Abstracts/Proceedings of the Conference, Place and Date, P. 17-23 (2000).
- [4] N. Surname, N. Surname. Paper title (2010). URL: <http://books.ifmo.ru/ntv>.
- [5] N. Surname, N. Surname. Patent Name. Patent No. 11111, Bul. No. 33, 5 pp. (2010).
- [6] N. Surname, N. Surname. Thesis Title. Thesis for full doctor degree in math. and physics, Saint Petersburg, 105 pp. (2000).

Requirements to illustrations

Illustrations should be submitted as separate black-and-white files. Formats of files – jpeg, eps, tiff.



NANOSYSTEMS:

PHYSICS, CHEMISTRY, MATHEMATICS

Журнал зарегистрирован

Федеральной службой по надзору в сфере связи, информационных технологий и массовых коммуникаций

(свидетельство ПИ № ФС 77 - 49048 от 22.03.2012 г.)

ISSN 2220-8054

Учредитель: федеральное государственное бюджетное образовательное учреждение высшего профессионального образования «Санкт-Петербургский национальный исследовательский университет информационных технологий, механики и оптики»

Издатель: федеральное государственное бюджетное образовательное учреждение высшего профессионального образования «Санкт-Петербургский национальный исследовательский университет информационных технологий, механики и оптики»

Отпечатано в учреждении «Университетские телекоммуникации»
Адрес: 197101, Санкт-Петербург, Кронверкский пр., 49

Подписка на журнал НФХМ

На второе полугодие 2014 года подписка осуществляется через
ОАО Агентство «Роспечать»

Подписной индекс 57385 в каталоге «Издания органов научно-технической информации»